Insight into Biological Small-Molecule Activation from Enzymes, Model Complexes, and X-ray Spectroscopy

Julian Avery Rees

A dissertation submitted in partial fulfillment of the requirements for the degree of

Doctor of Philosophy

University of Washington

2016

Reading Committee:

Julie A. Kovacs, Chair
Daniel R. Gamelin
Stefan Stoll

Program authorized to offer degree:

Chemistry

University of Washington

Abstract

Insight into Biological Small-Molecule Activation from Enzymes, Model Complexes, and X-ray Spectroscopy

Julian Avery Rees

Chair of the Supervisory Committee:

Professor Julie A. Kovacs
Department of Chemistry

This dissertation covers the investigation of biological strategies for activating inert small molecules. Chapters 1 and 2 respectively present an introduction to some notable biological systems of interest and the X-ray spectroscopic techniques used in their study. Chapter 3 focuses on the application of X-ray spectroscopy and density functional theory to investigate the underlying mechanisms of O-O bond activation by a manganese complex. Chapter 4 presents the discovery of a key structural feature of the vanadium-containing active site of V-dependent nitrogenases, and Chapter 5 provides a detailed comparison of the electronic structures of the Mo- and V-containing nitrogenase cofactors based on spectroscopic characterization of both enzymes and synthetic metallocubane models. Chapter 6 covers a fundamental study of the X-ray absorption and emission spectroscopic features of vanadium ions, providing a basis for the spectroscopic investigation of vanadium-containing enzymes, including nitrogenase. This work contains novel research into the structure-function relationship in both biological and synthetic systems that promote the activation of inert, abundant small molecules. The insight obtained from these studies may help to advance scientific understanding of the complex functions of transition metal ions in biological catalysis.

Table of Contents

List of Figures

List of Schemes

List of Tables

Glossary

ΔG°	standard free energy
$\Delta H^\ddagger$	enthalpy of activation
$\Delta S^\ddagger$	entropy of activation
cm^{-1}	wavenumber
Å	ångström
e$^-$	electron
acetyl-CoA	acetyl coenzyme A
ADP	adenosine diphosphate
ATP	adenosine triphosphate
Cat	catalase
CI	configuration interaction
CO	carbon monoxide
Cu	copper
DFT	density functional theory
DNA	deoxyribonucleic acid
EPR	electron paramagnetic resonance
ESEEM	electron spin echo envelope modulation
ESI-MS	electrospray ionization mass spectrometry
ET	electron transfer
eV	electron volt
EXAFS	extended X-ray absorption fine structure
Fe	iron
FeMoco	iron-molybdenum cofactor
FeVco	iron-vanadium cofactor
FWHM	full width at half maximum
Glu	glutamate
HAT	hydrogen atom transfer
HERFD	high energy resolution fluorescence detected
IWAE	intensity-weighted average energy
K	Kelvin
kcal	kilocalories
LHe	liquid helium
LO	lipoxygenase
mA	milliampere
Mg	magnesium
mg	milligram
mL	milliliter
MLCT	metal-to-ligand charge transfer
mM	millimolar
mm	millimeter
MMCT	metal-to-metal charge transfer
Mn	manganese
MO	molecular orbital
Mo	molybdenum
MoFe	molybdenum-iron protein
mol	moles
mV	millivolts
N$_2$	dinitrogen
NH$_3$	ammonia

Ni nickel

NRVS nuclear resonance vibrational spectroscopy

OEC oxygen-evolving complex

PCET proton-coupled electron transfer

PDB protein data bank

PSII photosystem II

RIXS resonant inelastic X-ray scattering

RNR ribonucleotide reductase

RXES resonant X-ray emission spectroscopy

S sulfur

s second

SAM *S*-adenosylmethionine

SOC spin-orbit coupling

SOD superoxide dismutase

SQUID superconducting quantum interference device

TD-DFT time-dependent density functional theory

TFY total fluorescence yield

TON turnover number

Tyr tyrosine

VtC valence-to-core

XANES X-ray absorption near edge spectroscopy

XAS X-ray absorption spectroscopy

XES X-ray emission spectroscopy

> *"Not everything that counts can be counted, and not everything that can be counted counts."*
>
> Albert Einstein
> *attributed*

Acknowledgements

My undergraduate research advisor once told me that graduate school was one of the most enjoyable periods of his life. At the time I was convinced he must have been remembering a different five year stretch of early adulthood, not in the least because Ann Arbor, Michigan is, well, cold. I think now however I can relate to the sentiment far more readily than when I was finishing my undergraduate studies. I have had a tremendous amount of fun during this adventure they call a Ph.D., due largely to the people I have been fortunate enough to interact with along the way.

Firstly, I am deeply indebted to my research advisor Julie Kovacs, for supporting me, my interests, and my work throughout my time in her group. I believe I have taken a somewhat nontraditional route in the lab, as it turns out my skills and my aspirations were not that closely aligned with one another when I began graduate school, and I am extremely grateful that she has allowed me the opportunity to wander from the normal path, even if it literally meant crossing oceans to do so.

I have a wonderful research group. I have seen and heard of groups and departments of the highest caliber where researchers are constantly arguing, fighting, and undermining each other's work, and I am so grateful that the Kovacs group, and in fact the Department of Chemistry here at the University of Washington as a whole, could not be further from that reality. Michael Coggins, Benjamin Leipzig, and Audra Johansen made me feel welcome, taught me a tremendous amount, and became my good friends over the many months we spent together. I am so thankful that they were there to patiently teach me about chemistry, grad school, and life. Helen Ferreira was my "classmate" in the lab, and we enjoyed the harrows of coursework, exams, and organic synthesis together. Despite her early exit from the group, I am very thankful that she was there for the early days, and she and I will graduate together this year.

My time in Germany was extraordinarily fruitful, both in terms of data and knowledge. It would not have been so without the gracious hospitality of Serena DeBeer, who was a phenomenal mentor and teacher for the better part of a year. I arrived in Mülheim as "the sample cook" and left a full-blown spectroscopist, and I am completely OK with it. Frank Neese has built a research department that is not only collegial, but full of world experts in their fields. My first foray into X-ray spectroscopy was guided by Vlad Martin-Diaconescu, who I am now confident was the perfect partner for my inaugural beamtime. He taught me about both the theory and practice of X-ray spectroscopy, and how to properly turn a project into a paper. I am also grateful to have shared an office with Nicole Wurster, for her hospitality at the farm, and for making me feel so welcome upon my arrival in Germany. I had the good fortune to also share an office with Mario Delgado-Jaime, who is responsible for my love / hate relationship with MATLAB and much of my philosophy regarding data fitting. Only some of which I think he would approve of. I am grateful to Joanna Kowalska and Matti van Schooneveld for their tutelage in synchrotron physics, and Joanna and I have also collaborated on projects both scientific and culinary in nature. It was wonderful to re-connect with Ben Van Kuiken in Germany, and become friends over many a half-liter of the King Lüdwig. Speaking of King Lüdwig, I have many fond memories of my time with Anselm Hahn, and a litany of witticisms crowned by the insurmountable "destiny biscuit". I would also like to acknowledge Alex Nyrow and Sergey Peredkov for not only their help with collecting some important pieces of data but also some more advanced instruction on the physics of X-ray spectroscopy. Likewise I am thankful to have had the help of Eckhard Bill and Thomas Weyhermüller in both learning and using the fantastic research facilities at the institute.

I also feel privileged to have been able to learn some intricacies of DFT from Vera Krewald, especially as we have a common interest in the same (wonderful) transition metal. I am very thankful for the "late night" crew at the institute: Rebeca Gomez Castillo and Jessica Barilone, and the enabler (provider of signatures) Nick Cox. I am further thankful that we had the opportunity to go for beamtime together, and I hope that Stefan and I were half decent instructors, even in the middle of the night. Speaking of Stefan, I am beyond thankful that we had the opportunity to meet, immediately recognize our common interests, and become fast friends. The A-team is a force to be reckoned with, either at beamtime or at the bars, and preferably not both at the same time. My time in Germany and my love of synchrotron science would certainly have both been worse off without him. I hope he will make good on his promise to visit.

Chris Pollock was my host on my first (day-long) visit to Mülheim, and it was in part due to his unbounded enthusiasm for his research there that I decided to come for a visit. Since then, we have often had the opportunity to overlap at various scientific events, and it is always a pleasure to talk science with someone so excited for, and gifted at, what they are doing. While Chris was formally part of Serena's group, he is also a part of the thriving bioinorganic community that I am so thankful to be a part of. In particular, Carsten Krebs has undertaken the biennial organization of the Penn State nerd circus, but has also become a good friend and beer-drinking colleague. Also, it is always wonderful to see *professor* Kelly Chacón, who likewise shares my love of coupling metals in biology with plenty of merriment.

I returned from Germany to a Kovacs group awash in new faces, and it has been truly enjoyable and rewarding to integrate into the group again. There is some very exciting research going on, and I have every confidence that Maike Blakely, Maks Dedushko, Penny Poon, and Abbie Ganas will excel in driving the Kovacs group in new and exciting directions. I wish all of them, and SoonCheong Kwan, all the best on their future endeavors.

I am also very grateful to the faculty and other mentors that I have been privileged to have. On my supervisory committee, it was eye-opening (in a good way) to learn phyisical inorganic chemistry from Daniel Gamelin, and it has been an honor to watch from down the hallway as Brandi Cossairt has built a phenomenally successful research group in the past four years. I am thankful to John Rehr for his physicist's insight into my doctoral research; far beyond the charge of a GSR. Finally, I am deeply indebted to Stefan Stoll for his meticulous dissection of this work, and also for an informal membership in his research group for social purposes.

In my undergradute days, I had essentially personal attention from some truly incredible faculty: Esther Gibbs (the best chemistry name possible), George Greco, Pam Douglass, Judy Levine, and my research advisor Scott Sibley. I finished my degree incredibly well-equipped to tackle not only graduate school but life as a (semi-functioning) adult. My contemporaries in chemistry, (soon-to-be Dr.) Evan Collins, Dr. Mike Rauch, and Dr. Jared Dropkin, are not only close friends, but were amazing classmates and the source of my willingness to argue about science to no end. I should also add that we as a whole are a testament to the success of the mentorship of the aforementioned faculty in chemistry. Also, my summer internship at Amgen was curated by Roger Perlmutter, and guided by Dave Meininger and Martin Wolfson. They are responsible for my keen interest in biologic medicine, and treated me to a huge diversity of lab techniques and instrumentation.

I have been fortunate to have some wonderful scientific collaborations during grad school as well, in particular Julia Schlesier and Daniel Sippel in the group of Oliver Einsle, and Claudia Kupper in the group of Franc Meyer. Together, I believe we have done some truly exciting work, and I am very thankful for their willingness to entrust me with both their precious samples and the analysis of the resultant data. My time in Germany was also very generously funded by the German Academic Exchange Service (DAAD), and I have endeavored to make the most of the opportunity that they provided.

Finally, I would like to acknowledge my close friends and family for their contributions towards my development as a creative and independent philosopher. I believe my parents provided the perfect ratio of indulgence and expectation, and together with my brother set an astronomically high bar for achievement, discipline, and character. My grandparents are exemplars of what one can achieve with hard work, intelligence, creativity, and an ability to life's hurdles into opportunities. My childhood friends, Garth, Kerry, and Jasiu, shared and amplified my creativity, independence, and excitement for learning new things. I know that all of their unknowing efforts have made significant contributions towards my own development in these areas.

I could not have hoped to meet anyone so special to me during graduate school. After all, it's a nerd circus here. Even when I saw Ellen standing in line for our orientation week barbeque in a Texas Sailing shirt, I couldn't have foreseen where we'd be today. I am beyond grateful, not just for having Ellen in my life, but also for her support, guidance, motivation, and love as we have undertaken our graduate studies together. I'm so excited for our next endeavor, and for all the ones after that as well. Thank you.

DEDICATION

For my family

CHAPTER CONTRIBUTIONS

Much of the work detailed in the following chapters would not have been possible without the valuable efforts of a number of collaborators. Their individual contributions are gratefully acknowledged below.

Chapter 3: Vlad Martin-Diaconescu processed and fit the XAS data and performed the TD-DFT calculations.

Chapter 4: Julia Schlesier and Daniel Sippel in the group of Prof. Oliver Einsle provided the samples of MoFe and VFe protein, and Ragnar Björnsson performed and analyzed the DFT calculations.

Chapter 5: Julia Schlesier, Daniel Sippel, and Oliver Einsle again provided samples of MoFe and VFe protein, as well as isolated FeMoco. Tabea Hamann and Thomas Weyermüller synthesized the Mo cubane model, and Ragnar Björnsson contributed most of the DFT calculations.

Chapter 6: Aleksandra Wandzilak processed and fit the XAS data and analyzed the XAS calculations. Dimitrios Maganas and Nicole Wurster constructed the embedded cluster models and ran initial DFT calculations, respectively. Stefan Hugenbruch, Nicole Wurster, and Fred Lima collected the XAS data, and Joanna Kowalska, Christopher Pollock, and Ken Finkelstein assisted with collection of the Kβ XES data.

Chapter 1

"If you want to understand function, study structure."

Francis Crick

Biological Small Molecule Activation

1.1 Bioinorganic Chemistry and the Function of Metal Ions

Scientific advances in molecular biology and bioinformatics have driven a rapid increase in the identification and characterization of new classes of proteins over the past decades. Of the over 100,000 entries in the Royal Society's protein data bank (PDB), over a third are now known to contain transition metal ions. As we begin to truly appreciate the structural and functional diversity of nature's molecular machinery, the importance of these transition metals becomes increasingly evident. The field of bioinorganic chemistry seeks to further our understanding of the roles of metal ions in biology, and out of neccessity sits at the junction of an array of scientific disciplines. It is definied by the coalescence of biochemistry, enzymology, coordination chemistry, and increasingly complex molecular spectroscopy, and therefore requires that the bioinorganic chemist possess a working knowledge of most, if not all, of these areas of study.

The problems facing bioinorganic chemists are equally diverse, stemming from the multitude of roles that transition metals play in nature. In contrast to the main group elements which comprise the overwhelming majority of biomass, metal ions can adopt a range of stable oxidation states, geometries, and coordination numbers. Additionally, metal ligand bonds can be exceedingly labile, and are easily made and broken with relatively small activation energies. Polycationic metals are also used to stabilize protein tertiary and quaternary structures *via* noncovalent Coulombic interactions; *e.g.* in zinc binding domains, or "zinc fingers". Transition metals also play key roles in electron transfer (ET) pathways, as one-electron chemistry induces simply a cycling between redox states rather than the generation of unstable organic radicals.

Perhaps the most critical function of metal atoms in biology is to promote chemical reactivity. Transition metals are found in the active sites of the most complex enzymatic catalysts, which often perform multielectron chemistry far more efficiently than current industrial solutions. Nature also frequently utilizes the same metal ion for a diverse range of functions, altering or "tuning" the properties of the metal through changes in the coordination environment. This exquisite manipulation of transition metal properties such as spin state, redox potential, and Lewis acidity is accomplished by alterations to the geometry and ligand identity in the primary and secondary coordination spheres. The complex relationship between structural and electronic properties, and thus function and reactivity, is a defining area of research in bioinorganic chemistry.

1.2 Manganese Metalloenzymes for O_2 and Reduced O_2 Activation

Manganese is the third most abundant transition metal in the Earth's crust, and is thus readily bioavailable. Under physiological conditions, oxidation states of II, III, and IV can be accessed, enabling a single Mn^{n+} ion to promote multielectron chemistry.[1] It is therefore a common metallocofactor in enzymes that catalyze chemical transformations. Additionally, the most common oxidation state of biological Mn, 2+, is consistently in the high-spin d^5 configuration ($S = \frac{5}{2}$), and has no ligand-field stabilization energy. As a result, Mn^{II} sites are often exceedingly kinetically labile and undergo rapid ligand exchange. This preference for an $S = \frac{5}{2}$ state eliminates the need for ligation by soft, covalent ligands such as sulfur, which would favor lower spin states due to the nephelauxetic effect. In fact, Mn-S bonds are notably absent from biochemistry, while ligation by hard donors such as oxygen and nitrogen are prevelant.[1,2] For these reasons, Mn is widely used to promote reactions involving dioxygen or its reduced derivatives, as highlighted in the following subsections.

1.2.1 Mn Superoxide Dismutase

Superoxide dismutases (SODs) catalyze the disproportionation of the toxic superoxide radical ($O_2^{-\cdot}$) to O_2 and hydrogen peroxide (H_2O_2)(Eq. 1.1).

$$2O_2^{-\cdot} + 2H^+ \longrightarrow O_2 + H_2O_2 \tag{1.1}$$

Superoxide can be generated by off-pathway respiration events, and is generally considered one of the most potentially harmful organic radicals present in biology. The SOD family thus tasked with its detoxification utilizes a range of metal ions in either mono- or binuclear active sites, including Ni, Mn, Fe, and the heterobinuclear Cu/ZnSODs.[3] While there is some diversity amongst the structures of these subgroups, the Fe and MnSODs are generally quite homologous with regard to their primary sequence.[4,5] In fact, some so-called cambialistic species are capable of promoting the SOD reaction using either a Mn or an Fe cofactor, although these are in the distinct minority.[6,7] X-ray structures of several MnSODs are known from both prokaryotes and eukaryotes, with all examples having structurally analagous active sites. The resting state of MnSOD consists of a $\mathrm{Mn^{III}}$ ion ligated by a trigonal plane of two histidine imidazoles and an aspartate carboxylate. Axial ligation by a hydroxide and a third histidine complete the nominally trigonal bipyramidal geometry (Scheme 1.1). The superoxide disproportionation reaction proceeds *via* a sequential "ping-pong"

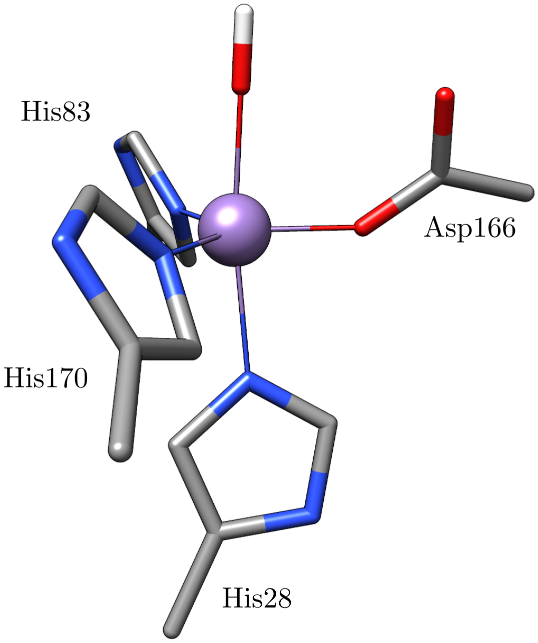

Scheme 1.1: Active site representation of MnSOD from *Thermus thermophilus*, PDB 3MDS

mechanism, in which a first equivalent of superoxide is oxidzed by the $\mathrm{Mn^{III}}$ site to form dioxygen and the reduced $\mathrm{Mn^{II}}$ form. A second equivalent of superoxide is then reduced by the enzyme, and concomitant addition of two protons yields the initial $\mathrm{Mn^{III}}$ state and an equivalent of hydrogen peroxide (Eq. 1.2, Eq. 1.3).

$$\mathrm{O_2^{-\cdot} + Mn^{III}SOD \longrightarrow O_2 + Mn^{II}SOD} \tag{1.2}$$

$$\mathrm{O_2^{-\cdot} + 2H^+ + Mn^{II}SOD \longrightarrow H_2O_2 + Mn^{III}SOD} \tag{1.3}$$

The aqueous properties of di- and trivalent Mn and Fe are additionally quite distinct, however Nature's management of redox potential and Lewis acidity through the ligand environment enables both metals to facilitate the same reaction. Additionally, despite highly similar active site structures, all but a few Mn and FeSODs require the native metallocofactor to function (*vide supra*). While the SODs are simply one example of this phenomenon, enzymatic preference for a particular metal ion in spite of seemingly identical active site structures is very much an active area of research.[8] At the least, this suggests that the biochemical strategies employed to tune and regulate reactivity can extend beyond solely the primary coordination sphere.

1.2.2 Mn Lipoxygenase

Lipoxygenases (LOs) catalyze the dioxygenation of polyunsaturated fatty acids with a *cis,cis*-1,4-pentadiene moiety, utilizing almost exclusively a mononuclear Fe cofactor in the active site and dioxygen as the terminal oxidant. The Fe-dependent LOs are well-studied, and X-ray crystal structures exist of FeLOs isolated from plant, animal, and prokaryotic organisms.[9] In 1998 Oliw *et al.* reported the isolation of a Mn-dependent lipoxygenase from the wheat fungus *Gäumannomyces graminis*, distinct in not only the identity of the metallocofactor but also the presence of valine at the C-terminus, in place of a well-conserved isoleucine in many FeLOs.[10] Since that report, the active site geometries of the MnLOs were presumed to be similar, however it was not until early 2016 that the first X-ray structure of a MnLO was reported. As shown in Scheme 1.2, the active site of the MnLO from the rice blast fungus *Magnaporthe oryzae* contains a facial triad of histidines,

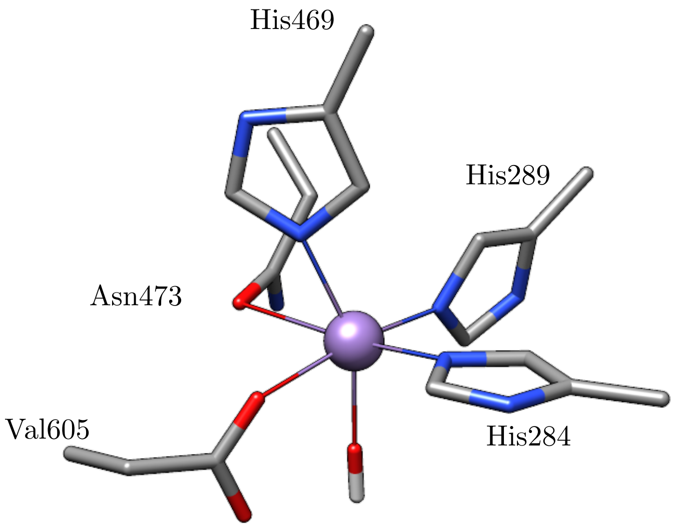

Scheme 1.2: Active site representation of Mn lipoxygenase from *Magnaporthe oryzae*, PDB 5FNO

an asparagine, and the C-terminal valine carboxylate.[9]

As exemplified above, Mn-dependent LOs are commonly found in organisms that are pathogenic to some plants, including important crops like wheat and rice. Thus, this isozyme may represent a potential target for more specific fungicides. The products of the LO reaction are fatty acid hydroperoxides; reactive precursors for the biosynthesis of signalling molecules. While the mechanism of the FeLOs has been studied in detail, resulting in the proposed Scheme 1.3, the Mn-dependent isozyme is less well understood. Many metalloenzymes affect oxidative transformations *via* high-valent intermediates, frequently metal-oxo species in the case of oxygenation reactions. In contrast, the proposed LO mechanism involves first a proton-coupled oxidation of the fatty acid olefin to form a water-bound, reduced metallocofactor and an alkyl radical.[11] The radial undergoes isomerization and is quenched by O_2 to form the alkylperoxy radical, and finally hydrogen atom transfer (HAT) from the active site water ligand regenerates the resting-state hydroxide and the desired product.[12]

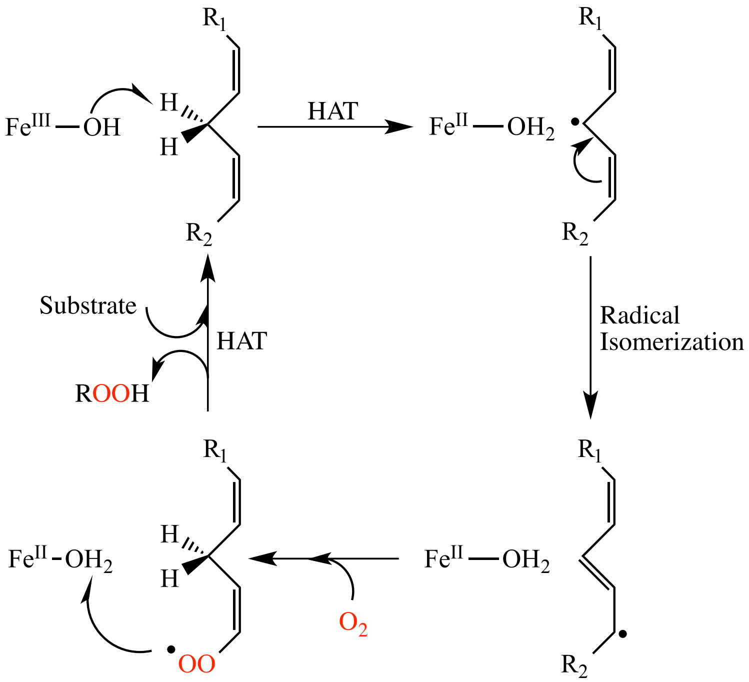

Scheme 1.3: Proposed mechanism of FeLO-catalyzed fatty acid oxidation

1.2.3 Mn Catalase

As previously discussed the deleterious superoxide radical, formed by the one-electron reduction of dioxygen, is a potent oxidizer. Further reduction by one electron and addition of two protons forms hydrogen peroxoide (H_2O_2), also a harmful oxidant but considerably less so. H_2O_2 is generated by the detoxification of superoxide (1.1), and therefore a mechanism for its removal must also exist. The catalytic disproportionation of H_2O_2 is performed by the catalase enzymes, producing water and dioxygen according to Eq. 1.4. At physiological conditions this reaction is thermodynamically very favorable (ΔG° = -57 kcal / mol), however there is additionally a substantial activation barrier, estimated at 18 kcal / mol.[13]

$$2H_2O_2 \longrightarrow 2H_2O + O_2 \tag{1.4}$$

The catalases found in many species of organisms utilize an iron heme active site to promote this reactivity. These heme catalases are known to be strongly inhibited by irreversible binding of azide or cyanide to the heme active site. In 1983 a non-heme catalase which was unaffected by azide or cyanide was purified from *Lactobacillus plantarum*, and shown to contain Mn as its metallocofactor.[14] Mn catalase (MnCat) enzymes have subsequently been found in a variety of organisms, and a few have been structurally characterized. As shown in Scheme 1.4, the MnCat from *L. plantarum* contains a binuclear Mn active site, with the Mn ions bridged by solvent-derived oxo and hydroxo ligands and a carboxylate side-chain from Glu 66.[13,14] Additionally, both Mn ions are coordinated by another glutamate residue and a histidine imidazole. The carboxylate of Glu 148 coordinates to the right Mn ion in a bidentate fashion, while the left Mn is coordinated by water.

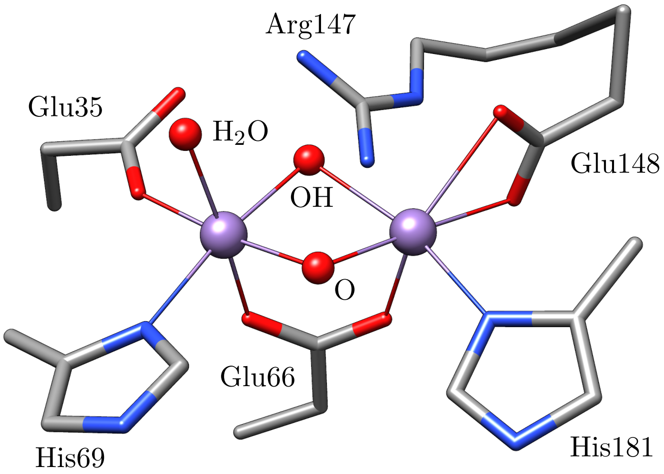

Scheme 1.4: Active site representation of Mn catalase from *Lactobacillus plantarum*, PDB 1JKU

A catalytic cycle proposed on the basis of spectroscopic data involves the binuclear cofactor cycling between the Mn_2^{III} and Mn_2^{II} states, first oxidizing a hydrogen peroxide molecule to O_2 and then reducing a second equivalent of substrate to two water molecules.

$$H_2O_2 + Mn_2^{III}Cat \longrightarrow O_2 + 2H^+ + Mn_2^{II}Cat \tag{1.5}$$

$$H_2O_2 + 2H^+ + Mn_2^{II}Cat \longrightarrow 2H_2O + Mn_2^{III}Cat \tag{1.6}$$

The initial oxidation step (Eq. 1.5) generates two protons which are then utilized in the reduction step (Eq. 1.6). The cofactor stores these protons on the briding ligands, as reduction of the Mn ions causes a decrease in Mn Lewis acidity and thus an increase in the basicity of the solvent bridges.[13] Oxidation of the Mn_2^{II} cofactor back to Mn_2^{III} in Eq. 1.6 liberates the protons by lowering the basicity of the bridging solvent molecules, using them to generate two equivalents of water from the second H_2O_2 substrate.

This two-step disproportionation reaction is reminiscent of the mechansim of the MnSODs (Eq. 1.2,1.3), and illustrates a fundamental theme in the evolutionary design of redox metalloenzymes. The mononuclear cofactor in MnSOD performs one-electron redox chemistry on the superoxide substrate, and the Mn cycles between 2+ and 3+ oxidation states. The oxidation or reduction of H_2O_2 however requires a two-electron commitment of the cofactor. As Mn^{I} is not typically thought to be accessible under physiological conditions, a mononuclear cofactor would be required to access the 4+ state to catalyze this reaction. Instead of generating high-valent, highly oxidizing Mn^{IV}, nature instead opts to employ a bimetallic active site to distribute the redox strain associated with performing this two-electron chemistry. Crystallographic characterization of an azide-bound cofactor shows displacement of the terminal water ligand and end-on coordination at that site, suggesting a similar binding mode for native substrate. The implied role of the second Mn ion is thus to serve as a redox resevoir, and to assist in the managment of protons in the active site, without directly participating in substrate binding.[13] This strategy is critical to the ability of metalloenzymes to perform multielectron chemistry with first-row transition metals, which typically prefer to undergo single-electron redox events.

1.2.4 Class Ib Ribonucleotide Reductase

An integral part of the success of evolutionary biology is the safeguarding of an organism's genetic code. Accordingly, mechanisms for the successful repair and replication of DNA must be in place. Throughout all kingdoms, the ribonucleotide reductase (RNR) enzymes perform a critical function in this process, converting nucleotide bases to their deoxy form and thus generating the monomeric building blocks of DNA. This enzyme is distinct from previous examples in that the metallocofactor is not the catalytic site of substrate reduction. Nucleotides are reduced at the surface of the protein by transient cysteine thiyl radical, however this cystine is oxidized by a stable tyrosyl radical, chaperoned out of the protein core *via* a proton-coupled electron transfer (PCET) pathway.[15–18]

In both the Fe-dependent class Ia and Mn-dependent class Ib RNRs, this tyrosyl radical is generated by the oxidation of a reduced bimetallic cofactor. As shown in Scheme 1.5 the active site of the *E. coli* class Ib RNR is a binuclear $\mathrm{Mn}_2^{\mathrm{II}}$ core, bridged by three glutamate residues. Two of them, Glu 98 and Glu 158, are coordinated in a bridging η^2 motif, while Glu 192 contributes a bridging η^1 oxygen with the other carboxylate oxygen coordinated only to one Mn ion.[19] Similar to the active site of Mn catalase, the coordination spheres are completed by a histidine imidazole, side-chain carboxylate, and water.

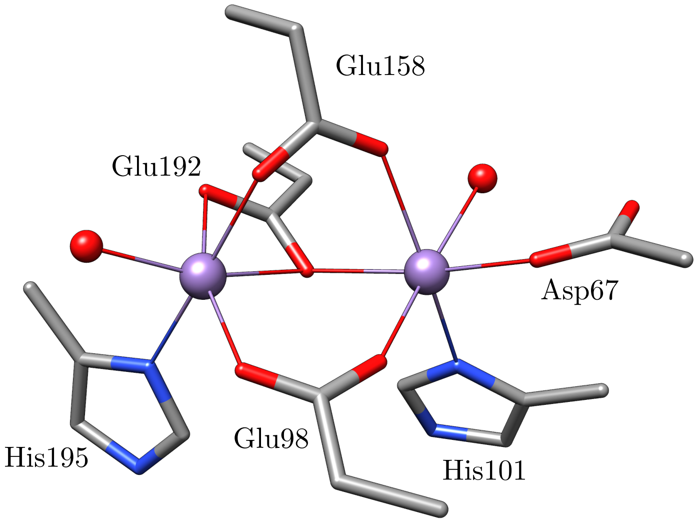

Scheme 1.5: Active site representation of Mn class Ib ribonucleotide reductase from *Escherichia coli*, PDB 3N37. Red spheres are water molecules

The terminal oxidant in class Ia enzymes is dioxygen, which reacts with the diiron(II) core to form the resting diferric tyrosyl radical state.[20] In contrast, the dimanganese(II) site in the class Ib isozymes has recently been shown to react with superoxide, which is generated from O_2 by the flavodoxin-like protein NrdI. The resting spin-coupled dimanganese(III) tyrosyl radical has been studied extensively,[21,22] and is known to be formed *via* a Mn(III/IV) intermediate.[20,23,24] As the class Ib RNRs are commonly found in pathogens, this affinity for the ($O_2^{-\cdot}$) radical may enable the Mn-dependent isozyme to function unhindered in the oxidatively stressful environment of an immune response.[25] Understanding the mechanism of class Ib tyrosyl radical generation, and in particular how it may differ from that of the structurally homologous class Ia, could provide an important therapeutic target for selectively disrupting DNA replication in pathogenic organisms.

Insight into the chemistry of manganese with O_2 and its reduced derivatives at a mechanistic level has been greatly advanced through the study of bioinorganic model complexes.[26,27] In particular, the binuclear peroxo-bridged dimanganese(III) species discussed in Chapter 3 constitutes the first characterized example of a proposed intermediate in the mechansim of class Ib RNR.[22,28,29] Comparison of the active site of Ib RNR (Scheme 1.5) to that of the Mn catalase (Scheme 1.4) reveals that while the latter is configured to (and does) bind substrate at a single manganese site (*vide supra*), the former is poised to coordinate a bridging reduced O_2 moiety. This is evidenced by the long manganese internuclear distance in this class Ib RNR (roughly 3.7 Å) in contrast to a separation of 3.0 Å in the *L. plantarum* MnCat. For comparison, the analogous distance in the complex studied in Chapter 3 is 4.11 Å.[28]

1.2.5 The Oxygen-Evolving Complex

As detailed above, Nature has evolved efficient strategies for handling the oxidative power of dioxygen and its reduced derivatives. Be it a controlled use as a terminal oxidant or detoxification of harmful oxidizing species, many of these enzymes rely on manganese as a metallocofactor. However, manganese also plays a crucial role in one of the most essential life-sustaining processes: the photosynthetic oxidation of water to aerial dioxygen in photosystem II (PSII) (1.7).[30]

$$2H_2O \longrightarrow O_2 + 4H^+ + 4e^- \tag{1.7}$$

This complex transformation, and the biological catalyst that promotes it, continues to be a subject of intense scrutiny. The geometric structure of the active site, the oxygen-evolving complex (OEC), is shown in Scheme 1.6. This tetramanganese cofactor is arranged in a cubane-type configuration, with three manganese, four oxo bridges, and a Ca^{2+} ion at the vertices. The remaining manganese, often termed the “dangling” manganese, is linked to one side of the cubane via a *bis*-μ-oxo motif.

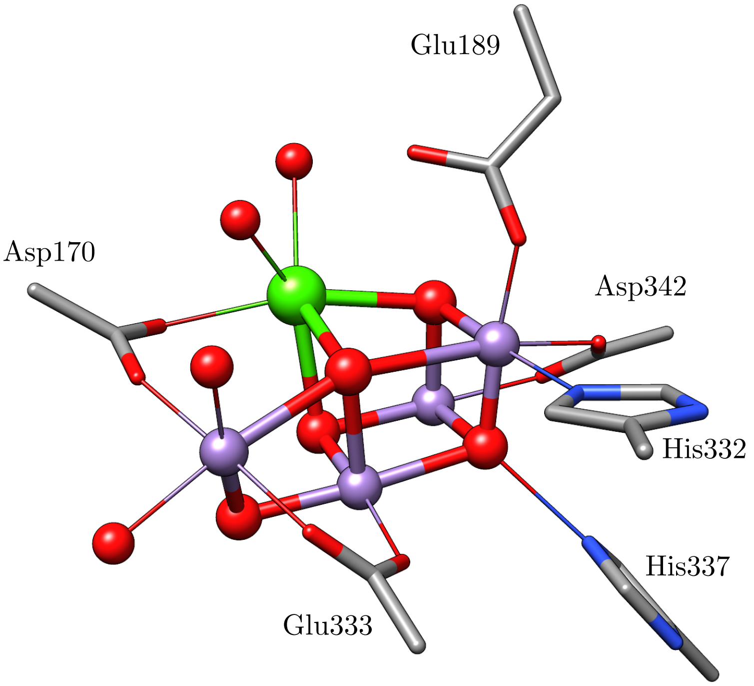

Scheme 1.6: Active site representation of the oxygen-evolving complex of photosystem II from *Thermosynechococcus vulcanus*, PDB 3WU2

Not shown is a conserved, redox-active Tyr residue in close proximity ($\mathrm{Tyr_Z}$), which participates in proton-coupled oxidation of the reaction center through formation of a tyrosyl radical.[31]

To date there is no concensus regarding the mechanim of this enzyme. While laser-flash experiments have obtained substantial insight into the early S-states of the so-called "Kok cycle",[32] the nature of the critical O-O bond formation step remains unclear. Proposed mechanistic strategies include the radical coupling of two manganese-bound oxygen atoms, or alternatively a nucleophilic attack-type mechanism. Also unknown is the functional role of the Ca^{2+} ion in the cofactor, which is unlikely to directly participate in redox chemistry but has a distinct perturbing influence on the electronic structure of the OEC.

Characterization of various S-states by electronic absorption, X-ray, and electron paramagnetic resonance (EPR) spectroscopies have provided considerable insight into the electronic structure of the OEC during catalysis.[33–38] Coupled theoretical investigations have further helped to interpret the spectroscopic data.[32,39,40] Fundamental to these studies however is the detailed mechanistic, structural, and spectroscopic characterization of synthetic manganese complexes which aim to mimic the structural motifs of the OEC. Investigations detailing mononuclear manganese peroxo[41–48] and oxo[49–51] complexes have described the reactivity of these chemical moieties, and furthermore have detailed the influence of redox-inactive metal ions on their properties.[50,52] Binuclear manganese complexes featuring oxo and hydroxo bridges have further aided in the elucidation of spectroscopic features of these motifs,[53,54] and a unique example of a binuclear peroxo-bridged manganese(III) dimer formed from dioxygen has provided new mechanistic insight into the activation of O-O bonds by manganese.[28,29] As outlined in Chapter 3, the X-ray spectroscopic and electronic structure characterization of this complex details how perturbations to manganese Lewis acidity can affect changes in O-O bond activation, and uncovers the specific molecular orbitals involved in this interaction. Finally, higher-nuclearity manganese oxido clusters that incorporate redox-inactive metal ions have recently been synthesized, providing high-resolution structural models for perturbations engendered by the binding of ions of calcium, sodium, strontium, etc.[55,56]

As introduced previously, the complexity of the redox chemistry promoted by the OEC is reflected in the nuclearity of the cofactor. The multi-step, four-electron oxidation of water to dioxygen is photon-dependent, and thus the OEC must be configured such that each redox event arrives at a nominally meta-stable species. Thus, much like the binuclear active sites of catalase and RNR, redox strain can be distributed between multiple manganese ions in the cofactor. It is noted however that the exact oxidation state distributions in each S-state remain a topic of some contest. Nonetheless, the fundamental principle of utilizing higher-nuclearity cofactors to achieve more complex catalytic function is exemplified regardless of the exact oxidation state distribution.

1.3 Biological Nitrogen Fixation: The Nitrogenase Family

The reduction of atmospheric dinitrogen (N_2) to bioavailable forms such as ammonia (NH_3), or nitrogen fixation, is essential for sustaining the majority of plant species on earth. In order to meet global demand for nitrogen-rich fertilizer, the industrial Haber-Bosch cycle catalyzes nitrogen fixation at high temperatures and pressures. In biology however, the same reaction proceeds at ambient conditions in the metalloenzyme nitrogenase. The organisms which are capable of fixing

N_2 are called diazotrophs, and thus far all known species contain a version of the nitrogenase enzyme. Despite diazotrophs comprising only a small subgroup of soil- and ocean-dwelling bacteria and archaea, they cycle roughly 10^8 tons of N back into the earth annually.[57] Significant efforts are being made to understand the function of nitrogenase, with the goal of eliminating ammonia production as a significant use of the world's energy supply.

1.3.1 Chemical Requirements for the Activation of N_2

Dinitrogen is one of the most inert molecules in all of chemistry. It is nonpolar and has a formal N≡N triple bond, with a bond dissociation energy of 226 kcal/mol. While the reduction of N_2 requires 6 e^-, the most efficient nitrogenases can affect the catalytic production of ammonia from N_2 using 8 e^- and 8 H^+, generating a single equivalent of H_2 per turnover.

$$\mathrm{N_2 + 8H^+ + 8e^- + 16MgATP \longrightarrow 2NH_3 + H_2 + 16MgADP + 16P}_i \tag{1.8}$$

1.3.2 Structure and Function of Nitrogenase

To date the most well-characterized of the nitrogenases is the molybdenum-dependent variant, which can be readily isolated from the soil bacterium *Azotobacter vinelandii*. The enzyme is comprised of two metalloproteins, both necessary for catalytic activity. The smaller Fe protein contains a single [4Fe-4S] cluster and functions as a reductase, hydrolyzing MgATP to MgADP and shuttling electrons to the larger MoFe protein. The MoFe protein is an $\alpha_2\beta_2$ heterotetramer comprised of almost 200,000 atoms, and contains two distinct types of unique metallocofactors. At the interface of each $\alpha\beta$ subunit pair is a [8Fe-7S] P-cluster, which has a fused double cubane structure with the upper and lower cubanes sharing a single sulfide bridge and two bridging cysteinate ligands (Scheme 1.7). Typical of iron-sulfur clusters, the P-cluster functions as an ET site, accepting reducing equivalents from the Fe protein and passing them on to the active site for N_2 reduction. Its unique structure is suggestive of the need to serve as a particularly powerful reductant compared to the majority of biological ET moieties. The resting, reduced P^N state is proposed to transfer either one or two electrons to the active site cofactor, with a reduction midpoint potential of -300 mV vs.

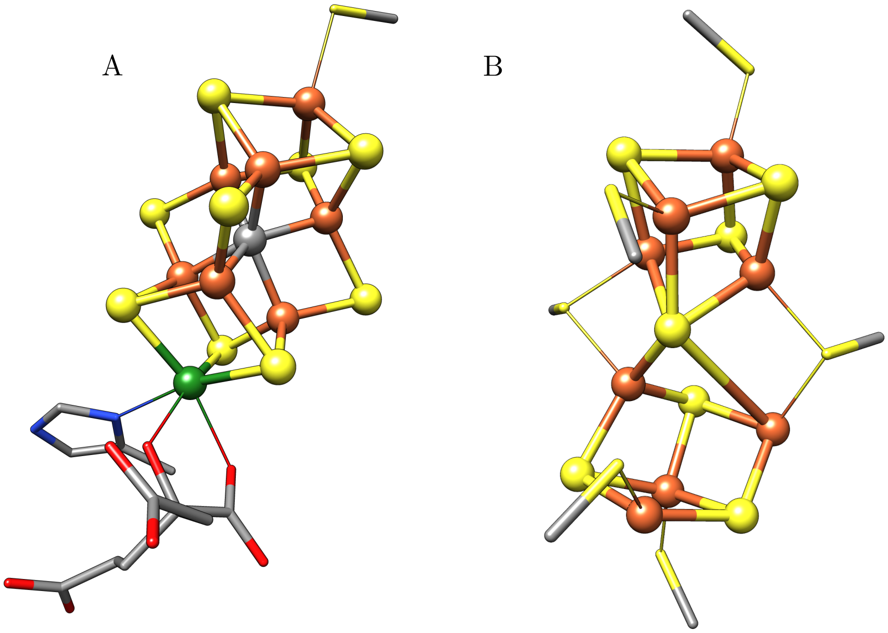

Scheme 1.7: Structures of the FeMo cofactor (A) and P-cluster (B) from *A. vinelandii*, PDB 3U7Q. Coloring scheme: Fe, orange; S, yellow; C, gray; Mo, green; N, blue; O, red. Cysteine thiolate ligands are shown as sticks, and inorganic sulfides as spheres.

NHE.[58] However, during turnover the cofactor is presumably much more difficult to reduce, and measuring redox potentials of the nitrogenase cofactors mid-turnover has proved elusive.

1.3.3 Molybdenum-Dependent Nitrogenase

Within each α subunit is the active site of the molybdenum-dependent nitrogenase: the iron-molybdenum cofactor (FeMoco). This [Mo-7Fe-9S-C] cluster has a roughly trigonal prismatic geometry, as shown in Scheme 1.7. At one end, the molybdenum ion is bound to the cofactor through a facial triad of bridging sulfides. A bidentate *R*-homocitrate, formed through the condensation of acetyl-CoA and α-ketoglutarate, and a histidine imidazole complete the octahedral coordination sphere. At the other end, the apical tetrahedral iron forms the end of the cofactor, and is bound to the protein by a cysteine thiolate.

The first X-ray crystallographic structure of FeMoco emerged in 1992, with a 2.7 Å resolution structure of the MoFe protein from *A. vinelandii*.[59,60] While the general structure has been confirmed many times over by subsequent reports,[61,62] the initial electron density map revealed a cavity within the cofactor. An improved 2.2 Å resolution structure the following year posited some degree of iron-iron bonding across the space, or potentially that the cavity served as a binding pocket for N_2.[63] However, in 2002 Einsle *et al.* published the 1.16 Å resolution crystal structure of *A. vinelandii* MoFe, which revealed the presence of a central ligand in the cluster.[64] Identified as a second-period atom, possibly nitrogen, this finding prompted nearly a decade's worth of experimental biochemical and biomimetic studies, as well as theoretical investigations, into the identity, source, and function of this interstitial light atom.[58,65–67]

In 2011, a combination of X-ray emission spectroscopy (XES),[68] high-resolution X-ray crystallography, and electron spin echo envelope modulation (ESEEM) pulsed electron paramagnetic resonance (EPR) spectroscopy[69] showed the central light atom in FeMoco to be a carbon atom. Formally a fully-valent carbide, C^{4-}, this was an entirely unprecedented motif in biology, and one that was, prior to the work herein, unique to FeMoco. As shown in Scheme 1.7, the central carbon atom is 6-coordinate, with two facial triads of Fe atoms above and below. Recently, additional XES studies[70] and ^{14}C radiolabeling experiments[71] have shown that the source of this carbon atom is the methyl group of *S*-adenosylmethionine (SAM), and that it is inserted into the cofactor *via* radical methyl group transfer in the cofactor assembly protein NifB. Far more ambiguous however is the role of the carbon atom, its influence on the geometric and electronic structure of the cofactor, and possible implications for reactivity.

Among the vast array of iron-sulfur cluster motifs found throughout biology, an additional motif unique to FeMoco is the apical molybdenum ion.[72] The molybdenum has been recently characterized as a Mo(III) ion, also unique in biology, with an unusual non-Hund spin configuration predicted by density functional theory (DFT) calculations. Interestingly, this non-Hund configuration arises due to molybdenum-iron bonding with the three nearest Fe atoms.[73] The resultant bonding orbitals should be populated by electrons of opposite spin, thus the electrons contributed from the iron atoms (↓↑↑, *vide infra*) induce a ↑↓↓ configuration on molybdenum.

1.3.4 Vanadium-Dependent Nitrogenase

In molybdenum-limited conditions, or at reduced temperatures, certain diazatrophs upregulate production of an “alternative” nitrogenase, which utilizes vanadium as a metallocofactor.[57,74] The corresponding VFe protein contains extra subunits compared to MoFe, with an $\alpha_2\beta_2\delta_n$ configuration, where $n = 2$ or 4 depending on the species.[57,75] Spectroscopic and genetic studies indicate that the VFe protein contains redox centers analogous to those found in MoFe (Scheme 1.7), however an X-ray crystal structure of VFe has yet to be reported. Thus, some ambiguity remains regarding the extent to which the redox cofactors are homologous. The presence of a corresponding Fe-V cofactor (FeVco) was first evidenced in 1987, where vanadium K-edge extended X-ray absorption fine structure (EXAFS) spectroscopy identified a series of V-S and V-Fe vectors analogous to that of a model complex discussed herein.[76,77] The presence of an interstitial carbon atom in FeVco, essentially confirming the structural homology of FeMoco and FeVco, was determined by valence-to-core X-ray emission spectroscopy (VtC XES), and is the topic of Chapter 4 in this work.

Despite seemingly isostructural cofactors, the stoichiometry and efficiency of the dinitrogen reduction promoted by the vanadium nitrogenase is strikingly different from the molybdenum-dependent isozyme. While the molybdenum nitrogenase consumes 16 equivalents of adenosine triphosphate (ATP) per turnover, and is coupled to the production of an obligate H_2 molecule (*vide supra*), the vanadium nitrogenase requires 40 ATP per turnover, and is typically quoted as producing three eqivalents of H_2 (1.9).

$$N_2 + 12H^+ + 12e^- + 40MgATP \longrightarrow 2NH_3 + 3H_2 + 40MgADP + 40P_i \tag{1.9}$$

It should be noted however that the H_2 stoichiometry has not been investigated using the highly precice pressure-dependent methods employed in the case of the molybdenum enzyme,[78] and there may be some error in this stoichiometry. Nonetheless, the expenditure of biological energy in terms of ATP is substantially higher. Furthermore, the turnover number (TON) of the molybdenum nitrogenase (2230) is more than an order of magnitude larger than that of the vanadium nitrogenase (112).[79] This indicates that FeMoco may be more suitably tuned for the dinitrogen reduction reaction, compared for FeVco.

1.3.5 Alternative Substrates for Nitrogenase

The semireduced diazene (N_2H_2) and hydrazine (N_2H_4) states of N_2 have been shown to be alternative substrates of nitrogenase.[80] Additionally, hydrazine can be isolated as a product upon the hydrolysis of nitrogenase in either acidic or basic conditions.[80] This is suggestive of the formation of such an intermediate at some point in the reaction pathway. Interestingly, the vanadium-dependent nitrogenase produces trace amounts of hydrazine during normal turnover, which points to at least some overlapping mechanistic steps between these two enzymes. It is thus possible to conceive a mechanism where N_2 is reduced by two electrons, and addition of two protons generates diazene, and subsequent addition of two electrons and two protons generates hydrazine. However, questions such as the coordination mode of these substrates, and the point of H_2 release, are difficult to address using this rationale.

In addition to reduced N_2 derivatives, various triply bonded molecules can also be reduced by nitrogenases, including acetylene to ethylene and azide to NH_3 and N_2.[81] The carbon monoxide (CO) molecule, isoelectronic to N_2, has also long been utilized as a surrogate for the physiological substrate of nitrogenase, however in contrast to previous examples, as early as the 1970's CO was recognized as a reversible inhibitor of nitrogenase, rather than a substrate.[82] The CO-bound form has been extensively spectroscopically characterized by EPR, X-ray, and nuclear resonance vibrational spectroscopy (NRVS).[83,84] More recently, crystallographic characterization of CO-inhibited FeMoco revealed a surprising coordination mode: displacement of a "belt" μ^2 sulfide ligand and replacement with CO.[85]

Intriguingly, treatment of the vanadium nitrogenase with CO results in reductive C-C bond coupling.[86] Short-chain saturated and unsaturated hydrocarbons as large as propane have been detected, with ^{13}C isotopic labeling confirming CO as the source of carbon. While it is remarkable that the same enzyme seemingly has the capacity to perform both Haber-Bosch and Fischer-Tropsch chemistry, and at ambient conditions, it is perhaps more striking that these structurally homologous cofactors are in fact quite distinct in their capacity to promote the reduction of diatomic gases.

An additional distinction between these isozymes is the binding of CO to the cofactor. In the case of FeMoco, the coordination of CO to the cofactor occurs only under turnover conditions, with presumably a reduced cofactor. In contrast, CO has recently been shown to coordinate to FeVco in the resting state, with EPR spectroscopy suggesting an analogous coordination mode.[87] Importantly, the isotopic labeling of the coordinated CO, detected by EPR spectroscopy, resulted in isotopically labeled hydrocarbon products. It is possible that by identifying the differences which may engender this unique reactivity, clues regarding Nature's evolutionarily optimized strategies for performing this complex chemistry can be obtained. Additionally, insight into the functional role of both the heterometal and the interstitial carbon may be garnered. These topics are addressed in detail in Chapter 5 of this work.

1.4 Concluding Remarks

This chapter presents an introduction to the biological inorganic chemistry of manganese-promoted O_2 and reduced O_2 chemistry and the nitrogenase enzymes responsible for the fixation of atmospheric dintrogen. Through its course, the selected examples illustrate what are, to me, some of the most fundamental inorganic principles evidenced by the evolutionary design of these catalysts: distribution of oxidation state changes, tuning of redox potentials, and control of geometric and electronic structure in order to achieve a desired function. In addition to these more inorganic properties, the entire enzymes must also carefully regulate other important factors such as substrate access and positioning, and controlled delivery of protons and electrons.

The final two examples highlighted, the OEC and the nitrogenase FeMoco and FeVco, are arguably the most complex metallocofactors in all of biology. Their unique structures enable them to promote the four-electron oxidation and six-electron reduction, respectively, of relatively inert chemical species. Both of these reactions are absolutely critical to life on this planet. Their remarkable design speaks volumes about the accumulation of chemical insight that Nature has acquired through millennia of evolution; that the proper placement of a calcium ion within a manganese cluster or a carbide ligated by six iron atoms could be the key for catalyzing these difficult reactions. Despite the substantial wealth of knowledge that we possess regarding the fundamental principles of chemistry, we do not have access to the immeasurable iterations of trial and error that produced these exquisite biomolecules. Instead, we must strive to better understand the glimpses that Nature has given us, with the hope that we may someday build upon them further.

Chapter 2

"X-rays... I'm afraid of them. I stopped experimenting with them two years ago, when I came near to losing my eyesight and Dally, my assistant practically lost the use of both of his arms."
Thomas Edison

Introduction to X-ray Spectroscopy

2.1 An Overview of X-ray Techniques in Chemistry

The past several decades have seen an exponential growth in the use of X-rays across all scientific disciplines. This is due in part to an increase in the availability, intensity, and portability of X-ray sources, which are now commonplace in medical facilities worldwide. Undoubtedly most impactful to chemical science is the use of X-rays to study the structure of molecules at an atomic level, *via* the diffraction of X-ray radiation by an ordered crystalline solid. This phenomenon was first demonstrated by Max von Laue in 1912, for which he was awarded the 1914 Nobel Prize in physics.

While X-ray crystallography remains the most definitive routine method for identification of molecular structure, it requires a relatively defect-free single crystal; a prohibitive obstacle for the study of many biomolecules in particular. Fortunately, diffraction is not the only meaningful way in which X-rays interact with matter. An alphabet soup of X-ray-based techniques are currently used to further the study of molecules, materials, and other matter, making use of additional forms of diffraction, scattering, and absorption processes.

2.1.1 The X-ray Spectrum

The X-ray regime of electromagnetic radiation sits to higher energy of the ultraviolet region and to lower energy of gamma radiation. There are further three regions of the X-ray spectrum: so-called "soft" X-rays to low energy (~0.1-3 keV), "tender" X-rays between 3 and 5 keV, and "hard" X-rays above 5 keV. While each region provides access to different chemical insight, experiments that utilize hard X-rays are of particular interest to (bio)inorganic chemists, as they encompass the 1s binding energies of the first-row transition elements.[88] Furthermore, hard X-rays are considerably more conducive to experiments involving biological samples.

The probability of an X-ray photoabsorption event scales approximately as $\frac{Z^3}{E^3}$, where Z and

E are the atomic number of the absorbing atom and the X-ray photon energy, respectively. Thus, lower energy soft X-rays are readily absorbed by diatomic gases in the atmosphere. Soft X-ray experiments are therefore often performed in ultra-high vacuum conditions not so amenable to measurements on frozen solutions. Additionally, the very small sample penetration depth of soft X-rays makes them relatively surface sensitive. In contrast, hard X-rays are less readily absorbed, and are a more effective probe of bulk samples. While absorption by gaseous molecules is still problematic, it is commonly sufficient to fill the flight path of hard X-rays with He gas to minimize attenuation of the beam's intensity, rather than evacuating the space.

2.1.2 X-ray Spectroscopy in Bioinorganic Chemistry

For the bioinorganic chemist, X-ray based methodologies provide a number of advantages for the characterization of metal sites in both biomolecules and synthetic inorganic complexes. The binding energies, or absorption edges, of the core and semi-core level electrons are energetically distinct for each element, and thus X-ray spectroscopy is inherently element selective. Despite the fact that a metallocofactor of interest may sometimes constitute only a fraction of a percent by mass of a sample, the remainder of the molecule (the protein "spinach") is essentially spectroscopically invisible. As mentioned previously, the 1s binding energies of the biologically relevant first-row transition elements fall into the hard X-ray region, from 5465 eV for vanadium 1s to 9659 eV for zinc. These hard X-rays are amenable to a range of sample environments, including neat and diluted powders and dilute solutions. From a practical perspective, solution samples should be ideally 10 millimolar (mM) in metal absorber, with 1 mM an approximate lower detection limit. One might imagine an increase in signal integration time as a viable alternative to this detection limit. However, as ionizing radiation, X-rays can readily induce photodamage in biological samples.[89] Particularly in the case of higher-valent metal ions, extreme care must be taken to limit the amount of X-ray beam exposure, often to less that 10 seconds at modern, high intensity synchrotron sources. This can be mitigated in part by data collection at cryogenic temperatures, often around 10 K, but photosensitivity is ultimately an intrinsic property of each distinct sample.

The distinct regions of the X-ray absorption and emission spectra, discussed in greater detail below, offer insight into a range of interesting chemical properties. This disstertation covers X-ray processes in the K-shell, where K denotes the $n = 1$, or 1s orbital. On the absorption side, the pre-edge region, corresponding to 1s→3d transitions for first-row metals, offers insight into metal ion coordination geometry. Deviations from centrosymmetry, as well as contributions from covalency, mixes the unoccupied 4p orbitals into the 3d, providing electric dipole transition intensity to a formally dipole-forbidden transition.[90] To higher energy, the K-edge region probes the metal ion oxidation state by measuring the binding energy of the 1s electrons. While there are some notable exceptions to this trend discussed in Chapter 5, metal ions of higher oxidation state generally have deeper 1s binding energies. Finally, to higher energy of the edge, the extended X-ray absorption fine structure (EXAFS) region can yield relatively precise measurements of metal-ligand bond lengths, through analysis of the scattering patterns of the ionized photoelectron wave from atoms in close proximity to the metal.[91]

The X-ray emission spectrum, which corresponds to fluorescent decay of high-energy core-hole ionized states, contains substantial chemical insight as well. However, the most probable (and thus most intense) Kα, or 2p→1s emission, involves only inner-shell orbitals. The Kα emission is split into two features due largely to 2p spin-orbit coupling (SOC), and thus Kα emission is typically not sensitive to chemical changes in the valence shell. To higher energy, the Kβ emission spectrum is comprised of two distinct regions: the Kβ mainline, which corresponds to 3p→1s transitions, and the valence-to-core (VtC) region, corresponding to emission from dominantly ligand-based molecular orbitals. The former spectral feature displays a pronounced sensitivity to the 3d local spin population of the metal ion, *via* exchange coupling of the unpaired 3p electron with the 3d shell. The local 3d spin population is modulated not only by metal ion spin state, but also by the covalency of the ligand environment.[92] The VtC region, which is substantially less intense than the Kβ mainline, arises from transitions involving ligand-based orbitals. Thus, in contrast to other X-ray based techniques, insight may be obtained regarding the electronic structure of the ligand environment surrounding a metal ion. A promising application of this method is the characterization of substrate activation at a metal center, as discussed in Chapter 3.

2.2 Brief Theory of X-ray Spectroscopy

To a large extent X-ray spectroscopy is purely an electronic spectroscopy, and as such is governed by the same principles that apply to *e.g.* optical absorption or fluorescence spectroscopy. The sizable difference in energy regimes at times requires different approximations to be made, but the simple picture of photon-induced electronic excitation presents an ideal starting point for a more quantum-mechanical description of X-ray spectroscopy (Figure 2.1). While parts of this chapter may seem overly technical, the essence of spectroscopy is the interaction of light with matter, and a detailed understanding of the fundamental physics which govern that interaction can only enhance the information presented. Furthermore, the implementation of these principles within the framework of theoretical treatments such as density functional theory (DFT) or *ab initio* configuration interaction (CI) wavefunction methods allows for the successful calculation and prediction of experimental observables. While the marriage of experiment and theory can maximize the information obtained from most experiments, an informed and critical analysis of the theory is essential for safeguarding against overinterpretation.

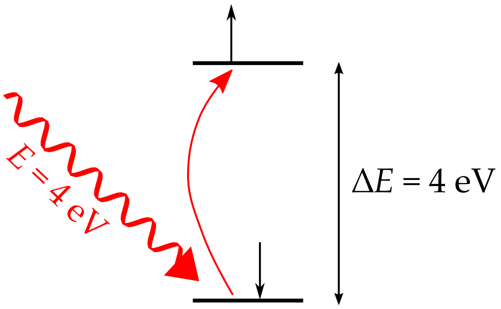

Figure 2.1: Schematic of a photoinduced single-electron excitation in the molecular orbital picture

2.2.1 Basic Physical Description

In a one-electron picture, electromagnetic radiation can induce a transition between two stationary states ψ if the difference in energy of the initial and final states, ΔE, is equal to the energy of the radiation, $h\nu$.

$$|E_i - E_f| = \Delta E = h\nu \tag{2.1}$$

Eq. 2.1 is known as the resonance condition, or the Bohr frequency condition, and is a requirement for electronic transitions to occur. For the valence excitations typically studied with optical absorption spectroscopy, these transition energies are on the order of 2-5 eV, approximately 1200-200 nm. In X-ray absorption spectroscopy, transition energies to core-hole excited states for first-row transition metals are larger by over three orders of magnitude: ≈5000 eV for the 1s electrons of V and ≈7100 eV in the case of Fe. When the resonance condition is satisfied, transitions with energy equal to $h\nu$ are possible.

2.2.2 Time-Dependent Perturbation Theory

A more rigorous treatment is the description of electronic spectroscopy by time-dependent perturbation theory. This approach allows for the *ab initio* calculation of spectroscopic observables from quantum mechanics, and is essential for extracting meaningful chemical insight from experimental results. The familiar time-independent Schrödinger equation, $\hat{H}\psi = E\psi$, provides the energy eigenvalue E of a given stationary eigenstate ψ, and is the basis for obtaining ΔE found in Eq. 2.1. While useful from a conceptual perspective, this is merely a special case of the more general time-dependent description, $\hat{H} \left|\Psi\right\rangle = i\hbar\frac{\partial}{\partial t} \left|\Psi\right\rangle$.

The first-order perturbative approximation to the time-dependent Schrödinger equation allows for the Hamiltonian to be expressed as a sum of a zeroth-order component $\hat{H}_0$, which is independent of time, and a time-dependent perturbation $\hat{H}'$. This can be expressed in the form

$$[\hat{H}_0 + \hat{H}'(t)] \left|\Psi\right\rangle = i\hbar\frac{\partial}{\partial t} \left|\Psi\right\rangle \tag{2.2}$$

where capital Ψ describes a perturbed state comprised of a superposition of stationary states ψ, which are eigenstates of the zeroth-order Hamiltonian. While Eq. 2.2 can be utilized for any time-dependent perturbation, in the case of X-ray spectroscopy the perturbation of interest is an electromagnetic field varying with time. The classical properties of the two interdependent fields are given by Maxwell's equations (Figure 2.2). Here, the properties of the electric field perturbation $\vec{E}$ are to a good approximation the limit of what must be considered, and the magnetic field $\vec{B}$ can

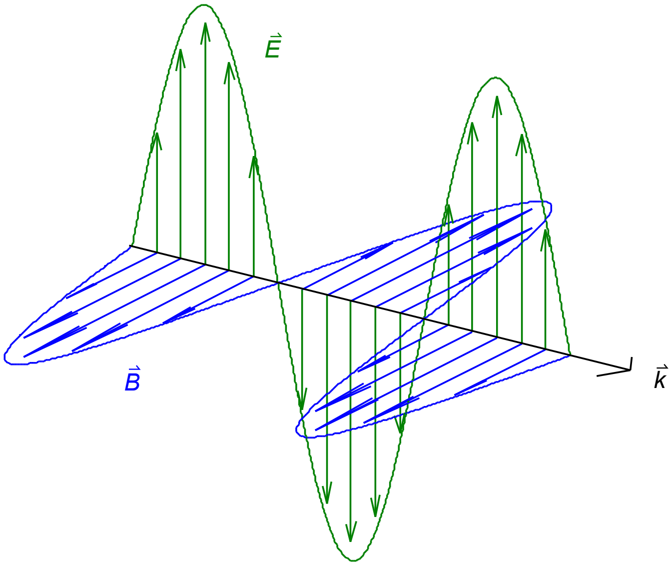

Figure 2.2: Oscillating orthogonal electric (green) and magnetic (blue) fields of propogating electromagnetic radiation

be neglected.

2.2.3 Obtaining Molecular Properties

The manner in which this perturbation interacts with molecules, within the confines of a description of X-ray spectroscopy, is determined by three molecular properties: the electric dipole moment $\vec{\mu}$, the magnetic dipole moment $\vec{\mu}_m$, and the electric quadrupole moment $\mathbf{\Theta}$. It is further important to note that these moments are both origin and orientation-dependent; the dipole moments are vector quantities (first-rank tensors) while the quadrupole moment is a matrix (second-rank tensor). The electric dipole and quadrupole moments for example take the form

$$\vec{\mu} = \sum_i q_i \vec{r}_i = \int \vec{r}\rho(\vec{r})d\vec{r} \tag{2.3}$$

$$\mathbf{\Theta} = \sum_i q_i \vec{r}_i \vec{r}_i = \int \vec{r}\vec{r}\rho(\vec{r})d\vec{r} \tag{2.4}$$

where q_i and $\vec{r}_i$ are the magnitude and position of a given charge i (electron or nucleus) and the quantity $\rho(\vec{r})$ is the charge density as a function of position. The orientation dependence of these quantities is fundamental to understanding transition selection rules based on symmetry.

Each classical quantity has an analogous quantum mechanical value, which can be obtained using the appropriate operator. The electric dipole moment operator for example is defined as

$$\hat{\mu} = e\sum_{\alpha} Z_{\alpha}\vec{R}_{\alpha} - e\sum_{i}\vec{r}_i \tag{2.5}$$

for nuclear charge of eZ_{α} at position $\vec{R}_{\alpha}$ and electrons at position $\vec{r}_i$. For a given total electronic and nuclear wavefunction Ψ_k, the permanent dipole moment $\vec{\mu}_k$ can be obtained by computing the expectation value

$$\langle\mu_k\rangle = \langle\Psi_k|\hat{\mu}|\Psi_k\rangle \equiv \int \Psi_k^{*}\hat{\mu}\Psi_k d\tau \tag{2.6}$$

Here $d\tau$ represents the volume integral, taken over all spatial and spin coordinates. The Dirac or bra-ket notation will be utilized henceforth. Within the Born-Oppenheimer approximation, the nuclear component of the total wavefunction Ψ_k is static (the nuclei are localized), and thus the nuclear positions can be extracted as the first term in Eq. 2.5, requiring a summation over fixed nuclear coordinates $\vec{R}_{\alpha}$ and integration over only the electronic wavefunction ψ_k for a given state k.

2.2.4 Interaction of Electromagnetic Fields with Molecules

As is understood from the one-electron picture, the interaction of light with matter can result in transitions between electronic states. The measured quantity in electronic spectroscopy is typically an intensity, either an absorption or emission process, as a function of photon energy $h\nu$. This measured intensity is proportional to the probability of a transition from an initial to a final state occurring in a given time, $P_{i\rightarrow f}(t)$. The most important physical affector of this quantity is the interaction of a time-evolving electric field $\vec{E}(t)$ and an electric dipole moment $\vec{\mu}$.[93] A note here is that the permanent dipole moment $\vec{\mu}_k$ from Eq. 2.6 is the dipole moment in the absence of a perturbation, however an electric field is of course expected to alter all of the molecular multipole moments. The dipole moment can be expressed as a Taylor series[94]

$$\hat{\mu} = \hat{\mu}_0 + \alpha \cdot \vec{E} + \frac{1}{2}\sum_{ij} \beta_{ij} \vec{E}_i \vec{E}_i + ... \tag{2.7}$$

where the leading term $\hat{\mu}_0$ is the permanent diople moment. The terms α and β are the polarizability and hyperpolarizability, respectively, however at the weak-field limit it is generally sufficient to consider only the leading term in this series. The dipole moment and the electric field define the first-order perturbative Hamiltonian from Eq. 2.2 as $\hat{H}'(t) = -\vec{\mu} \cdot \vec{E}(t)$.

An electric dipole-induced transition between two Born-Oppenheimer states is thus dependent on the transition matrix element

$$\langle \psi_f | \vec{\mu} \cdot \vec{E}_0 | \psi_i \rangle \tag{2.8}$$

for an electric field E_0 that is homogeneous over the volume of the absorbing species. It should be noted that a simplification has been made in the description of the perturbing electric field as homogeneous. One can readily observe from Figure 2.2 that the strength of the electric field of propagating light is not in fact constant, and that the field experienced by a molecule is dependent on its placement along the k direction. Thus, the magnitude of the electric-field perturbation at the molecule evolves in time as the field propagates.

The size of a typical molecule is generally small relative to the wavelength of visible light; therefore the electric field over the molecule is effectively homogeneous in optical spectroscopy.[94] There is typically little variation in the order of magnitude of molecular size, in this dissertation no more than 20 Å across (while entire proteins may be larger, the active sites of interest are small), so the validity of this so-called *long-wavelength approximation* is dependent almost entirely on the type of applied electromagnetic radiation. For optical spectroscopy, wavelengths of around 500 nm are on the order of 150 times larger than molecules, and thus electronic transitions in the visible region are to a very good approximation entirely electricdipole transitions. For X-ray spectroscopy however this approximation begins to break down, as the wavelength of X-rays are in the 2-10 Å range. The result is that the previously-neglected gradient of the electric field experienced by a molecule can couple two electronic states *via* the quadrupole transition matrix element $\langle \psi_f | \mathbf{\Theta} : \nabla \vec{E} | \psi_i \rangle$. While electric dipole transitions are still typically much stronger, in the absence of any dipole-allowed transitions, X-ray spectral intensity arising from quadrupole transitions can be observed.[90,95]

Having established a mechansim for light-induced transitions between electronic states, the measured quantity of interest, spectral intensity, can now be calculated. The dominant electric-dipole transition matrix element can be used to obtain the dipole transition probability per unit time, or transition rate w_{if} for a continuous perturbation using Fermi's golden rule

$$w_{if} = \frac{dP}{dt} = \frac{|\langle \psi_f | \vec{\mu} \cdot \vec{E}_0 | \psi_i \rangle|^2}{4\hbar^2}[\delta(\nu - \nu_{if})] \tag{2.9}$$

where the delta function $\delta(\nu - \nu_{if})$ is a restatement of the Bohr frequency condition, Eq. 2.1, and requires the that frequency of light ν match the transition frequency ν_{if}. It should be noted that this is not an "exact" match, as discussed in Section 2.2.7. The total transition rate, which corresponds to spectral intensity, simply requires inclusion of all nonzero coupling matrix elements. In the theoretical treatment employed in this dissertation, this is limited to consideration of the electric dipole and quadrupole and magnetic dipole coupling operators $\hat{\mu}, \hat{\Theta},$ and $\hat{\mu}_m$. A spectrum can be obtained by repeating this process for all possible initial and final states.

For spectroscopic measurements on a collection of randomly oriented molecules, *e.g.* a polycrystalline or frozen solution sample, the vectors of the molecular dipoles in the initial and final states are averaged over all possible orientations, and it is convenient to define a quantity μ_{if} as the electric dipole transition moment, independent of electric field orientation:

$$\mu_{if} \equiv \langle \psi_f | \hat{\mu} | \psi_i \rangle \tag{2.10}$$

Is is important to remember however that while orientational averaging removes the polarization dependence of a bulk sample with respect to the electric field perturbation, the dipole operator $\hat{\mu}$ is still a vector quantity. If μ_{if} is non-zero, the transition is said to be *electric dipole allowed.* Similarly, such quantities exists for electric-quadrupole and (usually negligible) magnetic-dipole transitions, with analogous definitions for each. Finally, it is necessary to introduce the quantity f, or f_{osc}, the oscillator strength, which provides the fundamental link between quantum theory and experiment.

The expressions for the oscillator strength can be derived from both the classical Lorentz model and the Kramers-Heisenberg-Dirac equation (see for example McHale[94] or Levine[96]), enabling the quantitative comparison of experimental and theoretical transition intensities. As most discussion of spectral intensities in this dissertation will be on the basis of group theory and molecular orbital theory, it should be sufficent to simply recognize that the intensity of a spectroscopic transition I, experimentally obtained from the integrated spectral area, is proportional to the cumulative squares of the transition moments.

$$I \propto f_{osc} \propto |\langle \psi_f | \hat{\mu} | \psi_i \rangle|^2 + |\langle \psi_f | \hat{\Theta} | \psi_i \rangle|^2 + |\langle \psi_f | \hat{\mu}_m | \psi_i \rangle|^2 \tag{2.11}$$

2.2.5 Quantum Mechanical Selection Rules

Unless the study of flat lines is appealing, it is important to now find the cases for which the matrix elements $\langle \Psi_f | \hat{O} | \Psi_i \rangle$ are non-zero, for a generic (but hopefully relevant) operator $\hat{O}$. Previously, the lowercase ψ was used to indicate the total electronic wavefunction as a component of Ψ, the electron-nuclear wavefunction. Here however, the total electronic Born-Oppenheimer wavefunction is now Ψ, comprised of one-electron wavefunctions ψ. A quick look at the form of the dipole moment operator in Eq. 2.5 provides a fundamental piece of insight: the operator consists of exclusively one-electron terms.[1] Thus, the transition between two many-electron states can be described by a sum of one-electron transition matrix elements (Eq. 2.12).

$$\langle \Psi_f | \hat{\mu} | \Psi_i \rangle = \langle \psi_{1_f} | \hat{\mu} | \psi_{1_i} \rangle + \langle \psi_{2_f} | \hat{\mu} | \psi_{2_i} \rangle + \cdots + \langle \psi_{n_f} | \hat{\mu} | \psi_{n_i} \rangle \tag{2.12}$$

X-ray spectroscopy is a core-level method, and so to a very good approximation, electronic transitions can be considered as being between atomic states. While the interaction of the delocalized valence molecular orbitals on the "atomic" orbitals of the metal is an important affector of spectral properties, many of the principles of atomic spectroscopy are valid and fundamental to understanding X-ray spectra. The first selection rule in atomic spectroscopy comes from separa-

---

[1] The same is true for $\hat{\Theta}$ and $\hat{\mu}_m$

tion of the one-electron wavefunction ψ into its spatial component ϕ and spin part σ, where the spin quantum number m_s can have the eigenvalues $\pm\frac{1}{2}$ corresponding to $|\alpha\rangle$ and $|\beta\rangle$, the two spin eigenfunctions of $\hat{S}_z$ indicating the projection of electron spin angular momentum along the z-axis. These spin functions are orthonormal,

$$\langle\alpha|\alpha\rangle = \langle\beta|\beta\rangle = 1 \qquad \langle\alpha|\beta\rangle = \langle\beta|\alpha\rangle = 0 \tag{2.13}$$

thus each transition matrix element contains the delta function $\delta_{m_s m_s'}$. It follows that the first fundamental selection rule for any isolated one-electron electric dipole (or quadrupole) transition is $\Delta m_s = 0$. As photons posess an angular momentum of 1, conservation of momentum dictates that for the transition $\langle\phi'|\hat{\mu}|\phi\rangle\,\delta_{m_s m_s'}$ the change must be in the *orbital* angular momentum quantum number ℓ, therefore the next selection rule is $\Delta\ell = \pm 1$.

These conclusions are sufficiently simple that many undergraduate students in chemistry can recite them. Beautifully, they hold to an excellent extent in the case of a single electron. Unfortunately however, there is a fairly limited amount of chemistry one can accomplish with single-electron systems, and thus some modifications must be made for the multielectron picture. In essence, the component one-electron wavefuctions ψ_i in Eq. 2.12 cannot be treated as *non-interacting.* While it is instructive to think about the spatial and spin angular momenta of a particular electron i through the use of the appropriate spherical harmonic $Y_{\ell m_\ell}$ (where m_ℓ is the z component of the orbital angular momentum ℓ), in reality one can never measure these quantities for a multielectron system. Instead, the appropriate sum over all occupied spatial and spin functions (spin-orbitals) provides the z projection of the total orbital and spin angular momenta L and S, denoted M_L and M_S.

A fundamental requirement of the total many-electron wavefunction is that it be antisymmetric upon the exchange of spatial and spin coordinates for any pair of electrons. This comes as a result of electrons being fermions, and leads to the formulation of the total wavefunction as a Slater determinant, $\Psi_{SD} = |\psi_i \ldots \psi_N|$, describing the collection of one-electron spin-orbitals. A Slater determinant is comprised of specific spin-orbitals, and therefore implies a particular electron *configuration*, or filling of electrons into orbitals. Many systems in bioinorganic chemistry, and likewise in this dissertation, contain unpaired electrons however, and as there are many possible ways to fill five d orbitals with five electrons, so too the many-electron wavefunction has many possible configurations. It is therefore described not by a single Slater determinant, as closed-shell systems are, but by a linear combination of Slater determinants.

The open-shell many-electron wavefunction is a complex entity; however, it is one that must be considered in a thorough description of electronic spectroscopy. The origin of the $\Delta\ell = \pm 1$ selection rule (conservation of angular momentum of a photon) more accurately applies not to the total orbital angular momentum L, but to the total orbital *and spin* angular momenta, given the symbol J. There are two mechanisms for arriving at a value of J: the LS coupling scheme, or Russell-Saunders coupling, and the jj coupling scheme. In LS coupling, the total orbital and spin angular momenta are obtained by summation of the individual components ℓ_i and s_i according to the triangle rule

$$L = \ell_1 + \ell_2,\ \ell_1 + \ell_2 - 1, \ldots,\ |\ell_1 - \ell_2| \tag{2.14}$$

which is also valid for S and s_i. One arrives at the total angular momentum J by then coupling L and S.

$$J = L + S, \ldots, |L - S| = \sum_i \ell_i + \sum_i s_i \tag{2.15}$$

In the jj coupling scheme however, the orbital ℓ_i and spin s_i angular momenta of each individual component (electron) are first coupled to obtain j_i, which are then summed to find J. In short, the jj coupling scheme treats the spin-orbit coupling (SOC) perturbation at the one-electron level, while in LS coupling SOC is a many-electron perturbation. In the case of atoms with smaller Z, typically including first-row transition metals, the LS case is more appropriate, as SOC is weak compared to interelectronic Coulomb forces. Thus, the LS coupling scheme for atomic term symbols is utilized in this dissertation.

2.2.6 Group Theoretical Selection Rules

As previously discussed, the major contribution to I is the electric-dipole component of f_{osc}, therefore transitions with $\mu_{if} \neq 0$ are of the most interest. The absence of any two-electron terms in Eq. 2.5 indicates that for a multi-electron system, the dipole moment operator is simply a sum of one-electron contributions. The same is true of the quadrupole and magnetic-dipole operators as well, and the nuclear coordinates are fixed within the Born-Oppenheimer approximation. The properties of these one-electron contributions, and thus the operators themselves, govern the value of f_{osc} for each one-electron transition.

In X-ray spectroscopy, the core orbital wavefunctions involved in each transition are to a very good approximation simply the atomic orbitals, in contrast to the molecular orbitals found in the valence shell. As such, a description of the core wavefunctions using the Russell-Saunders terms described above is largely accurate. This greatly aids the interpretation of X-ray spectra from a first-principles perspective. On the other hand, Russell-Saunders coupling can give rise to spectral features attributable to a series of spin multiplet states. Spectra of this nature, *e.g.* the Kβ mainline XES spectra in Section 2.4.2, cannot be calculated using single-determinantal DFT methods, which thus requires correlated wavefunction or CI theoretical treamtent.

In the absence of computational chemistry, group theory is by far the most powerful tool for predicting which transitions will have nonzero intensity. Recall from Section 2.2.4 that the electric dipole moment operator $\hat{\mu}$ is a vector, $\hat{\mu}_{x,y,z}$, and is thus antisymmetric with respect to inversion. As can be seen from the character table for a given point group, $\hat{\mu}$ therefore transforms according to the same symmetry as the p orbitals. For a transition to be electric-dipole allowed, the triple direct product $\Gamma_i \otimes \hat{\mu} \otimes \Gamma_f$ must equal or contain the totally symmetric representation (*e.g.* A_{1g}). The subscript g for *gerade*, or "even", denotes symmetry with respect to inversion, while the subscript u for *ungerade* ("odd"), *e.g.* $\hat{\mu}_u$, denotes antisymmetry with respect to inversion.

In this dissertation, the transitions involve the K-shell. Thus, either the donor or acceptor orbital *will be* the 1s, which also transforms according to the totally symmetric representation. A K-edge absorption transition can thus be written $\Gamma_g \otimes \hat{\mu}_u \otimes \Gamma_f$, and Γ_f must be *ungerade* for the transition to be allowed. For first-row transition metals, only p orbitals are *ungerade*, and thus X-ray spectral intensity depends largely on p orbital character present in Γ_f (or Γ_i for an X-ray emission transition). It should be noted that this result is clearly consistent with the $\Delta\ell = \pm 1$ selection rule from Section 2.2.5. The intensity mechanisms for K-shell XAS and XES transitions are summarized in Table 2.1.

Table 2.1: Intensity mechansims for K-shell X-ray spectral transitions

Process	Spectral Region	Orbital Transition	Allowed by:	Intensity
absorption	pre-edge	1s → 3d	$\hat{\Theta}, \hat{\mu}$ from p-d mixing	weak
	edge	1s → 4p	$\hat{\mu}$	strong
	EXAFS	1s → continuum	$\hat{\mu}$	strong
emission	Kα line	2p → 1s	$\hat{\mu}$	strong
	Kβ mainline	3p → 1s	$\hat{\mu}$	moderate
	Kβ valence-to-core	Ligand valence → 1s	$\hat{\mu}$ from Mp-L mixing	weak

2.2.7 Spectral Lineshapes

As with many spectroscopies, the information extractable from X-ray absorption and emission data, particularly with regard to intensities, can often be greatly enhanced by fitting. Strict adherence to the delta function in Eq. 2.9 would result in a spectrum consisting of a series of vertical transition "sticks", where the energy of the stick satisfies $\delta(\nu - \nu_{if})$ and the height corresponds to f_{osc}. As every spectroscopist knows however, this ideal case is never realized; rather each stick is broadened into a distribution of energies, with the extent of broadening termed *linewidth*. Understanding the origin of this broadening is fundamental to the implementation of sound fitting methodologies, which to varying degrees of confidence can be used to obtain the transition energies and intensities of the "unbroadened" stick spectrum.

The two primary sources of spectral broadening are those due to the chemical system and those due to the experiment. With most hard X-ray experiments however, the contributions of the latter are minimal, as modern absorption and emission spectrometers possess energy resolution well in excess of the systemic linewidth. There are also two distinct mechanisms for line broadening in the system, classified as homogeneous and heterogeneous broadening, depending on if they affect all molecules in the same way. Furthermore, they result in broadenings of different shapes. In X-ray spectroscopy, a common source of homogeneous broadening is is the so-called "natural linewidth", which is particularly problematic for X-rays as it is energy-dependent.

The uncertainly principle of Heisenberg, $\Delta x \Delta p_x \geq \frac{\hbar}{2}$, should be familiar to any student of chemistry, and dictates that simultaneous knowledge of both a particle's position and momentum has a minimum intrinsic uncertainty. It is obtained from the commutator of the position and momentum operators, $\hat{x}$ and $\hat{p_x}$. With a little manipulation, one can similarly determine the time-energy uncertainty formulation, which defines the natural, or "intrinsic" linewidth of a transition. For a non-stationary obvervable O of an initial state ρ_i,

$$\Delta_\rho O \Delta_\rho E \geq \frac{1}{2} | \langle [\hat{O}, \hat{H}] \rangle_\rho | \tag{2.16}$$

where $\Delta_\rho O = \sqrt{\langle O^2 \rangle_\rho - \langle O \rangle_\rho^2}$, or the *uncertainty* in O. Then, ρ_i, and thus E and O, is allowed to evolve in time. With the knowledge that commutators are related to the time evolution of expectation values, one finds that

$$\frac{1}{2} | \langle [\hat{O}, \hat{H}] \rangle | = \frac{\hbar}{2} \frac{d}{dt} \langle O \rangle_\rho \tag{2.17}$$

and thus

$$\Delta_\rho O \Delta_\rho E \geq \frac{\hbar}{2} | \frac{d}{dt} \langle O \rangle_\rho | \tag{2.18}$$

The certainty with which one can know the *rate of change* of the expectation value $\frac{d}{dt} \langle O \rangle_\rho$, is intrinsically linked to the initial certainty with which one knew the value of O in the first place (the initial state ρ_i). Therefore, the corresponding uncertainty in time (rate), $\Delta_\rho t_O$, is related to (as the quotient of) that initial uncertainty and the time evolution of the expectation value

$$\Delta_\rho t_O = \frac{\Delta_\rho O}{\frac{d}{dt} \langle O \rangle_\rho} \tag{2.19}$$

Revisiting Eq. 2.18, a simple substitution provides the time-energy uncertainty relation,

$$\Delta_\rho E \Delta_\rho t_O \geq \frac{\hbar}{2} \tag{2.20}$$

This relation dictates that for a given certainty of time, there is an associated uncertainty of energy, and *here* is where the same property which makes X-ray spectroscopy so chemically selective causes serious problems. If one excites a core electron to either a bound or unbound state at the K-edge, the resulting 1s hole is extremely unstable. As the binding energy of the 1s electrons become larger with increasing Z, the core hole also becomes increasingly unstable.

These unstable core-hole states decay after a finite and very short amount of time, called the "core-hole lifetime", which are typically on the order of picoseconds to femtoseconds. Short core-hole lifetimes result in very little uncertainty in the time of a transition between two states, and according to Eq. 2.20, this introduces uncertainty in the corresponding transition energy. Thus, the intrinsic linewidth, or broadening, of a transition is dictated by the length of the associated core-hole lifetime. For first-row transition metals, this can be on the order of 1-2 eV, however it is exacerbated as one moves across and down the periodic table.

Not only is the linewidth of X-ray transitions dictated by the core-hole lifetime, but the lineshape as well. Radiative decay of the excited state is a first-order rate process, and is described by an exponential function in the time domain. The associated spectra, recorded in the energy domain, display a natural lineshape described by a Lorentzian function; the result of a Fourier transformation on an exponential. Thus, homogeneous broadening, limited by the excited-state lifetime, imparts a Lorentzian lineshape to individual transitions. This is commonly seen in *e.g.* Mössbauer spectra, where the short nuclear excited-state lifetime broadens the discrete transition energies. Using an appropriate experimental method, it is actually possible to achieve spectral resolution better than the intrinsic linewidth, which is discussed later in this chapter.

In contrast, inhomogeneous broadening is an ensemble property, the result of different molecules in the sample having different transition energies due to *e.g.* structural heterogeneity. This is a statistical effect, and results in a distribution of transition energies which is Gaussian in shape.

These linebroadenings occur simultaneously, and so it is convenient to approximate the "true" spectral lineshape with a Voigt profile; a convolution of Gaussian and Lorentzian functions. In practice, a pseudo-Voigt profile is utilized, which can be written as

$$I \cdot \left(\left(\frac{1-G}{\pi \cdot W \cdot \left(1 + \left(\frac{x-E}{W}\right)^2\right)} \right) + \left(\frac{G \cdot \sqrt{2\log(2)}}{W\sqrt{2\pi}} \right) \cdot \exp\left(-\frac{(x-E)^2}{2\left(\frac{W}{\sqrt{2\log(2)}}\right)^2} \right) \right) \tag{2.21}$$

This is a linear combination of a Gaussian and Lorentzian function, in which the parameters that govern the component lineshapes, the energy position E, intensity I, and the width of the distribution (typically described by the full width at half maximum (FWHM), W), are shared. The final parameter to be varied is the percent composition of Gaussian and Lorentzian functions G, which is largely dependent on the nature of the transition in question. Those which are largely charge-transfer between a metal and ligand, for example, are dependent on heterogeneity in metal-ligand bond lengths and structural distortions. They will take on a more Gaussian lineshape than core-level transitions, which are more atomic in nature, insensitive to geometric changes, and thus more Lorentzian. A modification of this lineshape, suitable for modeling the absorption edge in an XAS spectrum, incorporates a smoothed step edge error function.

$$I \cdot \left((1-G) \cdot \left(\frac{1}{\pi} \tan^{-1}\left(\frac{x-E}{W}\right) + \frac{1}{2} \right) + \frac{G}{2} \left(1 + \mathrm{erf}\left(\frac{x-E}{\frac{W \cdot \sqrt{2}}{\sqrt{2\log(2)}}} \right) \right) \right) \tag{2.22}$$

where

$$\mathrm{erf} = \frac{2}{\sqrt{\pi}} \int_0^x e^{-t^2} dt \tag{2.23}$$

These models have been employed for the fitting of spectral data in this dissertation.

2.3 X-ray Absorption Spectroscopy (XAS)

The absorption of X-ray light can promote excitations or ionizations of inner-shell electrons, and XAS is generally classified (by letter) according to the principal quantum shell that is excited.

Transitions involving $n = 1$ electrons, the 1s, are termed K-edge transitions, while excitations at the $n = 2$ level, either 2s or 2p, are L-edge transitions. M-edges accordingly correspond to excitations at the $n = 3$ level, and are more commonly investigated in the case of second-row and third-row transition elements. As the number of orbital angular momentum subshells increases with increasing n, the XAS spectra become increasingly complex.

2.3.1 Metal K-edge XAS

This dissertation focuses exclusively on transitions at the metal K-edge. This has several advantages, including restricting the donor orbital space to solely the 1s. The interpretation of K-edge XAS spectra, either with the aid of theoretical quantum chemistry, group theory, or other principles, is thus generally more straightforward than other X-ray absorption edges. Furthermore, these 1s excitation energies for the first-row transition metals fall into the hard X-ray region, and the experimental conditions are thus more favorable for the investigation of biological and biologically-relevant samples.

There are three general types of transitions involving the excitation of a 1s electron, that give rise to the three primary regions of an XAS spectrum. The lowest-energy excitations are transitions into the lower-lying unoccupied LUMO orbitals. For first-row transition metals, these are often metal 3d in nature, and thus the pre-edge spectral region (Figure 2.3 is generally considered to contain 1s→3d transitions. As detailed in later chapters however, in some cases excitations into ligand-based orbitals can be observed, giving rise to metal-to-ligand charge transfer (MLCT) transitions. Finally, is it possible to observe transitions from one metal 1s orbital into the unoccupied valence levels of another metal. Examples of these metal-to-metal charge transfer (MMCT) transitions can be found in Chapter 5.

As with most absorption spectroscopies, one is primarily concerned with determining how the probablility of an absorption event changes as a function of energy. This is typically measured using the the absorption coefficient μ, or as a function of energy $\mu(E)$, defined as

$$\mu = \frac{-\ln(I_t/I_0)}{x} \tag{2.24}$$

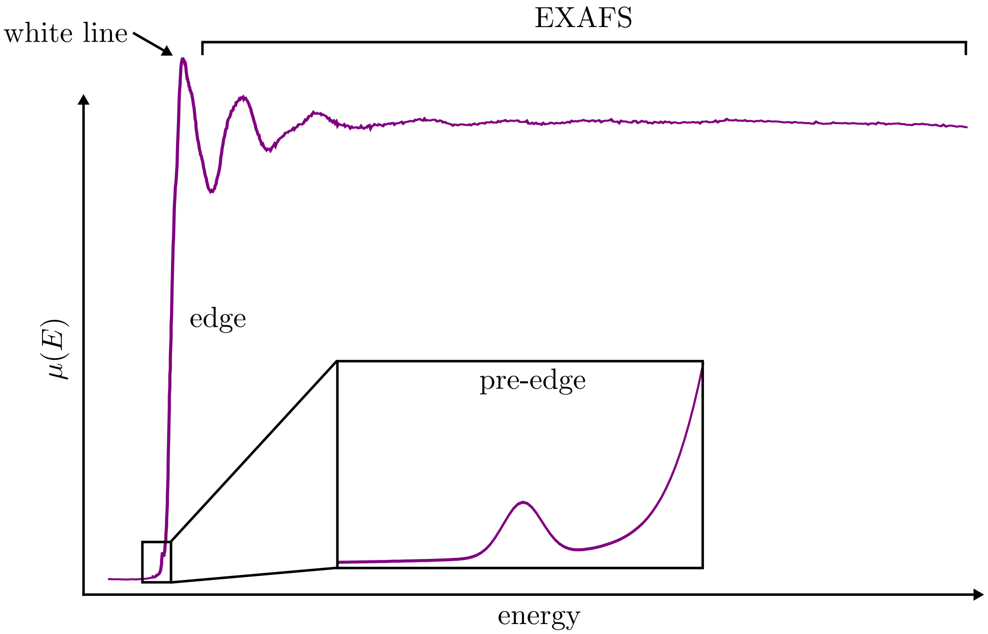

Figure 2.3: Generic K-edge X-ray absorption spectrum

where x is the thickness of the sample and I_0 and I_t are the number of photons striking and transmitted through the sample respectively. As discussed above, this probability ($\mu(E)$) is proportional to the oscilliator strength f_{osc}, and ultimately to the combined dipole and quadrupole transition moments (2.11). These pre-edge transitions to lower energy have comparatively small oscillator strengths, due to the formally dipole-forbidden 1s→3d transitions, or the two-center nature of the MLCT and MMCT transitions. In the octahedral limit, the 1s→3d transitions are forbidden by parity, as the $\mathrm{t_{2g}}$ and $\mathrm{e_g}$ d orbitals, like the 1s, are symmetric with respect to inversion. Thus, the electric dipole operator, which transforms according to T_{1u}, cannot produce intensity ($A_{1g} \notin T_{2g} \otimes T_{1u} \otimes A_{1g}$). As one deviates from centrosymmetry however, the 3d orbitals begin to mix with the metal p orbitals, and the parity selection rule is relaxed. In particular in the case of trigonally symmetric ligand fields (*e.g.* Chapter 3), substantial pre-edge intensity can be observed. It is noted that symmetry is not the only means for metal p-d mixing. In fact, as shown in Chapter 6, highly covalent ligands can also induce p-d mixing, and provide dipole-allowed transition intensity to the 1s→3d pre-edge features.

To higher energy of the pre-edge region is the edge. The edge region is comprised of excitation of the 1s electrons into the unoccupied 4p orbitals, as well as complete photoionization to the continuum. Accordingly, the energy of the absorption edge, which is commonly defined as the first inflection point in the indicated spectral region (Figure 2.3), provides an approximate measure of the binding energy of the 1s electrons. It is therefore commonly used as a marker of the oxidation state of transition metal ions, based on empirical trends from a range of known complexes. However, it has been observed that in some cases, particularly covalent iron-sulfur clusters, this correlation of edge position with oxidation state begins to break down.[97,98] This is further highlighted in Chapter 5, where changes in metal oxidation state in iron-sulfur clusters are instead found to manifest at the white line region of the XAS spectrum.

In general, the XAS spectra of first-row transition metals are broadened by the lifetimes of the 1s core-hole excited states, as discussed above. This lifetime broadening is on the order of 1-3 eV for first-row metals, and thus the resolution of transitions to different 3d orbitals, which may be separated by the same energy range, can become difficult. This problem is further exacerbated for heavier elements. However, by coupling XAS with high-resolution fluorescence detection (XES), it is possible to substantially mitigate this spectral broadening. This specific detection method, known as high energy resolution fluorescence detected (HERFD), is detailed in Section 2.5.2.

2.3.2 Extended X-ray Absorption Fine Structure (EXAFS)

At incident X-ray energies well above the K-edge, 1s electrons are photoionized. In this spectral region, known as extended X-ray absorption fine structure (EXAFS), scattering effects create oscillations in the spectral intensity. From a phenomenological standpoint, the ionized electron is considered to be propogating as a photoelectron wave. This wave can be modulated by the electrostatic potential of the electron clouds associated with atoms in close proximity, resulting in a scattering pattern arising from constructive and destructive interference. The complexity of these scattering patterns is highly system-dependent, as not only single but multiple scattering events can occur.

While the analysis of EXAFS data can be quite complex, relatively accurate metrical parameters can be obtained. In particular, metal-scatterer vectors, which often correspond to metal-ligand bond lengths, can be determined to a precision of 0.01 Å. While this is typically not as good as a high-resolution small-molecule crystal structure, it is vastly improved over the resolution typically achieved for X-ray structures of biological molecules. Thus, EXAFS can often provide the most accurate metrical parameters for metalloenzyme active sites. However, while EXAFS can yield reliable distance parameters, other pertinant information such as metal geometry / bond angles and ligand identities are less reliable. It is therefore optimally used in conjunction with other information, such as insight obtained from the pre-edge region regarding metal ion geometry.

2.3.3 Other X-ray Absorption Methods

While not discussed in this dissertation, it bears mention that XAS is not limited to the study of metal ions. In particular for the (bio)inorganic chemist, ligand K-edge XAS can provide substantive information regarding both metal-ligand covalency and the electronic structure of the metal active site(s).[99] K-edge XAS of third-row ligands such as sulfur and chlorine are more common due to the requisite X-ray energies, and in particular for biomolecules, as sulfur is in much lower abundance than other common biological ligands such as oxygen and nitrogen. Additionally, sulfur ligation provides unique properties to both iron- and copper-containing metalloenzyme cofactors.[100,101] A range of spectroscopic tools for the study of metal-sulfur bonding is thus desirable.

2.3.4 Experimental Considerations

The most basic requirement for an XAS experiment is a tunable source of X-rays with sufficient brilliance (intensity) to detect a signal. This is typically achieved using synchrotron radiation, whereby electrons traveling at relativistic speed are passed through a series of magnets in a so-called insertion device. Rapid changes in the angular momentum of the electrons results in the photoemission of X-rays. These X-rays are then monochromated to the desired energy using a series of crystal mirrors. Due to the nature of synchrotron radiation, the flux of incident X-ray photons is not constant, and anomolies in the synchrotron storage ring current can cause fluctuations in photon intensity. Additionally, the efficiency of insertion devices as well as monochromating optics are energy-dependent. To remove these artifacts from an XAS spectrum, it is customary to normalize the detected spectrum to the incident photon flux, measured using an ion chamber placed immediately before (upstream of) the sample.

Detection of the X-ray absorption spectrum is typcially accomplished in one of two ways. The first is by measuring a loss of photon transmission through the sample (transmission mode), again accomplished with an ion chamber immediately after (downstream of) the sample. This requires that the sample be of only a modest thickness, such that appreciable photons are transmitted. XAS can also be measured by detecting the total fluorescence yield (TFY) that occurs following a core-hole excitation. In this method, one assumes that the quantum yield of fluorescence events does not change as a function of incident energy, and that the number of fluorescent photons is proportional to the number of core holes created. In some cases, this latter method can further be improved by the use of an energy-resolving detector, which can be focused to a particular emission line in the spectrum. This substantially reduces the background noise due to unwanted scattering events, with minimal loss of signal intensity. As detailed below (Section 2.5.2), further improvement can be accomplished using HERFD XAS.

2.4 X-ray Emission Spectroscopy (XES)

As detailed above, excitation of a 1s electron gives rise to a highly unstable core-hole excited state. In the non-resonant limit of XES, the 1s electron is considered to be photoionized to the continuum, and one examines the various decay mechanisms by which this photoionized state relaxes. In the case of first-row transition metals, there are two regions of the XES spectrum, arising from fluorescent electronic relaxation from distinct prinicpal quantum shells.

2.4.1 Kα XES

The most probable fluorescent decay channel for a 1s excited state is for the 1s core hole to be refilled by a 2p electron, which is termed Kα emission. As shown in Figure 2.4, the Kα XES spectrum is comprised of two emission lines: the higher-energy and higher-intensity Kα_1 and the lower-energy, lower-intensity Kα_2. The highly contracted nature of the 2p orbitals results in minimal chemical sensitivity; instead, these two spectral features arise predominantly from spin-orbit coupling (SOC)

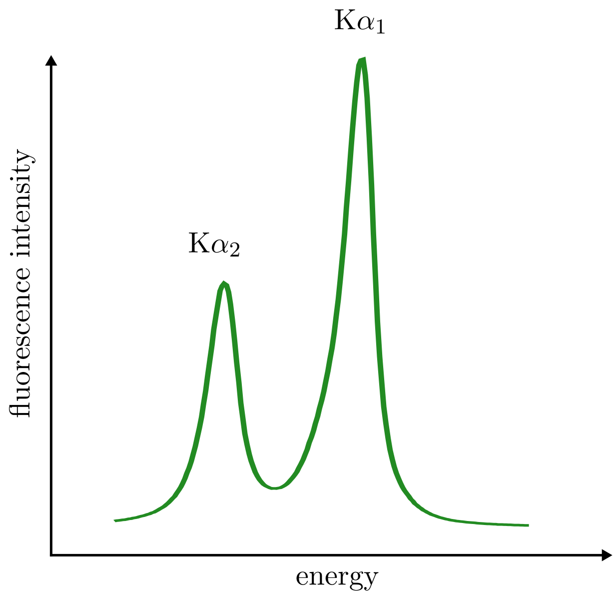

Figure 2.4: Generic Kα X-ray emission spectrum

in the $1\,s^2 2p^5$ final state. The Kα_1 line corresponds to a $^2P_{3/2}$ microstate, while the Kα_2 feature arises from a $^2P_{1/2}$ final microstate. It should be noted that the exchange coupling of the unpaired 2p electron with unpaired electrons in the 3d shell is also conceivable. Practically however, 2p SOC is significantly larger than 2p-3d exchange, and so the latter contribution can usually be neglected in non-resonant Kα XES. As this energetic splitting is nominally proportional to 2p SOC, it is found to increase with increasing atomic number Z. For reference, the splitting is roughly 8 eV for the vanadium Kα line, and approximately 23 eV for zinc.[88] While the Kα XES spectrum contains little insight into the properties of the valence shell, it is the most intense emission feature, and is thus of considerable use in resonant X-ray emission experiments detailed below.

2.4.2 Kβ XES

To higher energy of the Kα emission is the Kβ spectral region, which arises from transitions originating in the $n = 3$ shell. Fluorescent transitions from the 3p orbitals into the 1s core hole are roughly an order of magnitude less probable than the 2p→1s Kα transitions. However, while the 3p orbitals are not fomally part of the valence shell for first-row transition metals, their spatial and energetic proximity to the valence 3d and ligand orbitals engenders distinct chemical sensitivity to these spectral features. As shown in Figure 2.5, there are two regions of the Kβ XES spectrum: the intense, lower-energy Kβ mainline and the weaker, higher-energy Kβ valence-to-core (VtC).

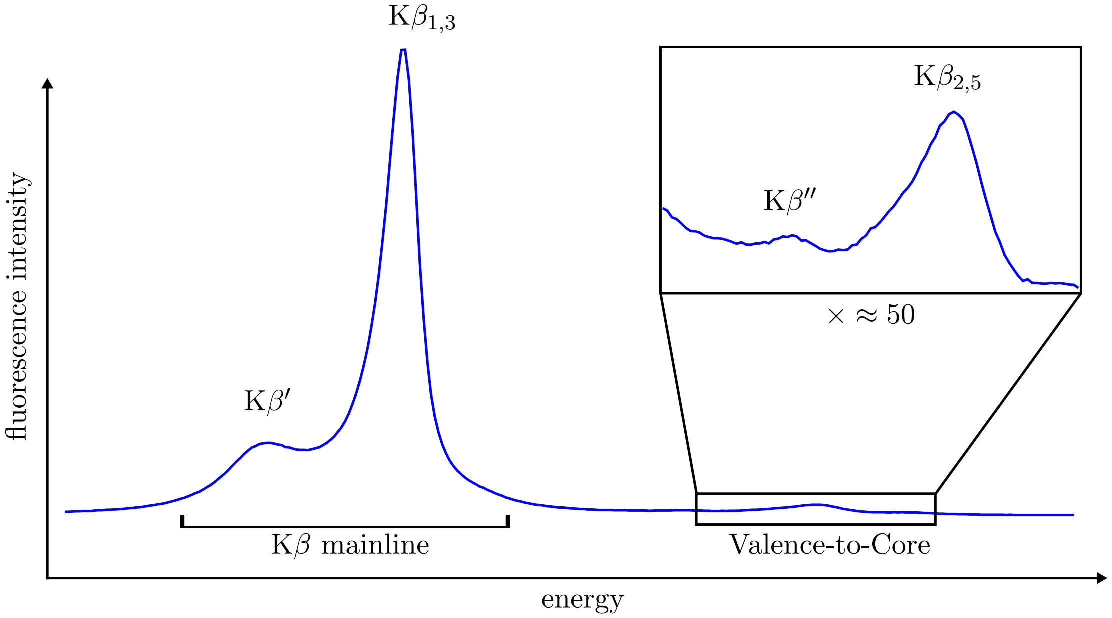

Figure 2.5: Generic Kβ X-ray emission spectrum

2.4.2.1 Kβ Mainline XES

The Kβ mainline corresponds to dipole-allowed 3p→1s transitions, and is typically comprised of two distinct features. The K$\beta_{1,3}$ peak is the most intense spectral feature, and is on the higher-energy side of the Kβ mainline. The weaker Kβ' feature is always to lower energy, and can appear as either a distinct peak (as in Figure 2.5), a low-energy shoulder of the K$\beta_{1,3}$, or in some cases is not clearly observed. In contrast to the Kα line, there are multiple contributors to the energetic splitting of the K$\beta_{1,3}$ and Kβ' spectral features, referred to as ΔE_{main}. The $3p^5$ hole gives rise to 3p SOC, however it is typically an order of magnitude smaller than the 2p SOC in the Kα line.[102,103] Thus, these contributions can be neglected to a reasonably good approximation. The spectral features of the Kβ mainline arise largely from the multiplets of the final state electron configuration, once the core hole has been quenched. Turning on 3p-3d exchange coupling, a $1s^2 3p^5 3d^n$ configuration gives rise to a series of pseudo-atomic multiplets within the Russell-Sauders (LS) coupling scheme. This is of course dependent on the number of unpaired electrons in the $3d^n$ subshell, and for simplicity's sake a high-spin $3d^5$ case (*e.g.* Mn^{2+} or Fe^{3+}) is discussed here.

In a ligand field of any symmetry, a high-spin d^5 ion is orbitally non-degenerate, and can be described by a ^6S atomic term symbol. Coupling this ^6S term to the ^2P of the $3p^5$ final state configuration in Kβ mainline fluorescence, one arrives at either a ^7P or a ^5P state, with three possible parent $3d^5$ states contributing to the latter. Schematic representations of the two possible final states arising from the ^6S d^5 configuration are shown in Figure 2.6. In the higher-multiplicity ^7P state, the unpaired 3p electron is aligned parallel to the unpaired 3d electrons, and thus 3p-3d exchange coupling is operable. In contrast, the spins in the 3p and 3d subshells are aligned antiparallel in the ^5P case, and 3p-3d exchange in quenched.

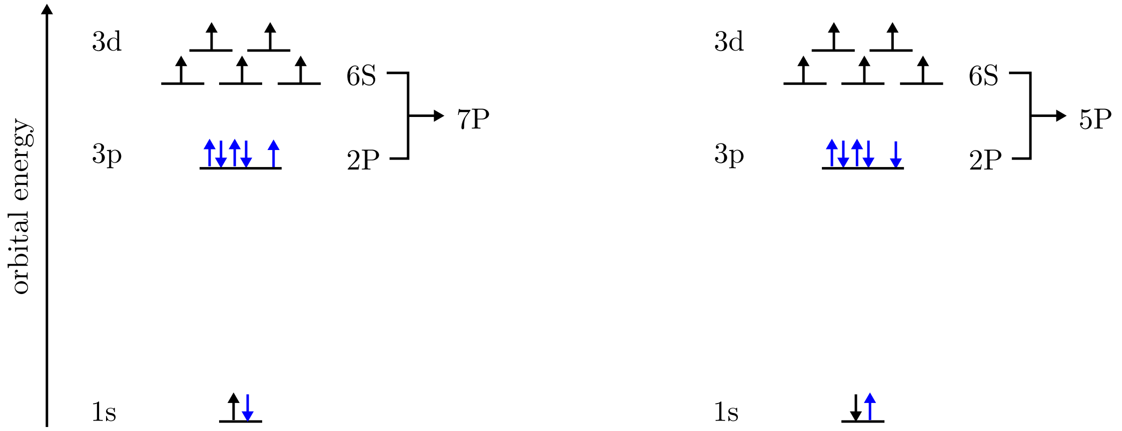

Figure 2.6: Schematic of the spin multiplets that arise from a parent ^6S high-spin d^5 configuration for a non-resonant Kβ XES final state

In a somewhat simplified picture, these two states are the major contributors to the Kβ mainline features. The 3p-3d exchange coupling stabilizes the ^7P final state, leading to larger transition energies than the lower-multiplicity ^5P. Thus, the ^7P state generally underlies the K$\beta_{1,3}$ spectral feature, and the Kβ' arises from the ^5P. If one neglects 3p SOC, as well as charge-transfer multiplets,[102] the experimentally observable quantity ΔE_{main} can be correlated to the 3p-3d exchange stabilization energy. It should be noted that while this is by no means a rigorous analysis of the

Kβ mainline region, the approximations made to arrive at this picture are generally good, and are certainly valid in the case of the data presented in this dissertation. This level of detail also provides the necessary foundation to develop the origins of the chemical sensitivity of the Kβ mainline.

As mentioned above, the range of possible final state multiplets depends on the 3d electron configuration. Similarly, the magnitude of the 3p-3d exchange stabilization depends on the number of unpaired 3d electrons, and thus, the ΔE_{main} parameter of the Kβ mainline is sensitive to the 3d spin population. Importantly, because of the highly localized nature of the 3p orbitals, the exchange coupling depends on *local* 3d spin population. ΔE_{main} can therefore provide a measure of the local spin projection, even for antiferromagnetically coupled systems that may be formally diamagnetic.

A particularly powerful application of this insight however is the ability to quantify the covalency of metal-ligand bonds.[92] In the free-ion limit, the 3d orbitals are "purely" 3d in character. The total d orbital manifold ψ_d can be described by the component 3d orbitals

$$\psi_d = \alpha\phi_{3d} \tag{2.25}$$

where α is the coefficient of 3d orbital character, in this case unity, and ϕ_{3d} are the 3d orbitals themselves. In this scenario the d orbital manifold is highly localized at the metal, and has maximal exchange coupling with the 3p. However, upon formation of a coordination complex, the 3d orbitals are delocalized *via* the nephelauxetic effect, and in the molecular orbital (MO) picture ligand-based orbitals of appropriate symmetry can mix with the 3d.

$$\psi_d \approx \alpha\phi_{3d} + (1-\alpha^2)^{\frac{1}{2}}\phi_L \tag{2.26}$$

As α becomes smaller, the fraction of ligand-orbital character ϕ_L mixed into the d manifold increases. Assuming that the two-center exchange integrals $\langle\phi_L\phi_{3p}|\phi_L\phi_{3p}\rangle$ are much smaller than the analogous one-center exchange integrals $\langle\phi_{3d}\phi_{3p}|\phi_{3d}\phi_{3p}\rangle$, decreasing α results in smaller exchange couplings. In this fashion, the ΔE_{main} provides a sensitive measure of α, the extent of covalent metal-ligand orbital mixing. A final note that will be subsequently developed in the discussion of resonant X-ray emission spectroscopy (RXES) is that the final state multiplets in Figure 2.6 involve 3p→1s transitions in different spin manifolds. As Pauli exclusion requires that the 1s electrons be paired, these two final states correspond to initial 1s ionizations of electrons with opposite spin states.

2.4.2.2 Kβ Valence-to-Core (VtC) XES

The higher-energy features of the Kβ XES spectrum comprise the valence-to-core (VtC) region. As the name suggets, these peaks correspond to transitions from the valence shell. In the case of first-row transition metals, these are the metal 3d and ligand 2s/2p or 3s/3p orbitals. Transitions from metal 3d orbitals into the 1s are dipole forbidden ($\Delta\ell = -2$), however in low-symmetry sites, metal p/d mixing can impart some dipole transition intensity, as exemplified in Chapter 3.[29,104] Interestingly, spectral features that arise from ligand-based orbitals can also be observed. These transitions gain dipole intensity through metal p orbital mixing into the ligand MOs, and although weak, they contain a wealth of information regarding the electronic structure of the coordinating moieties around a metal center.[105,106]

The VtC spectral region is generally comprised of two peaks: the higher-energy K$\beta_{2,5}$ and lower energy Kβ''. Roughly, these correspond to metal p-type and s-type orbitals, respectively. However, a successful interpretation of VtC spectra often requires an MO-based approach, and thus atomic-type labels are only sometimes applicable. As is detailed throughout this dissertation, particularly in Chapters 3, 4, and 6, the VtC region is sensitive to changes in ligand electronic structure. This is of particular utility in the quantification of small-molecule activation (O_2,[29] N_2,[107] NO[108]). Additionally, VtC XES is capable of identifying differential bonding of similar atoms,[95] or the identity of light-atom ligands in biological molecules.[68,109]

2.4.3 Experimental Considerations

Hard X-ray emission spectroscopy of biologically relevant first-row transition metals occurs approximately in the 5000-10000 eV energy range. As with any spectroscopy, proper spectral resolution is critical to the success of a given method. Here, energy resolution in the X-ray emission spectrum must be on the order of 1 eV, in particular for the VtC region, which corresponds to a resolving power, defined as $\frac{E}{\Delta E}$, of at least 5000. Modern X-ray detectors have some capacity for energy windowing, however they lack nearly an order of magnitude in resolving power. To achieve the requisite resolution, many X-ray emission spectrometers utilize analyzer crystals and Bragg optics.

Bragg's law, which describes the coherent scattering or diffraction of light from a perfect crystal lattice, can be expressed as

$$n\lambda = 2d \sin\theta \tag{2.27}$$

where n is an integer, λ is the wavelength of the incident light, d is the spacing between lattice layers in the selected analyzer crystal material, and θ is angle between the incident ray and the plane of the scattering surface. For a given lattice spacing d, the energy (inversely proportional to λ) can be scanned by changing the angle of incidence θ. This can be achieved by defining three points on a Rowland circle: the source of fluorescent X-rays (the sample), the crystal analyzer, and a detector. The source is fixed by necessity (focusing of the X-ray beam), and the remaining two elements are scanned through a range of angles.

There are a number of practical considerations which further complicate this design strategy. Firstly, the spectrometer is required to achieve a high degree of precision in terms of angle space, however this is readily accomplished by moving to larger radii. However, at larger radii the solid angle which is captured by a single analyzer crystal (*i.e.* the percentage of fluorescent photons detected) scales as $\frac{1}{r^2}$ (the surface area of a sphere), and data collection times concomitantly increase. Finally, at smaller radii, the actual manufacture of perfect crystal surfaces, which must be spherically bent according to the curvature of the Rowland circle, becomes extremely difficult.[89]

A typical compromise of these offsetting considerations is a spectrometer that utilizes mutliple intersecting Rowland circles, all sharing a common source and detector focal point as shown in Figure 2.7. This requires an array of crystal analyzers, which can all move in tandem to perform an energy scan. Many spectrometers are focused to a Rowland diameter of 1 meter, and the individual optical elements require careful alignment prior to data collection. It should be noted that upon changing energy windows, either from Kα to Kβ fluorescence or to a new absorber,

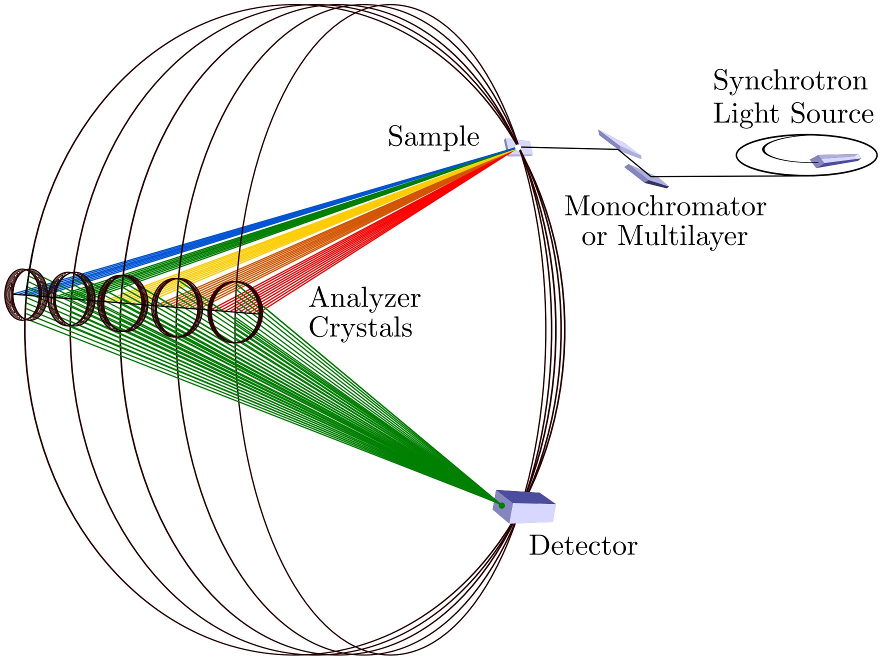

Figure 2.7: Schematic of a Rowland geometry XES spectrometer

the crystals must be exchanged according to their lattice spacing d. For example, an Fe Kβ XES spectrum can be collected with the (620) surface of a Ge crystal, while Mn Kβ XES requires a Si(440) surface. Additional details, and descriptions of alternative spectrometer configurations for dispersive measurements, can be found in a recent review article.[89]

2.5 Two-Dimensional X-ray Spectroscopy

While X-ray absorption and emission spectroscopies are powerful in their own right, their integration into a single methodology adds literally another dimension to the depth of the chemical insight. In practice, the experiment is a simple combination of variable, monochromatic incident X-rays with a high-resolution XES spectrometer. As a photon-in/photon-out method, both the energy of the incoming photon and the energy (or more commonly the energy or momentum *transfer*) of the emitted photon are manipulated. This spectroscopic method goes by different terminology in the literature, and unfortunately there is not yet a clear distinction between them. Some common names include resonant inelastic X-ray scattering (RIXS), resonant X-ray emission spectroscopy (RXES), and resonant X-ray Raman scattering.

As is apparent from these acronyms, the process is *resonant*, in contrast to the prior discussion of XES in the non-resonant limit. The distinction is in the fact that the energy of the incident X-rays is tuned close to a resonant absorption edge, and electrons are excited to bound states rather than the continuum. As shown in Figure 2.8, a resonant Kβ XES process for a high-spin d^5 metal ion can result in a d^6 final state configuration, due to the resonant excitation of the 1s electron. In contrast, the non-resonant Kβ XES final states in Figure 2.6 remain d^5.

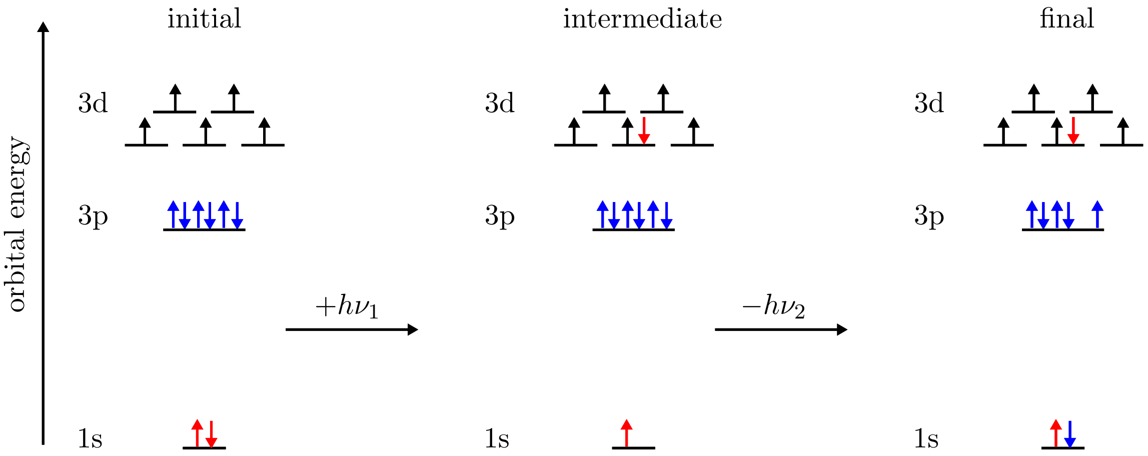

Figure 2.8: Three-state schematic of a resonant X-ray emission process

2.5.1 Resonant X-ray Emission Spectroscopy (RXES)

As a two-dimensional method, it can be convenient to plot each dimension (incident energy and energy transfer) on an axis, resulting in a plane of data. To collect such data however requires sampling all possible data points in the plane, and this can present some practical problems. Ideally, one could envision a dispersive detector arrangement capable of sampling an entire spectrum in a “single shot”. Then, a scan of the incident energy (akin to an XAS experiment) would, with sufficient signal averaging, produce a complete “RIXS plane” as shown in Figure 2.9. While this is more common with soft X-rays at transition metal L-edges, it is more challenging to obtain the necessary resolving power and signal intensity with higher-energy hard X-rays. Thus, “slices” of the plane can be taken at particular energies. A vertical slice would correspond to an XES spectrum with resonant excitation (RXES), while a horizontal scan corresponds to an XAS scan

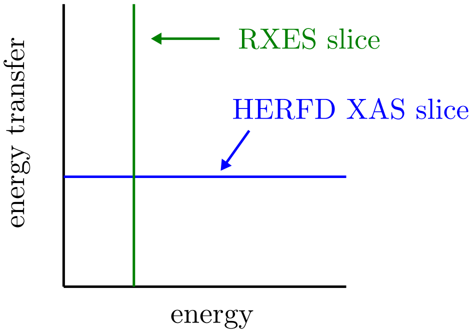

Figure 2.9: General construction of a RIXS plane, illustrating the direction of RXES and HERFD XAS slices

with narrow-band emission detection.

2.5.2 High-Energy Resolution Fluorescence-Detected (HERFD) XAS

It is somewhat of a misnomer to refer to this latter slice as an XAS experiment, because in fact one still detects X-ray emission, simply at various excitation energies. However, the information content and shape of the resulting spectrum, plotted as the fluorescence intensity vs. incident energy, is indeed akin to an XAS experiment. There are two principal ways in which the HERFD method can enhance the information content of an XAS experiment. The first, detailed using a discussion of Kα-detected HERFD, is to provide enhanced spectral resolution better than the intrinsic 1s core-hole lifetime. The second, discussed with Kβ-detected HERFD, is the enhanced selectivity of the XAS experiment to specific decay channels corresponding to different spin multiplets.

2.5.2.1 Kα HERFD

The Kα emission line is the most intense emission feature by roughly an order of magnitude. Accordingly, HERFD XAS experiments on dilute samples such as frozen solutions of protein benefit from Kα detection. The principal advantage of Kα HERFD XAS is that the spectral resolution obtained from this experiment is better than what is dictated by the 1s core-hole lifetime. Instead, the apparent spectral resolution is more consistent with intrinsic lifetime broadening of the $1s^2 2p^5$ final state.[110] Figure 2.10 shows a schematic of the Kα HERFD XAS process, including an approximate detection bandwidth and three-state energy diagram. For both the intermediate and final

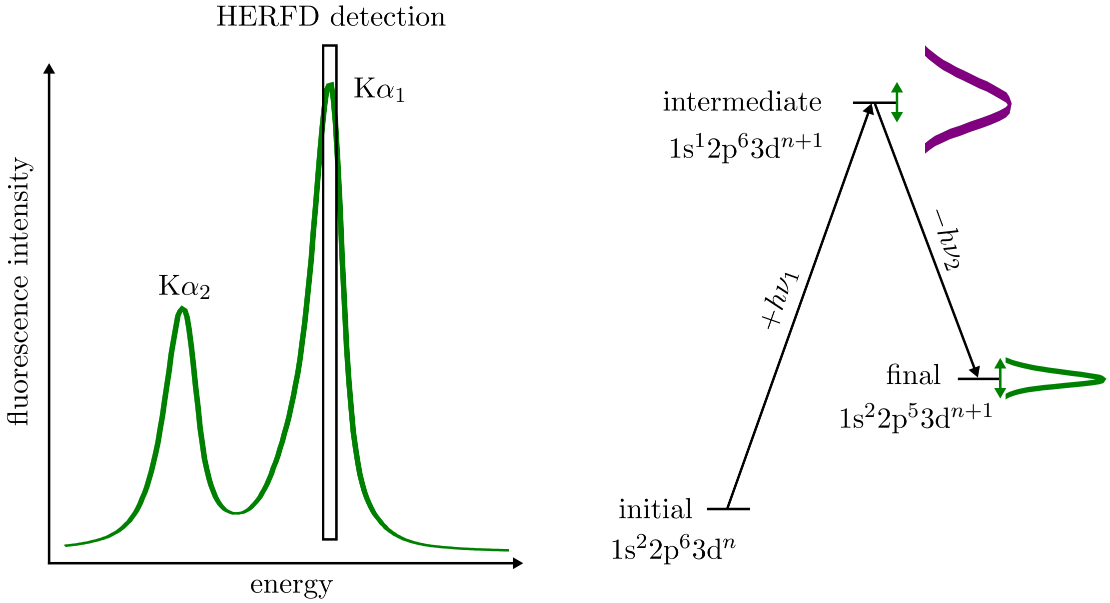

Figure 2.10: Schematic of the spectral sharpening mechanism of the HERFD XAS process, with approximate emission bandwidth resolution for a Kα XES spectrum

states, the approximate lifetime broadening associated with the inner-shell holes (see Figure 2.8 for an example with Kβ HERFD) is indicated by the Lorentzian-type lineshapes at right, with the higher-energy core-hole excited state displaying more significant broadening.

The HERFD method selects for only specific Kα final states, with a lifetime broadening corresponding to the 2p hole. As shown by the vertical box in Figure 2.10 left however, the bandwidth of the fluorescence detection, represented by the arrow labeled $-h\nu$ in Figure 2.10 right, is much more narrow than the intrinsic linewidth of the Kα_1 line. Thus, the *length* of the $-h\nu_2$ arrow in Figure 2.10 right is static. The final state selection now also limits the vertical position of that arrow (shown by the green arrows), which selects for only a subset of the distribution of intermediate state energies. As only those intermediate state energies will be detected by narrow-band fluorescence, the observed spectral linewidth in the HERFD XAS spectrum, represented by the $+h\nu$ arrow, must be confined to transitions with an energetic distribution similar to that of the final state lifetime broadening. Thus, HERFD can improve the XAS spectral resolution beyond the limit of the core hole lifetime broadening, sometimes by a factor of two or three.[110,111]

2.5.2.2 Kβ HERFD

The advantages of spectral resolution improvement discussed above pertain also to HERFD XAS using the Kβ emission features. At the expense of roughly an order of magnitude in signal intensity, Kβ HERFD can in some cases also permit the resolution of the α and β spin manifolds in XAS transitions.[112] As shown in Figure 2.6, the ^{7}P and ^{5}P final states in the Kβ mainline arise from the fluorescent relaxation of 3p electrons *of differing spin*. In the non-resonant picture, the spin state of the 1s electron that was initially excited must match the spin state of the fluorescing 3p electron. In the resonant picture however, the 1s electron is excited into a bound state, and Pauli exclusion limits the spin state of the excited electron. Figure 2.8 illustrates this phenomenon, as the analogous three-state scheme cannot be achieved with a 1s electron of opposite spin state. In a high-spin d^5 configuration, only 1s→3d excitations of minority spin state (spin-down, β), are allowed according to Eq. 2.13.

When this realization is coupled with the ability to select for different final state multiplets in the Kβ emission spectrum (Figure 2.5), only transitions detected at the higher-energy ^{7}P K$\beta_{1,3}$ feature give rise to 1s→3d transitions. In contrast, detection at the Kβ' results in a suppression in pre-edge intensity, as illustrated in Figure 2.11 and Chapter 5. Interestingly, because this mutliplet (and thus spin state) sensitivity of the Kβ mainline is a *local* property, it is not dependent on the total spin S_{total}. There are thus instances where the spin sensitivity of the Kβ HERFD XAS experiment could differentiate between *e.g.* antiferromagnetically coupled high-spin / high-spin or low-spin / low-spin sites; a property that is extremely challenging to measure. Finally, in systems possessing metal ions of differing spin state but the same identity, Kβ HERFD can be utilized to obtain a "site-selective" XAS spectrum through preferential selection of particular spin multiplets.[113]

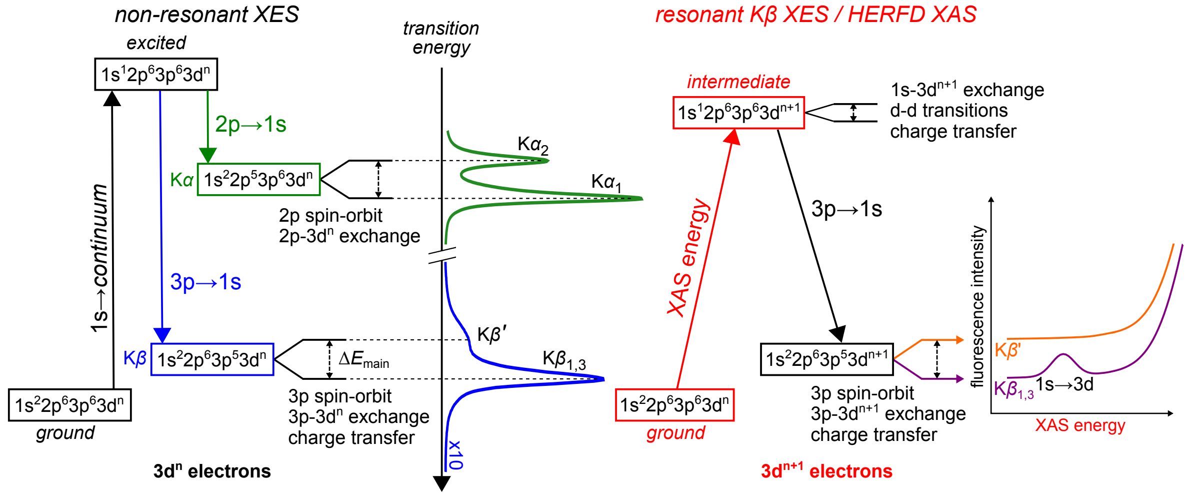

Figure 2.11: Left: Schematic of the non-resonant Kα and Kβ mainline XES processes and the spectral features that arise from them. Right: Schematic of resonant Kβ XES and Kβ-detected HERFD XAS, with the pre-edge XAS spectra expected from detection at different Kβ mainline features. The boxed electron configurations represent the one-electron picture, and the branched levels show the energetic splitting of the one-electron picture as a result of the specified interactions.

2.6 Concluding Remarks

In this chapter, I have endeavored to provide a primer on the X-ray spectroscopic methods employed in this work. Given the paucity of experimental time often available to conduct these experiments, an informed choice and design of experiments is critical for maximizing the data one can obtain. Additionally, strategies for practical data collection and a rigorous analysis grounded in the fundamental physics are discussed. Finally, some relevant applications of X-ray spectroscopy for the study of (bio)inorganic molecules are highlighted. While each subsequent chapter offers a review of the pertinent information herein, a thorough understanding of this chapter stands the reader in good stead to enjoy the remainder of this dissertation.

Chapter 3

"There are no facts, only interpretations."
FRIEDRICH NIETZSCHE

X-ray Absorption and Emission Study of Dioxygen Activation by a Small-Molecule Manganese Complex

Portions of this chapter have been adapted or reprinted with permission from: Rees, J. A.; Martin-Diaconescu, V.; Kovacs, J. A.; DeBeer, S., *Inorg. Chem.* **2015**, *54*, 6410-6422. Copyright 2015 American Chemical Society.

3.1 Introduction

Molecular oxygen (O_2) provides nature with a virtually inexhaustible source of oxidizing equivalents with which to perform chemical transformations. It has therefore been incorporated into many vital biological cycles of aerobic organisms, including the synthesis of DNA bases, the metabolism of chemicals and toxins, and the synthesis of ATP *via* aerobic cellular respiration. Despite the considerable oxidizing potency of dioxygen, it is a relatively inert, and thus benign molecule, a result of the strong O=O bond of 119 kcal/mol. The effective use of O_2 thus requires catalysts in the form of metalloenzymes to overcome this significant activation barrier. Nature has incorporated a variety of transition metals into enzymes tasked with the activation of dioxygen, including Fe, Mn, and Cu. A molecular-level understanding of these systems in the form of mechanistic insight is highly desirable, as many metalloenzymes outperform the best synthetic catalysts, however the direct study of dynamic, large protein systems has many associated challenges.

While a variety of metal-bound reduced dioxygen intermediates have been implicated in the mechanisms of many O_2-reducing metalloenzyems, much of what is known about these transient species has been discovered *via* the study of synthetic inorganic complexes. In particular, synthetic complexes of Fe and Cu with peroxide, the two-electron reduced form of dioxygen, have been studied extensively as analogues for putative intermediates of respective enzyme systems. Considerably less is known about Mn peroxo complexes however, due in part to a lack of available characterized model complexes. In addition to promoting O_2 reduction, Mn is the only redox-active metal involved in biosynthesis of O_2 *via* the 4 e^- oxidation of water in the oxygen-evolving complex (OEC) of PSII. A Mn peroxo moeity has been invoked as a critical step of O-O bond formation in the mechanism of the OEC, proposed to occur immediately preceeding O_2 evolution. The rational development of improved synthetic catalysts for reactions such as water oxidation to dioxyen, highly desirable for applications in the domain of carbon-neutral energy applications, or for the controlled activation of O_2 would therefore likely benefit greatly from insight into the chemical properties of Mn peroxo complexes and the ways in which this the O-O bond is formed or activated.

Recent work by Coggins *et al.* has resulted in groundbreaking insight into the properties of Mn peroxo moeities. The reaction of the Mn(II) complex $[\mathrm{Mn^{II}}(\mathrm{S^{Me2}}(\text{6-Me-DPEN}))]^+$ (**1**) with molecular oxygen yielded a novel, metastable, binuclear $\mathrm{Mn(III)_2}$ peroxo-bridged dimer, $\{[\mathrm{Mn^{III}}(\mathrm{S^{Me2}}(\text{6-Me-DPEN}))]_2(\textit{trans}-\mu\text{-}1{,}2\text{-}O_2)\}^{2+}$ (**2**), which forms *en route* to the final product, an unsupported mono μ-oxo bridged $\mathrm{Mn(III)_2}$ complex $\{[\mathrm{Mn^{III}}(\mathrm{S^{Me2}}(\text{6-Me-DPEN}))]_2(\mu\text{-O})\}^{2+}$ (**3**) (Scheme 3.1).[28] The peroxo-bridged dimer **2** was characterized by X-ray crystallography, stopped-flow UV-vis and resonance Raman spectroscopies, and SQUID magnetometry. Additionally, intermediate **2** was shown to convert quantitatively to the final product **3**, and both ESI-MS and resonance Raman experiments using $^{18}O_2$ demonstrated that the peroxo and oxo bridges are derived from dioxygen. Finally, an O-O bond length of 1.452(5) Å and an O-O stretching frequency of 819 cm^{-1} indicates that relative to other examples in the literature, the peroxo bond in **2** is highly

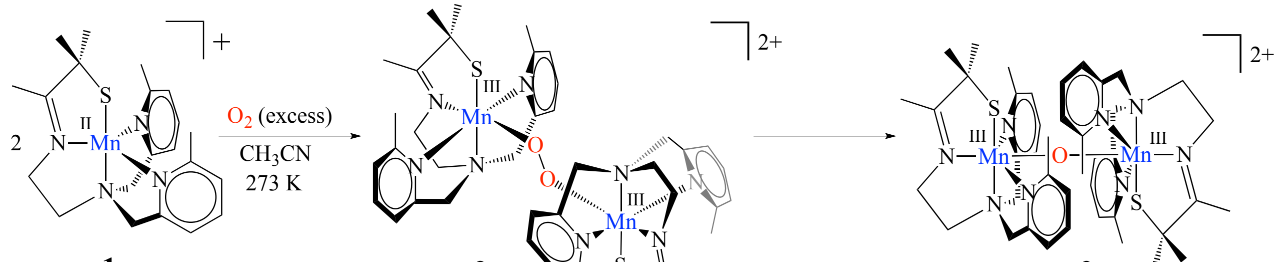

1 $S = {}^5/_2$

2 2 x (S=2) J = 0 cm^{-1}

3 2 x (S=2) J = -125.6 cm^{-1}

Scheme 3.1: Structure and dioxygen reactivity of Mn(II) complex **1**, showing formation of metastable intermediate **2** and final product **3** activated. Employing a set of systematic variations of ligand scaffold of **1**, a series of six structurally analogous monomeric Mn(III) alkylperoxo complexes was also structurally characterized by the reaction of the requisite Mn(II) precursor with either cumyl peroxide or *tert*-butyl peroxide, with the peroxo ligand coordinated in an η^1 end-on fashion.[41,42] To date these remain the only examples of isolable Mn(III) alkylperoxo complexes.

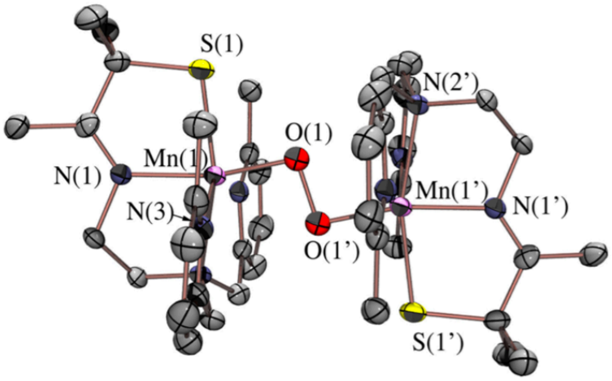

Figure 3.1: ORTEP diagram of $\{[\mathrm{Mn^{III}}(\mathrm{S^{Me2}}(6\text{-Me-DPEN}))]_2(\textit{trans}-\mu\text{-}1,2\text{-}\mathrm{O_2})\}^{2+}$ (**2**), showing 50% probability thermal ellipsoids

A systematic correlation in structural metrics was observed between the length of the peroxo O-O bond and the average Mn-N-heterocyclic amine distance for four *tert*-butylperoxomanganese(III) complexes, indicating that the N-heterocycles were in some fashion "tuning" the degree of activation of the O-O bond (Figure 3.2). Variation in the O-O metrical parameters also manifested in trends in O-O stretching frequency and the activation parameters $\Delta H^{\ddagger}$ and $\Delta S^{\ddagger}$, and DFT calculations determined that the interaction of the N-heterocyclic amine modulated the Lewis acidity of the Mn(III) ion. The result of a decrease in Mn(III) Lewis acidity was found to be diminished Mn d orbital character in the peroxo π^*_{v}, *i.e.* a more localized π^* orbital and thus a weaker O-O bond.

Figure 3.2 shows that the metrical parameters for peroxo **2** closely follow the correlation of the alkylperoxo bond lengths, suggesting that the structural and electronic effects responsible for the observed trend are also present in **2**. Peroxo-bridged **2** is still the only structurally-characterized binuclear $\mathrm{Mn(III)_2}$ peroxo complex to have been reported, as well as one of few examples of a dioxygen-derived peroxomanganese complex. As such, a more complete understanding of the electronic structure of this molecule is highly desirable, as the insight obtained may enable rational

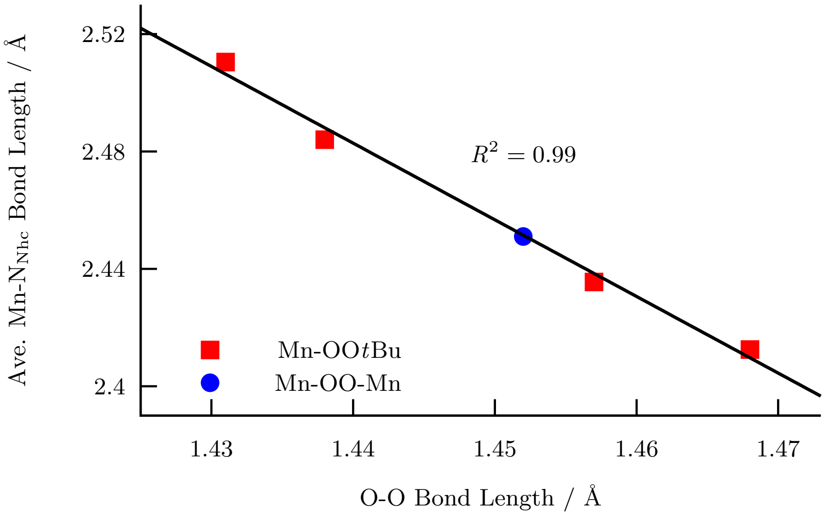

Figure 3.2: Plot of O-O bond length [Å] vs. average Mn(III)-N-hetercycle bond length [Å] for Mn(III)-alkylperoxo complexes (red square) and the Mn(III)$_2$ peroxo dimer **2** (blue circle). Metrics for **2** are not included in the correlation.

ligand design choices with regard to expanding the library of Mn(III)$_2$-O$_2$ complexes or increasing the stability of other putative intermediates in the reaction pathway. Furthermore, given the demonstrated importance of at least some structural factors on the degree of activation of the O-O bond (*vide supra*), determining the manner and degree of the N-heterocyclic amine interaction with Mn in greater detail is of significant interest. Finally, given the novelty of **2**, this molecule presents for the moment a unique opportunity to obtain benchmark spectroscopic parameters for a bridging peroxomanganese(III) moiety; a motif similar to key catalytic intermediates proposed for a range of Mn metalloenzymes.

As detailed in the latter sections of Chapter 2, X-ray spectroscopic techniques are an ideal tool for investigation of the electronic structure of peroxo-bridged **2**. In particular, K-edge X-ray absorption spectroscopy (XAS) and X-ray emission spectroscopy (XES) are complimentary methods which facilitate the study of both the lowest unoccupied, or virtual, orbitals and the occupied valence levels, respectively.

3.2 Experimental

3.2.1 Synthesis and Sample Preparation

$[\mathrm{Mn^{II}(S^{Me2}(6\text{-}Me\text{-}DPEN))}]^{+}$ (**1**), $\{[\mathrm{Mn^{III}(S^{Me2}(6\text{-}Me\text{-}DPEN))}]_2(\textit{trans}\text{-}\mu\text{-}1,2\text{-}\mathrm{O_2})\}^{2+}$ (**2**), and $\{[\mathrm{Mn^{III}(S^{Me2}(6\text{-}Me\text{-}DPEN))}]_2(\mu\text{-}\mathrm{O})\}^{+2}$ (**3**) were synthesized as previously reported.[28,114] Solution samples for absorption measurements were prepared as saturated solutions of crystalline solid in acetonitrile (**1** and **3**) or propionitrile (**2**) at 10-15 mM. Solutions were loaded into 1 mm cells with a 38 μm Kapton tape window and immediately frozen in liquid N_2. Solid samples for emission measurements were prepared by diluting crystalline solid of **1-3** with boron nitride (approximately 1:1 by mass). The mixture was ground into a homogeneous powder with a mortar and pestle, sealed in Al spacers with Kapton tape, and frozen in liquid N_2. Due to the thermal instability of **2**, samples of this compound were prepared at 195 K in a freezer, or on a bed of dry ice. To prevent condensation of water, solid samples were prepared under a blanket of Ar.

3.2.2 XAS and XES Measurements

Data were collected at the European Synchrotron Radiation Facility (ESRF) beam line ID-26, equipped with a Si(111) double crystal monochromator, and a LHe cryostat (10 K) sample chamber. $K\beta$ X-ray emission spectra were measured at an incident energy of 6700 eV using five Si(440) crystal analyzers and an avalanche photo diode detector (APD) in a Rowland geometry (Figure 2.7). X-ray absorption data were measured in both total fluorescence yield (TFY) and $K\beta$ detection modes using discrete photodiodes. $K\beta$-detected high energy resolution fluorescence detected (HERFD) XAS were measured by holding the angle for the analyzer crystals fixed to the maximum energy of the Mn $K\beta_{1,3}$ emission line for each respective compound. The incident flux at the sample was $\approx 10^{13}$ photons/second in a 0.2 x 1.5 mm^2 beam spot. In order to assess radiation damage and determine the acceptable dwell time per sample spot, short (5 to 6 seconds) $K\beta$-detected XANES scans were measured to assess the rate of photoreduction. If necessary, aluminum foils were inserted into the beam path to attenuate the incident flux. Only scans that showed no evidence of radiation damage were included in the final analysis. Acceptable scans were averaged using PyMCA.

3.2.3 Analysis of XAS Spectra

Mn K-edge XAS spectra of $KMnO_4$ were used as an energy calibration reference, with the pre-edge maximum at 6543.3 eV.[115] For all XAS data, a linear pre-edge function and a quadratic polynomial for the post-edge were used for background subtraction, followed by normalization of the edge jump to unity. In order to extract intensities and energy positions, the pre-edges were fit pseudo-Voigt functions, and a cumulative pseudo-Voigt function was used to model the edge jump. The intensity of the features corresponds to the integrated area under the peaks. The software package PeakFit v. 4.12 was used for the fitting.

3.2.4 Analysis of XES Spectra

The mainline regions of all spectra were modeled with a sum of 4 pseudo-Voigt functions and fit using MATLAB. The VtC region of **1** was then modeled using a sum of 5 pseudo-Voigt functions to identify contributions from the N and S atoms of the ligand. These functions were used as a start point to model the VtC regions of **2** and **3**, where the peak positions and intensities were allowed to float but the FWHM and Lorentzian fraction were held fixed to within 5%. For initial modeling of **2** and **3** the region between 6512 and 6522 eV, corresponding to the Kβ'' observed in **3**, was excluded and the remainder of the VtC region fit using the functions present in **1**. An additional function was then added to describe the O contribution in the Kβ'' , and a fit of solely that function performed for **2** and **3**. Finally, all constraints were removed and fits of the full XES spectra were performed. The intensities of the final fits were then used to normalize the total integrated XES spectral areas to 1000. It should be noted that fits for **2** and **3** using two functions instead of one to model the O contribution produced solutions with lower adjusted R^2 values. Due to intrinsic errors associated with this method of modeling the mainline background in the VtC region, previous error estimates of $\approx$ 10% in experimental VtC areas have been made.[116] In the present case of highly related compounds however, the expected error associated with the relative VtC area determinations is likely lower.

3.2.5 Computational Details

All calculations were performed using the ORCA quantum chemistry package v. 3.0.[117] The zeroth-order regular approximation for relativistic effects (ZORA),[118] the dispersion correction of Grimme and co-workers (D3BJ),[119,120] and the scalar-relativistically recontracted def2-TZVP(-f) basis set[121] were used throughout. A dense integration grid (ORCA Grid4, 302 Lebedev points) was employed, along with the fully decontracted def2-TZVP/J auxiliary basis set[122] and and conductor-like screening model (COSMO) using dichloromethane as the solvent ($\epsilon = 9.08$).[123] Geometry optimizations and subsequent analytical frequency calculations were initiated from X-ray crystallographic coordinates using the BP86 functional[124,125] with the resolution of the identity (RI) approximation.[122] Valence-to-Core XES calculations were performed within a one-electron DFT model, and were corrected for spin-orbit coupling using the spin-orbit mean-field method[126] as previously described.[53,116,127] XAS calculations were performed using the B3LYP functional and the TD-DFT method employing the Tamm-Dancoff[128,129] and the RI chain of spheres (RIJCOSX) approximations.[130–132] Fragment anaylsis was performed with MOAnalyzer,[133] and orbital isosurfaces and transition difference densities were visualized with UCSF Chimera.[134] Normal mode trajectories were animated and visualized using Avogadro.

3.3 Results and Discussion

3.3.1 Experimental K-Edge XAS Data

Mn K-edge XAS spectra were recorded for **1-3** in both total fluorescence yield (TFY) and Kβ high energy resolution fluorescence detected (HERFD) modes. As previously discussed, HERFD detection is expected to mitigate spectral broadening due to finite core-hole lifetimes.[102,135,136] Indeed, the HERFD data shown in Figure 3.3 exhibit significantly improved spectral resolution in the pre-edge region compared to those collected in TFY. The spectra were fit using a series of pseudo-Voigt functions (2.21) to model the transitions in the pre-edge and rising edge. As a detailed examination of the EXAFS region is not necessary given the availability of X-ray crystal structures of all three complexes, pseudo-Voigt functions were similarly used to fit the EXAFS

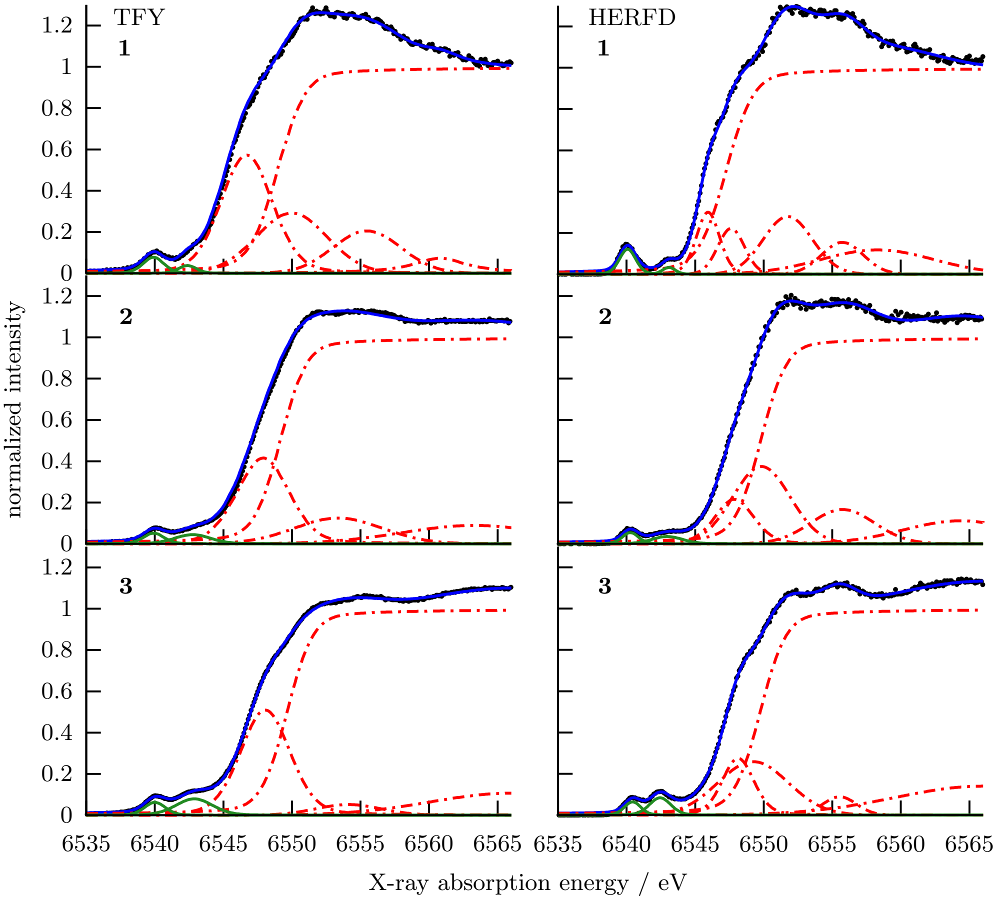

Figure 3.3: Experimental data (points) and fits of the Mn K-edge X-ray absorption spectra of **1-3** collected in TFY (left) and Kβ HERFD (right). Total fit is shown in blue, with component functions in dashed red and features denoted as pre-edge in green.

oscillations, on top of a modified cumulative pseudo-Voigt function (2.22) to fit the edge jump. The results of the fitting for all datasets is shown in Figure 3.3 and provided in Table 3.1. While detection at the K$\beta_{1,3}$ line should theoretically select preferentially for excitations of the β spin core electrons, quantitative comparison of the TFY and Kβ HERFD XANES spectra reveals no significant changes aside from a sharpening of the pre-edge features. This suggests that either there is sufficient multiplet structure in the mainline within the resolution of the spectrometer to negate this effect or that the contributions of α spin excitations are negligible.[102] While the latter is certainly true in the case of **1** given the high-spin d^5 configuration, it is likely that a combination of both effects contribute to the absence of significant differences in the intensity trends of the TFY

Table 3.1: Experimental HERFD and calculated Mn K-edge XAS parameters

		expt pre-edge (1s to 3d)		calcd pre-edge (1s to 3d)		expt pre-edge 2 (MLCT)	
HERFD	edge energy (eV)	energy (eV)	intensity (x10^2)	IWAE (eV)	intensity (x10^6)	energy (eV)	intensity (x10^2)
Mn(II) **1**	6545.5	6540.1	20	6540.1	56.3	6543.1	9
peroxo **2**	6547.6	6540.3	9	6540.8	52.0	6543.0	11
oxo **3**	6547.6	6540.4	10	6540.8	34.7	6542.4	17
TFY							
Mn(II) **1**	6545.4	6540.0	16	6540.1	56.3	6542.5	7
peroxo **2**	6547.3	6540.1	11	6540.8	52.0	6542.9	16
oxo **3**	6547.5	6540.0	13	6540.8	34.7	6542.9	29

and HERFD data. Due to the improved resolution, continued analysis using the HERFD XAS data is preferable, however it should be noted that when compared to the TD-DFT calculations, the physical representation is not strictly accurate.

Normalized Kβ HERFD XAS spectra for **1-3** are shown in Figure 3.4. The energy of the rising edge is found to increase by ≈ 2.1 eV upon conversion of **1** to peroxo **2**, indicating a one-electron oxidation of the Mn (Table 3.1). The identical rising edge energy of **3** is again consistent with an increase in oxidation state relative to **1**. Preceding the rising edge, all complexes exhibit a pre-edge consisting of two well-resolved features at ≈ 6540 eV and ≈ 6542.5 eV (Figure 3.4 right). For Mn complexes with extended π systems, the low and higher energy pre-edge features have previously been assigned as 1s→3d and metal-to-ligand charge transfer (MLCT) transitions, respectively.[115]

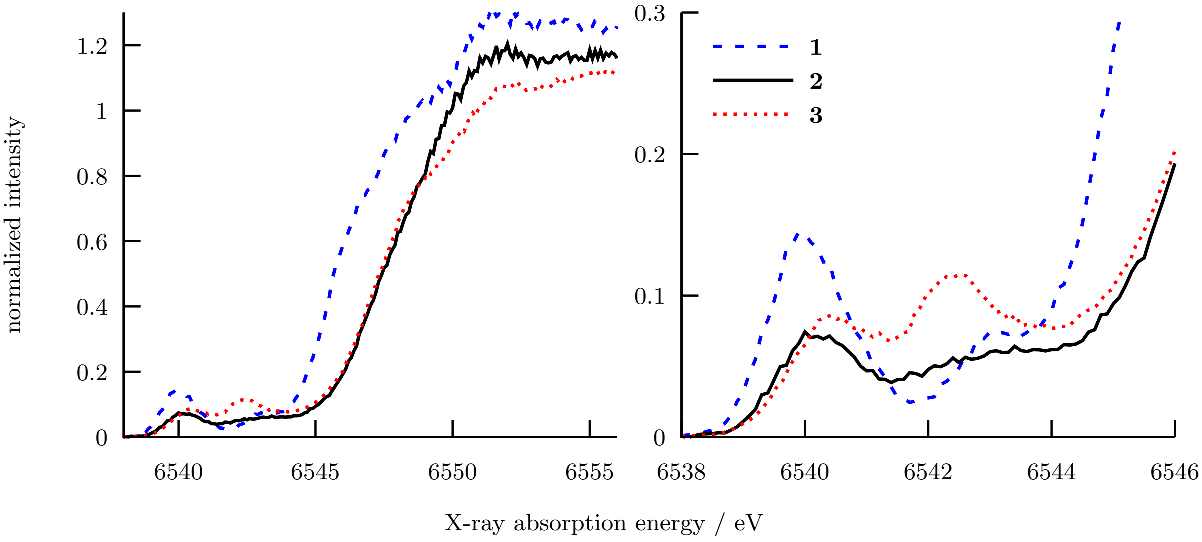

Figure 3.4: Left: Overlay of experimental HERFD X-ray absorption spectra of **1-3**. Right: Expansion of the pre-edge region

Comparison of the first pre-edge feature for Mn(II) **1** and peroxo **2** reveals a distinct decrease in intensity in **2** despite the increase in oxidation state. As X-ray absorption intensities are dominated by dipole character, a decrease in intensity in the 1s→3d feature is consistent with a decrease of p mixing into the 3d manifold, which is often governed by the symmetry at the metal center. The distorted trigonal bipyramidal geometry of **1** ($\tau = 0.59$) should allow for more efficient p-d mixing than in six-coordinate **2** or **3**. A marked increase in the area of the second pre-edge (MLCT) feature in **3** is observed upon comparison of the two $\mathrm{Mn(III)}_2$ compounds **2** and **3**. Inspection of the X-ray crystal structures of these compounds reveals that upon conversion of **2** to **3** the weakly coordinated pyridine ligands elongate further (mean distance of 2.451 Å to 2.541 Å), which should serve to decrease the intensity of charge transfer transitions into the pyridine π^* framework. The opposite change observed in the data could be explained by MLCT acceptor orbitals of a different nature, or by some mechanism for increasing the transition dipole moment integral along the Mn-pyridine vector. To further understand the observed trends, as well as the properties of these transitions, time-dependent density functional theory (TD-DFT) calculations were carried out for all compounds (*vide infra*).

3.3.2 Experimental Kβ XES Mainline Data

The profile of Kβ mainlines is highly dependent on the 3p-3d exchange coupling, modulated by total spin and covalency of the metal center. The Kβ mainline of **1** shown in Figure 3.5 is consistent with a high spin Mn(II) complex, having a K$\beta_{1,3}$ energy of $\approx$ 6491 eV and a well resolved Kβ' feature. Upon oxidation to Mn(III) a shift of the K$\beta_{1,3}$ to lower energy for complexes **2** and **3** is observed, as well as a decrease in the Kβ' intensity. This was previously described as being due to the decrease in spin at the metal from $S = \frac{5}{2}$ to $S = 2$, resulting in a diminished p-d exchange integral, which causes a decrease in the Kβ'-K$\beta_{1,3}$ splitting (ΔE_{main}) and a lowering of the K$\beta_{1,3}$ energy.[137] A further contraction in the ΔE_{main} is observed upon conversion of **2** to **3** (Table 3.2). As both **2** and **3** have two high spin Mn(III) ions as previously reported and further evidenced by XAS analysis, the modest difference in the Kβ'-K$\beta_{1,3}$ splitting splitting can be attributed to increased Mn-O covalency in **3**.[138]

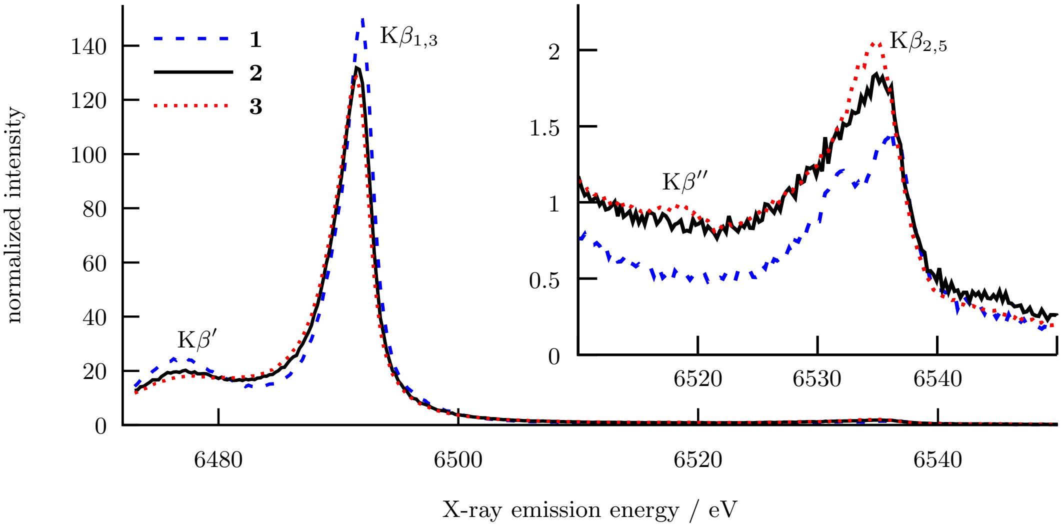

Figure 3.5: Experimental Kβ X-ray emission spectra of **1**-**3**. Inset: Expansion of the Valence-to-Core region

Table 3.2: K$\beta_{1,3}$ and Kβ' energies and corresponding ΔE_{main}

	K$\beta_{1,3}$ [eV]	Kβ' [eV]	ΔE_{main} [eV]
Mn(II) **1**	6492.0	6477.2	14.8
peroxo **2**	6491.6	6477.2	14.4
oxo **3**	6491.4	6477.6	13.8

3.3.3 Experimental Kβ XES Valence-to-Core Data

The higher-energy VtC region provides complementary information on the properties of the primarily ligand-based valence molecular orbitals. Experimental data and fits for the VtC regions are shown in Figure 3.5 (right) and Figure 3.6, and the corresponding energies and experimental and calculated VtC areas are reported in Table 3.3.

3.3.3.1 Comparison of the K$\beta_{2,5}$ Regions

The K$\beta_{2,5}$ region of **1** is comprised of two well-resolved peaks (Figure 3.6 top), in significant contrast to the spectra of **2** and **3**. Features in this spectral region typically arise from the highest-energy occupied ligand valence orbitals, which in the case of these compounds are the nitrogen and oxygen 2p and sulfur 3p orbitals. The presence of two distinct peaks in **1** suggests two sets of

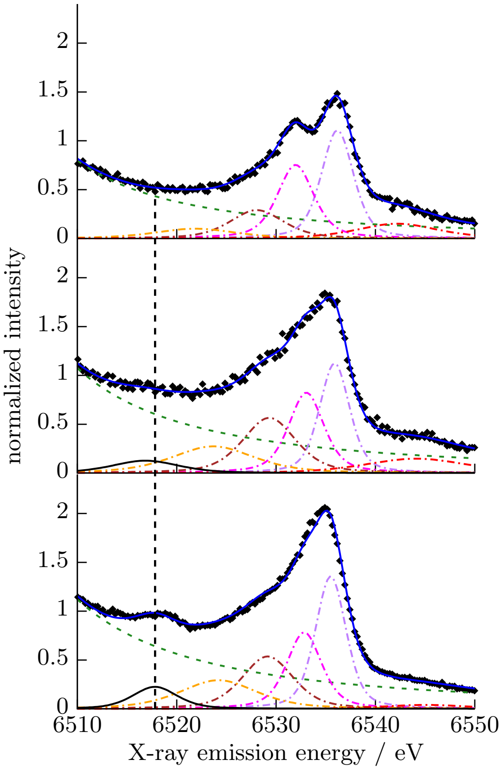

Figure 3.6: Experimental data (black points) and fits of the VtC regions of **1** (top), **2** (middle), and **3** (bottom). The dashed green trace represents the fit of the Kβ mainline tail, and the black solid trace is the fit component assigned as the 2s orbital of the oxygenic ligands. The vertical dashed line is centered on the oxygen 2s fit component of **3**, showing the redshift in the analogous component in **2** and its absence in **1**.

donor orbitals with significantly different ionization potentials.[105] Valence-to-core transitions gain intensity through introduction of metal p-character into the donor orbitals, so generally transitions with observable intensity correspond to donor orbitals that interact with the metal in a σ-fashion. The distorted 5-coordinate geometry of **1** however is expected to significantly mix the pseudo-trigonal plane (*vide supra*), resulting in intensity not only from ligand orbitals but also potentially Mn d orbitals as well.[137] The presence of two peaks of different energies in the K$\beta_{2,5}$ feature of **1** could therefore be rationalized as higher-energy transitions being mostly Mn d in nature and lower-energy transitions originating from imine and pyridine π or sulfur p orbitals. Additionally, there is a marked increase in the experimental areas of the VtC for **2** and **3** compared to **1** (Table 3.3). The increase in oxidation state should lead to an increase in VtC intensity *via* contraction of most of the metal-ligand bonds, and coordination of a sixth (per)oxo ligand should also increase the number of transitions.

Table 3.3: Kβ'' energies and K$\beta_{2,5}$ IWAEs, experimentally-determined Valence-to-Core areas, and calculated Valence-to-Core areas

	Kβ'' [eV]	K$\beta_{2,5}$ [eV]	expt area	calcd area
Mn(II) **1**		6534.3	12.7	15.0
peroxo **2**	6516.8	6534.5	18.7	20.5
oxo **3**	6517.9	6534.4	19.5	21.8

3.3.3.2 Comparison of the Kβ'' Regions

The more clearly assignable features of the peroxo- and oxo-based orbitals are found in the Kβ'' region, and correspond to orbitals which are oxygen 2s in character.[127] This is most clearly observed in the Kβ'' region of **3**, where the black fit component centered at $\approx$ 6518 eV has been assigned as VtC emission originating from an oxo 2s orbital (Figure 3.6 bottom). Comparison of the same fit component for **2** reveals distinct changes indicative of a change in the coordinated species. The Kβ'' feature is shifted to lower energy by $\approx$ 1 eV (Table 3.3), and has only 84% of the intensity of **3**. The full width at half maximum (FWHM) of the black fit component is also increased to 150% of that of **3**. These changes are all consistent with the assignment of the black fit component in **2** as representative of transitions originating from peroxo 2s orbitals. The peroxo ligand is expected to have VtC transitions arising from both 2s-2s bonding and 2s-2s antibonding combinations.[107] Though not resolved in this spectral region, the significant increase in the FWHM is consistent with discrete transitions at different energies in place of a single transition expected in **3**. Furthermore, the decreased intensity can be attributed to the longer (by 0.072 Å) Mn-O bonds in **2** vs. **3**. The lack of any significant deviation from the Kβ mainline tail (green dashed trace, Figure 3.6) below $\approx$ 6518 eV (vertical dashed line) for **1** is consistent with the absence of any oxygen ligands, while in the case of **2** and **3** this divergence begins at $\approx$ 6511 eV. This illustrates of the ability of the

VtC XES technique to accurately distinguish the identity of light-atom ligands, and supports the presence of a additional fit component in this region for **2**.[103,139]

3.3.4 Density Functional Theory Calculations

To further understand the electronic structure and XAS / XES spectra of the complexes examined herein, DFT calculations were performed. In all cases, the optimized geometries were found to be in good agreement with the crystallographically determined structures, with an average deviation in first-coordination sphere metrics of 0.0206 Å. A detailed comparison is shown in Figure 3.7). Importantly, the average deviation of the Mn-N_{py} distances in **2** and **3** is only 0.030 Å, suggesting

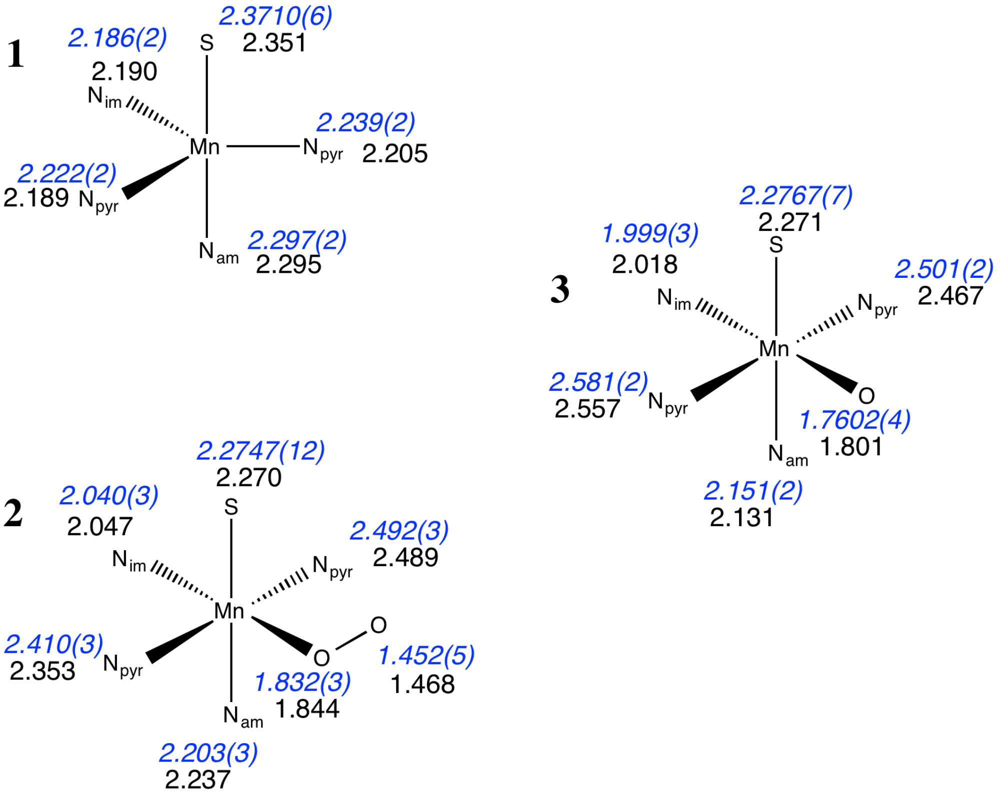

Figure 3.7: Comparison of crystallographic (blue) and DFT-optimized (black) metrical parameters for **1-3**

that the effects responsible for these unusually long distances observed in the crystal structures are successfully represented in the calculations. The distorted trigonal-bipyramidal geometry of **1** and the ^6S ground state at the Mn(II) free ion limit lead to a substantially hybridized d-manifold, making definitive assignment and ordering challenging.

The d-manifold of the peroxo **2** is somewhat better defined, and inspection of both the orbital contributions and the isosurface plots provides considerable insight into the electronic structure of this complex. As shown in Figure 3.8, the molecular z-axis is oriented along the Mn-pyridine vector, with the unoccupied $d_{x^2-y^2}$ pointed at both the sulfur and peroxo ligands. In the α spin manifold the singly occupied d_{z^2} thus points at the pyridine nitrogens, and is σ-antibonding with the nitrogen lone pairs. This highly unfavorable interaction is likely the rationale for both the long Mn-pyridine distances as well as the correlation shown in Figure 3.2. The Mn d_{xy} orbital is also worth mention, as this formally Mn-ligand antibonding combination is shown to in fact have a π-type bonding interaction with the in-plane peroxo π^*. In the β spin manifold the three highest-lying molecular orbitals are combinations of sulfur p and out-of-plane peroxo π^*. As can be seen from the isosurface plots, there is Mn character in these orbitals, despite the fact that they are formally occupied peroxo orbitals and the Mn ions are d^0 in the β spin manifold. This delocalization of peroxo O-O antibonding electron density onto the Mn likely helps to stabilize this intermediate species. Finally, the lowest-energy β orbital shown is the in-plane peroxo π^*, which,

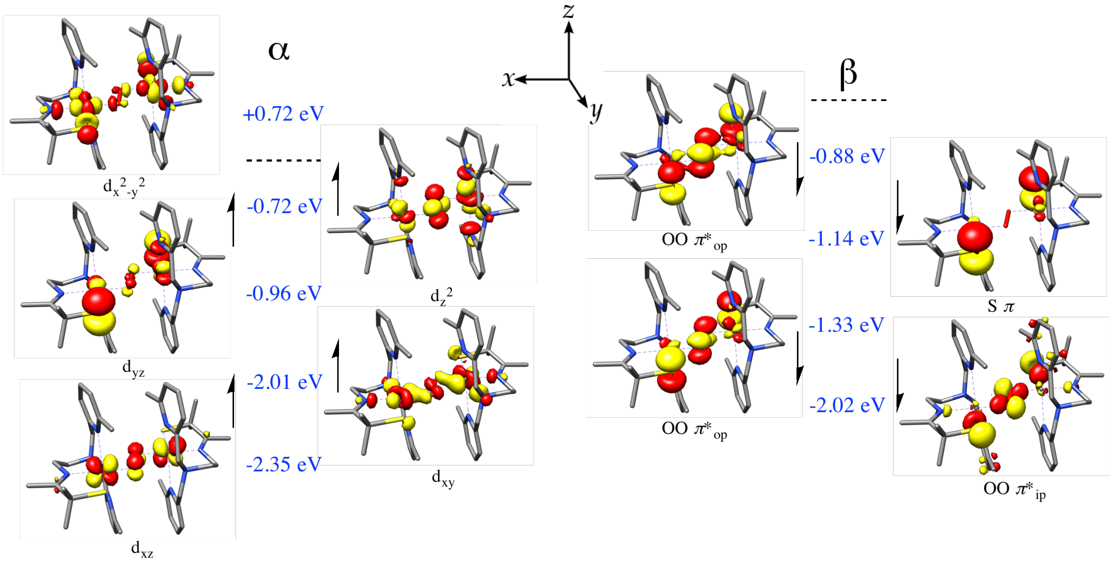

Figure 3.8: Molecular orbital diagram for peroxo-bridged **2**, showing the orientation and ordering of the d manifold. Canonical orbitals are displayed at an isovalue of 0.05 $a_0^{-3/2}$.

like the α-spin LUMO, also has correct symmetry to mix with the σ-interacting sulfur 3p_y. The electronic structure for **3** was found to be similar, with an identical orientation of the d-manifold and less mixed Mn orbitals as a result of the loss of the high-energy peroxo antibonding orbitals. Additionally, a single-point calculation performed on **3** utilizing the B3LYP functional and the broken-symmetry formalism for magnetic coupling[140] correctly predicted the sign and magnitude of the coupling constant $J = -126$ cm^{-1} (experimentally determined: $J = -125.6$ cm^{-1}).[114] The implications of these results relating to possible mechanisms of O-O bond activation will be discussed following comparison of calculated XAS and XES spectra to experimental results.

3.3.5 Calculated K Pre-Edge XAS Spectra

In all cases the calculated pre-edge spectra (Figure 3.9) are found to have two distinct features: a low-energy peak arising from transitions to Mn 3d orbitals and a higher energy peak found to be mostly due to MLCT transitions. A 32.6 eV blueshift was applied to all calculated spectra in order to align theory with experiment,[115] and for **3** the low-spin broken symmetry solution was utilized. In the case of **1** the 1s→3d pre-edge feature consists of transitions to five d orbitals acting as acceptors for 1s β-spin excitations. The distorted trigonal-bipyramidal geometry at the metal center greatly favors p-d mixing, and the calculated % Mn p character in the pre-edge for **1** ($\approx$ 6% p) is thus significantly higher than in **2** and **3** ($\approx$ 1.7% p). The MLCT peak in **1** predominantly consists of transitions from the Mn 1s to the π^* of the pyridine ligands, which is also indicative of substantial p-d mixing within the trigonal plane. For **2** and **3** the lowest-energy calculated pre-edge feature also consists of 1s→3d transitions, as evidenced by the difference density surfaces in Figure 3.9. In both cases the calculated 1s→3d transitions show roughly the same percentage of p character, and are dominated by excitations into the empty $d_{x^2-y^2}$. The K$\beta_{1,3}$ HERFD detection method filters out transitions lower final-state multiplicities (Section 2.5.2.2). In a rough approximation the transitions in the α spin manifold, which are fully weighted in the TD-DFT-calculated spectra, are suppressed in the experimental data. The total pre-edge transition intensity in the calculated spectra of the Mn(III)$_2$ complexes **2** and **3** is therefore larger than the experimental spectra, as a single α spin transition is expected in the high-spin d^4 configuration. The pseudo-octahedral

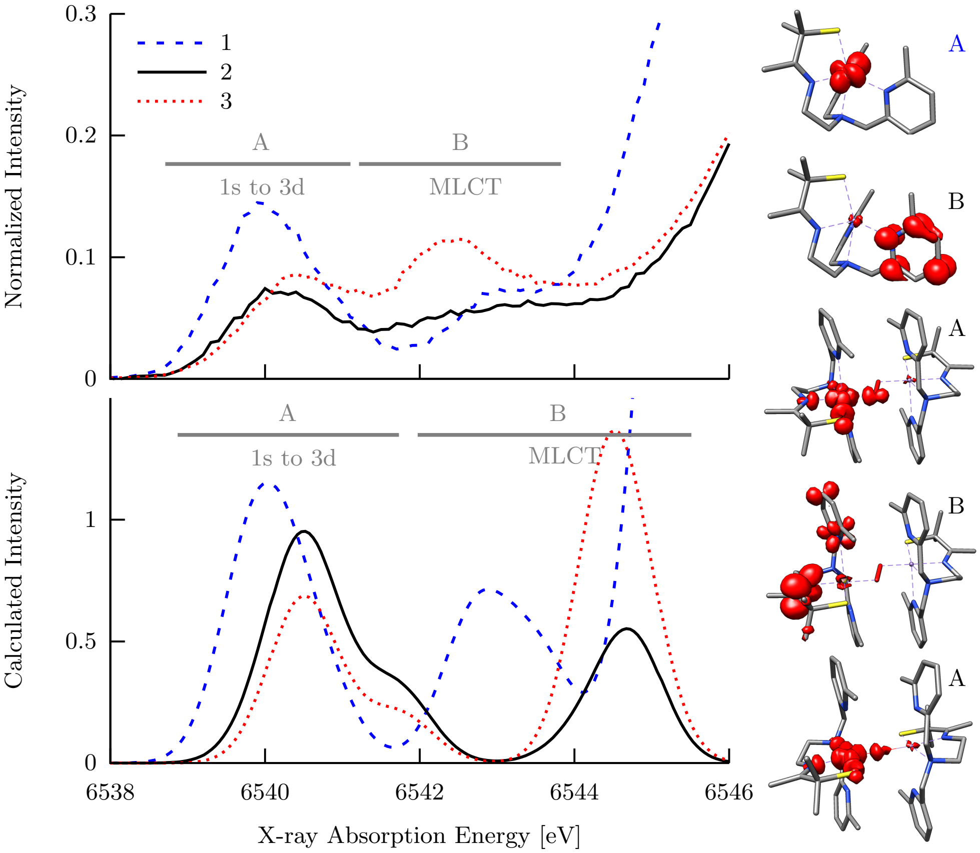

Figure 3.9: Experimental (top) and calculated (bottom, 1 eV broadening) pre-edge XAS spectra. Representative transition difference densities are shown at an isovalue of 0.005 a_0^{-3}.

geometry of these compounds should disfavor geometric p-d mixing mechanisms, and instead, metal p character is introduced *via* covalent bonding with both the sulfur and oxygen ligands, as also seen in the displayed transition difference densities. Coordination of the pyridine ligands despite their long metal-ligand distances is substantiated by MLCT transitions to the pyridine ligands found in both **2** and **3**. In addition, MLCT transitions to the peroxo bridge in **2** and the oxo bridge in **3** are also present. The total % Mn p character in the calculated MLCT feature in **3** is slightly higher than in that of **2**, consistent with a more intense transition and a more covalent metal-ligand interaction. Given the strong electronic coupling of the two Mn(III) ions in oxo-bridged **3**, the peak at ≈ 6542.5 in the experimental spectrum could be a metal-to-metal charge transfer excitation. Transitions of this nature are known to be a shortcoming of the TD-DFT method. The incorporation of exact

Hartree-Fock exchange in hybrid density functionals exacerbates the inability of the Gaussian-type basis functions to capture long-range interactions, and this could rationalize the absence of this feature in the calculated XAS spectrum.[111]

3.3.6 Calculated Valence-to-Core Spectra

To gain additional insight into the spectral features of the VtC region, theoretical spectra were calculated based on the results of the DFT calculations similar to published procedures.[127] In order to visually compare the calculated VtC spectra with experimental results, the tails of the mainline fits (Figure 3.6, dashed green traces) were subtracted from the total fits of the XES spectra. These background-subtracted fits and the calculated VtC spectra are shown in Figure 3.10. Several key

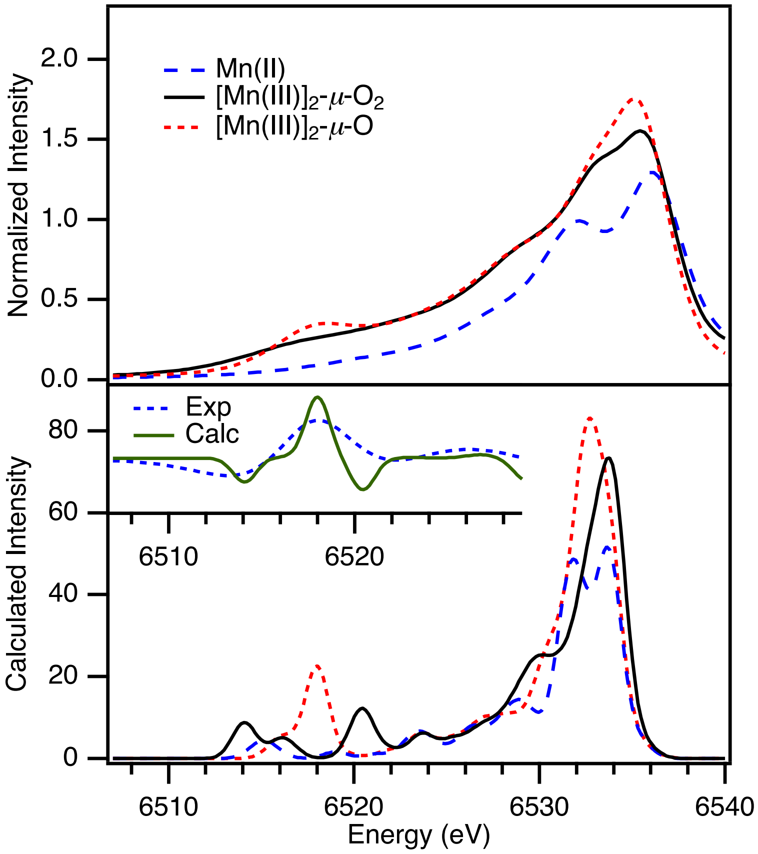

Figure 3.10: Background-subtracted experimental (top) and DFT-calculated (bottom) VtC XES spectra of **1-3**. Inset: Experimental and calculated difference spectra, **3-2**

features of the experimental fits are faithfully reproduced in the calculated spectra. In the Kβ'' region the presence of a pronounced peak in oxo-bridged **3** at 6518 eV and two lower intensity features in peroxo-bridged **2** are consistent with the experimental data, as well as the lack of significant Kβ'' intensity in **1**. The inset highlights the differences in the experimental Kβ'' regions between **3** and **2**, which are accurately predicted in the calculated spectra. The two Kβ'' features at ≈ 6514 and ≈ 6520.5 eV in the calculated spectrum of **2** are expected to arise from the peroxo 2s-2s bonding and antibonding combinations respectively, and are consistent with a splitting of ≈ 7 eV observed by X-ray photoelectron spectroscopy.[141] As previously discussed, the increase in the FWHM of the corresponding fit component for **2** is also consistent with this assignment, however there is not sufficient resolution from the mainline tail to permit quantitative determination of this splitting in the experimental data. The splitting of the K$\beta_{2,5}$ peak of **1** however is both experimentally resolved and well-reproduced in the calculated spectrum. Comparison of the calculated K$\beta_{2,5}$ features also shows **2** as having the highest-energy peak and **3** the most intense peak, both of which are consistent with the values reported in Table 3.3. Lastly, there is a strong correlation between the experimental and calculated VtC areas, the former obtained from integrated intensity of the VtC fits, both including and excluding the Kβ'' region (Figure 3.11).

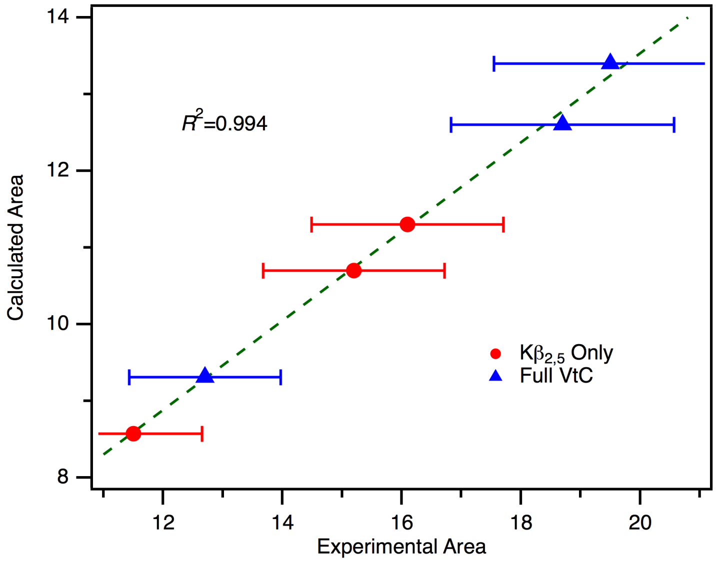

Figure 3.11: Correlation between experimental and calculated VtC integrated spectral areas

3.3.7 Spectral and Mechanistic Insight from DFT Calculations

The successful calculation of the experimental VtC spectral features, as well as the relative integrated spectral intensities, suggest a good electronic structure description of both the energy and Mn p composition of the occupied valence orbitals. Additionally, the presence of two features, the first with roughly correct intensity, in each of the calculated XAS spectra indicate that the DFT virtual orbitals are likely also consistent with the true electronic structure. This is of particular interest given the unoccupied $d_{x^2-y^2}$ configuration in the Mn(III) complexes **2** and **3**. It has been previously shown that the unique *trans* bridging peroxo core in **2** possesses a highly activated O-O bond, and that this species decays via peroxo bond scission.[28] To assess the integrity of the presented DFT calculations with regard to an accurate description of O-O bond activation, calculated vibrational frequencies for **2** were compared to those previously determined by resonance Raman spectroscopy. As shown in Table 3.4, the absolute energies of both the Mn-O and O-O stretching modes are consistent with experiment. Perhaps more importantly, the predicted shifts resulting from double ^{18}O substitution are in excellent agreement, indicating that the calculated force constants, and thus respective bond strengths, are correct. The calculation of consistent X-ray absorption and emission spectra and the accuracy of the predicted vibrational frequencies provide strong evidence for the fidelity of the electronic structure calculations. Insight into the structure and reactivity of these complexes, as well as notable features of the X-ray spectra, can therefore be obtained from the calculations with confidence that they accurately reflect the experimental findings.

Table 3.4: Comparison of experimental and calculated vibrational frequencies for Mn-O and O-O stretching modes of peroxo **2**

stretch	expt (^{18}O) [cm^{-1}]	calcd (^{18}O) [cm^{-1}]	expt shift (^{16}O-^{18}O)	calcd shift (^{16}O-^{18}O)
Mn-O	611 (586)	608 (582)	25	26
O-O	819 (772)	806 (759)	47	47

3.3.7.1 Fragment Analysis and MO Contributions to Calculated VtC Spectra

To begin to construct a picture of individual ligand contributions to the VtC regions, the calculated spectra were broken down by contributions per ligand fragment. Contributions from the peroxo and oxo fragments in **2** and **3** respectively are of obvious specific interest, as well as the determination of sulfur-based intensity for all compounds. Additionally, in an effort to assess the involvement and degree of coordination of the pyridine ligands (*vide supra*), contributions from the N-heterocyclic nitrogens and the backbone imine and amine nitrogens were split into two fragments. An advantage of employing a one-electron approximation for calculation of the VtC XES spectra is that the transition donor orbitals are simply the canonical orbitals obtained from a single-point DFT calculation. As such, visualization of the significant contributions to intensity requires only the inspection of the correct Kohn-Sham orbital. Unfortunately, the density of donor orbitals in the $K\beta_{2,5}$ region makes distinguishing the individual orbital contributions extremely challenging, however the $K\beta''$ region is typically comprised of a smaller number of transitions. The peaks in the $K\beta''$ region for **2** and **3** shown in Figure 3.12 are as expected primarily (per)oxo in character. As the $K\beta''$ region is reflective of ligand molecular orbitals comprised of predominantly atomic s orbital character, these are expected to be the peroxo 2s-2s bonding and antibonding combinations and the oxo 2s atomic orbital, respectively. The shoulder present at ≈ 6515 eV in both spectra is from nitrogen 2s-based orbitals originating from the backbone imine and amine nitrogens. Although this feature is not experimentally observable, it is worthwhile to note that in the case of **1** the nitrogen 2s peak in the $K\beta''$ is made up of contributions from both backbone and pyridine 2s orbitals. Given the strong distance dependence of VtC intensity this is not altogether surprising, and additionally the increase in centrosymmetry of the new z-axis in **2** and **3** should reduce p-d mixing. Despite this there is still significant pyridine nitrogen p intensity in the $K\beta_{2,5}$ peak in **2** (Table 3.5), further supporting pyridine involvement in coordination. As shown in Figure 3.12 and Table 3.5 however, the pyridine contribution to the total calculated VtC spectrum of **3** is significantly reduced relative to **2**, likely due to the further elongation of these bonds (by ≈ 0.09 Å). Conversion of the peroxo ligand in **2** to a more covalent, shorter oxo ligand in **3** forms a stronger σ^* interaction with the

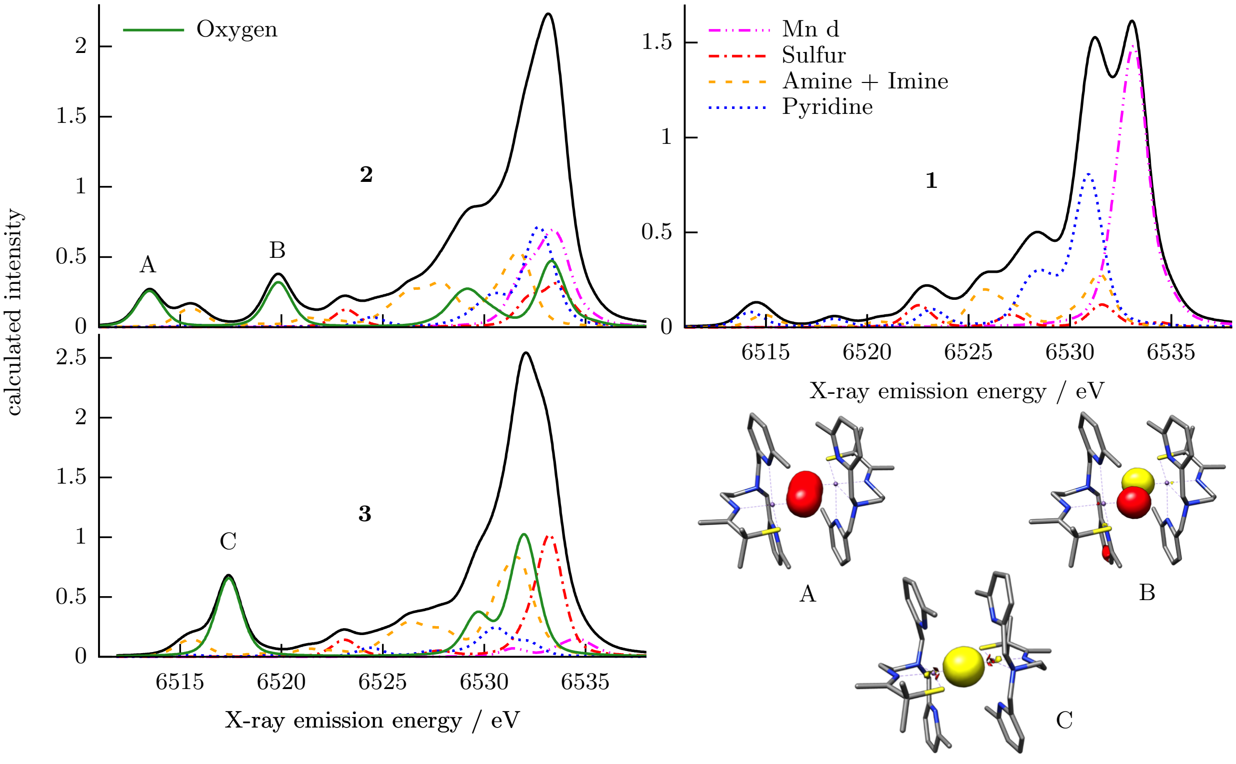

Figure 3.12: Fragment analysis of calculated VtC spectra based on donor molecular orbital contributions for Mn(II) **1** (top right), peroxo-bridged **2** (top left), and oxo-bridged **3** (bottom bottom). Bottom right: Canonical orbitals are shown at an isovalue of 0.05 $a_0^{-3/2}$, and oxygen-based contributions are shown as a solid green trace.

torus of the d_{z^2}, which seemingly results in an elongation along the molecular z axis. The large amount of Mn d character in the VtC of **1** (Table 3.5) is attributed to significant p-d mixing due to the geometry. While it is somewhat uncommon to find such a large contribution from metal 3d orbitals, the result nicely parallels the findings from the analysis of the XAS pre-edge region (*vide supra*). The relatively large amount of Mn d character in **2** relative to **3** is rationalized by inspection of the isosurfaces in Figure 3.8, which show significant mixing of the peroxo π^* orbitals into both α and β d-manifolds. The loss of these high-lying ligand orbitals in **3** should decrease this mixing and thus Mn d character. A similar effect explains the increase in sulfur contributions from peroxo **2** to oxo **3**, as the highest-lying ligand orbitals are now S 3p in character rather than peroxo π^*. Finally, the increase in oxygen character upon conversion of **2** to **3** is reflective of both increasing covalency and a shorter metal-ligand bond length.

Table 3.5: Percentage of total calculated VtC intensity from each ligand fragment

	% Mn d	% S	% Pyr	% Am + Im	% total N	% O
Mn(II) **1**	37	7	30	15	45	
peroxo **2**	17	9	18	23	41	22
oxo **3**	4	19	8	29	37	29

3.3.7.2 Contributions to O-O Bond Activation

With an experimentally-supported electronic structure description in hand, the factors affecting O-O bond activation were considered. The strong dependence of O-O bond length on the Mn-N-heterocyclic amine interaction can be explained by the σ^* orientation of the singly-occupied d_{z^2} (*vide supra*), which results from the preferential orientation of the unoccupied $d_{x^2-y^2}$ towards both the stronger-field peroxo and thiolate ligands.[100] This interaction makes the Lewis acidity of the Mn highly sensitive to changes along this vector. The long Mn-N_{py} bonds in peroxo **2** should lead to a more Lewis acidic Mn(III) ion, and thus a stabilized peroxo O-O bond as previously shown.[41] Contraction of the Mn-pyridine distances, and thus decreasing Lewis acidity, should therefore lead to localization of more electron density in the peroxo π^* orbitals, weakening the peroxo bond and ultimately promoting O-O bond scission. A schematic for the mechanism of decreasing the Lewis acidity of the Mn ion is shown in Figure 3.13, and illustrates the contributing factors and the resultant localization of negative charge into peroxo antibonding orbitals. Given these interactions, a molecular vibration along the Mn-pyridine vector ultimately leading to O-O bond scission could be a possible mechanism for the decay of this intermediate. This is consistent with not only the thermal instability of **2**[28] but also the established correlations between O-O bond length (and thus Mn-N-heterocycle bond length) and the activation parameters $\Delta H^\ddagger$ and $\Delta S^\ddagger$ (*vide supra*).[41]

3.3.8 Spectroscopic Features of the Mn-Peroxo Moiety

This study represents the first application of XES to a Mn(III) peroxo complex of any kind. Given the novelty of the Mn(III)-peroxo dimer **2** in this work, as well as the importance of Mn peroxo moieties in catalytic function, some consideration was given to the spectroscopic parameters asso-

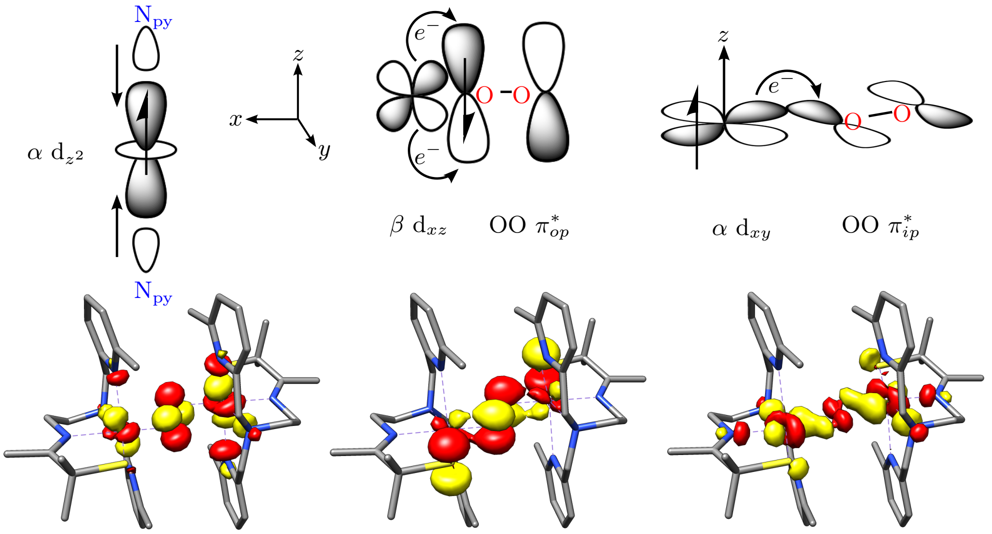

Figure 3.13: Schematic of the cause (left) and effect (middle, right) of decreased Mn Lewis acidity based on canonical spin-orbitals shown (from Figure 3.8).

ciated with this type of species. In particular, the spectral features pertaining to two key pieces of information for which XAS provides little insight were considered: the identification of peroxo binding mode and the quantification of O-O bond activation. The large density of donor orbitals that comprise the K$\beta_{2,5}$ region make the assignment of distinguishing features in this region difficult, however the distinct energy of the peroxo 2s-2s combinations in the Kβ'' region, given sufficient resolution, are more amenable to systematic assignment.

3.3.8.1 Peroxo Binding Mode

Most Mn-peroxo compounds characterized to date have the peroxo unit coordinated in a side-on η^2 fashion,[45] therefore investigation of the effect of coordination geometry on the relevant spectral features was of significant interest. VtC spectra were calculated for two additional structures using the same computational approach presented above. The first structure was generated by rotating the peroxo moiety of **2** such that it is entirely side-on relative to both Mn atoms. Bond lengths and angles of the Mn_2O_2 core were fixed and the other coordinates were optimized. The second example is from the literature, and utilizes a previously reported "end-on" monomeric Mn(III) alkylperoxo ($[Mn^{III}(S^{Me2}(6-Me-DPEN))(OOtBut)]^+$, Mn-O-O = 112°).[12] As shown in

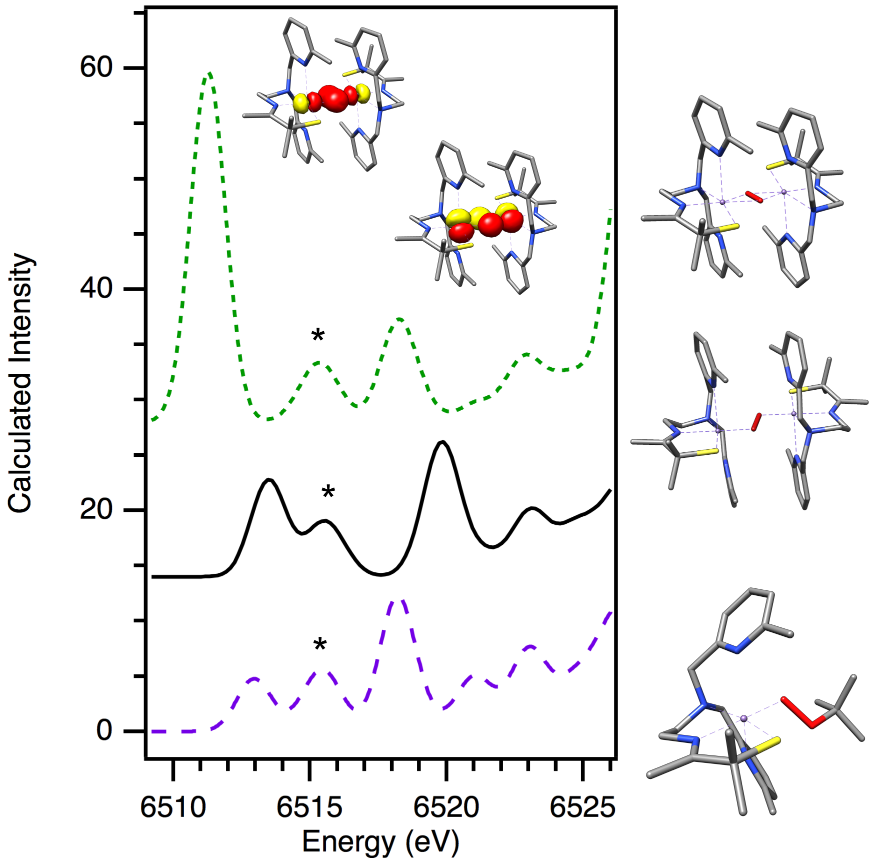

Figure 3.14: Calculated VtC $K\beta''$ spectra for side-on **2** (top, green dotted trace), **2** (middle, black solid trace), and $[\mathrm{Mn^{III}}(\mathrm{S^{Me2}}(6-\mathrm{Me}-\mathrm{DPEN}))(\mathrm{OOtBut})]^+$ (bottom, purple dashed trace). Peaks marked with a * correspond to nitrogen 2s contributions from the ligand backbone, to lower energy are the 2s-2s bonding combinations, and to higher energy the antibonding combinations, as shown. Canonical orbitals are displayed at an isovalue of 0.05 $a_0^{-3/2}$.

Figure 3.14, all structures exhibit two peroxo features in the $K\beta''$ region: one to lower energy in the 6511-6513 eV range and one to higher energy around 6518-6520 eV. Similar to the peroxo dimer **2**, the lower energy feature can be assigned as the oxygen 2s-2s bonding combination while the higher energy peak corresponds to the antibonding combination. As spectral intensity is governed by the mixing of Mn p character into these ligand orbitals, the coordination mode is shown to greatly influence the relative intensity of these two peaks. When the peroxo moiety is bound in a side-on fashion (Figure 3.14) the bonding combination expectedly has optimal overlap with the Mn $3p_\sigma$ orbitals, while the antibonding combination is approximately orthogonal. Intensity in the antibonding combination was instead found to be due to the Mn $3p_\pi$ orbital, and the weaker π interaction expectedly results in diminished intensity. Isosurface plots of the bonding and antibonding combinations along with the relevant Mn 3p orbitals are also shown in Figure 3.14. As the optimized Mn-O-O bond angle is increased to 100° for the peroxo **2** and finally to 112° for the alkylperoxo, the ratio of bonding and antibonding intensity is found to change dramatically, as the 2s-2s bonding combination moves further from the Mn and the antibonding combination is increasingly oriented towards the Mn $3p_\sigma$. It is noted that investigation of a hypothetical end-on coordination mode was attempted in light of previous work on dinitrogen with a small-molecule iron complex (*vide infra*),[138] however the sp hybridization of the oxygen required to accommodate this geometry is somewhat unrealistic and produced unsatisfactory results. The coordination mode of the peroxo unit in **2** thus has suboptimal orientation to provide appreciable $K\beta''$ intensity, and is likely the reason for the poor experimental resolution of this feature. These results suggest that the relative intensities in this spectral region may in future be used to determine the binding mode of Mn peroxo adducts.

3.3.8.2 Quantifying O-O Bond Activation

As previously mentioned, the vast majority of reported small-molecule Mn peroxo complexes have the peroxo unit bound in an η^2 side-on fashion. This binding mode is expected to result in significant $K\beta''$ intensity from the 2s-2s bonding orbital (Figure 3.14), and an accurate experimental determination of the energy of this feature should therefore be possible. Determining the degree of O-O bond activation based on this spectral feature could be highly desirable for the investigation of O_2 activation processes in both industrial and biological catalysis. Therefore, the spectral changes expected to occur upon systematic variation of the O-O bond length have been investigated by theoretical VtC XES. For this study, the Mn(III) 14-TMC-O_2 complex reported by Nam and coworkers was employed.[142] A relaxed surface scan was performed, varying the O-O bond length and calculating a VtC XES spectrum at each geometry, again using the aforementioned computational approach (Section 3.2.5). Figure 3.15 shows the results of these calculations, and a marked change in the energy of the peak due to the 2s-2s bonding combination is evident along with a

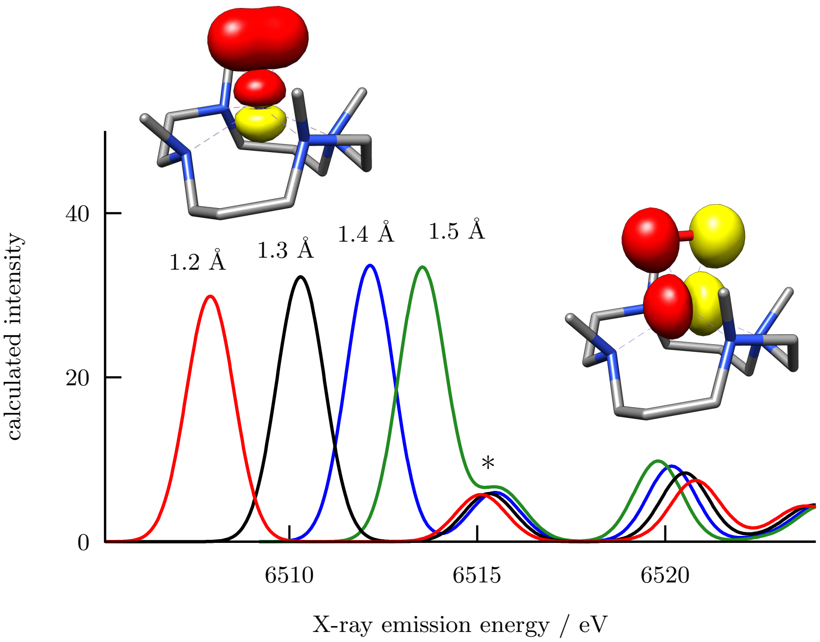

Figure 3.15: Calculated VtC Kβ'' spectra for $[\mathrm{Mn^{III}(14-TMC)(O_2)}]^{+}$[142] for varying O-O bond length. Canonical orbitals giving rise to spectral intensity (peroxo 2s-2s combinations and Mn $3p_\sigma$ and $3p_\pi$) are shown at an isovalue of 0.05 $a_0^{-3/2}$. Peak marked with a * is from the cyclam N ligands.

negligible change in the energy of the antibonding combination. The destabilization of the bonding orbital upon elongation of the O-O bond is predicted from basic molecular orbital theory, however the calculated change in energy, approximately 2 eV per 0.1 Å, is quite substantial. Modern solid-angle X-ray fluorescence spectrometers are capable of achieving energy resolution better than ≈ 0.2 eV;[103] thus, determining changes in O-O bond length of 0.01 Å are within reason. It is noted however that in light of the previous section, an orientation that promotes significant intensity of this feature is required. It is known from both previous studies on higher-valent Mn oxo complexes,[53] as well as from the characterization of oxo-bridged **3**, that in the limit of a fully cleaved O-O bond, Kβ'' spectral features are observed which have been shown to be atomic oxygen 2s in origin. As shown in Figure 3.10, these transitions occur to higher energy of the peroxo bonding combination and to lower energy of the antibonding combination. Furthermore, an oxo ligand fragment will posses only the spherically-symmetric atomic 2s donor orbital, rather than orientation-dependent bonding and antibonding combinations; therefore spectral intensity is expected regardless of the coordination mode. This should allow for spectroscopic insight into not only the degree of activation of O_2 or reduced O_2 ligands but also the identification of a change in speciation upon cleavage of the O-O bond.

3.3.9 Generalization to the Study of Small-Molecule Activation

For chemical systems where high-resolution structural data are not available, assessing small-molecule activation in a quantitative and site-selective fashion is integral to advancing mechanistic understanding. VtC XES offers unique capabilities in this regard, as demonstrated both in the present work and in a recent investigation of dinitrogen activation by a small-molecule Fe complex.[138] A brief comparison of these two studies reveals some key similarities and differences that should help to define both the potential and the limitations of VtC XES in this application. Perhaps most important are the factors contributing to intensity, which are governed by mixing of metal p character into the ligand valence orbitals. The 3p shell of Mn is expected to be more diffuse than for Fe based on Slater's rules, which should lead to increased relative VtC intensity for Mn compounds of identical oxidation state, consistent with previous studies.[105,116,127] As detailed in this work however, the coordination mode of a diatomic small-molecule substrate is also of great importance for determining which of the 2s-2s combinations will dominate the $K\beta''$ intensity (Section 3.3.8.1). In this regard the end-on coordination mode found in Pollock *et al.*'s Fe N_2 study is expected to produce more favorable results. Not only is the dominant antibonding combination more diffuse, and thus more likely to mix with the metal p orbitals, but it also occurs to higher energy and is therefore expected to be better resolved from the tail of the $K\beta$ mainline. Finally, it has recently been demonstrated that the angle of a light-atom ligand with respect to the orientation of the metal p manifold plays a role in governing VtC intensity, and in a simple Walsh diagram picture, σ-type ligand orbitals which bisect the Cartesian axes of the metal should provide maximum metal p mixing.[143] The observation of appreciable VtC intensity is dependent on favorable conditions with regard to at least some of these considerations.

3.4 Summary and Conclusions

This work presents the first XES study of a Mn-peroxo compound, and provides further electronic and structural insight into the only reported binuclear Mn(III)-peroxo complex to date. As such, it establishes essential spectroscopic reference data for analogous studies on less well-characterized systems. Furthermore, it is one of few examples of a combined XAS / XES study, and highlights the complementary nature of the information provided with regard to metal and ligand electronic structure. With the aid of DFT calculations, the origins of spectral intensity in both absorption and emission spectra have been identified, and it has been shown how p-d mixing can be affected by both geometric effects and by highly covalent metal-ligand interactions. Correlations between experimental and calculated spectra have provided validation for the electronic structure description, and permitted assignment of observed spectral features to specific ligands and orbitals.

Analysis of the calculated electronic structure has allowed for the determination of both the ordering and the orientation of the Mn d manifold peroxo-bridged 2. This insight has been used to answer questions regarding the degree of ligation of the pyridine ligand(s) in **2** and **3**, and to rationalize these exceptionally long metal-ligand bonds. It has also allowed for the proposal of a mechanism for O-O bond activation in this system involving both covalent charge donation by the thiolate sulfur as well as modulation of the Mn Lewis acidity *via* a strong σ^* Mn-pyridine interaction. The specific orbitals that may contribute to this process have also been identified, and these results suggest that synthetic adjustments may be possible to either further promote or disfavor O_2 activation. The following chapter details work in this area.

Finally, comparison to a previous Kβ VtC XES study of dinitrogen activation has also illustrated some of the factors that may determine the success of this technique in future applications. Theoretical investigations based on reported compounds suggest that given the proper metal and ligand geometry, this technique may provide insight into not only changes in speciation but also determination of both the coordination mode and bond length of small-molecule substrates. The elemental selectivity of this technique, its quantitative nature, and novel information content serve to further highlight its potential application to small-molecule activation processes in both catalysis and bioinorganic chemistry.

“Nature is pleased with simplicity. And Nature is no dummy.”
ISAAC NEWTON

Chapter 4

Geometric Structure of the Fe-V Cofactor of Vanadium Nitrogenase

Portions of this chapter have been adapted or reproduced with permission from: Rees, J. A.; Bjornsson, R.; Schlesier, J.; Sippel, D.; Einsle, O.; DeBeer, S., *Angew. Chem. Int. Ed.* **2015**, *54*, 13249-13252. Copyright 2015 John Wiley & Sons.

4.1 Introduction

The reduction of atmospheric dinitrogen N_2 to ammonia, in the form of ammonium salts, is one of the most complex reactions that occurs in nature. It is promoted almost exclusively by the nitrogenase enzymes; multicomponent metalloenzymes which occur in diazotrophic bacteria and archea.[58,144] These enzymes utilize highly complex Fe-S clusters to effect N_2 reduction, and in the case of the more widely studied Mo-dependent nitrogenase, the redox centers of the protein have been characterized by X-ray crystallography.[69] The active-site containing MoFe protein, an $\alpha_2\beta_2$ heterotetramer, uses an [8Fe-7S] cluster (P-cluster) as an electron transfer relay, and the [Mo-7Fe-9S-C] Fe-Mo cofactor (FeMoco) as the catalytic site of N_2 reduction (Scheme 4.1).

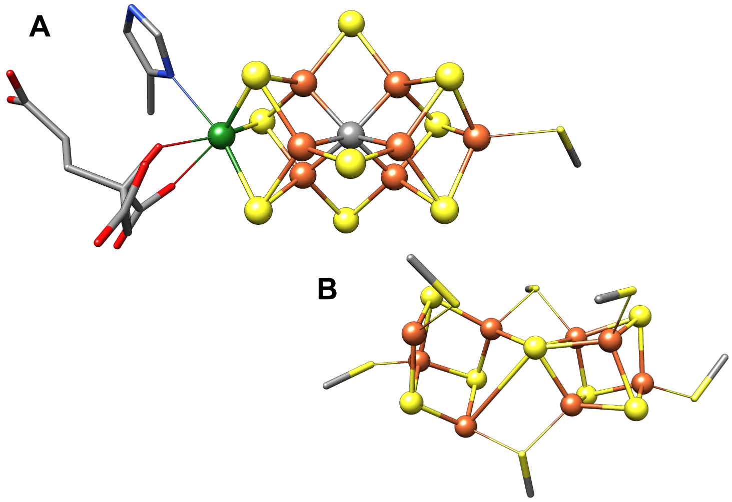

Scheme 4.1: Structures of the FeMo cofactor (A) and P-cluster (B) from *A. vinelandii*, PDB 3U7Q. Coloring scheme: Fe, orange; S, yellow; C, gray; Mo, green; N, blue; O, red. Cysteine thiolate ligands are shown as sticks, and inorganic sulfides as spheres.

Despite the identification of an interstitial light atom at the center of FeMoco in 2002,[64] it was not until 2011 that the identity of the so-called "X" atom was definitively shown to be carbon by a combination of high-resolution X-ray crystallography, pulsed electron paramagnetic resonance (EPR) spectroscopy,[69] and Kβ valence-to-core (VtC) X-ray emission spectroscopy (XES).[68] This fully valent carbide, ligated by 6 Fe atoms, is unprecedented and unique in biology. Genetic, spectroscopic, and isotopic radiolabeling experiments have determined the source of this carbon atom to be a radical *S*-adenosylmethionine (SAM), and shown that the C is inserted into the cofactor *via* methyl group transfer in the cofactor assembly protein NifB.[70,71] The effect of this carbide ion on the electronic structure of the cofactor, and its role in promoting N_2 reduction, is still unknown.

Vanadium was first discovered as a promoter of nitrogen fixation in 1933,[74] and subsequently a V-dependent nitrognease was identified in 1986.[145] In contrast to the well-characterized Mo nitrogenase, relatively little is known about the V nitrogenase despite nearly 30 years of research. At ambient conditions the enzyme is a far poorer nitrogen fixation catalyst than the Mo analogue, capable of N_2 reduction at a rate of only 660 nmol / mg nitrogenase / min compared to 1040 nmol / mg nitrogenase / min for the Mo nitrogenase in the *A. vinelandii* system.[146] Furthermore, the V nitrogenase requires an additional 4 reducing equivalents, 24 more ATP per turnover, and has a significantly lower turnover number (112) than Mo nitrogenase (2230).[79]

It has recently been shown that in addition to N_2 reduction, the V nitrogenase can perform reductive C-C bond coupling using CO and protons.[86] Intriguingly, it also does so at $\approx$ 700 times the activity of the native Mo nitrogenase.[147] Engineered Mo nitrogenase have been shown to catalyze CO reduction as well, and at rates comparable to V nitrogenase, albeit with the loss of N_2 reduction ability.[148,149] The dramatic differences in the reactivity of these enzymes, and the ability of the vanadium enzyme to promote Haber-Bosch and Fischer-Tropsch chemistry at ambient conditions, has led to renewed interest in understanding the differences between the active site cofactors in the Mo and V nitrogenases.

The atomic structure of the V nitrogenase protein is not known. Instead, the available structural information on the protein and its redox centers has come from spectroscopic and genetic studies.

The latter have shown that while the two nitrogenases share common precursors in their biosynthetic pathways, including the *nifB* gene responsible for radical SAM-dependent carbon insertion, distinct genetic factors promote final cofactor maturation.[57] Additionally, the V nitrogenase protein contains additional δ_n subunits, where $n = 2$ or 4 depending on the species.[75,150]

Much of the spectroscopic data collected on V nitrogenase has also indicated substantial differences from Mo nitrogenase. As early as 1987, Arber and George independently reported V extended X-ray absorption fine structure (EXAFS) data indicating that the V, contrary to expected changes base on periodic trends, was more displaced from the remainder of the cofactor than the Mo.[76,77] More recent studies employing Fe X-ray absorption spectroscopy (XAS) and EXAFS, and EPR spectroscopy have also shown marked differences in the electronic structures of the V nitrogenase metallocofactors. These differences are significant enough to prompt the authors to interpret their data as indicating a cubically symmetric iron-vanadium cofactor (FeVco) and two separated [4Fe-4S] clusters in place of the trigonal FeMoco and fused P-cluster shown in Scheme 4.1.[150–153] Despite this, some recent publications have portrayed graphical models of the redox centers of the V nitrogenase as being structurally analogous to those of Mo nitrogenase known from X-ray crystallography, in contradiction to the published data.[154,155] No direct evidence for an analogous cofactor structure has been presented in support of such models. This has led to the somewhat widespread belief that the structure of FeVco is identical to FeMoco, and that similarities in atomic composition and geometry are a foregone conclusion.

The present investigation endeavors to provide definitive data as to the structure of FeVco. While it may seem likely that the vanadium- and molybdenum-containing cofactors are indeed homologous, this is a critically important facet of the nitrogenase puzzle, and should not be simply assumed to be true. Interestingly, the implications of structural homology are of some note. The functional role of both the interstitial carbon and the heterometal are still unknown, and the presence of the former in both isozymes seemingly contraindicates the carbon as the origin of the differential reactivity discussed above. However, as an organism is required to expend subtantial energy to install in the interstitial carbon in the cofactor,[70] it likely plays an important role in promoting the N_2 reduction reaction. To lay the foundation for further studies aimed at addressing these questions, the definitive determination of the structural homology of FeVco and FeMoco is detailed below.

4.2 Experimental

4.2.1 Cell Growth and Purification

MoFe protein of nitrogenase was produced and isolated following established protocols.[69] To obtain VFe protein, *Azotobacter vinelandii* (Lipmann 1903, ATCC 478) was cultured in molybdenum-free Burke medium[156] under nitrogen-limited conditions. The production of vanadium nitrogenase was monitored by activity assays.[157] All purification steps were performed under strict exclusion of dioxygen, using an anaerobic chamber or modified Schlenk techniques. Cells were disrupted using an Avestin Emusiflex at a pressure of 1000-1500 bar, and cell debris was separated by centrifugation. The supernatant was loaded onto a 5 mL HiTrapQ HP column equilibrated with 50 mM Tris/HCl buffer at pH 7.4. VFe protein eluted in a linear gradient of 0 mM to 500 mM NaCl. Pure protein was obtained after an additional size-exclusion step on a 26/60 Superdex 200 gel filtration column (GE Healthcare).

4.2.2 X-ray Emission Spectroscopy

Fe Kβ X-ray emission spectroscopy (XES) experiments were performed at beamline ID-26 at the European Synchrotron Radiation Facility (ESRF) in Grenoble, France. Incident photon energy was 7800 eV, selected using a Si(111) double crystal monochromator. Photon flux at the sample was $\approx 1 \times 10^{13}$ photons / s, with a maximum ring current of $\approx$ 200 mA and energy of 6.03 GeV. The beam spot size on the sample was 0.1 mm x 1 mm. Protein samples were in aqueous solution at $\approx$ 100 mg / mL, and maintained at 10 K during measurements using a LHe cryostat. Fe Kβ X-ray emission was analyzed with a Johann-type spectrometer, using five spherically-bent Ge(620) crystals in a Rowland geometry, as described in Chapter 2 (Figure 2.7) and detected using a dead-time corrected Ketek Si drift diode detector. To determine the acceptable dwell time per sample spot, rapid Fe Kβ HERFD XANES were recorded on the same sample spot, and the data examined for evidence of change during the course of sample dosing. For all XES measurements, the photon dose was well below the acceptable limit. Multiple scans on the same sample were normalized to incident flux and averaged using MATLAB. Data were referenced to the K$\beta_{1,3}$ and K$\beta_{2,5}$ features of Fe_2O_3[116] and normalized to a total integrated spectral intensity of 100 by numerical integration.

4.2.3 Density Functional Theory Calculations

All calculations were performed using the ORCA program package developed by Neese and coworkers.[117] 225 atom cluster models of FeMoco and FeVco active sites were based on the X-ray structure of MoFe protein,[69] and were geometry optimized using the TPSSh density functional according to previously reported protocols.[73] Charges on the metal clusters were -1 for FeMoco ($[MoFe_7S_9C]^{1-}$) and -2 for FeVco ($[VFe_7S_9C]^{2-}$), to maintain a valence isoelectronic configuration and a spin of $S=\frac{3}{2}$. While other cofactor charges are conceivable, previous studies have shown that VtC spectra are relatively insensitive to changes in cofactor charge,[68] and thus they have not been considered here. Analogous broken-symmetry solutions were found. Valence-to-Core XES spectra were calculated within a one-electron approximation implemented in ORCA.[116] These calculations used the BP86 functional[124,125] and the DKH relativistic approximation,[158–160] with DKH-recontracted def2-TZVP triple-zeta basis sets[121,161] and the COSMO dielectric model ($\epsilon = 4$).[123]

4.3 Results and Discussion

In an effort to provide more definitive evidence for the structure of FeVco, this work reports the Fe Kβ VtC XES spectrum of the VFe protein of *A. vinelandii* nitrogenase (Figure 4.1). Additionally, the concomitant re-measurement of the analogous spectrum of the MoFe protein shows that the Kβ'' feature at ≈7100 eV, previously shown to be indicative of fluorescent emission from the 2s atomic orbital of the central carbide in FeMoco, is identically placed in the spectrum of VFe. Additionally, the difference spectrum shows only minute deviations in the intensities and energies in all spectral regions.

In 2011, it was shown that the energy of the distinctive Kβ'' peak in FeMoco was inconsistent with any other interstitial light atom besides C, and that in the absence of such an atom, *e.g.* in

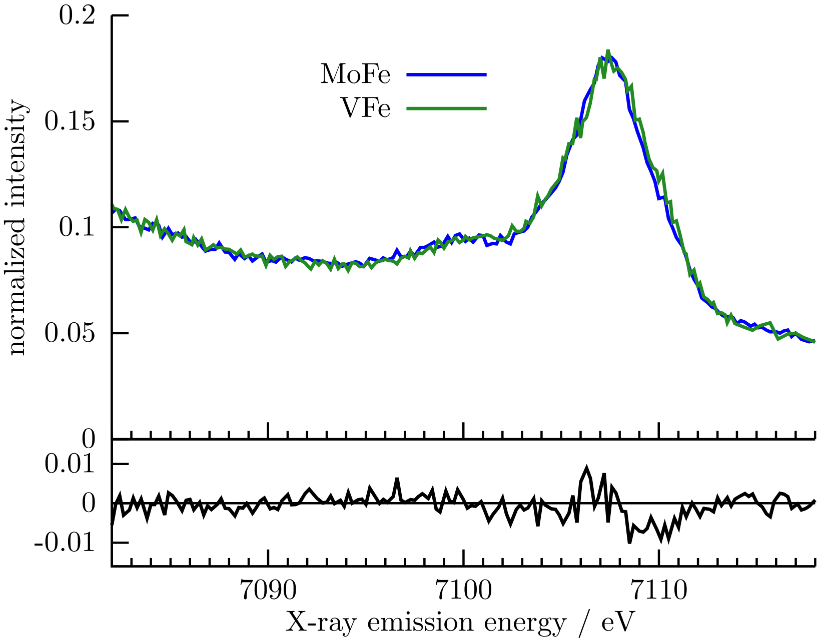

Figure 4.1: Top: Kβ VtC spectra of MoFe and VFe proteins Bottom: Difference spectrum (MoFe - VFe)

the P-cluster, the intensity of the Kβ'' feature was significantly diminished.[68] Given the virtually identical VtC spectra of the MoFe and VFe proteins, these data strongly indicate the presence of an analogous interstitial carbide in FeVco, thereby providing the first direct evidence for a structurally homologous cofactor in the V N2ase.

To provide additional support for this conclusion, density functional theory (DFT) calculations were performed on large, 225 atom models of both cofactors, based on the published crystal structure of MoFe. The FeMoco model was previously utilized in the report of the Mo(III) assignment in FeMoco,[73] and the FeVco model was constructed to be isostructural and valence isoelectronic (see Section 4.2). The optimized structure of the FeVco active site model results in V-Fe distances that are ≈0.11 Å longer than the Mo-Fe distances of optimized FeMoco, in reasonably good agreement with experimental metrical parameters from EXAFS (≈0.08 Å longer).[77] VtC XES spectra were calculated within a one-electron approximation, and the averages of the spectral contributions from all cofactor Fe atoms are presented in Figure 4.2

The calculations, like the experiment, show strikingly similar spectra in both the K$\beta_{2,5}$ and

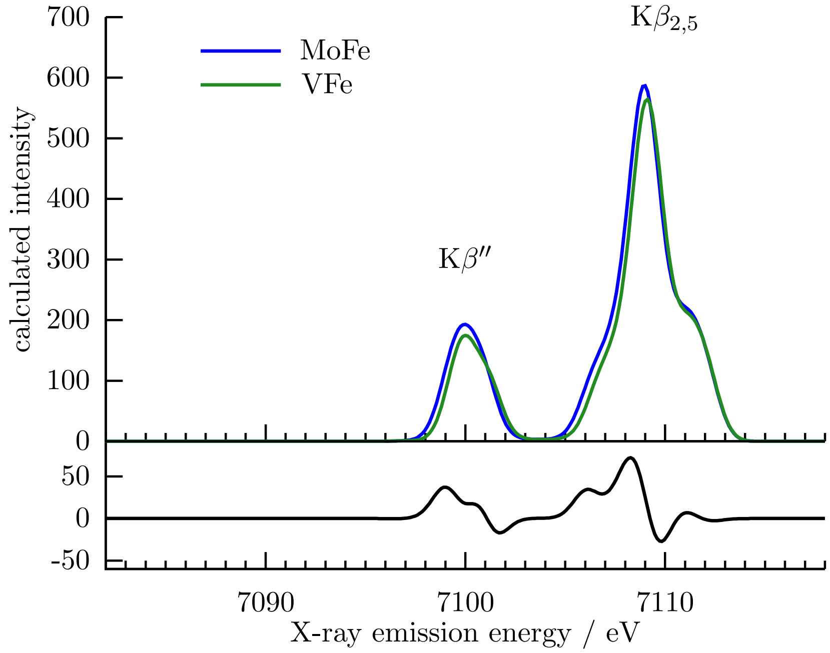

Figure 4.2: Top: Calculated Kβ VtC spectra of MoFe and VFe proteins Bottom: Difference spectrum (MoFe - VFe)

Kβ″ regions, where the latter is dominated by S 3s and C 2s contributions and the former by S 3p contributions. The subtle differences in the calculated spectra are highlighted by a difference spectrum, which again agrees well with experiment (Figure 4.1). In particular, the derivative shape under the Kβ$_{2,5}$ is reproduced by the calculations and may be attributed to the sulfur 3p orbitals being shifted to slightly higher energy in FeVco than in FeMoco. Some caution should be exercised however, as due to the limited experimental resolution, a more quantitative analysis is prohibitive. Nonetheless these spectra clearly establish the presence of a carbide in FeVco.

4.4 Conclusions

A more detailed study of the electronic structural differences between these cofactors will need to rely on new experimental methodologies geared towards probing electronic, rather than geometric structure. As detailed in the following chapter, such an investigation makes use of high energy resolution fluorescence detected (HERFD) XAS and Kβ mainline XES, and examines both the

MoFe and VFe proteins as well as synthetic metallocubane models for the Mo and V cofactors. The present work takes an initial step toward directly defining the structure of FeVco. The presence of a second biological cofactor with an interstitial carbide has now been experimentally established. With this finding, the groundwork has been laid for more focused studies aimed at understanding how perturbations to electronic structure, likely engendered by the heterometal, differentially tune these remarkable enzymes, enabling reactions as diverse as N_2 activation and C-C bond coupling.

Chapter 5

"To achieve great things, two things are needed; a plan, and not quite enough time."

Leonard Bernstein

Comparative Electronic Structures of Nitrogenase FeMoco and FeVco

5.1 Introduction

The nitrogenase enzymes are Nature's catalysts for the fixation of aerial dinitrogen to more reduced, bioavailable forms.[58,144,162] At ambient conditions, the most competent of the nitrogenases is the Mo-dependent variant, and decades of research have been aimed at understanding its structure, function, and mechanism.[58,61,62,80,162] The active site for N_2 reduction, the iron-molybdenum cofactor (FeMoco), is contained in the $\alpha_2\beta_2$ heterotetrameric MoFe protein. In 2011, the complete atomic structure of FeMoco was determined using valence-to-core (VtC) Fe Kβ X-ray emission spectroscopy (XES),[68] pulsed electron paramagnetic resonance (EPR), and high-resolution X-ray crystallography.[69] The decade-old "X" atom at the center of the cofactor[64] was shown to be a μ^6 carbide ligand; heretofore unprecedented in biology, and coordinated by the "core" Fe atoms as depicted in Figure 5.1.[163]

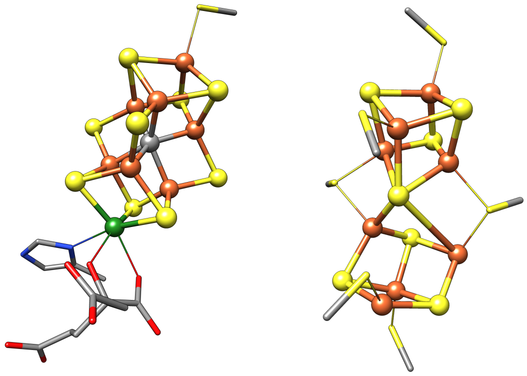

Figure 5.1: Structural representations of FeMoco (A) and the P^{OX} P-cluster (B) from *Azotobacter vinelandii* nitrogenase, adapted from PDB 3U7Q. Color scheme for atoms: Fe = orange, S = yellow, C = gray, Mo = green, N = blue, O = red. Inorganic sufides are shown as spheres, cysteinate residues are shown as sticks, and hydrogen atoms have been omitted.

Both FeMoco ($MoFe_7S_9C$) and the P-cluster (Fe_8S_7) (Figure 5.1), which serves as an electron transfer relay, are entirely unique to nitrogenases. The presence of at least 15 distinct iron atoms in the protein complicates the interpretation of results from iron-specific techniques such as ^{57}Fe Mössbauer and X-ray spectroscopies. However, with advances in gene deletion protocols, the characterization of cofactor-deficient proteins has aided in deconvoluting spectral contributions from different metalloclusters.[70,164,165] Recent studies of the electronic structure of FeMoco have focused on properties such as oxidation state distribution and cofactor charge,[66,98,166,167] including a previous determination of the molybdenum oxidation state as Mo(III).[73] However, while progress towards understanding this enzyme continues to be made, significant questions regarding its electronic structure and the mechanism of dinitrogen reduction remain unanswered.[80,168]

Molybdenum-limited conditions or reduced temperatures can stimulate increased production of a vanadium-dependent nitrogenase, which has many similarities, yet several key distinctions from the molybdenum isozyme.[57] Structurally, the VFe protein of vanadium nitrogenase includes a third δ subunit, with the overall subunit stoichiometry varying by species.[75] While VFe protein contains metalloclusters presumed to be similar to those shown in Figure 5.1,[76,150,162] the exact atomic structures of the VFe redox centers are currently unknown, and conflicting accounts regarding their geometry exist in the literature.[75,77,151] The first evidence for an interstitial carbon atom at the center of the iron-vanadium cofactor (FeVco) is presented in Chapter 4,[109] a finding that has been subsequently supported by independent work.[87] These results establish the structural homology of the two cofactors. While prior theoretical studies have examined the impact of heterometal substitution,[169] to my knowledge a comparative investigation of the complete geometric and electronic structures of FeMoco and FeVco has yet to be undertaken until now.

A detailed study of the differences between these isozymes is of great interest given their dissimilar reactivities towards substrates.[57,79] At ambient conditions, the molybdenum nitrogenase is a superior N_2 reduction catalyst, while at reduced temperatures the vanadium is more active. Furthermore, the vanadium nitrogenase requires additional expenditure of ATP and reducing equivalents (Table 5.1), which is likely coupled to the production of additional equivalents of H_2. While it is often stated that the vanadium nitrogenase produces three equivalents of H_2 per turnover, to my knowledge a more accurate pressure-dependent study (analogous to that of Simpson and Burris on molybdenum nitrogenase[78]) has not been performed, there may be some error associated with

Table 5.1: Enzyme activities of *A. vinelandii* molybdenum and vanadium nitrogenase. Values for usage and production during N_2 reduction are in molar equivalents per N_2, and approximate activities for CO reduction are reported as molar equivalents per protein per minute.[86,147]

N_2	Mo nitrogenase	V nitrogenase
MgATP used	16	40
e^- used	8	12
H_2 produced	1	3^a
activity^b	1040	660
TON	2230	112
CO (eq. / min)		
C_2H_4	0.006	7.5
C_2H_6	0.001	2.5
C_3H_8	0.002	1.5

---

[a] As noted in the text, there may be some error associated with this number

[b] units of nmol mg^{-1} nitrogenase min^{-1} at ambient conditions

this number. These differences in reactivity appear to correlate with heterometal identity; however, the actual role of the heterometal in tuning enzyme function remains an open question. Changes in electronic structure, potentially engendered by the heterometal, could provide a rationale for the disparate activities towards substrate.

Recent studies of nitrogenase activity towards CO have added significant import to the question of heterometal functionality. Notably, Ribbe and coworkers have shown that the vanadium nitrogenase performs reductive C-C bond coupling using CO as a substrate, with orders of magnitude increased activity than the molybdenum analogue (Table 5.1).[86,154] Furthermore, the crystallographic characterization of CO-bound FeMoco identified a binding mode in which a "belt" sulfur atom is replaced by a bridging μ^2 carbonyl.[85] The relevance of this CO coordination mode to the native N_2 substrate interaction remains unclear; however, the recent demonstration of site-selective selenium incorporation into the belt sulfur positions of FeMoco during native substrate turnover raises questions regarding the catalytic relevance of sulfide lability.[170] Finally, it is intriguing that while CO only binds to FeMoco under turnover conditions, it has recently been shown to coordinate to FeVco in the resting state of vanadium nitrogenase.[87]

From a structural perspective, the study of synthetic iron-sulfur clusters has yielded considerable

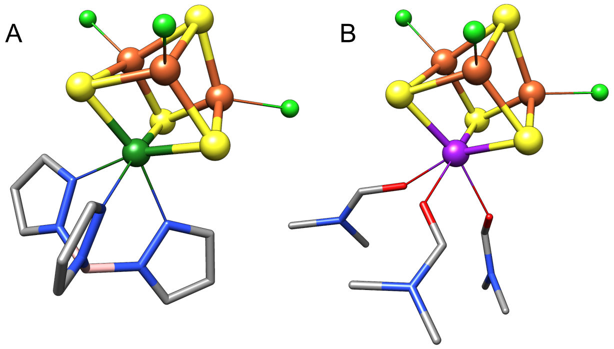

Figure 5.2: Structural representations of the molybdenum and vanadium cubane iron-sulfur cluster models $(Et_4N)[(Tp)MoFe_3S_4Cl_3]$[177] (A) and $(Me_4N)[VFe_3S_4Cl_3(DMF)_3]$[178] (B) used in this study. The $[MoFe_3S_4]^{3+}$ and $[VFe_3S_4]^{2+}$ cubane cores are valence isoelectronic, with an $S = \frac{3}{2}$ ground state identical to the cofactors. Color scheme for atoms: Fe = orange, S = yellow, C = gray, Mo = green, N = blue, O = red, V = purple, Cl = light green, and B = pink. Hydrogen atoms and counterions have been omitted for clarity.

insight into the redox cofactors of nitrogenase. Research efforts in the laboratory of R. H. Holm and others have produced an extensive library of iron-sulfur clusters, containing a variety of heterometals and with a range of stoichiometries.[67,171–173] Since the first structural models for FeMoco were proposed in the late 1970's, these synthetic complexes have been utilized in the study of both molybdenum and vanadium nitrogenases.[76,77,150,174–176]

In the present work,two single-cubane clusters have been employed as structural models for FeMoco and FeVco: $(Et_4N)[(Tp)MoFe_3S_4Cl_3]$[177] and $(Me_4N)[VFe_3S_4Cl_3(DMF)_3]$[178] (Figure 5.2). Both synthetic models have been shown to have a high degree of homology with their respective enzyme cofactors, including analogous $S = \frac{3}{2}$ ground states and similar spectroscopic properties.[67,144,171,177–180] The cubane models also successfully reproduce differences in metrical parameters between the Mo and V cofactors.[174] Finally, despite their similar quartet spin states, which arise from valence delocalization, the iron atoms in the V cubane are more reduced than in the corresponding Mo cubane, as demonstrated by a combination of crystallographically determined metrical parameters and zero- and applied-field ^{57}Fe Mössbauer spectroscopy.[179]

The vanadium cubane, first synthesized by J. Kovacs in 1986,[178] was integral to the initial reports of the structure of FeVco by Arber[76] and George,[77] based on vanadium K-edge X-ray absorption spectroscopy (XAS). Additionally, the molybdenum cubane served as a reference model for determining the Mo(III) oxidation state in FeMoco, using high energy resolution fluorescence detected X-ray absorption spectroscopy (HERFD XAS) at the molybdenum K-edge.[73,174] As exemplified by these studies, X-ray spectroscopy has been extensively utilized in the investigation of nitrogenase, as detailed in recent reviews.[61,97,181] However, the interpretation of iron extended X-ray absorption fine structure (EXAFS) data has been particularly problematic for both the MoFe and VFe proteins, because they possess a large number of iron atoms (*vide supra*). While vanadium[76,77] and molybdenum[73,182–184] XAS are more site specific (for the cofactor heterometal), drawing direct comparisons between the nitrogenase variants is difficult without a common spectroscopic target. However, an investigation of the similarities and differences between FeMoco and FeVco is fundamental to understanding their differential reactivity. Hence, X-ray spectroscopic experiments have been performed based on Fe 1s core excitations, utilizing both high-resolution X-ray absorption and X-ray emission spectroscopies to enhance the insight obtained in the presence of multiple iron atoms. The data presented herein include non-resonant and resonant XES at the Kα (2p→1s) and Kβ (3p→1s) emission lines of Fe, as detailed below. These data thus allow for quantitative comparisons to be made between FeMoco, FeVco, and the corresponding synthetic cubane clusters. It is noted that the high-resolution X-ray spectroscopic methods employed herein provide superior spectral resolution compared to previous Fe XAS studies.[150,151,185–187] This has allowed for the acquisition of new insights into the electronic structures of the enzyme cofactors from both the pre-edge and edge regions. The results of the X-ray spectroscopic studies are correlated to density functional theory (DFT) calculations in order to obtain more quantitative insight into the differences between the Mo and V cubane models and the FeMoco and FeVco cofactors. Changes in cofactor oxidation states, as well as differences in intra-cluster bonding and covalency, are discussed in the context of reactivity differences, particularly in the case of CO. These findings aid in elucidating possible roles for both the heterometal and the interstitial carbide.

5.2 Methods

In the the present study, a combination of both non-resonant and resonant XES is utilized in order to obtain detailed insights into the changes in the electronic structure of both the $[MoFe_3S_4]^{3+}$ and $[VFe_3S_4]^{2+}$ cluster models (Figure 5.2) and the protein active sites. In a non-resonant XES experiment the incident energy is tuned well above the absorption threshold, *e.g.* the Fe K-edge, resulting in the ionization of a 1s electron to the continuum. The core hole excited state may then decay by 2p→1s or 3p→1s fluorescence, giving rise to the Kα and Kβ mainline XES spectra, respectively. The spectral features of the former will be dominated by 2p spin-orbit coupling contributions, while the latter is dominated by 3p-3d exchange. Hence, the energetic splitting of Kβ mainline (ΔE_{main}) is sensitive to spin state, but may be further modulated by metal-ligand covalency.[92,102] Covalent delocalization of the 3d electrons, *i.e.* the nephelauxetic effect, decreases the amount of metal-centered spin density, leading to smaller couplings and smaller ΔE_{main}.[29,92,98,104] Thus, for complexes with analogous spin states, the Kβ mainline region provides a sensitive measure of covalency.

Alternatively one may perform a resonant XES (RXES) measurement, in which the incident energy is tuned into the pre-edge and edge region, and the subsequent fluorescence is monitored as a function of incident energy. When RXES is monitored at a single emission energy it is referred to as HERFD XAS. HERFD can be performed in principle at any emission line, and it results in spectral sharpening relative to standard total fluorescence measurements.[110,188] The 2p→1s, or Kα emission, provides the most intense fluorescence, and thus Kα-detected HERFD XAS provides an optimal detection channel for dilute samples.[73,111,189] Sacrificing roughly an order of magnitude in intensity, the 3p→1s, or Kβ-detected HERFD XAS, offers a more selective detection method. As first demonstrated by Cramer *et al.*, HERFD detection at the Kβ mainline can provide spin-selective XAS spectra.[112,190,191] The K$\beta_{1,3}$ and Kβ' features that comprise the Kβ mainline arise from different final-state spin multiplets as a result of 3p-3d exchange coupling.[102] For higher spin transition metal ions, detection at the lower multiplicity Kβ' channel can result in suppression of 1s→3d pre-edge intensity, as illustrated in Figure 2.11, right.[112] Alternatively, one may utilize this multiplet-dependent detection to decouple spectral contributions from metal sites of differing oxidation state.[113,192,193] Further details on these spectroscopic methods can be found in Chapter 2.

5.3 Experimental

5.3.1 Sample Preparation

The MoFe[69] and VFe[109] proteins were expressed and purified as previously described, and samples for X-ray spectroscopic measurements were also prepared as previously reported.[109] FeMoco was extracted from MoFe protein by treatment with NMF and DTT. The extraction of FeMoco was performed using 1 mL of NMF for 25 mg of protein, and used without further concentration. The final concentration of cofactor is estimated to be ≈0.2 mM, though it is noted that this is not a definitive number. An aliquot of the NMF and DTT solution of extracted cofactor was placed in a Delrin cell with a 38 μm Kapton tape window, and immediately frozen in liquid N_2.

The model compounds $(Et_4N)[(Tp)MoFe_3S_4Cl_3]$[177] and $(Me_4N)[VFe_3S_4Cl_3(DMF)_3]$[178] were synthesized as previously reported, and handled under inert atmosphere. Samples were prepared by grinding solid compound into a fine powder in a mortar and pestle. The powders were then pressed into 1 mm thick Al spacers and sealed wth 38 μm Kapton tape. For non-resonant XES measurments, the solid samples were measured without dilution, and for HERFD XAS measurements they were diluted ≈1:10 by mass with BN to minimize self-absorption.

5.3.2 Data Collection

X-ray spectroscopic experiments were conducted at beamline ID-26 at the European Synchrotron Radiation Facility (ESRF), France, and at beamline C-1 at the Cornell High Energy Synchrotron Source (CHESS), NY, USA. For all experiments, the flight path of the emitted X-rays was filled with He gas to minimize signal attenuation due to aerial scattering. Samples were maintained at cryogenic temperatures, using a continuous flow liquid He cryostat at 10 K at ESRF and a He displex cryostat at 40 K at CHESS.

Non-resonant Fe Kβ XES measurements were performed at both ESRF and CHESS. At ESRF, the incident energy was set to 7800 eV, selected using a Si(111) double crystal monochromator, with an storage ring electron current of approximately 200 mA and energy of 6 GeV. The photon flux at the sample was approximately 10^{13} photons / sec, with a beam spot on the sample of 0.1 mm x 1 mm. Kβ fluorescence was analyzed using a Johann-type spectrometer, employing five spherically bent Ge(620) crystals and a dead-time corrected Ketek Si drift diode detector, configured in a Rowland geometry as described previously.[194]

At CHESS, the incident energy was set to approximately 9000 eV, selected using a pair of Mo/B_4C multilayers for approximately 1% bandpass, with a storage ring electron current of 85 mA operating in 90 minute decay mode. Photon flux at the sample was approximately 2×10^{12} photons / sec, with a beam spot size of 1 mm x 2 mm. Fe Kβ fluorescence was analyzed using DAVES, the dual-array valence emission spectrometer, using five spherically-bent Ge(620) crystals similarly arranged in a Johann-type configuration. Analyzed emission was captured on a spatially-resolved Dectris Si pixel detector in a Rowland geometry, and a digital region of interest was selected to tightly enclose the reflections from all 5 analyzer crystals.

Resonant Fe Kβ XES measurements were also performed at ESRF and CHESS. At CHESS, the multilayers were replaced by a Si(111) monochromator, and photon flux decreased to approximately 10^{10} photons / sec. At both beamlines, HERFD XAS spectra were obtained by scanning the incident energy while detecting narrow bandwidth fluorescence at either the maximum of the K$\beta_{1,3}$ or Kβ' emission features (Table 5.2). Initially, spectra were recorded from 7080 eV to 7600 eV to include the EXAFS region for normalization, and the incident energy was calibrated to the first inflection point of an iron foil (7111.2 eV). Repeated spectra were then collected from 7080 eV to 7200 eV to improve the signal-to-noise ratio (S/N) in the pre-edge and edge regions.

Resonant Fe Kα XES measurements were performed at beamline ID-26 at ESRF. For these experiments, the incident energy was selected using a Si(311) double crystal monochromator, with a storage ring electron current of approximately 90 mA and energy of 6 GeV in 16-bunch operating mode. Photon flux at the sample was approximately 5×10^{11} photons / sec, with a beam spot size of 0.1 mm x 0.7 mm. Kα fluorescence was analyzed using the same Johann-type spectrometer, employing four Ge(440) crystals and a Ketek detector. HERFD XAS spectra were obtained by scanning the incident energy while detecting narrow bandwidth fluorescence at the maximum of the Kα_1 emission line (6404 eV). For normalization, spectra including the EXAFS region were collected from 7000 eV to 8000 eV, and the incident energy was calibrated to the first inflection point of an iron foil (7111.2 eV). Repeated spectra were then collected from 7105 eV to 7180 eV to improve the S/N in the pre-edge and edge regions.

Radiation damage assessments were conducted at the beginning of data collection for each sample. To determine the acceptable dwell time per sample spot, rapid Fe Kβ (resp. Kα) HERFD XAS spectra were recorded on the same location, scanning over the edge region. At ESRF, the XAS spectra were found to be superimposable up to (and in some cases well beyond) well beyond 25 (resp. 50) seconds of beam exposure, which was chosen as the maximum irradiation time. The cubane model complexes were found to be more susceptible to radiation damage than the proteins. Accordingly, while data with poor S/N were obtained at ESRF, the Kβ XES and Kβ HERFD XAS spectra from CHESS provide improved S/N without evidence of radiation damage. The smaller photon flux density (flux / beam spot area) due to a larger beam spot size is expected to decelerate damage. It should be noted that the spectra of the synthetic cubane models obtained on both beamlines, as well as spectra of an Fe_2O_3 calibrant, are superimposable for a given sample post processing.

5.3.3 Data Analysis

For all experiments, individual scans of the same sample were normalized to the incident photon flux and averaged to improve S/N using PyMCA.[195] The averaged spectra were further processed using MATLAB. The non-resonant Kβ XES spectra were calibrated using the Kβ emission features of Fe_2O_3 (Kβ' = 7045.2 eV, K$\beta_{1,3}$ = 7060.6 eV, Kβ'' = 7092.0 eV, K$\beta_{2,5}$ = 7107.2 eV). Correcting the energy axis using a second-order polynomial produced identical peak positions (by first spectral moment) for Fe_2O_3 spectra collected at CHESS, ESRF, and previous Fe Kβ XES spectra from the Stanford Synchrotron Radiation Lightsource (SSRL) beamline 6-2. Consistent calibration with the SSRL data allowed for comparison to the previously reported Fe Kβ XES spectrum of $\Delta nifB$, *vide infra.*[68,70] Following energy calibration, Fe Kβ XES spectra were normalized to 100 by numerical integration.

The averaged resonant Fe Kβ XES data were plotted as narrow bandwidth fluorescence yield (detector counts) at the desired emission feature, as a function of incident energy, to obtain HERFD XAS spectra. The spectra which included the EXAFS region were plotted and the intensity was scaled to achieve a superimposable EXAFS tail for all spectra. The high energy side of all the spectra was normalized to unity (Figure S1). The corresponding spectrum of each sample which encompassed just the edge region, with superior S/N, was then scaled such that it overlayed the pre-edge and edge of the normalized EXAFS traces.

The energy positions of the pre-edge and edge features were determined from plots of the first moments of all spectra. These were obtained by simultaneous smoothing and differentiation, using the Savitzky-Golay filter as implemented in EasySpin 5.0.2.[196] Plots of the first derivatives of the Kα-detected HERFD XAS and Kβ XES spectra are provided in Figures S2 and S3, respectively.

5.3.4 DFT Calculations

All calculations were performed using the ORCA program package developed by Neese and coworkers.[117] 225 atom cluster models of FeMoco and FeVco active sites, based on the X-ray structure of MoFe protein,[69] were TPSSh-optimized as previously described.[73,109] Charges on the metal clusters were -1 for FeMoco ($[MoFe_7S_9C]^{1-}$) and -2 for FeVco $[VFe_7S_9C]^{2-}$, to maintain a valence isoelectronic configuration and to be consistent with an experimental spin of $S = \frac{3}{2}$ for both cofactors. Analogous $M_s = \frac{3}{2}$ broken-symmetry solutions were found for FeMoco and FeVco. Time-dependent DFT (TD-DFT) Fe XAS calculations used the BP86 functional[124,125] and the DKH relativistic approximation,[158–160,197] with DKH-recontracted def2-TZVP triple-zeta basis sets[121,161] and the COSMO dielectric model ($\epsilon = 4$).[123] TD-DFT calculations for XAS of Fe pre-edges were performed using previously reported protocols.[90,198] The donor orbitals for XAS calculations were chosen as the Fe 1s and all virtual orbitals were selected as possible acceptor orbitals. Up to 300 roots were calculated. Individual Fe 1s excitations from all component irons were averaged to obtain the cluster spectra.

5.4 Results

5.4.1 DFT Calculations

In the 2014 report regarding the Mo(III) oxidation state assignment in FeMoco, a qualitative spin coupling scheme was described for both FeMoco ($[MoFe_7S_9C]^{1-}$, assuming a -1 charge) and the $[MoFe_3S_4]^{3+}$ cubane cluster model (Figure 5.2) that gives rise to an unusual non-Hund doublet configuration on molybdenum, according to DFT calculations.[73] Using similar DFT methods and the 225-atom model employed in a previous study of FeVco,[109] a similar spin coupling scheme for FeVco arises from the calculations, and is found to be analogous to the $[VFe_3S_4]^{2+}$ cluster as well. As shown in Figure 5.3, both the cubanes and the lower portion of the protein cofactors have two ferromagnetically coupled $Fe^{2.5+}$ ions that share a delocalized minority spin (down) electron. The remaining iron atom (of the lower triad in the cofactors) is antiferromagnetically coupled to the former. The iron atoms in the other cubane half of FeMoco/FeVco are not discussed here but they also feature mixed-valence delocalization and antiferromagnetic coupling. Both cofactors and cubane models have an $S = \frac{3}{2}$ ground state, and are valence isoelectronic to one another.[144,179,180] Similar to the Mo(III) ion, the vanadium ion is in the 3+ oxidation state, however, as Mo and V have a diagonal relationship in the periodic table, V(III) is a d^2 ion, in contrast to the d^3 Mo(III). This distinction gives rise to a key difference between the molybdenum and vanadium clusters: the

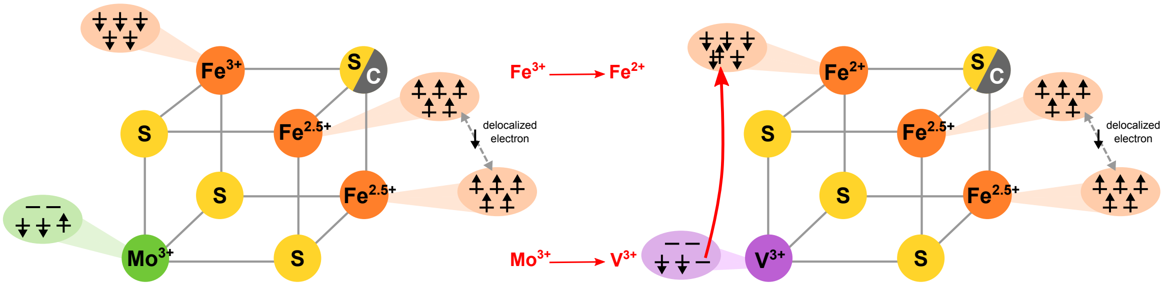

Figure 5.3: Spin coupling diagram for Mo (left) and V (right) protein cofactors and cubane models. In all four cases, DFT calculations predict a trivalent heterometal. The spin-up electron on the non-Hund Mo(III) ion is found to relocate to the antiferromagnetically-coupled iron in the vanadium clusters, resulting in its reduction from Fe^{3+} to Fe^{2+}.

oxidation state of the minority spin iron, which is found to be Fe^{3+} in the molybdenum clusters, has been reduced by one electron to Fe^{2+} in the vanadium clusters.

In the case of the cubane models, previous work by Carney *et al.* provides experimental verification for these DFT-calculated differences in electronic structure.[179] Namely, both heterometals were determined to be trivalent, and the iron complement of the $[VFe_3S_4]^{2+}$ cubane was shown to be more reduced on the basis of zero-field ^{57}Fe Mössbauer spectroscopy.[179] Furthermore, an identical spin coupling arrangement was proposed from the applied field ^{57}Fe Mössbauer spectra, with the authors noting "Two inequivalent subsites with a 2:1 intensity ratio . . . in which the magnetic moments of the Fe atoms of the more and less intense subsites are parallel and antiparallel, respectively".[179] Experimental support of the spin coupling arrangement shown in Figure 5.3 lends credence to the DFT calculations; therefore the calculated changes in intra-cluster bonding were examined in light of the more reduced iron complement in the vanadium analogues.

Pipek-Mezey localized Kohn-Sham orbitals from DFT calculations have been previously utilized to understand the electronic configuration of FeMoco and the $[MoFe_3S_4]^{3+}$ cubane.[73] In summary, it can be concluded that the non-Hund Mo(III) configuration appears to be stabilized by the substantial Mo-Fe bonding character of the three Mo t_{2g} type orbitals. The formation of such bonding orbitals, or double exchange, dictates antiparallel spin alignment of the bonding electrons; thus the three iron atoms with dominantly up-up-down spin require the corresponding Mo-based electrons to have a non-Hund down-down-up alignment. As has been previously noted, such a configuration on molybdenum is consistent with a ^{2}E term, which in moderate to strong ligand fields is the lowest excited state on the d^3 Tanabe-Sugano diagram. However, this unusual non-Hund spin configuration has yet to be verified experimentally.

For the vanadium clusters, the electronic rearrangement suggests that some bonding interaction has been lost. A quantitative comparison of the localized orbital compositions (at the BP86 DFT level) of the heterometal t_{2g} d-orbitals of the cubanes reveals more equally distributed Mo/Fe contributions (α 47/51%, β 53/43%, β 53/43%) than in the analogous V/Fe contributions (α 34/64%, β 60/36%, β 61/35%). This is consistent with the spin-up α electron relocating from the heterometal to the minor-spin iron, as shown in Figure 5.3. Furthermore, the Mayer bond orders and Mulliken spin populations of the canonical DFT orbitals indicate less covalency in the vanadium clusters (Table S1). It is noted that the Mo-based d-orbitals are very Mo-Fe bond-like, although the orbital composition percentages depend on the amount of HF exchange in the functional. Thus, one should not read too much into the absolute percentages (which are functional dependent). The relative change in orbital composition on going from the Mo clusters to the V clusters (at the same level of theory), however, reveals clear electronic structural differences between the two, in agreement with the ↑ Mössbaer data (*vide supra*). Additional details and figures are provided in the SI.

This loss of heterometal-iron bonding in the both the $[VFe_3S_4]^{2+}$ cubane and FeVco manifests in the metrical parameters of the clusters as well. In the cubane models, for which high-resolution crystal structures are available, the average V-Fe distance (2.78 Å)[178] is longer than the average Mo-Fe distance (2.73 Å).[177] Similarly, the average V-Fe distance in FeVco (2.76 Å, from extended X-ray absorption fine structure (EXAFS) analysis)[77] is longer than the Mo-Fe distances in FeMoco (2.69 Å).[69] These differences in metrical parameters are contrary to the expected changes based on periodic trends and the Shannon radii,[199] which would lead one to predict *shorter* V-Fe distances. Thus, the metrical parameters of the cubanes and protein cofactors are suggestive of increased heterometal-iron bonding in the molybdenum analogues.

While the comparative experimental study of the electronic structures of the $[MoFe_3S_4]^{3+}$ and

$[VFe_3S_4]^{2+}$ cubanes[179] supports the DFT calculations detailed above, the validity of extending this insight to FeMoco and FeVco has not been previously demonstrated. To investigate whether these electronic structural differences found in the cubane models are representative of differences between the enzyme cofactors, the X-ray spectroscopic experiments detailed herein were performed.

5.4.2 Fe Kα HERFD XAS

The Fe Kα HERFD XAS spectra of the MoFe and VFe proteins and the synthetic Mo-Fe and V-Fe cubane clusters are shown in Figure 5.4. Typical of iron-sulfur clusters,[97] the spectra exhibit a rising edge inflection at ≈7120 eV, a white line maximum at ≈7125 eV and a pre-edge feature at ≈7112 eV, as determined from the first derivatives of the spectra (Figure S2). The changes that occur in each of these three spectral regions between the Mo/V cubanes and MoFe and VFe protein data are systematically discussed below. It should be noted that the MoFe and VFe protein spectra

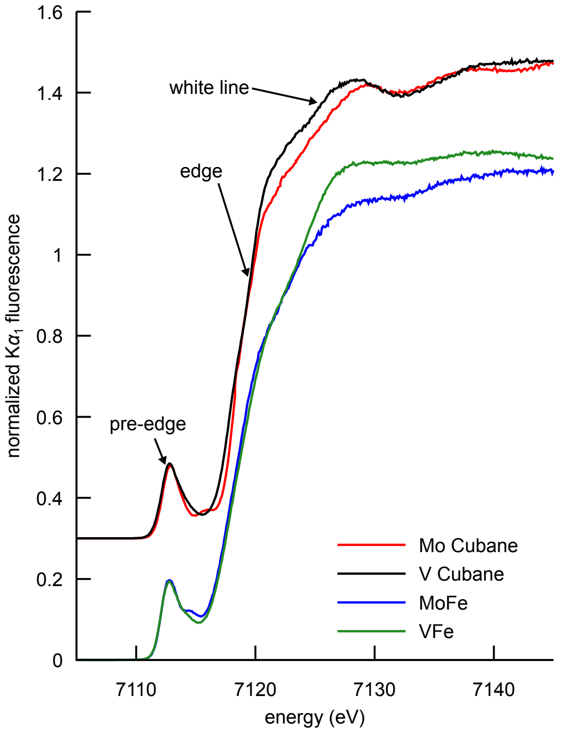

Figure 5.4: Comparison of the Fe Kα-detected HERFD XAS spectra of Mo and V cubanes, MoFe, and VFe. Cubane spectra have been vertically offset by 0.3 units.

have contributions from all iron atoms in the proteins, and not solely the cofactors (*vide supra*).

Recent studies have shown that the rising edge region of iron-sulfur clusters may be diagnostic of the extent of delocalization of redox events within an iron-sulfur cluster.[98] Localized redox events have been shown to affect no shift in the rising edge inflection energy, while delocalized redox events show a clear energetic shift in the rising edge. Hence, the similar edge inflections of the Mo and V cubanes at $\approx$7120 eV (Figure S2) seem to suggest a somewhat "localized" reduction of one Fe in the V cubane relative to the Mo cubane. This is consistent with the picture derived from previous Mössbauer data[179] as well as the DFT calculations described herein, in which the iron undergoing redox change upon going from the V to the Mo cluster is not part of a mixed-valent pair. It is noted however that there are changes in the $\approx$7117 eV region of the synthetic cubane cluster spectra (clearly illustrated by the first moments in Figure S2), with the V cubane spectrum appearing at lower energies relative to the Mo analogue. While the origins of the $\approx$7117 eV feature are not presently understood, the observed differences could result from differences in delocalization within the cubane, as well as differences in Fe-heterometal interactions. This unfortunately limits the quantitative information that can be deduced from the rising edge region for these synthetic cubane models. For the proteins, the picture is further complicated by the large number of contributing irons not incorporated in the cofactors, as noted above. Thus, one is cautioned that while the rising edge energies are consistent with a localized redox event, no firm conclusions can be derived from this spectral region.

In contrast to the rising edge region, there are clear differences in the protein and cubane spectra observed at the white line region, as indicated in Figure 5.4. In both pairs of spectra, the vanadium-containing clusters have a more intense white line relative to their respective molybdenum analogues. In contrast to the pre-edge region (*vide infra*), the nature of the underlying transitions at the white line are not well understood, and neither DFT models or multiple scattering based calculations are presently able to reliably calculate this spectral region in iron-sulfur models.[98] Nonetheless, empirical interpretation of this spectral regions can be made based on the existing body of XAS studies on iron-sulfur clusters.[97,98] For structurally homologous iron-sulfur clusters, an increase in iron oxidation state manifests as a loss of white line intensity. This behavior is

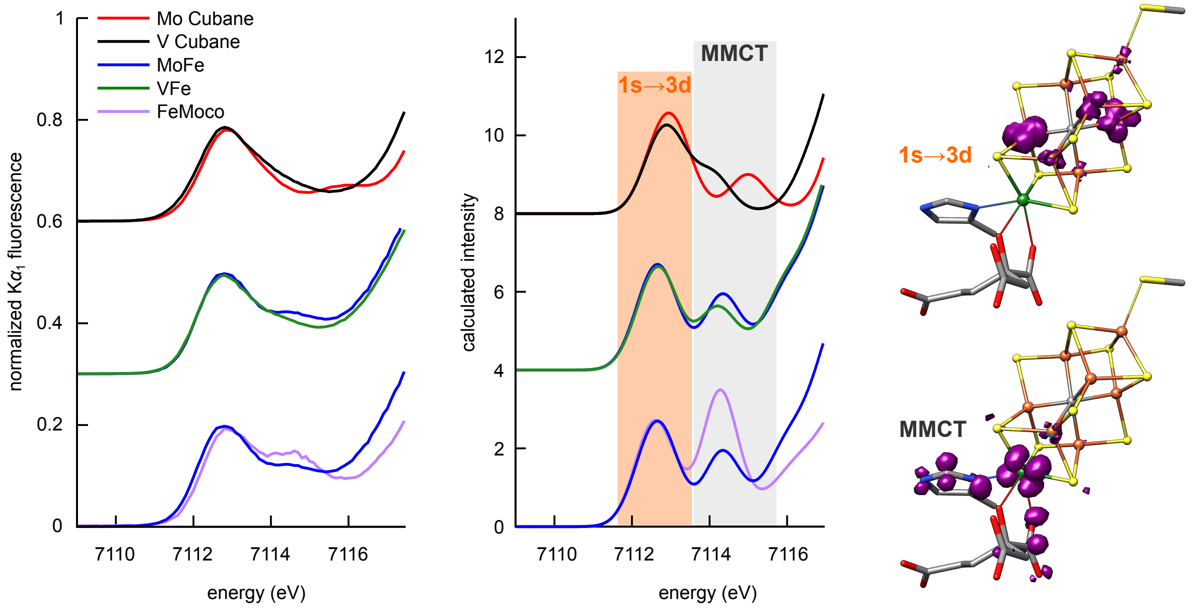

Figure 5.5: Comparison of the pre-edge regions of experimental Fe Kα-detected HERFD XAS (left) and TD-DFT-calculated XAS (middle) spectra of Mo and V cubanes, MoFe, VFe, and isolated FeMoco. Experimental data are offset in intervals of 0.3 units and calculated spectra in intervals of 4 units. A scalar shift of 122.1 eV and Gaussian broadening of 1.5 eV was added to the calculated transition energies to align theory with experiment. Right: TD-DFT-calculated transition difference densities for selected 1s→3d and metal-to-metal charge transfer transitions at the indicated peaks. The purple isosurface is a positive density difference (acceptor), shown at a contour level of 0.004 a_0^{-3} for FeMoco (analogous transitions are found for FeVco and the cubane models, and the negative density difference, or donor is the highly contracted 1s, which is not visible).

clearly observed in the case of both synthetic complexes[98,200] as well as the [Fe_8S_7] P-cluster and [Fe_4S_4]-containing Fe protein.[201,202] Hence, the observed changes in the white line region of both the cubanes and the proteins suggest that the V analogues are overall more reduced than the Mo analogues. Here, it is of interest to note that the P-cluster of VFe has been suggested to be one electron more oxidized than the all-ferrous P-cluster of the MoFe protein.[75,153,180] This would suggest an even greater complement of reduced iron in FeVco relative to FeMoco.

At ≈7112 eV, the 1s→3d pre-edge feature is observed. These transitions are formally dipole forbidden, but gain intensity due to symmetry-allowed 3d-4p mixing in the local ∼Td symmetry.[90,203,204] Closer inspection of the pre-edge region in Figure 5.5 shows the presence of additional features to higher energy at ≈7114.5 eV. For both the proteins and the cubanes, this second feature is found to be more pronounced in the case of the molybdenum clusters, whereas in the respective vanadium analogues it appears as a high energy shoulder. In addition, when comparing MoFe to isolated FeMoco, one notes that FeMoco has a higher intensity ≈7114.5 eV feature. This suggests that FeMoco makes the primary contribution to this spectral region, as opposed to the P-cluster. The presence of this second feature in the spectra of the synthetic cubanes further suggests that it may somehow arise from the iron-heterometal moiety, as opposed to the interstitial carbon. It is noted that in addition to 1s→3d transitions, pre-edge transitions can also arise due to metal-to-ligand charge transfer (MLCT) transitions, particularly when ligands posess low-lying unoccupied orbitals, *e.g.* an extended π^* system.[29,45,54,115] For iron-sulfur clusters with weak-field sulfide ligands and tetrahedral geometry, however, a small Δ_T and the absence of CT-accepting ligands generally precludes observation of more than one pre-edge peak. Accordingly, multiple pre-edge peaks are somewhat atypical for iron-sulfur clusters, but are present in heterometallic nitrogenases[151] and synthetic cubane clusters. Hence empirically, it appears that this feature may arise from *metal-to-metal charge transfer* (MMCT) transitions.

To further investigate the origin of the differences observed in the pre-edge region, TD-DFT calculations were performed to obtain the XAS spectra of the proteins and cubane models. The calculated spectra shown in Figure 5.5 are in good agreement with experimental findings, successfully reproducing the differences observed between molybdenum- and vanadium-containing clusters. Thus, the nature of the pre-edge transitions can be determined from the calculations with reasonable fidelity. TD-DFT-calculated difference densities (between excited state and ground state) were generated for the most intense transition moments under each feature. As expected, the lower energy pre-edge peak is found to correspond to transitions into Fe 3d orbitals (there are also weak transitions into orbitals with heterometal $\mathrm{t_{2g}}$ character).

As also surmised from an empirical assessment of the data (*vide supra*), the higher energy pre-edge feature is an MMCT transition, with the Mo or V $\mathrm{e_g}$ orbitals acting as the CT acceptor (Figure 5.5 right). The correlation between the intensity of this spectral feature and the heterometal identity supports this assignment. Furthermore, the intensity of these MMCT transitions, determined largely by the electric dipole transition matrix elements, is predicated on overlap between donor and acceptor wavefunctions. Given the highly localized nature of the Fe 1s donor, the observation of MMCT transitions indicates mixing of the iron and heterometal valence orbitals. The decreased MMCT transition intensity found in the vanadium clusters thus indicates less V-Fe orbital mixing compared to Mo-Fe. In part, this may be due to the less diffuse 3d valence orbitals of vanadium compared to the 4d valence shell of molybdenum, however, the weaker V-Fe bonding (compared to Mo-Fe) evidenced by both DFT calculations and changes in metrical parameters (*vide supra*) may contribute to the diminished intensity as well.

With regard to metrical parameters, oxidation state distribution, and heterometal bonding, the synthetic cubane clusters seemingly constitute effective models for the changes to cofactor electronic structure arising from the modification of heterometal identity. However, the synthetic cubane clusters do not contain the unique interstitial carbon atom found at the center of the cofactors.[68,109] Thus, comparison of the carbon-containing cofactors to the cubane models may provide some insight into the perturbations engendered by the interstitial carbon. In previous work, incorporation of highly basic light atom donors into iron-sulfur clusters was found to decrease the extent of Fe-S orbital interaction.[138] Preferential bonding of the irons to the interstitial carbide, rather than the bridging sulfides, suggests that the carbide increases the overall covalency of the cluster.

5.4.3 Fe Kβ XES

The Kβ mainline region of the X-ray emission spectrum, which corresponds to 3p→1s fluorescent transitions, provides a sensitive probe of metal covalency. As has been recently shown, formation of increasingly covalent metal-ligand bonds delocalizes the 3d valence orbitals of first-row transition metals, resulting in a loss of metal-localized 3d spin population.[92] The final state of the 3p→1s fluorescence contains an unpaired electron in the 3p shell, which can exchange couple to unpaired electrons of the same spin in the 3d orbitals. However, as the 3p orbitals are relatively localized, the covalent delocalization of 3d spin population decreases the magnitude of this exchange coupling. This manifests in the Kβ XES spectrum as a decrease in the energetic splitting of Kβ' and K$\beta_{1,3}$ spectral features, termed ΔE_{main}, as shown in Figure 2.11.[92]

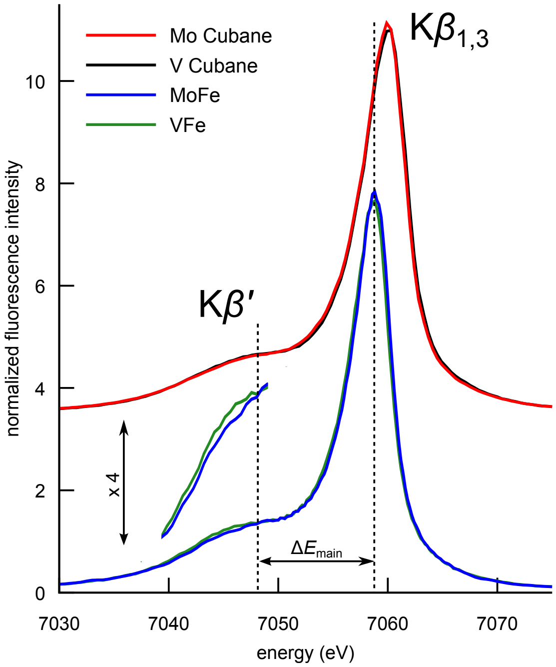

Figure 5.6: Comparison of the Fe Kβ mainlines of Mo and V cubanes, MoFe, and VFe. Cubane spectra have been vertically offset by 3.5 units. The inset shows a vertical expansion of the Kβ' of the proteins and the increased intensity in VFe. Vertical dashed lines are placed at the peak positions for the proteins given in Table 5.2.

Figure 5.6 shows the mainline region of the Fe Kβ XES spectra of the Mo and V cubanes, MoFe, and VFe. The energies of the K$\beta_{1,3}$ and Kβ' features of the protein spectra, the latter appearing as low energy shoulders, are indicated by the vertical dashed lines, and provided in Table 5.2. While all four spectra display similar Kβ mainline features, the ΔE_{main} of the cubane spectra are larger, by 1 eV or more, than that of the proteins. Furthermore, closer inspection reveals subtle differences between Mo and V analogues; namely an increased Kβ' shoulder intensity in the spectrum of VFe (compared to MoFe) and a slightly larger ΔE_{main} for the V cubane (compared to the Mo cubane).

Interestingly, the spectra all exhibit a ΔE_{main} that is smaller than what is generally observed for high-spin ferrous or ferric complexes, which typically fall in the 15-18 eV range.[92,116] It is noted that even for covalent, monomeric iron tetrathiolates and iron-sulfur dimers, the smallest previously reported ΔE_{main} is still larger than ≈13 eV.[92,98] Hence the present data are indicative of a substantially diminished spin population on the iron atoms, that in principle could be rationalized by either a highly covalent ligand environment or by iron atoms that are not "locally" high

Table 5.2: Kβ Mainline Emission Energies for Proteins and Cubanes Determined From First Spectral Moments

	Kβ' (eV)	K$\beta_{1,3}$ (eV)	ΔE_{main} (eV)
VFe	7048.0	7058.7	10.7
MoFe	7048.0	7058.7	10.7
$\Delta nifB$ MoFe[a]	7048.0	7059.9	11.9
V Cubane	7048.5	7060.5	12.0
Mo Cubane	7048.5	7060.1	11.6

---

[a] $\Delta nifB$ MoFe protein does not contain FeMoco, and reflects spectral contributions from the P-cluster only.[70]

spin. Despite the fact that covalent ligands (such as the sulfide / carbide / thiolate ions in these complexes) are known to promote low-spin metal ions by lowering the spin pairing energy,[100] the small tetrahedral ligand field, as well as DFT calculations (*vide supra*), strongly favor the former scenario.

While significant covalency of the protein and cubane iron atoms could be expected given their incorporation into iron-sulfur clusters, the smaller ΔE_{main} of MoFe and VFe as compared to the cubane models is likely reflective of increased covalency in the proteins. However, in addition to FeMoco and FeVco, the proteins contain P-clusters, which in the case of MoFe is known to be all-ferrous, and lack both the interstitial carbon and a heterometal. To exclude the possibility that the increased covalency observed in the protein spectra may somehow be due to contributions from the P-cluster, the present data were compared to the previously reported Fe Kβ X-ray emission spectrum of the $\Delta nifB$ MoFe protein, which contains *only* the P-cluster.[70] As reported in Table 5.2 the Kβ mainline of the P-cluster appears far more consistent with the synthetic cubane clusters, and in fact with other iron-sulfur clusters examined by ourselves and others.[97,98] Thus, the data show that the iron atoms in FeMoco and FeVco are more covalently bonded compared to other synthetic and biological iron-sulfur clusters, including those synthetic clusters that contain a Mo or V heterometal. This implies that it is in fact the interstitial carbon atom that imbues the cofactors with increased covalency; it is noted however that some ambiguity remains concerning the geometric and electronic structure of the P-cluster in VFe.

As mentioned previously, there are also more subtle differences observed between the Kβ mainlines of the Mo- and V-containing clusters. The more reduced iron complement of the V analogues should lead to a loss of iron-centered spin, as shown in Figure 5.3, and a smaller ΔE_{main} is therefore expected. However, the opposite change is observed for the synthetic cubane cluster spectra, and while the energies of the protein spectral features do not change, the increased shoulder intensity of VFe parallels the difference in the synthetic clusters. In addition to a loss of spin due to iron reduction, a concomitant loss of bond covalency is expected, which induces the opposite change in ΔE_{main}. As has been previously observed,[98] these counteracting effects can lead to superimposable Fe Kβ mainlines in iron-sulfur clusters of differing oxidation state. Thus, in addition to being more reduced, the V-containing clusters would seem to be less covalent than their corresponding molybdenum analogues.

Thus far, the Kα HERFD XAS data have shown the perturbations to electronic structure resulting from an alteration in heterometal identity; namely a weakening of iron-heterometal bonding and a reduction of the iron complement upon changing from Mo to V. The Kβ XES spectra further illustrate the increase in cluster covalency that occurs upon incorporation of the interstitial carbon atom in FeMoco and FeVco. Finally, these findings have been reaffirmed using a single, unified spectroscopic method, as detailed below.

5.4.4 Spin-Polarized Fe Kβ HERFD XAS

The sensitivity of the Kβ mainline emission spectrum to metal-localized spin population is derived from the underlying multiplet structure.[92,102,103] In the high-spin d^5 case, *e.g.* tetrahedral ferric iron, the final state that is stabilized by 3p-3d exchange coupling (*i.e.* when the unpaired 3p electron is aligned parallel to the 3d electrons) can be described as a ^{7}P state in the Russell-Saunders atomic limit. This stabilized final state results in higher transition energies, and is the dominant contributor to the K$\beta_{1,3}$ spectral feature.[92] In contrast, if the final state unpaired 3p electron is aligned antiparallel to the 3d electrons, 3p-3d exchange is quenched, and a ^{5}P state gives rise to the Kβ' feature (Figure 2.11). The two final state terms have spin-up and spin-down unpaired 3p electrons, meaning that spin-down and spin-up 3p electrons relaxed to fill the 1s core hole, respectively (it is assumed for the sake of this discussion that the majority spin population is up).

Pauli exclusion thus dictates that the initial 1s excitations occurred on different spin manifolds.[193]

These energetically distinct spin manifolds enable the HERFD XAS experiment to achieve spin selectivity when performed at either the K$\beta_{1,3}$ or Kβ' spectral features, corresponding to spin-down and spin-up transitions respectively.[112,205] In the high-spin d^5 case however, pre-edge transitions into the 3d orbitals are only allowed for spin-down transitions, according to the $\Delta M_s = 0$ spin selection rule. The Kβ HERFD XAS spectra of the MoFe and VFe proteins and synthetic cubane clusters, along with schematics of the pre-edge excitations, are shown in Figure 5.7.

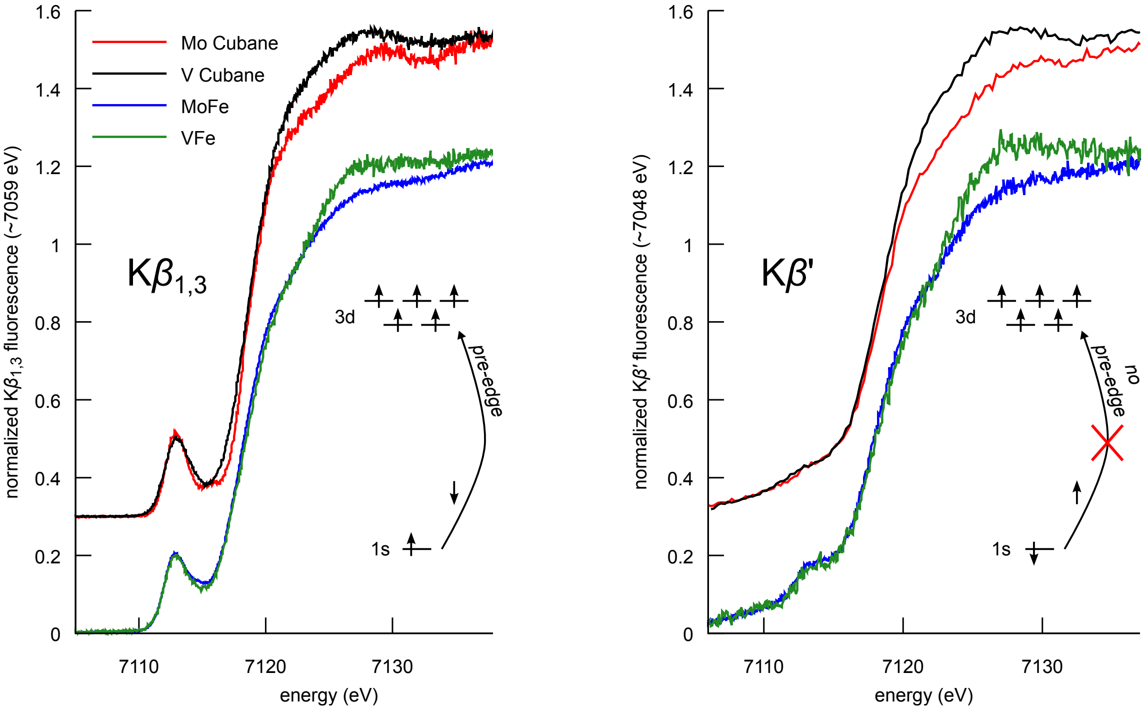

Figure 5.7: Comparison of the Fe K$\beta_{1,3}$- (left) and Kβ'- detected (right) HERFD XAS spectra of Mo and V cubanes, MoFe, and VFe. Cubane spectra have been vertically offset by 0.3. In a one-electron picture, the schematics illustrate how spin selectivity results in a loss of 1s→3d transitions.

The K$\beta_{1,3}$-detected HERFD spectra (Figure 5.7, left) have a strong resemblance to the Kα HERFD spectra in Figure 5.4, including pronounced differences in white line intensity, as well as more subtle differences in the pre-edge region and in the rising edge of the synthetic cubane clusters. These spectral perturbations, as discussed above, may be attributed to a decrease in overall iron oxidation state and diminished iron-heterometal bonding in the V cubane and V-containing protein, relative to their Mo analogues. In the Kβ'-detected HERFD spectra (Figure 5.7, right) however, while differences at the white line are still clearly present, the pre-edge feature is drastically reduced in intensity in the protein spectra, and essentially absent in the case of the synthetic cubane clusters.

The phenomenon of pre-edge intensity suppression has been previously observed for high-spin d^5 complexes of both iron and manganese, and can be rationalized using the spin selection rule discussed above.[112,191,206] It may thus appear somewhat surprising to observe the residual pre-edge intensity in the protein spectra (Figure 5.7, right). However, achieving this spin selectivity is predicated on the ability to energetically resolve the different spin multiplets underlying the Kβ mainline. The small ΔE_{main} of the proteins likely reflects an energetic compression of the spin multiplets, seemingly to such an extent that spin-up and spin-down manifolds begin to coalesce. The modest pre-edge intensities in the Kβ'-detected HERFD XAS spectra of the proteins can therefore be attributed to a small fraction of the spin-down transition envelope at the Kβ' feature. Importantly, these data provide clear experimental evidence that the electronic structures of the protein cofactors are clearly distinct from those of the synthetic cubane clusters. It is noted that while the spin-polarized Kβ HERFD XAS data are not available for the P-cluster ($\Delta nifB$), the Kβ mainline data (Table 5.2) suggest that the spin multiplets are less compressed than in the cofactors.

5.5 Discussion

Using a combination of XES and high-resolution XAS, supported by DFT calculations, it has been demonstrated that the electronic structures of both the protein cofactors and the synthetic cubane clusters are modulated by the heterometal identity. Relative to the Mo clusters, the iron complement of the V analogues is found to be more reduced and less covalent, and the triad of proximal iron atoms have weaker bonding interactions with the heterometal. This interpretation is consistent with both the spectroscopic data as well as changes in metrical parameters (*vide supra*). In addition, it has been demonstrated that the interstitial μ^6 carbon atom in FeMoco and FeVco increases the covalency of the iron atoms relative to the cubane models. Some potential implications of these findings regarding the function and design of these active site cofactors are discussed below.

The more reduced iron complement of the V clusters, while maintaining a valence isoelectronic configuration, is accompanied by the loss of a single heterometal d-electron. In the case of the synthetic cubane clusters, the resultant V^{3+} oxidation state has been previously determined,[179] however to my knowledge the vanadium oxidation state in FeVco has not been established. In light of the present data, as well as the highly similar V K-edge XAS spectra of VFe and the synthetic vanadium cubane cluster,[76,77] it seems likely that FeVco contains a V^{3+} ion, analogous to the Mo^{3+} recently identified in FeMoco. However, the premise of valence isoelectronic cofactors is based on the $S = \frac{3}{2}$ EPR spectra, which do not necessarily preclude changes in valence electron count by ± 2. While a more oxidized FeVco is unlikely considering the results herein, it has been proposed that the VFe P-cluster may be more oxidized than the corresponding MoFe P-cluster.[75,153,180] In this case, the more intense white line of the Fe K-edge XAS spectrum of the VFe protein could indicate a substantially more reduced iron complement in FeVco. A word of caution, however, that this is fairly speculative, as the geometric and electronic structures of the VFe P-cluster are not definitively known. Furthermore, while the correlation of white line intensity to oxidation state in iron-sulfur clusters has been well documented,[97,98,164,200–202,207] the underlying physical origins of this sensitivity are not well understood. Thus, a more quantitative interpretation is currently not feasible.

In addition to structural considerations, several intriguing reports have recently emerged concerning the interaction of nitrogenase with CO, which is isoelectronic to the native N_2 substrate. In particular, the V-dependent isozyme has been shown to affect CO reduction to short-chain hydrocarbons, as detailed above.[86,147] In contrast, CO acts as a reversible inhibitor of the Mo isozyme, coordinating to FeMoco in a μ^2 bridging fashion and displacing the S2B belt sulfur atom.[85] While CO binding to FeMoco requires reduction of the enzyme under turnover conditions, CO was recently shown to coordinate to FeVco in the resting E0 state, with EPR spectroscopy suggesting an analogous coordination mode.[87] From the perspective of inorganic coordination chemistry, CO is known to prefer more reduced metal centers, which have a greater capacity for backbonding into the unoccupied CO π^* molecular orbitals; thus CO binding to E0 of FeVco but not FeMoco can be easily rationalized by a more reduced iron complement of FeVco, and may explain the marked differences in isozyme activity towards CO.

The TONs of the Mo- and V-dependent nitrogenases (Table 5.1) further suggest that FeVco is weaker and more fragile than FeMoco. This is further evidenced by the preferential expression of the molybdenum-dependent isozyme at ambient conditions.[57] As both cofactors are now known to contain an interstitial carbon,[109] these differences likely result from changes in heterometal-cluster interactions. As detailed above, the molybdenum clusters have increased bonding between Mo and Fe, and more covalent bonding within the clusters. Thus, weaker Fe-V bonding (relative to Fe-Mo) may manifest as a decrease in structural integrity and the significantly lower TON. This points to a possible functional role of the heterometal as an apical "anchor" for the cofactor.

A final point of discussion is the increased covalency of the cofactors relative to other iron-sulfur clusters. The covalency engendered by the interstitial carbon atom (*vide supra*) represents a significant modulation in the electronic structure of the cofactors relative to other iron-sulfur clusters, which perform solely electron transfer. This is an important distinction, as the nitrogenase cofactors must accumulate reducing equivalents over the course of the catalytic cycle.[62,80,208] Thus, similar to the heterometal, the interstitial carbon may serve to anchor the six ligating iron atoms together via strong, highly covalent bonds, in particular during the more reduced E states of the Thorneley-Lowe cycle.[80] Futhermore, covalent delocalization of the iron 3d orbitals (the Nephelauxetic effect) decreases electron-electron repulsion (the Racah B parameter).[100] As reduction of the cofactors likely involves the addition of spin-paired 3d electrons, the increased covalency may also shift the cofactor reduction potential in a more positive direction. It is of further interest to consider the presence of this covalent anchor in the context of mechanisms where surface hydrides provide a repository for the cofactor's reducing equivalents.[80] Both the hydride protonation and reductive elimination mechanisms invoke the conversion of bridging hydrides to terminal hydrides via cleavage of a covalent Fe-H bond. Such an isomerization would likely be facilitated by the presence of a highly covalent carbon, potentially through competition for the iron 3d orbitals. It is also possible, though highly speculative, that the carbon may lower the energetic barrier for accessing excited spin states along the reaction pathay.

In addition to affecting the intermediate states of the cofactor, the highly covalent Fe-C bonding weakens the Fe-S bonding in the resting E0 state. It has been previously shown *in silico* that this preferentially affects the μ^2 belt sulfides of FeMoco.[138] Interestingly, Spatzal *et al.* have recently shown that during catalysis, the FeMoco S2B belt sulfur atom will selectively exchange with selenium, and they indicate that this lability may be catalytically relevant. While the other belt sulfides will eventually exchange, it is intriguing that S2B is the same sulfur that is displaced by the binding of CO, which could suggest that its release from the cofactor may be by design. Thus, while this is certainly speculative and remains to be investigated in the case of FeVco, the covalent interstitial carbon may additionaly serve to labilize the S2B belt sulfur atom, opening a site for substrate binding.

5.6 Concluding Remarks

The results presented herein directly illustrate differences in electronic structure between FeMoco and FeVco. In particular, a less covalent and more reduced iron complement in FeVco may be an important factor governing the differential stability and activity of these enzymes. One can rationalize key differences in metrical parameters, preferential CO binding, and cofactor activity and stability (as determined by turnover number) using tenets of inorganic chemistry such as π backbonding and the nephelauxetic effect. Also, while still qualitative, increased white line intensity for structurally analogous iron-sulfur clusters can be interpreted as a decrease in overall cluster oxidation state. The vanadium oxidation state in FeVco is assigned as V^{3+}, analogous to the Mo^{3+} in FeMoco. The presence of direct iron-heterometal bonding has also been established from spectroscopic observation of metal-to-metal charge transfer transitions in the Fe K-edge HERFD XAS spectra. Diminished spectral intensity in the case of the VFe protein and the vanadium cubane cluster points to a decrease in this heteroatom-iron bonding interaction. Finally, it has been shown that the presence of the interstitial carbon in FeMoco and FeVco serves to increase the overall covalency and structural integrity of the cofactors. Thus, it is proposed that the carbon provides a strong, covalent anchor at the center of the cofactor, and that it may also serve to labilize the μ^2 belt sulfur atoms that are proposed to exchange during catalysis. In summary, the insights garnered herein advance the understanding of the structure, evolutionary design principles, and catalytic function of the complex active site cofactors of the molybdenum and vanadium nitrogenases.

Chapter 6

> *"Back where I come from, we have universities, seats of great learning, where men go to become great thinkers. And when they come out, they think deep thoughts, and with no more brains than you have."*
>
> THE WIZARD OF OZ

Experimental and Theoretical Correlations Between Vanadium K-Edge X-ray Absorption and Kβ X-ray Emission Spectra

Portions of this chapter have been adapted or reproduced from: Rees, J. A.; Wandzilak, A.; Maganas, D.; Wurster, N. I. C.; Hugenbruch, S.; Kowalska, J. K.; Pollock, C. J.; Lima, F. A.; Finkelstein, K. D.; DeBeer, S., *J. Biol. Inorg. Chem.* doi:10.1007/s00775-016-1358-7 Copyright 2016, the authors, under a Creative Commons License.

6.1 Introduction

Vanadium plays an essential role in both biochemical and industrial catalysis. A number of solid-state catalysts employ vanadium in various oxide-type formulations, notably for the oxidative dehydrogenation of short chain alkanes, a highly desirable chemical transformation.[209,210] While the natural abundance of vanadium is only 0.015% in the earth's crust, it is found in the oceans at concentrations as high as 30 nM, making it readily bioavailable.[211] At physiological conditions vanadium is stable in the +3 to +5 oxidation states, and in its most oxidized forms is a potent Lewis acid. It is most commonly found in biology as some form of the vanadate ion, VO_4^{3-}, though some enzymes that promote mostly oxidative transformations require vanadium as a metallocofactor.[212–214]

For example, vanadium-dependent haloperoxidases promote the two-electron oxidation of halides using hydrogen peroxide as the terminal oxidant; or, in the absence of an organic substrate, can perform halide-dependent catalase-like disproportionation of hydrogen peroxide to water and dioxygen.[215] These haloperoxidases can also catalyze the oxidation of thioethers to sulfoxides, exhibiting oxo-transfer reactivity that is well established for high-valent vanadium complexes.[216] Interestingly, this sulfoxidation chemistry is the inverse of the reaction catalyzed by some molybdenum-dependent oxotransferases, such as DMSO reductase, which generate thioethers from the corresponding sulfoxide substrate at a molybdopterin active site.[211]

The diagonal relation of molybdenum and vanadium and their use in similar, albeit complementary, biochemical sulfoxidation reactivity serves to further highlight their involvement in the promotion of arguably nature's most complex chemical transformation: the 6-electron reduction of aerial dinitrogen. Biological nitrogen fixation is catalyzed by the nitrogenase enzymes, which contain three distinct types of [Fe-S] clusters. A [4Fe-4S] cluster in the Fe protein provides reducing equivalents via hydrolysis of ATP, while in the MoFe or VFe protein an [8Fe-7S] P-cluster serves as an electron transfer relay, reducing the active site [M-7Fe-9S-C] cofactor, where M = Mo or V.[57,58,68,69,109,144] Extensive studies of these enzymes using a range of spectroscopic techniques continue to provide novel insight into the structure and function of nitrogenase, however significant questions such as the role of the heterometal or the location of N_2 binding still remain unanswered.[68,73,80,97,111,208]

In many of these enzymes, the identities of important intermediates, often including the catalytically competent species, are still unknown. Characterization of the spin state, oxidation state, and coordination environment of vanadium in a catalytic cycle are important prerequisites for mechanistic understanding. Existing methods often utilized in such studies include ^{51}V nuclear magnetic resonance (NMR)[217] and various pulsed electron paramagnetic resonance (EPR) spectroscopies,[218,219] as well as X-ray based methods: vanadium K- and L-edge X-ray absorption spectroscopy (XAS) and extended X-ray absorption fine structure (EXAFS).[76,77,220] Some of these techniques have limited applicability to enzyme systems however. For example, L-edge XAS experiments are conducted in high-vacuum environments not ordinarily amenable to biological samples. Furthermore, as magnetic resonance methods have specific spin-state requirements, certain intermediates may be spectroscopically "silent", rendering NMR and EPR unapplicable at certain steps during a catalytic cycle. Thus, the advancement of additional biologically amenable spectroscopic techniques, particularly those capable of probing a variety of changes in electronic structure without preference for oxidation or spin state, is highly desirable. Herein, a combined X-ray spectroscopic study is described, utilizing both V K-edge XAS and Kβ X-ray emission spectroscopies (XES). Calibration to density functional theory (DFT) calculations provides an insightful, element-specifc probe of vanadium geometric and electronic structure, using experimental methods well-adapted to the study of biological molecules.

In K-edge XAS, a 1s electron is excited into either bound states or to the continuum. In the former case, transitions into singly or unoccupied 3d orbitals give rise to the pre-edge region, which can provide insight into the energies of the 3d manifold. Additionally, the intensities of these 1s→3d transitions, while formally quadrupolar, are largely governed by metal p-d mixing, and thus the dipole selection rule.[90,203] Changes in metal-ligand bond covalency[221] and geometric distortion from centrosymmetry both serve to modulate the intensity of the pre-edge transitions through perturbations in p-d mixing.[204] Time-dependent DFT (TD-DFT) calculations have been shown capable of correctly predicting relative energies and intensities of these pre-edge features, and through careful analysis and comparison to experiment, additional insight into geometric and electronic structure can be obtained.[90,115,198] Even with the aid of theoretical insight however, probing the electronic structure of ligand-based orbitals is a challenge for XAS, and in this area, XES holds significant promise.

Following the 1s ionization described above, in a one-electron picture, Kβ emission is the fluorescent decay of an electron from the $n = 3$ shell into a 1s core hole. In the case of first-row transition metals, for which these are the valence levels, the different regions in the Kβ spectrum provide complementary chemical insight. The Kβ mainline feature arises from metal 3p→1s transitions, and is sensitive to the oxidation state and local spin at the absorber atom.[92,103,193] This dipole-allowed transition is intense, and is readily observable in low concentrations of metal atom emitter. This feature has seen extensive prior use as a marker for oxidation and spin state, as the number of unpaired 3d electrons modulates the 3p-3d exchange coupling, and thus the multiplet-derived energetic splitting of the Kβ mainline peaks. However, care must be taken in the interpretation of this splitting, as Pollock *et al.* have recently shown that the spectral features can be significantly modulated by metal-ligand covalency.[92,104,191]

To higher energy, the weaker Valence-to-Core (VtC) region of the Kβ XES spectrum probes the valence shell, and corresponds to transitions from molecular orbitals (MOs) which are typically dominated by ligand character. Accordingly, the VtC region has been shown to have a high degree of sensitivity to the identity, nature, and electronic structure of the first coordination sphere of ligands.[104–106,116,127,137,194,222–224] As expected from a simple MO picture, the highest-energy K$\beta_{2,5}$

peaks are found to originate from ligand p-type orbitals, while the lower-energy Kβ'' features are ligand s-type in nature. It is important to note that the "donor" orbitals in these VtC transitions are in fact MOs, rather than atomic orbitals, and thus the transition energies reflect the energetic ordering found in an MO diagram.[105,225] Similar to XAS transitions, the intensities of the VtC transition are almost purely electric dipole transitions, and are dependent on the degree of metal p character mixed into the ligand MO.[105] Generally, those MOs which are more diffuse have more metal p character and intense spectral features, while more contracted MOs (typically the Kβ'') have weaker transitions. This dependence on metal p mixing also makes the VtC features highly sensitive to changes in metal-ligand bond lengths.

The sensitivity of VtC XES to changes in ligand electronic structure is in stark contrast to the insight obtained from EXAFS. In the latter method, subtle perturbations to a given scatterer, such as substrate bond activation or protonation at a basic ligand site, must be inferred solely from changes in bond length. In addition, for scatterers with similar Z, resolving their identities or individual bond lengths can be challenging. However, VtC XES has demonstrably detected evidence of substrate activation, *e.g.* the cleavage of an N_2 bond[107] and changes in NO speciation[226] in homogeneous and heterogeneous iron systems, respectively. Additionally, VtC XES has previously been used in concert with XAS to study the activation of manganese peroxo and oxo adducts, in part in Chapter 3, and these methods were shown to be capable of detecting both O-O bond activation[29] and the protonation of bridging oxo ligands.[53,54]

The present study couples standard vanadium K-edge XAS methods with TD-DFT calculations, and also explores the highly complementary chemical insight that can be derived from Kβ XES and ground-state DFT calculations. A series of molecular and extended lattice compounds were studied (Table 6.1), and correlations have been made between XAS and XES spectral features, as well as experimental and calculated parameters. As combined XAS and XES studies have previously been utilized to understand simultaneous changes in both metal and ligand electronic structure in the case of iron[226,227] and manganese,[29,53,54] this study paves the way for similar investigations involving vanadium. It is conceivable to envision this XAS / XES approach as an ideal tool for the mechanistic investigation of vanadium-catalyzed reactions in both chemistry and biology, including

Table 6.1: Vanadium compounds examined in this study, and relevant properties thereof

Compound	Oxidation State	d count	Coordination	Nominal Symmetry	Ligand Type(s)	Bond Length[a] (Å)
Na_3VO_4	V	0	Lattice (4)	T_d	V-O	1.71 (1.69-1.73)
$NaVO_3$	V	0	Lattice (4)	T_d	V-O	1.72 (1.64-1.81)
V_2O_5	V	0	Lattice (6)	O_h	V-O	1.96 (1.59-2.79)
V_2O_4	IV	1	Lattice (6)	O_h	V-O	1.93 (1.76-2.05)
$VO(acac)_2$	IV	1	5	C_{4v}	V-O, V=O	1.59, 1.99
VCp_2Cl_2	IV	1	4	dist. T_d	V-Cp[b], V-Cl	2.31, 2.41
V_2O_3	III	2	Lattice (6)	O_h	V-O	2.01 (1.96-2.07)
$VCl_3{\cdot}3\,THF$	III	2	6	O_h	V-O, V-Cl	2.32, 2.08
$V(acac)_3$	III	2	6	O_h	V-O	1.98
VCl_3	III	2	Lattice (6)	O_h	V-Cl	2.42
VCl_2	II	3	Lattice (6)	O_h	V-Cl	2.53

---

[a] Entries are given as mean (range)

[b] Cp = η^5-cyclopentadienyl

the synthesis of halogenated biomolecules and the role of vanadium in the reduction of dinitrogen, promoted by vanadium nitrogenase.

6.2 Experimental

All compounds are commercially available, and were obtained from Aldrich except Na_3VO_4, which was purchased from Spectrum. They were used without further purification, and when necessary samples were prepared, transported, and stored in an inert N_2 atmosphere. Samples of all compounds were prepared by grinding the solid material into a fine powder in a mortar and pestle, which was then pressed into an aluminum spacer and sealed with 38 μm Kapton tape. To minimize self-absorption during XAS measurements, samples were diluted approximately 9:1 by mass with boron nitride.

6.2.1 Data Collection

6.2.1.1 XAS

Vanadium K-edge XAS measurements were performed at the XAFS2 beamline at the Laboratório Nacional de Luz Síncrotron (LNLS) in Brazil, with a ring energy of 1.37 GeV and a current of 250 mA. Incident energy was selected using a Si(111) double-crystal monochromater, focused using a

Rh-coated cylindrical mirror, and shuttered to a beamspot of 0.4 x 0.4 mm^2. Photon flux at the sample was approximately 10^{10} photons / sec. Samples were held below 80 K during measurements in a closed-cycle LHe cryostat. Spectra were collected in both transmission and fluorescence modes, with the former using a He/N_2-filled ion chambers and the latter utilizing an energy-resolving 15-element Ge detector (Canberra, Inc.). The fluorescence signal was obtained by integrating counts within a 170 eV window, centered at the V Kα emission line (approximately 4.9 keV). Rapid scans over the XANES region were performed to screen for radiation damage, and data were collected and averaged from multiple sample spots so as to maintain a radiation dose per spot well below any observed damage threshold.

6.2.1.2 XES

Vanadium Kβ XES measurements were performed at beamline C-1 at the Cornell High Energy Synchrotron Source, with a ring current of 110 mA and ring energy of 5.3 GeV, operating in 90 minute decay mode. The incident energy was set to approximately 9 keV using a pair of W/B_4C multilayers for a 1% bandwidth. The beam spot size on the sample was 2.0 x 1.0 mm^2, with an approximate flux of 2.6 x 10^{12} photons / sec on the sample, and during measurements, samples were maintained at approximately 40 K using a closed-cycle He cryostat. V Kβ fluorescence was analyzed and collected using an array of three spherically bent Ge(422) crystal analyzers and a detector configured in a Rowland geometry (Figure 2.7). Data were initially collected using a Vortex Si drift detector (SDD), however data analysis indicated that during measurements, the angular scanning motion of the crystal array caused a systematic shift in the focal points of the outer analyzer crystals, which resulted in artificially suppressed spectral intensity in the higher energy region. To correct for this clipping of intensity, a second set of experiments were performed using a spatially resolved Si pixel detector (Pilatus) in place of the SDD. This allowed for the visual monitoring of the transverse focal point of each crystal in the array, and optimization of the optical alignment throughout the entire range of spectrometer angles. Additionally, a digital region of interest (ROI) was chosen to tightly enclose the focal point, maximizing the signal to noise ratio (S/N). Finally, a larger, concentric ROI was chosen of four times the area, to collect and subsequently correct for background radiation.

6.2.2 Data Analysis

6.2.2.1 XAS

For each compound, between four and 11 transmission spectra were averaged to improve S/N. The pre-edge and post-edge background subtraction was performed using a second-order polynomial function, and the edge jump was normalized to unity. Experimental edge energies were obtained from plots of the second spectral moments. The pre-edge features were modeled with pseudo-Voigt peaks (2.21) and fit with a least-squares regression, using BlueprintXAS,[228] and pre-edge energies were determined from the intensity-weighted average energies (IWAEs) of the pre-edge peaks.[54,90] Individual contributions of the Gaussian and Lorentzian functions to the pseudo-Voigt peaks did not exceed 80%. The FWHM of all peaks were between 0.55 and 1 eV to represent the observed intrinsic transition linewidths. The integrated areas of the pre-edge peaks (Figure C.2 to Figure C.5) were summed to obtain the experimental pre-edge intensities reported in Table 6.2. An estimated error of 5% is associated with the reported intensities due to pre- and post-edge background subtraction, normalization, and fitting.[90,198]

6.2.2.2 XES

Multiple scans of X-ray emission data were merged using PyMCA.[195] MATLAB was used for subsequent processing. The data were calibrated to the K$\beta_{1,3}$, Kβ'', and K$\beta_{2,5}$ energies of V_2O_5 reported by Jones and Urch (5426.3, 5448.1, and 5462.9 eV, respectively).[229] The background was removed using the concentric ROI data, and the spectra were normalized to an integrated area of 1000. The experimental energies of the mainline and VtC features were determined from the first spectral moment. Each spectrum was then modeled using a sum of pseudo-Voigt profiles and least-squares fitting was performed to optimize the peak positions, intensities, FWHM, and percent composition of Gaussian and Lorentzian functions for each component profile. The peaks fitting the lower-energy mainline region were subtracted to obtain a background-subtracted VtC spectrum. The integrated areas of the peaks in the VtC region were summed to obtain the experimental VtC intensities in Table 6.3. An estimated error of 10% is associated with the reported intensities due to subtraction of the tailing Kβ mainline, normalization, and fitting procedures.[116,127]

6.2.3 Calculations

DFT and TD-DFT calculations were performed with the ORCA program package, v.3.0.3.[117] Protocols similar to those that have been previously established for the calculation of pre-edge XAS[90,115] and VtC XES[116,127] spectra were utilized. The present work uses the def2-TZVP basis and def2-TZV/J auxiliary basis sets of Ahlrichs and coworkers.[230] Geometry optimizations, initiated from crystallographic coordinates available from the Cambridge Structural Database or the Inorganic Crystal Structure Database, as well as VtC XES calculations employed the BP86 functional,[124,125] and TD-DFT calculations of the XAS spectra used the B3LYP[124,231] functional and the Tamm-Dancoff approximation.[128,129] For all spectral calculations, a very large integration grid was used on vanadium (Grid7), and tight SCF convergence criteria were required. For compounds possessing an extended lattice morphology, rather than molecular structures, a quantum cluster was selected for the DFT and TD-DFT calculations, and was embedded in a point charge field with a boundary region, as has been previously reported.[232] Calculated XAS and XES spectra were obtained by a 1 and 2 eV Gaussian broadening of the calculated combined transition moments, respectively, including electric and magnetic dipole and electric quadrupole contributions. Calculated spectral intensities and energies were determined from the sum of all combined transition moments in the spectral region and from IWAEs respectively, as previously reported.[53,54,90,116] Example input files are provided in the Supplemental Information.

6.3 Results and Discussion

This study aims to elucidate the complementary nature of the XAS and XES spectra herein, and to improve understanding of which methods and spectral regions offer what chemical insight. Additionally, correlations between fundamental chemical properties observed from both XAS and

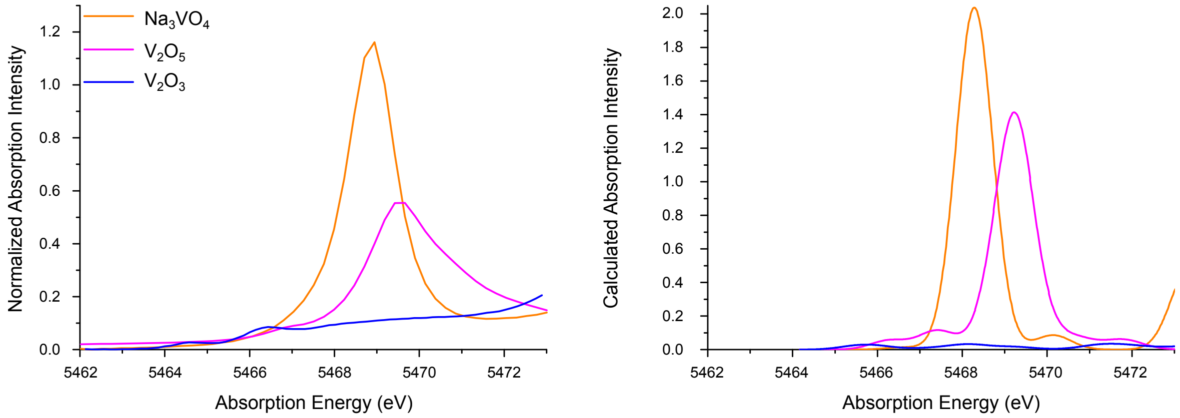

Figure 6.1: Experimental (left) and calculated (right) pre-edge regions of the XAS spectra of Na_3VO_4, V_2O_5, and V_2O_3. Calculated pre-edge spectra are blueshifted by 115.1 eV

XES, as well as between experiment and theory, maximize the available information, and enhance the applicability of this work to future studies involving more complex chemical systems. To achieve these goals, two subsets of data have been chosen and discussed in detail below.

6.3.1 XAS spectra

The pre-edge features in the XAS spectrum give the energies of the lower lying core-hole excited states. These correspond to 1s→3d excitations, and thus the pre-edge region can probe the energies and compositions of the unoccupied 3d orbitals. Figure 6.1 shows the pre-edge regions of the XAS spectra of Na_3VO_4, V_2O_5, and V_2O_3, and marked differences in pre-edge energy and intensity are clearly visible. As reported in Table 6.2, a clear shift to higher edge energies for more oxidized compounds is also found, indicative of a larger vanadium 1s binding energy (full pre-edge and edge spectra are shown in Appendix C).[220] There is also a substantial range of total pre-edge intensities, or integrated spectral areas, determined by least-squares fitting (*vide supra*). As the intensity of the pre-edge is dominantly governed by the dipole selection rule, increased intensity corresponds to increased transition dipole moments.[204,233] This can be understood in terms of increased mixing of vanadium p-orbital character into the 3d acceptor orbitals, and these data illustrate two key ways of modulating this p-d mixing.

Table 6.2: Comparison of experimental and calculated XAS parameters

Compound	Experimental[a] Edge energy (eV)	Experimental Pre-Edge Energy (eV)	Experimental Pre-Edge Intensity[c]	Calculated Pre-Edge[b] Energy (eV)	Calculated Pre-Edge[b] Intensity
Na_3VO_4	5481.8	5469.1	261	5469.3	262
$NaVO_3$	5482.0	5469.3	301	5469.6	300
V_2O_5	5480.5	5470.0	198	5470.1	227
V_2O_4	5477.1	5468.7	102	5470.0	41
$VO(acac)_2$	5480.8	5468.4	149	5468.7	198
VCp_2Cl_2	5475.7	5468.4	28	5467.5	4.0
V_2O_3	5475.0	5469.1	73	5469.8	18
$VCl_3{\cdot}3\,THF$	5475.5	5467.4	26	5467.1	3.8
$V(acac)_3$	5479.3	5467.5	20	5467.3	7.2
VCl_3	5473.7	5467.5	31	5466.4	0.8
VCl_2	5471.2	5466.2	16	5466.0	1.3

---

[a] Full edge regions are shown in Appendix C

[b] Calculated IWAEs have been shifted by 115.1 eV and intensities are scaled by a factor of 9.7 from calibrations in Figure 6.7

[c] Total intensities have been multiplied by 100

In addition to changes in electronic structure, oxidation perturbs the structure of the oxide lattice. The vanadium ions occupy octahedral holes in the lattice, and upon oxidation the V-O bonds contract due to an increased Coulombic attraction. The shorter bonds promote p-d mixing, and thus a larger pre-edge intensity is observed for V_2O_5 relative to V_2O_3.[221,234] In contrast, V_2O_5 and Na_3VO_4 are both in the vanadium(V) oxidation state. While they have similar edge energies (Table 6.2), the pre-edge intensity of Na_3VO_4 is substantially increased. The sodium cations intercalated in the Na_3VO_4 lattice cause the vanadium ions to occupy tetrahedral sites, reducing the centrosymmetry at the vanadium center. The resultant increase in p-d mixing, here a function of geometry, increases the transition dipole moment and thus the pre-edge area.

The two molecular acetylacetonate (acac) complexes also present an interesting case study, as their related structures give rise to vastly different pre-edge spectra (Figure 6.2). $V(acac)_3$ is an octahedral complex ligated exclusively by carboxylate oxygens, and the small pre-edge intensity is typical of highly centrosymmetric metal centers. Without a mechanism for p-d mixing, the transition dipole moment is essentially zero. Accordingly, the calculated pre-edge transitions for the $V(acac)_3$ spectrum shown in Figure 6.2 are largely quadrupolar in origin (*vide infra*). However, the $VO(acac)_2$ pre-edge has considerable dipolar intensity, which reflects subtantial p-d mixing.

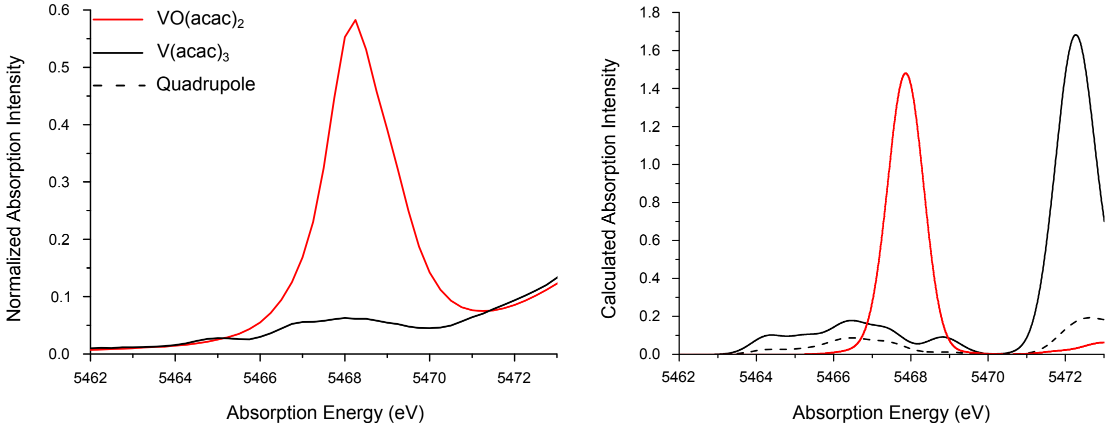

Figure 6.2: Experimental (left) and calculated (right) pre-edge regions of the XAS spectra of $VO(acac)_2$ and $V(acac)_3$. Calculated pre-edge spectra are blueshifted by 115.1 eV, the calculated $V(acac)_3$ spectrum has been scaled up by a factor of 10 for clarity, and the quadrupole contribution to the pre-edge of $V(acac)_3$ is shown as the dashed trace

Lacking a trigonal or tetrahedral ligand field, in this case the terminal oxo ligand induces p-d mixing due to the highly covalent bond it forms with vanadium, as well as a reduction in symmetry to C_{4v}.[221,234] Of particular note is the inequivalence of the oxygen ligands' influence on both the pre-edge spectrum and the underlying electronic structure; in short, there are two different "types" of oxygen ligands (the conjugated $acac^-$ and the vanadyl O^{2-}). Distinctions of this sort can, for example, be lost solely from interpretation of the EXAFS region, where only the ligand distance and approximate identity can be deduced. The pre-edge region clearly holds additional insight with regard to bonding and electronic structure, which can be understood using fundamental principles of coordination chemistry.

These data demonstrate the large range of pre-edge intensities possible for vanadium sites with similar oxidation states and coordination geometries. For example, the range of pre-edge intensities of octahedral vanadium ions spans over a factor of 20 from V(III) to V(V) ions (Table 6.2). Additionally, $V(acac)_3$ and V_2O_3 are both octahedral V(III) ions ligated exclusively by oxygen atoms, yet the pre-edge intensity of the latter is over three times greater. Changes in bond length, coordination geometry, and covalency are thus all found to have a profound influence on the area of the pre-edge features. As all of these factors can effectively modulate the extent of p-d mixing, it is impossible to isolate changes in pre-edge area to a given coordination number, metal geometry, or bond length. While relative changes within a series of structurally similar vanadium sites can be qualitatively insightful, more quantitative understanding relies on computational insight (*vide infra*).

Finally, it is of some interest to compare the pre-edges of the V XAS spectra to those of other transition metals commonly found in biology. As an early first-row element, vanadium d-electron counts are generally lower for biologically-relevant oxidation states, compared to iron or manganese.[214] Thus, an increased number of transitions into unoccupied 3d orbitals promotes pre-edge intensity. V_2O_5 has a pre-edge intensity of 198 units (Table 6.2), while *e.g.* the high-spin Fe(III) complex $[Fe_2O(OAc)_2\{[OP(OEt)_2]_3Co(C_2H_5)\}_2]$ has a pre-edge intensity of 13.9 units; an intensity difference of roughly a factor of 14.[204] Importantly, both metal sites are exclusively ligated by oxgenic ligands in an octahedral geometry, with relatively similar bond lengths (Fe-O average (range): 2.01 Å (1.79-2.14),[235] V-O: 1.96 Å (1.59-2.79) (Table 6.1)) As discussed above however, there are many factors that govern pre-edge intensity. Reducing the number of possible transitions as one moves across the periodic table is but one of these considerations.

In the octahdral limit, addition of electrons to the vanadium 3d manifold generally results in population of t_{2g} orbitals, rather than the antibonding e_g as in later first-row metals. This has a less significant impact on metal-ligand bond lengths; an important component of pre-edge intensity (*vide supra*). Additionally, while reduction from a d^9 Cu(II) center to d^{10} Cu(I) occupies all the 3d orbitals, quenching pre-edge intensity, the low d-electron counts of vanadium ions provide a means for pre-edge intensity even in lower oxidation states. Again in the octahedral limit, reduction from V(IV) to V(III) quenches only one of the nine 1s→3d excitations, or roughly 11%. As a cautionary note however, this picture breaks down in lower-symmetry systems, where the particular d-orbital that is occupied (or vacated) in an oxidation state change can significantly alter the expected impact on the pre-edge intensity. Population of a 3d orbital with miminal p-d mixing should have a negligible impact on pre-edge intensity, while in contrast occupation of a 3d orbital with substantial p-d mixing should significantly decrease the pre-edge intensity. This distinction further emphasizes the need for careful interpretation of pre-edge intensities aided by computational methods, rather than reliance on simple, qualitative trends.

6.3.2 XES spectra

As discussed above, the Kβ XES spectrum arises from $n = 3 \rightarrow$1s fluorescence. The intense, dipole-allowed Kβ mainline is due to electronic relaxation from the 3p shell, giving a $1\,\mathrm{s}^2 3\mathrm{p}^5 3\mathrm{d}^\mathrm{n}$ final state. However, the transition energy of the Kβ mainline is not solely dependent on the 1s and 3p binding energies; instead, multiple additional factors impact the observed spectral features. Most significantly, the unpaired 3p electron can exchange couple to unpaired 3d electrons, giving rise to a series of psuedo-atomic multiplets of discrete energies. Charge-transfer states and 3p spin-orbit coupling (SOC) can additionally contribute to the features of the Kβ mainline region.[92,102,236,237]

For first-row transition metals with high multiplicities, *e.g.* high-spin Fe(III) and Mn(II), the energetic splitting (ΔE_main) of the Kβ mainline features, the K$\beta_{1,3}$ and Kβ', can be as large as 15 eV, due primarily to 3p-3d exchange coupling.[29,92,102] Furthermore, it has recently been shown that the magnitude of ΔE_main can be significantly influenced by metal-ligand covalency, within a series of high-spin ferric complexes.[92] Increased covalency delocalizes the 3d spin density via the Nephelauxetic effect, which in turn decreases 3p-3d exchange and the mainline splitting.[191] For lower multiplicity metal ions such as those in the present work, 3p-3d exchange is significantly diminished.

Figure 6.3 shows the Kβ mainline regions of several complexes in this study. As highlighted by the vertical dashed line, a decrease in vanadium oxidation state is found to result in K$\beta_{1,3}$ transitions shifted to higher energies. However, reduction of the vanadium ion concomitantly increases the 3d electron count, and thus the magnitude of the 3d-3d exchange coupling. Therefore, the observed shift in energy cannot conclusively be attributed to changing oxidation state. In fact, the K$\beta_{1,3}$ energy of vanadium metal is 5427.3 eV;[88] within the range of the V(III)-V(V) complexes reported herein (Table 6.3).

Using a rough approximation of exchange energy corresponding to 3 eV per unpaired electron,[29,92] a coupling of around 3 and 6 eV is expected for the V(IV) and V(III) complexes, respectively. The horizontal markers in Figure 6.3 show that subtle but distinct features corresponding to

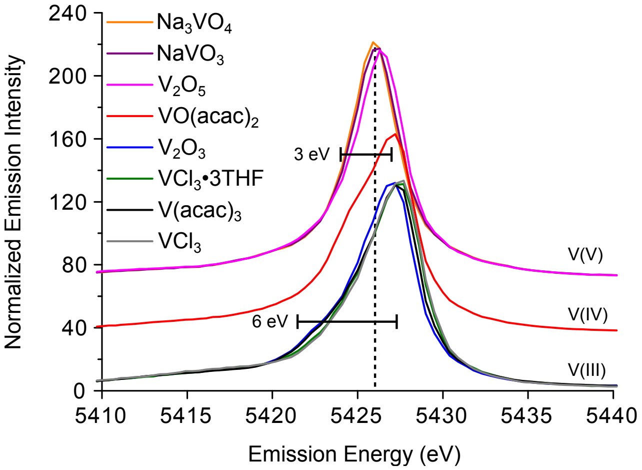

Figure 6.3: Mainline regions of the Kβ XES spectra. The dashed vertical line is a visual guide for the shift in peak maxima to higher energy upon reduction. The horizontal markers show the expected magnitude of 3p-3d exchange, corresponding to 3 eV per unpaired electron, and the right edges are aligned with the average K$\beta_{1,3}$ maximum for the V(IV) and V(III) oxidation states

roughly the correct exchange stabilization energies are present in the spectra. Interestingly, taking the average energy of the 3p-3d exchange-split states (the center of the horizontal markers) to reflect the relative 3p energies in the absence of exchange coupling, a trend of higher transition energies for more *oxidized* vanadium ions is observed. This is consistent with a larger Z_{eff} for the more oxidized ions, as has been previously observed in a series of vanadium L-edge (2p) XAS spectra.[220]

It is of some note that despite the absence of exchange coupling in the $3d^0$ V(V) compounds in this study, differences among them, in both spectral shape and energy, are still observed. As mentioned above, these could be attributed to either charge-transfer states or to 3p SOC.[102,103] In the latter case, the stabilizing effect is roughly an order of magnitude smaller than the 2p SOC, which can be determined from the vanadium Kα emission line (2p→1s, 7.6 eV[88]). Therefore, 3p SOC is conservatively placed at less than 1 eV. Orbital angular momentum is quenched upon orbital delocalization, and as evidenced by the experimental pre-edge (Table 6.2) and VtC intensities (Table 6.3), Na_3VO_4 and $NaVO_3$ have greater 3p and 4p mixing into both the vanadium 3d and the ligand valence orbitals compared to V_2O_5. Additionally, compared to previous studies at later first-row metals such as iron,[116] where both the metal 3p and 4p orbitals contribute to VtC

Table 6.3: Comparison of experimental and calculated XES parameters

Compound	Experimental Mainline energy (eV)	Experimental VtC Energy (eV)	Experimental VtC Intensity (x10^{-1})	Calculated VtC Energy (eV)[a]	Calculated VtC Intensity
Na_3VO_4	5426.1	5447.8, 5464.4	69.4	5448.3, 5462.6	69.5
$NaVO_3$	5426.1	5447.3, 5463.8	71.1	5448.3, 5462.6	69.5
V_2O_5	5426.3	5448.1, 5462.9	58.5	5448.7, 5462.1	68.1
$VO(acac)_2$	5427.0	5446.8, 5458.0	51.8	5448.3, 5461.7	56.6
V_2O_3	5427.0	5441.5, 5458.5	45.7	5449.3, 5463.1	47.3
$VCl_3 \cdot 3\,THF$	5427.4	5445.7, 5462.6	38.8	5451.4, 5462.0	38.9
$V(acac)_3$	5427.3	5446.0, 5456.8	47.2	5443.9, 5457.7	48.4
VCl_3	5427.4	5450.0, 5462.0	35.1	5451.1, 5462.0	36.0

---

[a] Calculated IWAEs have been shifted 141.9 eV from the calibration in Figure 6.6

intensity via mixing with the ligand orbitals, the 3p orbitals of vanadium should play an increased role. Therefore, the less localized 3p character of Na_3VO_4 and $NaVO_3$ results in decreased orbital angular momentum and a smaller SOC contribution. A loss of spin-orbit stabilization should lower the energy of the mainline transitions, consistent with the spectra shown in Figure 6.3.

To higher energy of the mainline, the VtC region can provide detailed insight into the occupied ligand valence orbitals, often from a simple molecular obital picture.[106] As discussed previously, VtC peaks can be understood as a valence to metal 1s transition, and thus the transition energies provide a direct probe of the relative binding energies of the valence orbitals.[194] Similar to the pre-edge region of the XAS spectrum, the intensity mechanism in the VtC region is almost exclusively electric dipole, and therefore the amount of metal p character mixed into the donor ligand orbital has been found to strongly correlate with VtC intensity.[105,116,127]

The Kβ VtC XES spectra of V_2O_3, V_2O_5, and Na_3VO_4 are shown in Figure 6.4. The highest-energy K$\beta_{2,5}$ features, which are due to ligand p-type orbitals,[106] must arise from oxygen 2p orbitals. The sharp peak in the Na_3VO_4 spectrum indicates more homogeneous transition energies than in the case of V_2O_5. Additionally, the spectral features of V_2O_5 are shifted to slightly lower energies. Perturbations to the oxide 2p energies are expected to occur upon changes in bonding, in particular due to bond lengths. Decreased Coulombic attraction of the oxide 2p electrons to the V^{5+} ion in V_2O_5, due to a longer bond length, should destabilize the oxygen 2p orbitals, resulting in transitions

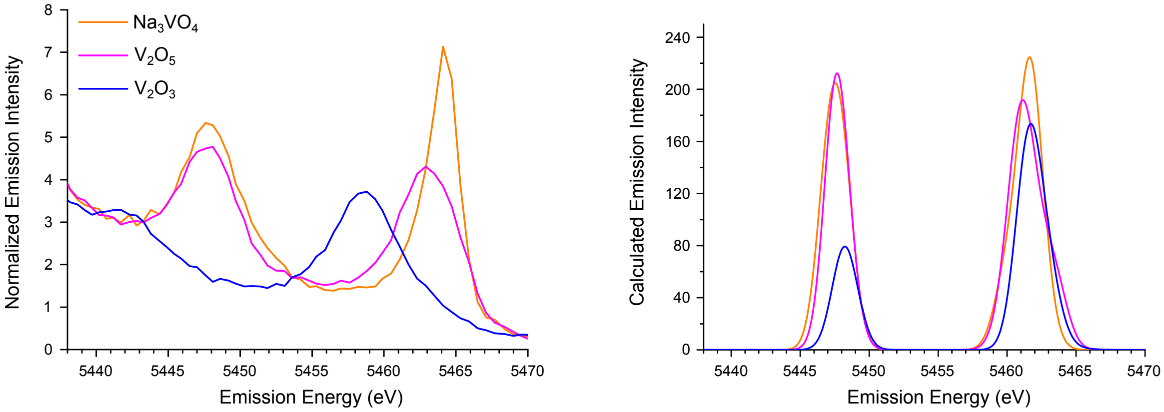

Figure 6.4: Experimental (left) and calculated (right) VtC regions of the Kβ XES spectra of Na_3VO_4, V_2O_5, and V_2O_3. Calculated VtC spectra are blueshifted by 141.9 eV

shifted to lower energy. Thus, the longer average V-O bonds in V_2O_5, by 0.37 Å (Table 6.1), cause the VtC transitions to shift to lower energies. Furthermore, the deviation in V-O bond length in V_2O_5 (1.2 Å) is significantly larger than that of Na_3VO_4 (0.04 Å). This heterogeneity in bond lengths results in a larger distrubtion of transition energies, which is manifest in the broader shape of the K$\beta_{2,5}$ peak.

Compared to V_2O_5 and Na_3VO_4, the Kβ'', which is due to O 2s orbitals, and K$\beta_{2,5}$ peaks of the vanadium(III) oxide V_2O_3 are shifted to substantially lower energy, by approximately 6 eV. As discussed above, the longer average bond length (by 0.05 Å) constitutes a good rationale this observation. Additionally, a two-electron reduction lowers the vanadium effective nuclear charge (Z_{eff}) experienced by the oxygenic ligands. This further serves to raise the orbital energies, and thus decrease the transition energy. This is consistent with previous studies that found a one-electron reduction of iron would shift the VtC peaks of structurally analogous complexes to lower energy by approximately 1.2 eV.[116] However, in the case of manganese, a similar reduction resulted in peak energies that were shifted to *higher* energy by about 0.2 eV.[127]

There are additionally clear trends observed in the intensities of the VtC features. While the K$\beta_{2,5}$ peak height of Na_3VO_4 is substantially larger than V_2O_5, the increased width of the latter feature results in comparable integrated intensities between the two (Table 6.3). The tetrahedral geometry of Na_3VO_4 results in shorter V-O bonds however, which should increase VtC intensity.[106,116] While the individual O→V 1s transition moments are larger for Na_3VO_4, the presence of two additional ligands (and the accompanying transitions) in V_2O_5 seemingly offsets the shorter bond lengths. The Kβ'' feature shows a definite sensitivity to V-O bond length however, as the peak intensity in the V_2O_5 spectrum is lower despite the two additional ligands, and the Kβ'' of V_2O_3 is much weaker. Given the contracted nature of the oxygen 2s atomic orbitals, changes in bond length seemingly have a larger impact on metal p mixing into the 2s, compared to the more diffuse 2p.

Whereas EXAFS is sensitive to the average radial distributions of scatters with similar Z, VtC XES can differentially probe specific metal-ligand bonds, even with the same ligating atom. Comparison of the VtC XES spectra of VO(acac)$_2$ and V(acac)$_3$ in Figure 6.5 reveals higher energy K$\beta_{2,5}$ regions of similar intensity, whereas the Kβ'' peak at about 5447 eV in the spectrum of VO(acac)$_2$ is clearly absent in the V(acac)$_3$ spectrum. Unlike the XAS pre-edge region, low centrosymmetry is not required for VtC intensity, because in an octahedral geometry, ligand orbitals which interact with the metal in a σ fashion can mix with the metal p.[105] The acac$^-$ valence orbitals, which are a combination of oxygen and carbon 2p orbitals, therefore give rise to K$\beta_{2,5}$ regions of comparable intensity in both spectra.

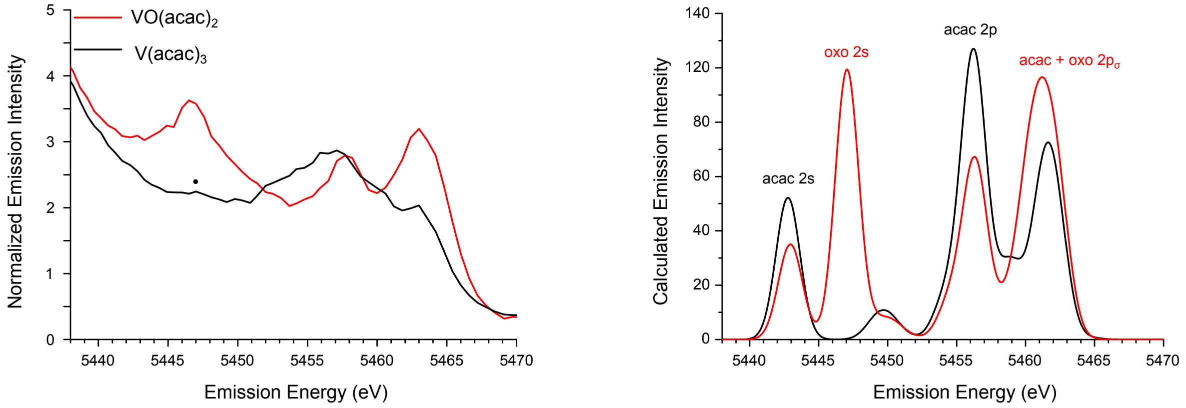

Figure 6.5: Experimental (left) and calculated (right) VtC regions of the Kβ XES spectra of VO(acac)$_2$ and V(acac)$_3$. The · denotes the Kβ'' feature of V(acac)$_3$ determined from the first spectral moment. Calculated VtC spectra are shifted by 141.9 eV, and the major orbital contributions to the calculated transitions are assigned

The Kβ'' peak is due to ligand orbitals that are dominantly s-type, thus this feature should correspond to an O 2s atomic orbital. Close examination reveals that the V(acac)$_3$ spectrum also has a Kβ'' feature at similar energy. As both metals are ligated entirely by oxygen atoms, VtC transitions from O 2s orbitals are in fact expected in both spectra. The vastly increased intensity in the case of the VO(acac)$_2$ is due to the markedly different bonding of the vanadyl oxo compared to the acac ligand. The short, covalent oxo bond results in considerably more vanadium p mixing with the oxo 2s, and increased transition intensity. Similarly, the increased intensity of the highest-energy K$\beta_{2,5}$ feature in the VO(acac)$_2$ indicates stronger bonding with orbitals that are O 2p in character. Considering that ligand orbitals require a σ orientation to interact with metal p orbitals, this peak can likely be attributed to the vanadyl O $2\,\mathrm{p}_\sigma$ orbital.

6.3.3 Spectral Calculations

6.3.3.1 VtC XES

To obtain additional insight into the trends observed in these data, the VtC XES spectra were calculated using a well-established ground-state DFT method.[105,116,127,194] The calculated spectra corresponding to the examples discussed previously are shown in Figure 6.4 and Figure 6.5, and satisfactory reproduction of the experimental trends are found. Interestingly, the calculations fail to capture the shift to lower energy of the V_2O_3 features compared to V_2O_5. A similar shortcoming was found in a previous manganese study.[127] This suggests that there may be contributions to the observed oxidation state trends, *e.g.* core-hole relaxation effects, which are not captured within this computational model. Examination of the calculated V(acac)$_3$ and VO(acac)$_2$ spectra (Figure 6.5) reveals good agreement between calculated and experimental energies and intensities. Consistent with the interpretation of the experimental data, the large Kβ'' peak in the VO(acac)$_2$ spectrum arises from a transition from the vanadyl oxo 2s atomic orbital to the vanadium 1s. The short, covalent nature of this bond increases vanadium p mixing into the oxo 2s and thus the transition intensity.

As with previous work in the case of iron,[116] manganese,[127] and chromium,[223] the accuracy of

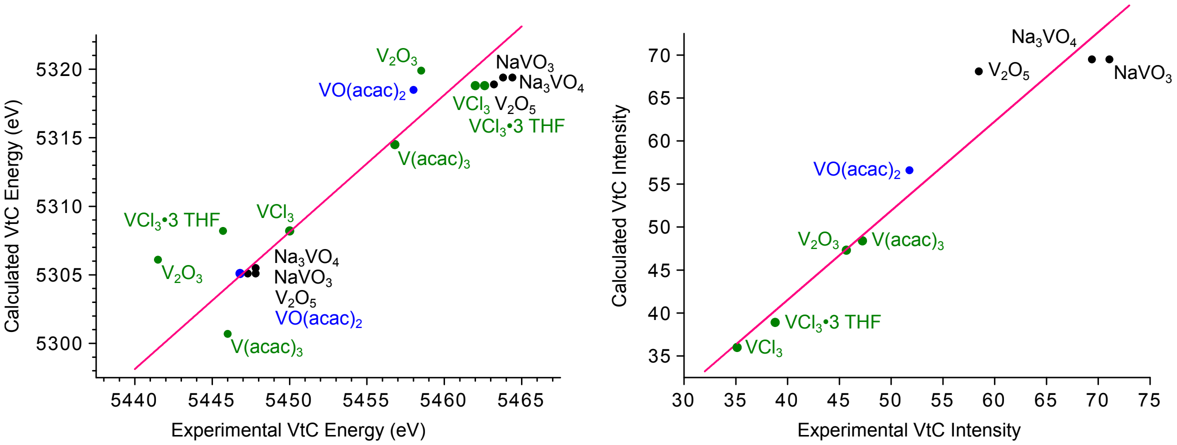

Figure 6.6: Correlations between experimental and calculated VtC energies (left) and intensities (right). Markers are color-coded by vanadium oxidation state, with green = V^{3+}, blue = V^{4+}, and black = V^{5+}. Equations for the linear fits: $E_{calc} = E_{exp} - 141.9$ ($R^2_{adj} = 0.84$), $I_{calc} = 1.04 \times I_{exp}$ ($R^2_{adj} = 0.99$)

the selected computational method can be evaluated by quantitative comparison of the experimental and calculated transition energies and intensities. The linear correlations shown in Figure 6.6 demonstrate in particular the high fidelity of the calculated transition intensities, derived from the calculated vanadium p-orbital character found in the donor ligand orbitals. The larger VtC intensity upon increasing oxidation state is rationalized by the generally shorter metal-ligand bonds, which promotes vanadium p-orbital mixing with filled ligand orbitals. Additionally, the intercept and slope of the energy and intensity correlations, respectively, provide correction factors used for this computational protocol (*vide supra*).

6.3.3.2 XAS pre-edges

The nature of the pre-edge transitions observed herein was also investigated using TD-DFT-calculated XAS spectra. As shown in Figure 6.1, experimental differences in intensity and energy between V_2O_3, V_2O_5, and Na_3VO_4 are well reproduced. The largest intensity of the Na_3VO_4 pre-edge, due to the tetrahedral geometry, is correctly calculated, as is the lower-energy pre-edge and diminished intensity of V_2O_3 given the lower oxidation state and longer bond lengths. Figure 6.2 shows the calculated pre-edge spectra of $V(acac)_3$ and $VO(acac)_2$, which are also in very good agreement with the experimental data. As discussed previously, the octahedral V(acac)$_3$ has minimal transition dipole intensity, as mechanisms for 4p mixing are effectively quenched, while the square pyramidal geometry and highly covalent vanadium-oxo bond provide ample 4p mixing. The 1s→3d pre-edge excitations can directly occur via the quadrupole transition operator however, though these are roughly two orders of magnitude less intense than a fully allowed electric dipole transition.[90,204] Examination of the calculated pre-edge spectrum reveals that roughly half of the spectral intensity derives from quadrupole transitions, and furthermore that the featured, albeit weak, experimental pre-edge is reproduced with high fidelity. Thus, even without a mechansim for p-d mixing and significant pre-edge intensity, meaningful insight can still be extracted from the pre-edge region using the TD-DFT method.

Similar to the XES calculations above, comparison of the experimental and calculated energies and intensities reveals good agreement (Figure 6.7), providing evidence for the success of the TD-DFT method. Thus, the insight obtained from the calculations above can be taken to respresent the experimental findings with reasonable confidence. In particular, the calculations illustrate that XAS pre-edge intensity should be interpreted with regard to metal p-d mixing, rather than utilizing geometry and oxidation state. For example, VCp$_2$Cl$_2$ and VO(acac)$_2$ both have V^{4+} ions. The former has a 4-coordinate, distorted tetrahedral geometry, while VO(acac)$_2$ is a 5-coordinate,

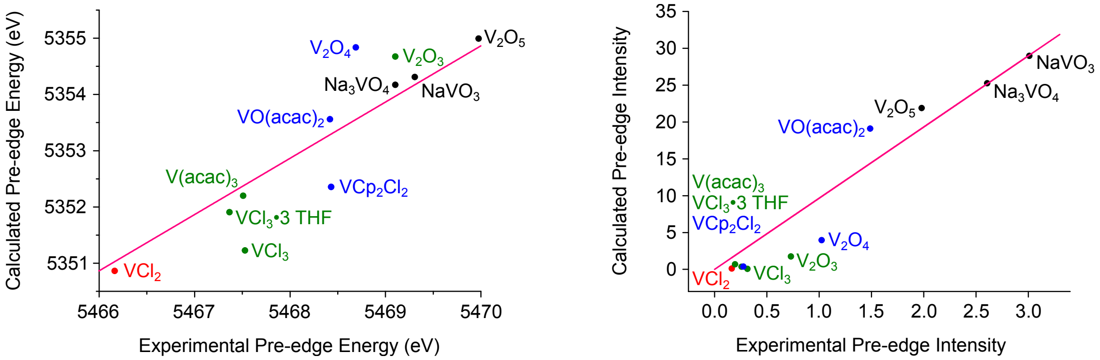

Figure 6.7: Correlations between experimental and calculated XAS pre-edge energies (left) and intensities (right). Markers are color-coded by vanadium oxidation state, with red = V^{2+}, green = V^{3+}, blue = V^{4+}, and black = V^{5+}. Equations for the linear fits: $E_{calc} = E_{exp} - 115.1$ ($R^2_{adj} = 0.80$), $I_{calc} = (9.7 \times 10^{-2}) I_{exp}$ ($R^2_{adj} = 0.95$)

distored square pyramid. A conventional interpretation would likely lead to the conclusion that VCp_2Cl_2, being lower coordinate and with less centrosymmetry, should have considerably higher pre-edge intensity. In fact, the opposite is observed in the experimental data, and the TD-DFT calculations are in excellent agreement. While elucidating the exact cause of this observation is challenging, the highly covalent nature of the vanadyl unit compared to the ligand bonds in VCp_2Cl_2 is a likely contributor.

6.4 Conclusions

This study illustrates the complementary nature of vanadium XAS and XES, and provides archetypal methods for interpretation of the spectroscopic data using both fundamental principles and theoretical calculations. The sensitivity of VtC XES to the nature of metal-ligand bonding, and not solely the identity of the ligand or its bond length, renders it a powerful tool for the study of fundamental principles of coordination chemistry. Differentiating molecular orbitals arising from two “types” of the same ligating atom, as demonstrated herein, is a significant advantage considering this method is easily applicable to metalloenzyme systems. The XAS data demonstrate multiple ways in which the extent of metal p-d mixing is modulated, including geometry, covalency, and oxidation state. Consideration of all factors, ideally with the aid of DFT calculations, is key for correctly interpreting spectral properties such as pre-edge intensity. A combined XAS and XES study allows interrogation of both occupied and virtual metal orbitals, as well as ligand-based MOs which XAS typically cannot probe. Such methods, broad in their applicability and robust in their interpretation, are powerful tools for the continued investigation of transition metal catalyzed reactions in complex, biological systems.

Appendix A

Notes on Electronic Structure Calculations and Analyzing Results

This appendix contains instructions for software setup, descriptions and examples of the input code for performing the quantum chemical calculations used in this dissertation, as well as procedures for analyzing and interpreting the results. All calculations have been performed using the ORCA quantum chemistry package developed by Frank Neese and coworkers at the Max-Planck-Institute for Chemical Energy Conversion. This appendix is by no means a substitute for the ORCA manual, which contains detailed explanations of all of this material, and is available *via* the world wide web at:

http://orcaforum.cec.mpg.de/downloads.php

At a minimum, an input file must contain the type of calculation desired (*e.g.* DFT, Hartree-Fock, Møller-Plesset, *etc.*), a set of basis functions (basis set) to use, and a geometric and electronic structure including nuclear coordinates, charge, and multiplicity. Many additional parameters can be specified, however every input must contain these elements. The "simple input" method is the most expedient way to specify most of these parameters, and is invoked by beginning the line of text with "`!`". The following input file requests a Hartree-Fock single-point calculation (energy determination) on the O_2 molecule, which has a triplet ground state.

```
! UHF SV
* xyz 0 3
O 0 0 0
O 0 0 1.2
*
```

Here, the `UHF` requests a spin-unrestricted (open-shell) Hartree-Fock calculation, and `SV` requests the Ahlrichs split valence basis set. The `* xyz 0 3` denotes the beginning of the geometry input, using nuclear coordinates to follow, a charge of 0 on the molecule, and a multiplicity of 3.

The general computational approach for this dissertation will be explained by way of sample inputs for the calculations. The calculation of various molecular properties for comparison to experiment is most often the goal. For large molecules, it is generally more convenient to give the nuclear coordinates in a separate file, in a `mygeometry.xyz` format, rather than to include them in every input file. Additional compuational parameters and specific protocols are often invoked using "blocks" in the input file. These are specified using the `%` symbol, and are usually terminated by `end`.

Geometry Optimizations

The first step in most computational procedures is to optimize the geometry of a given molecule. This involves iterative adjustment of nuclear coordinates followed by an energy evaluation to coarsely map a gradient of energy with respect to nuclear positions, and ideally arrive at the minimum energy configuration. It can be a time-consuming process, and it is desirable to begin as close to an equilibrium energy geometry as possible. When available, the crystallographic coordinates provide an ideal starting point for a geometry optimization.

```
! Opt UKS BP86 def2-TZVP def2-TZVP/J RI D3BJ ZORA COSMO PAL8
! TightOpt SlowConv TightConv Grid4 NoFinalGrid
! XYZFile NormalPrint

%scf
MaxIter 500
end

* xyzfile 1 6 my_geometry.xyz
```

This file will perform a geometry optimization on the molecule in **`mygeometry.xyz`** using parameters typical of the calculations in this work. The first simple input lines gives the desired options for performing the calculation:

`Opt` - Requests that a geometry optimization be performed

`UKS` - Use the unrestricted (open-shell) Kohn-Sham (DFT) method. For closed-shell molecules, `RKS` chooses restricted DFT

`BP86` - Use the BP86 density functional

`def2-TZVP` - Selects the Ahlrichs def2 triple-zeta valence basis set

`def2-TZVP/J` - Selects the associated def2-TZVP auxiliary basis set for Coulomb fitting

`RI` - Invokes the "resolution of the identity" approximation

`D3BJ` - Chooses the atom-pairwise dispersion correction with Becke-Johnson damping

`ZORA` - Use the zeroth-order regular approximation for scalar relativistic effects. Note that when given on the same line as the basis and auxiliary basis sets, this will choose the appropriate relativistically-recontracted versions of the specified basis sets

`COSMO` - Use the conductor-like screening model for solvation effects (if no solvent is given, an infinite dielectric is used)

`PAL8` - Run the calculation on 8 processors in parallel

The next line of simple input further modifies these options to improve the results of the calculation.

`TightOpt` - Invokes tight convergence criteria for the optimization

`SlowConv` - Tells the calculation to expect a slow convergence of the self-consistent field (SCF) procedure. This is often a wise choice for calculations involving transition metal ions

`TightConv` - Requires that the SCF converge to tight criteria

`Grid4` - Specifies the size of the numerical integration grid

`NoFinalGrid` - Turns off the default larger integration grid for the final energy evaluation

The final two options request specific outputs from the calculation

`XYZFile` - Asks the calculation to generate a .xyz file of nuclear coordinates

`NormalPrint` - Increases the default level of information in the output file. This keyword includes printing of the Löwdin population analysis per molecular orbital, often desirable during analysis

Following the simple input, the `%scf` block gives additional information of the handling of the SCF procedure. The keyword `MaxIter` increases the maximum number of SCF iterations to 500 from the default of 125. The geometry containined in `my_geometry.xyz` is read in, with a charge of +1 and multiplicity of 6 (for example, a high-spin Mn(II) complex).

Frequency (IR and Raman) Calculations

If the result of the geometry optimization is satisfactory, one may then proceed to the calculation of molecular properties and/or spectra. Probably the most straightforward calculation to request, though quite time consuming, is a vibrational calculation, which automatically generates the information required for an IR spectrum. Additionally, it is good practice to perform a frequency calculation following any geometry optimization; the absence of imaginary (negative) frequencies is indicative of a successful geometry optimization.

A frequency calculation can be performed by either analytical or numerical differentiation of the analytical gradient. The former option is memory-intensive and does not provide all of the capabilities of the latter (*e.g.* Raman intensities[1]), however it is considerably faster. Additionally, the analytical gradient is not currently available for the COSMO solvation model, so geometry optimizations and frequency calculations should be performed without COSMO. The analytical frequency calculation is requested with `! Freq` or `! AnFreq` and the numerical frequency with `! NumFreq`. Both can also be combined with a geometry optimization, and the frequencies will be calculated after the optimized geometry has been found. If the calculation of Raman intensities is also desired it is necessary to request the polarizability through the use of the `%elprop` block. The following calculation performs a geometry optimization, followed by a numerical frequency calculation with Raman intensities. Note that this is a very expensive calculation, and is often not required even if you are looking to compare your results to resonance Raman data. The energy of the vibrational modes can be obtained with a `AnFreq` calculation only.

```
! Opt NumFreq ...

%elprop
Polar 1
end

* xyzfile 1 6 my_optimized_geometry.xyz
```

Following a frequency calculation, one can obtain a spectrum through the use of the orca_mapspc

---

[1] Raman intensities are related to, but not the same as the intensities obtained from a *resonance* Raman calculation. While it is possible to calculate which modes should be resonantly enhanced by laser excitation of a particular energy, this is considerably more complex.

spectrum generator. To plot an IR spectrum following a frequency calculation with an output file called CHstretch.out from 500 to 3000 wavenumbers, with a transition FWHM of 20 wavenumbers and 5000 points in the spectrum, one calls

```
orca_mapspc CHstretch.out ir -x0500 -x13000 -w20 -n5000
```

The default energy unit is wavenumbers. Two ascii files will be generated. CHstretch.out.ir.dat will have 5 columns, in the order of energy, % transmittance, and x, y, and z polarization of the transition moment. The first two columns can be visualized using any plotting program and will provide the spectrum. The second file, CHstretch.out.ir.stk, contains the discrete transitions in energy, transition probability, and x, y, and z polarizations, and can be used to create a stick spectrum.

Identifying particular vibrational modes of interest, both in the calculation and in experiment, is most easily accomplished through the use of isotopic labeling. It is straightforward and efficient to insert an isotopic label into the calculation, because the *electronic* structure, and thus the hessian matrix, is independent of the masses of the individual atoms. The `.hess` file can therefore be edited (ideally one should make a copy of the `.hess` file first) to include the new isotope(s), in the section that begins `The atoms:  label mass x y z`. Then the `orca_vib` utility can be used to create a new output file containing the isotopically labeled spectrum, which is plotted in the same fashion as above.

```
orca_vib edited_hessian_file.hess > my_new_outputfile.out
```

Comparison of the two spectra should clearly identify the energy of the relevent vibrational modes. The energy of a particular mode can identify the mode *number* in the output file, and then the `orca_pltvib` utility can be used to generate an animation trajectory file of the vibration to confirm the assignment. More details can be found in the ORCA manual.

Kβ Valence-to-Core X-ray Emission Calculations

The calculation of Kβ VtC XES spectra requires more involved input, however the computational procedure is straightforward. As the physical process is spontaneous emission, there is no need for a time-dependent treatment. Therefore, standard ground-state methods suffice. Furthermore, the use of "pure" GGA density functionals such as BP86 is preferred as the interpretation of the donor molecular orbitals is far more straightforward (hybrid functionals have a tendency to create highly delocalized orbitals). The input for an XES calculation reads as follows.

```
! UKS BP86 def2-TZVP def2-TZVP/J DeContractAux RI D3BJ ZORA COSMO PAL8
! TightOpt SlowConv TightConv Grid4 NoFinalGrid
! XYZFile NormalPrint
! MORead

%moinp "input_orbitals.gbw"

%maxcore 4096

%basis
newGTO Fe "CP(PPP)" end
end

%method
SpecialGridAtoms 26
SpecialGridIntAcc 7
end

%xes
CoreOrb 0,0
OrbOp 0,1
end

* xyzfile 1 6 my_optimized_geometry.xyz
```

A new simple input keyword, `MORead`, has been used. This tells the program to begin the calculation using the orbitals from a previous calculation, specified by `%moinp`. As this calculation uses the geometry-optimized coordinates from a previous calculation, using the orbitals from the same calculation as a start point for the SCF usually accelerates convergence significantly. Additionally, the keyword `DeContractAux` has been added, which decontracts the core orbitals (modeled by an effective core potential) in the auxiliary basis set. This leads to more accurate calculations. A maximum memory allocation has also been given in MB. This is often a good idea on any calculation, but should be chosen so as not to exceed the memory capacity of the workstation.

The `%basis` block is used to specify a new basis set for all Fe atoms. The `newGTO` command (new Gaussian-type orbital) invokes the special CP(PPP) basis set, optimized for the calculation of core properties such as X-ray absorption, emission, Mössbauer, and EPR hyperfine couplings. Note the additional `end` at the conclusion of the line. In conjuction, the `%method` block is used to increase the radial integration grid size on Fe to Grid7 (in contrast to Grid4 for the remaining atoms). This is also important for the calculation of core properties.

Finally, the `%xes` block requests the calculation of XES transitions. The desired acceptor orbital in the transition, typically the metal 1s (usually orbital 0), is specified by `CoreOrb` twice, once for each spin manifold, where `OrbOp` selects operators 0 (α) and 1 (β). In the case of metal dimers, one can obtain the XES spectrum for both atoms

```
%xes
CoreOrb 0,0,1,1
OrbOp 0,1,0,1
end
```

or in the case of the multinuclear [Mo-3Fe-4S] cubane model, the Fe XES spectrum would be calculated starting from orbital 1, as the Mo 1s is to lower energy.

```
%xes
CoreOrb 1,1,2,2,3,3
OrbOp 0,1,0,1,0,1
end
```

Printing a spectrum is accomplished similarly to the IR spectrum above, this time asking for units of eV

```
orca_mapspc my_xes_calculation.out xes -eV -x06000 -x16500 -w2.5 -n5000
```

It should be noted that the *complete* XES spectrum will be calculated: Kα, Kβ mainline, and Kβ VtC transitions. Due to considerable spin-orbit coupling in the Kα transitions and the multireference character of the Kβ mainline, only the VtC region can be calculated with any fidelity using this method.

XES calculations as detailed above use the Kohn-Sham orbitals for these transitions, which is why it is only valid for the VtC. The transition energies are thus simply the difference in orbital energies, described as

$$E^{\sigma}_{IF} = \epsilon^{\sigma}_{j} - \epsilon^{\sigma}_{i} \tag{A.1}$$

where E^{σ}_{IF} is the transition energy between the core-hole state and the valence-hole state for spin-manifold σ (α or β) and ϵ is the Kohn-Sham orbital energy. The intensity of the VtC transitions is computed from the metal p orbital population in the donor Kohn-Sham orbital, and contributions from the electric and magnetic dipole and electric quadrupole transitions are included. In practice however, appreciable intensity is limited to electric dipole transitions.

Visualization of the VtC donor orbitals is typically an excellent way to obtain insight into the nature of the transitions. To create reasonably attractive figures in Chimera, create the KS orbital isosurfaces using the following procedure:

```
orca_plot my_xes_calculation.gbw -i
```

This will open the interactive orca_plot utility. Set the number of grid intervals to 80, and set the file format to Gaussian cube. Then select the appropriate MO number(s), create the .cube files, and open them and the .xyz file in Chimera.

Mössbauer Parameters

Similar to the calculation of nuclear hyperfine couplings, the electronic properties at an Fe nucleus can be used to obtain Mössbauer parameters for comparison to experiment. The two quantities of interest are the isomer shift, δ, and the quadrupole splitting, ΔE_Q. The isomer shift measures changes in the absorption energy of a γ photon relative to a standard. This transition energy is sensitive to changes in bonding due to indirect perturbation of s electron density as a result of the shielding of 3d electrons. The isomer shift cannot be calculated directly, however it is straightforward to calculate the electron density at the nucleus, ρ (rho). This property can be used to obtain the isomer shift by insertion into the equation

$$\delta = \alpha(\rho - C) + \beta \tag{A.2}$$

Values for α, β, and C for some common combinations of density functionals and basis sets have been obtained by calibration against experiment (M. Römelt, S. Ye, and F. Neese, *Inorg. Chem.* 2009, *48*, 784-785).[238] The calculation of ρ is highly dependent on computational method, so it is important to check your computational protocol carefully by calculating a test structure from this (or a similar) work.

The quadrupole splitting is a measure of the asymmetry of the electric field gradient at the nucleus. A γ photon at 14.4 keV induces a transition from the $I = \frac{1}{2}$ ground state of the ^{57}Fe nucleus to the $I = \frac{3}{2}$ nuclear excited state. The quadrupole moment of the nuclear excited state interacts with the electric field gradient to split the excited state and produce the classic Mössbauer quadrupole doublet. The magnitude of this splitting is proportional to the extent of asymmetry of the electric field gradient, is relatively straightforward to calculate, and can be read directly from an ORCA output file in mm/s.

To obtain an accurate description of the core electron density, it is highly advisable to employ the CP(PPP) core properties basis set and to increase the size of the integration grid at the Fe, similar to XES calculations. The calculation of nuclear properties, including Mössbauer, EPR hyperfine couplings, and NMR shifts, is performed using the %eprnmr block.

```
%eprnmr
nuclei = all Fe {fgrad, rho}
end
```

The `frgrad` and `rho` commands request the electric field gradient and electron density ρ, respectively. Alternatively, the `all Fe` request can be replaced with specific Fe atoms by atom number. It is important to note that the `%eprnmr` block must appear *after* the nuclear coordinates or the `*xyzfile` line.

K-edge X-ray Absorption Calculations with TD-DFT

The calculation of K-edge XAS spectra is accomplished by time-dependent DFT, owing to the time-dependent nature of the electric field perturbation which induces the transition. Note that the `#` sign in the input file indicates a comment; all content following it on a given line will be ignored.

```
! UKS B3LYP def2-TZVP def2-TZVP/J DeContractAux RIJCOSX D3BJ ZORA COSMO PAL8
! TightOpt SlowConv TightConv Grid4 GridX4 NoFinalGrid
! XYZFile NormalPrint
! MORead

%moinp "input_orbitals.gbw" # orbitals are read from previous calculation

%maxcore 4096 # maximum memory allotted per processor in MB

%basis
newGTO Fe "CP(PPP)" end  # specifies a new basis set on Fe
end

%method
SpecialGridAtoms 26  # invokes a special grid on Fe atoms
SpecialGridIntAcc 7  # specifies the special grid size as Grid7
end

%tddft
nRoots 50
MaxDim 500
OrbWin[0] 0,0,-1,-1
OrbWin[1] 0,0,-1,-1
DoQuad true
end

* xyzfile 1 6 my_optimized_geometry.xyz
```

The `%tddft` block controls the parameters for XAS transition calculations. `nRoots` sets the number of transitions to be calculated; this is dependent on the size of the molecule but will require more computational time for a greater number of roots. The `MaxDim` parameter sets the number of expansion vectors to be used for the solution of the CI equations. This should typically be a multiple of the number of roots given. The `OrbWin[0 or 1]` line specifies the transitions to be calculated for the given operator, where 0,0 selects orbital 0 as the transition donor and -1,-1 allows transitions into all unoccupied orbitals. Finally, `DoQuad true` requests the calculation of higher-order terms in the light-matter interaction expansion: the electric quadrupole and magnetic dipole transition moments.

Changes have occured in the first simple input line. The BP86 functional has been replaced with the hybrid B3LYP functional, as GGA functionals are typically not as accurate for TD-DFT. Additionally, the RI approximation has been changed to the RIJCOSX, or RI-chain-of-spheres approximation, which is the appropriate choice for hybrid functionals. As the COSX approximation is invoked, an additional grid parameter, GridX4, specifies the size of the chain-of-spheres grid.

An XAS spectrum can be obtained using

```
orca_mapspc my_xas_calculation.out absq -eV -x06800 -x17000 -w1 -n5000
```

where the `absq` adds the aforementioned quadrupole and magnetic dipole contributions to the normal absorption spectrum.

Unlike XES calculations, XAS transitions do not involve a single Kohn-Sham orbital acting as an acceptor. Therefore, it is necessary to visualize the nature of the transition in a different way. A convenient method is using a transition difference density, which represents where electron density is being lost, the donor(s), and where it is being gained, the acceptor(s). In the case that the donor is the 1s orbital, it is often not visible. The difference density is described simply as

$$\Delta = \mathbf{P}_{\text{ex}} - \mathbf{P}_0 \tag{A.3}$$

where $\mathbf{P}_0$ and $\mathbf{P}_{\text{ex}}$ are the ground and excited state density matrices, respectively. These difference densities can also be visualized with the orca_plot utility,

```
orca_plot my_xas_calculation.gbw -i
```

Again set the number of grid intervals to 80 and set the file format to Gaussian cube. Then instead of selecting an orbital number, choose option 6 to create transition difference densities. You will be asked to give the .cis file (default name should be correct), followed by a list of states to calculate. Enter the states of interest (usually the ones contributing most to the spectrum), and then follow the directions on the screen and go for a beer.

Configuring and Installing ORCA

The installation of ORCA is fairly straightforward; it requires only the download and unpacking of the component binaries and the appropriate path entry. For MacOS, a binaries installer is available at the above website. For installation without GUI access, *e.g.* on the department computing cluster, the following steps should suffice.

1. Download the linux archive, a .tbz file. In the terminal (or PuTTY), upload the archive to your home folder. Use the current version numbers in place of n-n-n

```
scp orca_archive_vn-n-n.tbz user@clustername.chem.washington.edu:~/
```

2. Log in to your cluster account. Move the location of the .tbz file to `~/bin`. If the folder doesn't exist, you'll need to create it first (`mkdir ~/bin`)

```
mv orca_archive_vn-n-n.tbz ~/bin
```

3. Unpack the tarball archive, and then rename the resulting directory to something shorter yet distinct, to make your life easier.

```
tar -xjf orca_archive_vn-n-n.tbz
mv orca_archive_vn-n-n orcannn
```

   Your files should now be in `/home[some number]/user/bin/orcannn`. My directory is home1, so I'll use that from now on, but check where your account is located by typing `pwd` and use the appropriate number.

4. You're now ready to download OpenMPI, the parallelizer that allows ORCA to run across multiple processers. This is, after all, probably the reason you're on the cluster. Starting from ORCA 3.0, OpenMPI version 1.6.5 is required. You can download OpenMPI from the web at www.open-mpi.org, and upload it to your home directory in a manner similar to 1.

5. Unpack this archive as well, but as you'll be compiling it, there's no need to move it.

```
tar -xf openmpi-1.6.5.tar.gz
```

6. Now you'll need to create a folder for your OpenMPI installation, move into your newly unpacked download folder, and configure your installation appropriately. I suggest the following:

   ```
   mkdir ~/lib/openmpi-1.6.5
   cd ~/openmpi-1.6.5
   ./configure --prefix=/home1/user/lib/openmpi-1.6.5
   ```

   A bunch of text will now scroll past the screen. Once it has finished, run

   ```
   make all install
   ```

   Again, a bunch of text will scroll past. This may take some time. Once it has finished, OpenMPI should be installed.

7. You will however need to add the correct path entries so that ORCA knows where to look for the files. In your .bashrc file (assuming you are using a bash shell), add the following lines

   ```
   export LD_LIBRARY_PATH=/home1/user/lib/openmpi-1.6.5/lib:$LD_LIBRARY_PATH
   export PATH=/home1/user/lib/openmpi-1.6.5/bin:$PATH
   alias orca='/home1/user/bin/orcannn/orca'
   ```

   This should now allow orca to be run in parallel from your home folder. The cluster has a queuing protocol however, and so this should not be done. Instead, you will need to submit your calculations to the queue, and this requires a submit script. I have pasted mine below.

8. Create a file (mine is named orca30) and copy the following into it.

   ```
   #!/bin/bash
   ############### Make directory where job was submitted the working directory
   #$ -cwd
   ############### Combine standard error and standard out in one output file
   #$ -j y
   ############### Send email notification on job begin and end
   #$ -m be
   #$ -M jarees@uw.edu
   ############### Assign your job name
   #$ -N v1
   ############### Submit to queue "smp.q" for all parallel jobs
   ############### Use "serial.q" for single processor jobs.
   #$ -q stf.q
   ```

```
#$ -pe impi 8

############## Execute the users shell startup script to define the environment
export LD_LIBRARY_PATH=/home1/jarees/lib/openmpi-1.6.5/lib:$LD_LIBRARY_PATH
export orcaDIR=/home1/jarees/bin/orca303
export PATH=$orcaDIR:/home1/jarees/lib/openmpi-1.6.5/bin:$PATH

RUNJOB="v1"
XYZINP="geominput"
MOINP="moinput"
JOBDIR=$PWD
# User has no permission to create any folder or file in the node.
# A temporary folder for you will be created as
# /state/partition1/random#_queue by system.
NODEDIR=$TMPDIR

cp $JOBDIR/$RUNJOB.inp $NODEDIR
cp $JOBDIR/$XYZINP.xyz $NODEDIR
cp $JOBDIR/$MOINP.gbw $NODEDIR
cd $NODEDIR
echo "[NOTE]Your job is running at $NODEDIR"
nohup $orcaDIR/orca $RUNJOB.inp >& $RUNJOB.out
rm -f *.tmp
rm -f *.tmp*
rm -f *proc*
cp $RUNJOB.* $JOBDIR

# This $NODEDIR ($TMPDIR) folder will be annihilated by system to
# ensure empty scratch space
```

Correct the relevant entries for email address, username, and any differences in path location.

9. To run a new job on the cluster, first modify the entry following `-N` under `...## Assign your job name` (this will be the name given to all the output files), and the `RUNJOB` entry. If you use a file extention other than `.inp`, make sure to change that in the `cp` section. Also, if you are using an `.xyz` file or `.gbw` file to in your calculation, edit those names also.

10. Submit to the queue

```
qsub orca30
```

To check on the status of the queue, you can use the command `qstat`, or for only your jobs, `qstat -u username`. I find it convenient to create an alias in the .bashrc file for the latter command.

Appendix B

Appendix to Chapter 5

B.1 Supplementary Figures

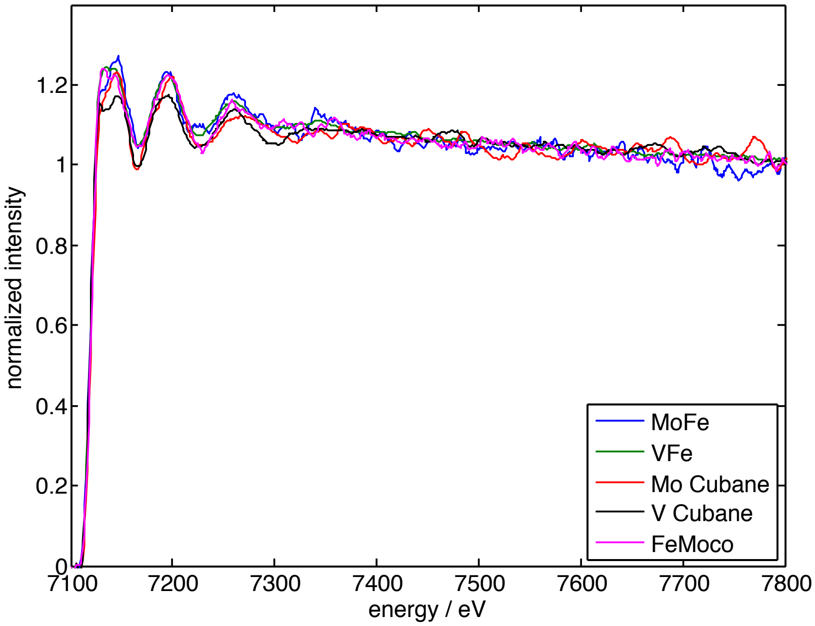

Figure B.1: Overlay of Kα-detected HERFD XAS spectra of MoFe, VFe, and cubane models. The EXAFS region is included, illustrating normalization to the EXAFS tail.

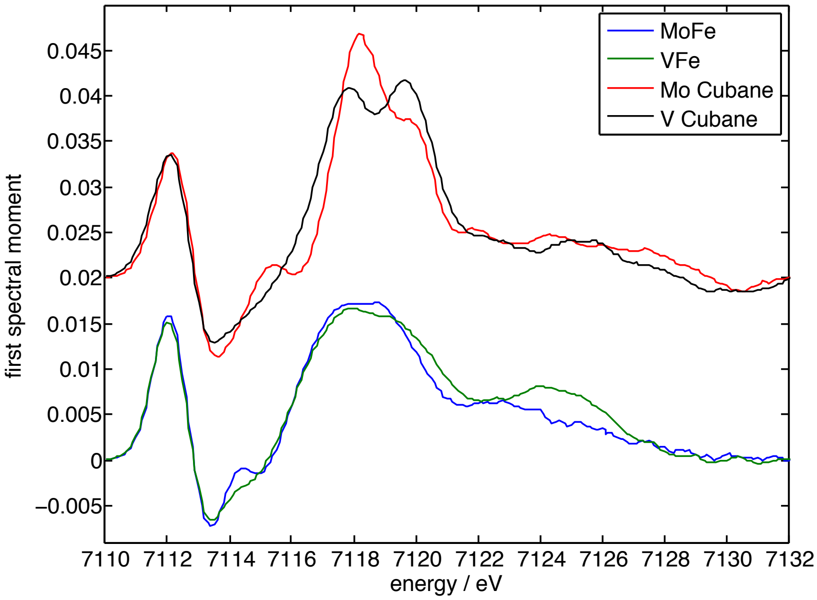

Figure B.2: First spectral moments of the Fe Kα-detected HERFD XAS spectra of Mo and V cubanes, MoFe, VFe, and FeMoco for peak position determination. Cubane spectra have been vertically offset by 0.02. Numerical differentiation and data smoothing was performed using the Savitzky-Golay filter as implemented in EasySpin 5.0.2[196]

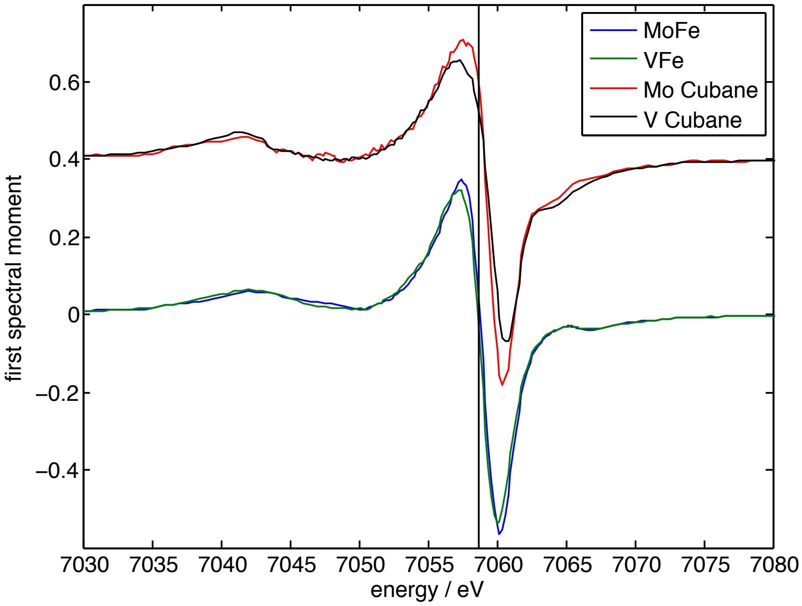

Figure B.3: First spectral moments of the mainline region of the Fe Kβ XES spectra of Mo and V cubanes, MoFe, VFe. The cubane spectra have been vertically offset by 0.4. The vertical line at the K$\beta_{1,3}$ peak position of the protein spectra (7058.7 eV) highlights the difference in the peak position of the cubane spectra. Numerical differentiation and data smoothing was performed using the Savitzky-Golay filter as implemented in EasySpin 5.0.2[196]

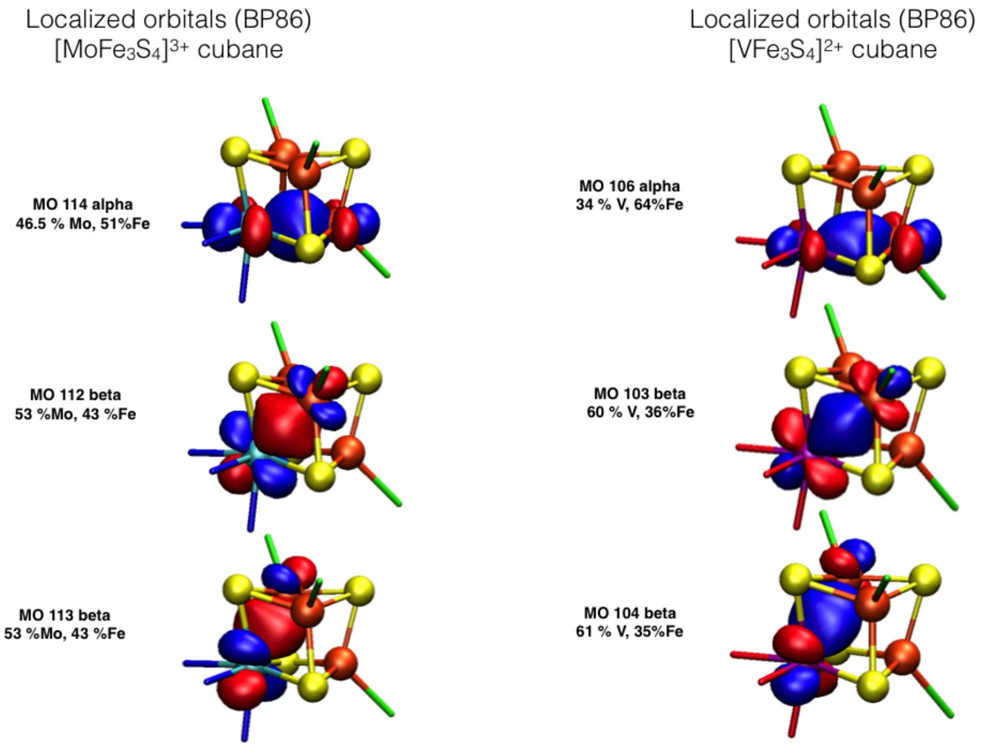

Figure B.4: Occupied Pipek-Mezey localized bonding orbitals of the $[\mathrm{MoFe_3S_4}]^{3+}$ and $[\mathrm{VFe_3S_4}]^{2+}$ model cubanes

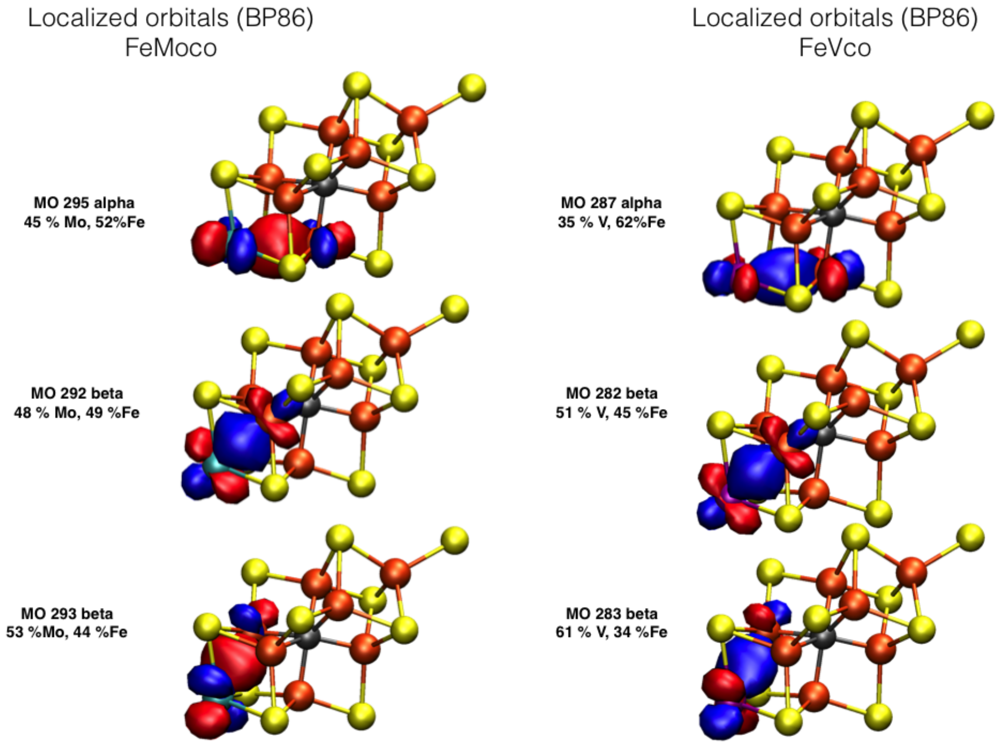

Figure B.5: Occupied Pipek-Mezey localized bonding orbitals of FeMoco and FeVco

Appendix C

Appendix to Chapter 6

C.1 XAS Data

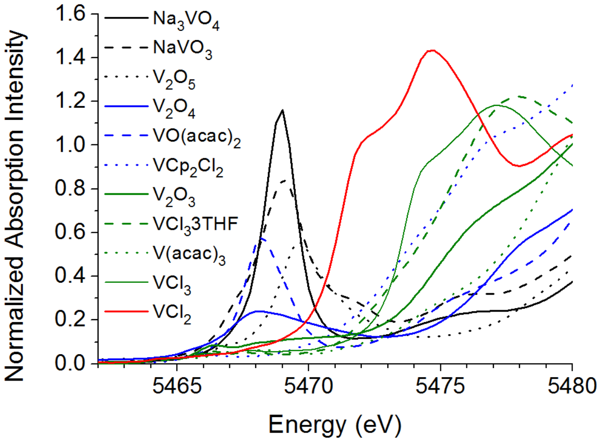

Figure C.1: Overlay of experimental XAS spectra showing the full edge region and colored by oxidation state

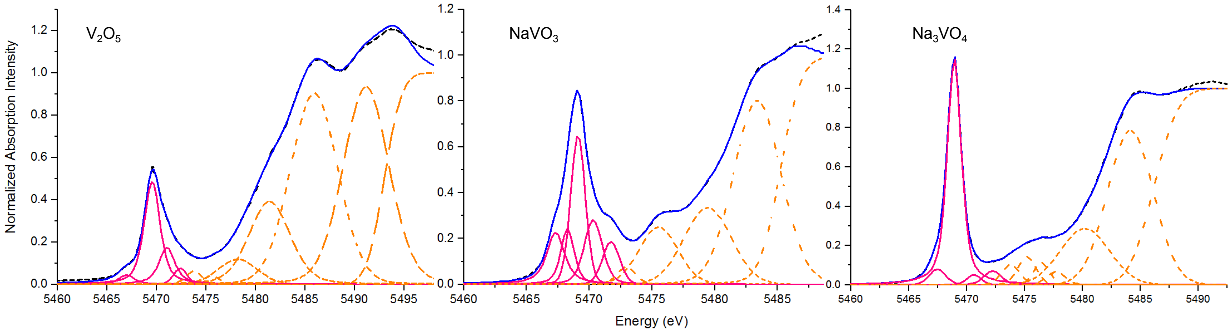

Figure C.2: Experimental XAS spectra and fits of the V(V) compounds. Black dashes are experimental data, blue trace is total fit, and magenta peaks are those included in the pre-edge area

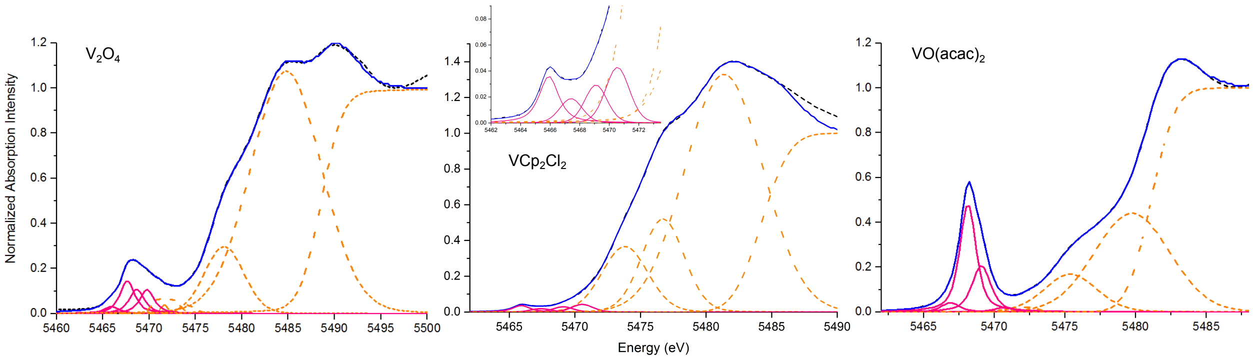

Figure C.3: Experimental XAS spectra and fits of the V(IV) compounds. Black dashes are experimental data, blue trace is total fit, and magenta peaks are those included in the pre-edge area

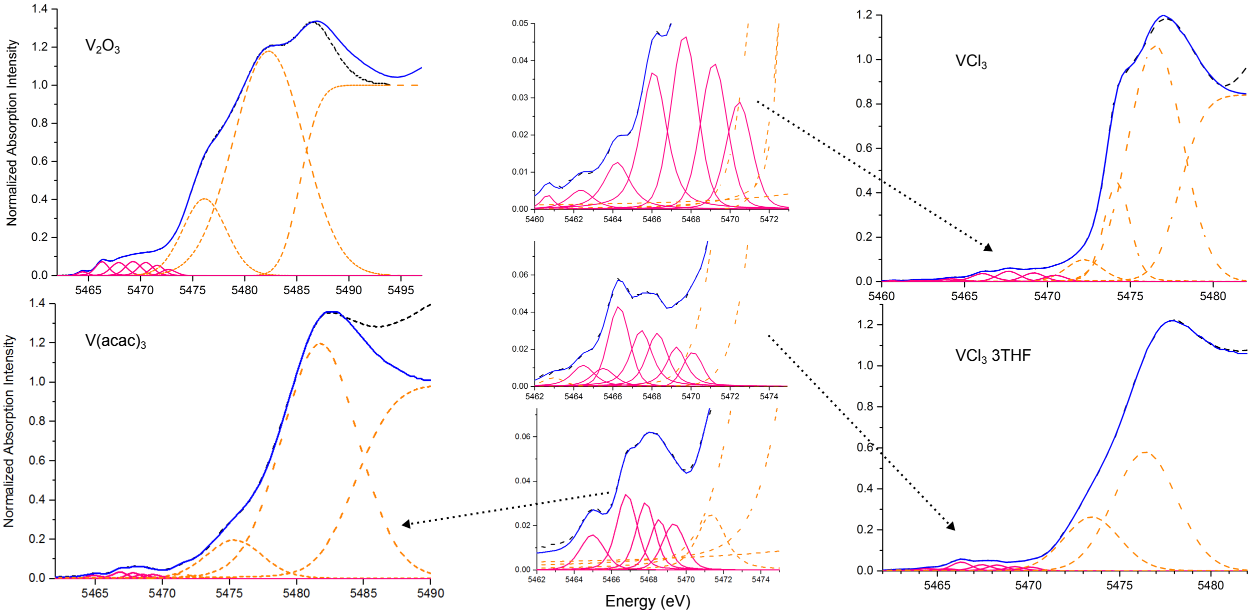

Figure C.4: Experimental XAS spectra and fits of the V(III) compounds. Black dashes are experimental data, blue trace is total fit, and magenta peaks are those included in the pre-edge area. The central column shows enlargements of the pre-edge regions for selected compounds

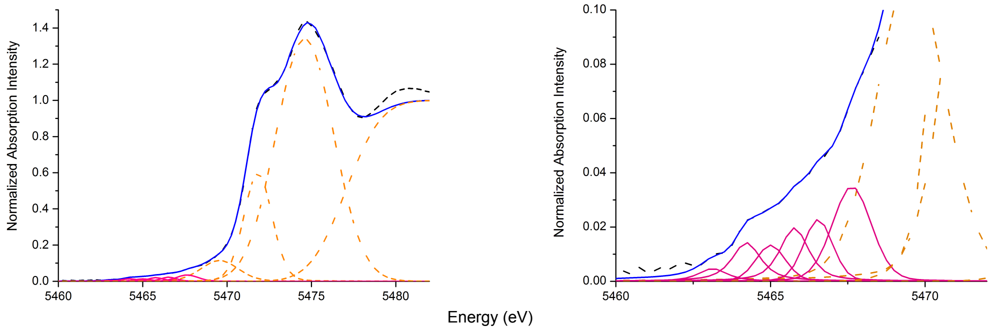

Figure C.5: Experimental XAS spectrum and fit of VCl_2. Black dashes are experimental data, blue trace is total fit, and magenta peaks are those included in the pre-edge area. Left: complete XANES region. Right: enlargement of the pre-edge region

C.2 XES Data

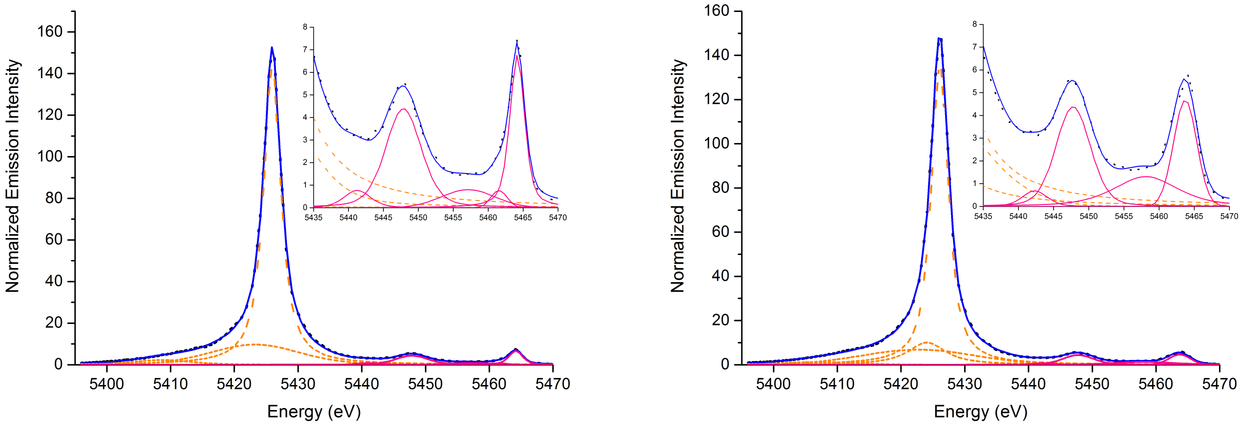

Figure C.6: Experimental XES spectra and fits of Na_3VO_4 (left) and $NaVO_3$ (right). Black dashes are experimental data, blue trace is total fit, and magenta peaks are those included in the VtC area. Inset: enlargment of the VtC region

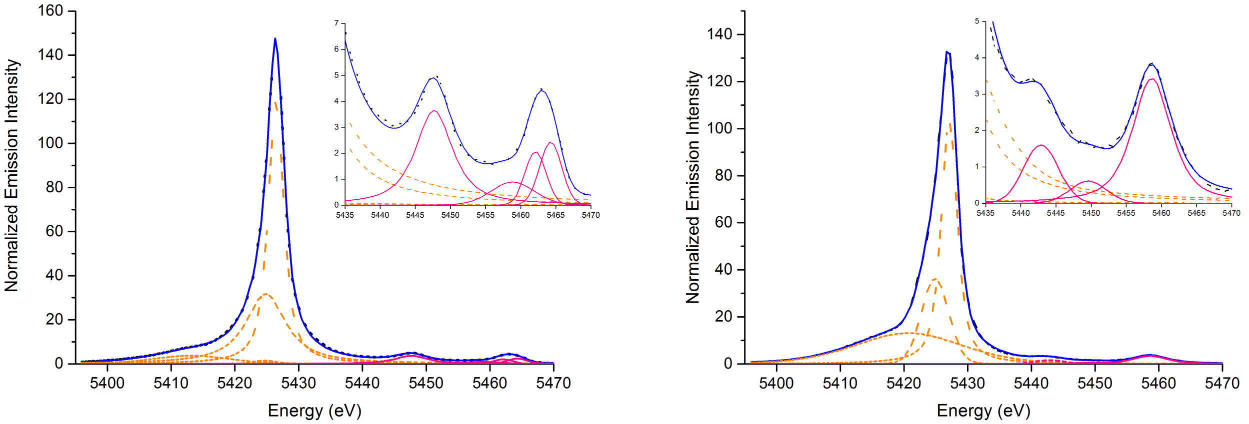

Figure C.7: Experimental XES spectra and fits of V_2O_5 (left) and V_2O_3 (right). Black dashes are experimental data, blue trace is total fit, and magenta peaks are those included in the VtC area. Inset: enlargment of the VtC region

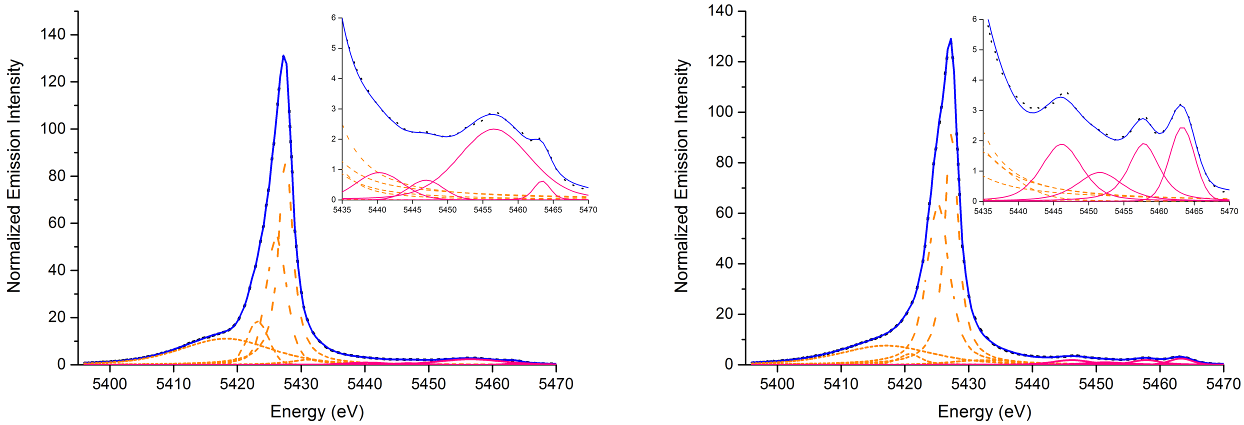

Figure C.8: Experimental XES spectra and fits of V(acac)$_3$ (left) and VO(acac)$_2$ (right). Black dashes are experimental data, blue trace is total fit, and magenta peaks are those included in the VtC area. Inset: enlargment of the VtC region

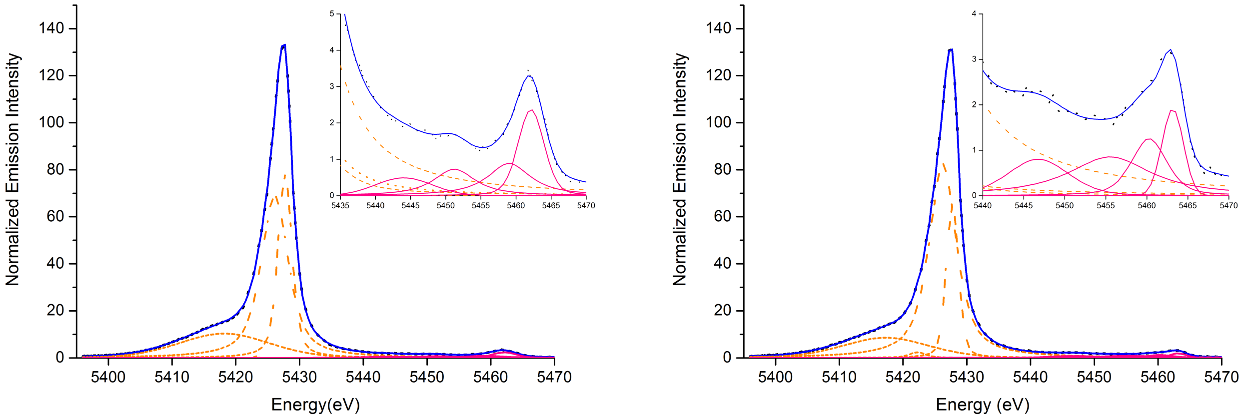

Figure C.9: Experimental XES spectra and fits of VCl$_3$ (left) and VCl$_3 \cdot 3\,$THF (right). Black dashes are experimental data, blue trace is total fit, and magenta peaks are those included in the VtC area. Inset: enlargment of the VtC region

C.3 Sample Input Files

The following are representative input files for the geometry optimizations and spectral calculations of molecular and extended lattice compounds.

A generic geometry optimization was performed using the following input:

```
! UKS Opt BP86 def2-TZVP def2-TZV/J TightSCF
! VerySlowConv Normalprint PAL8

%maxcore 4000

* xyzfile 0 3 V_acac3.xyz
```

An XES calculation was performed using the following input:

```
! UKS BP86 def2-TZVP def2-TZV/J TightSCF
! VerySlowConv Normalprint PAL8

%maxcore 4000

%method
 SpecialGridAtoms 23
       SpecialGridIntAcc 7
end

%xes
  CoreOrb 0,0
 OrbOp 0,1
end

* xyzfile 0 3 V_acac3.xyz
```

An XAS calculation, in this case showing the protocol for an extended lattice solid, was performed using the following input:

```
! UKS B3LYP def2-TZVP def2-TZV/J TightSCF
! VerySlowConv Normalprint PAL8

```

```
%pointcharges "V2O3.pc"

%scf
  MaxIter=2000
end

%maxcore 4000

%method
  SpecialGridAtoms 23
        SpecialGridIntAcc 7
end

%tddft
   NRoots 50
   MaxDim 150
  OrbWin[0]=0,0,-1,-1
   OrbWin[1]=0,0,-1,-1
   DoQuad true
end

* xyz -14 5
O  0.917 10.01 15.179
O  3.257 8.66 15.179
O  5.871 10.01 15.179
O  3.257 11.361 15.179
O  5.733 12.95 15.179
O  1.697 8.501 12.844
O  4.174 10.09 12.844
O  4.174 12.791 12.844
O  1.559 11.44 12.844
O  6.513 11.44 12.844
V  2.477 10.01 13.824
V  4.954 11.44 14.198
V> 0.7496 0 8.58 16.159 NewECP "SD(10,MDF)" end
V> 0.7496 2.477 10.01 16.534 NewECP "SD(10,MDF)" end
V> 0.7496 4.954 8.58 16.159 NewECP "SD(10,MDF)" end
V> 0.7496 7.431 10.01 16.534 NewECP "SD(10,MDF)" end
V> 0.7496 2.477 12.87 16.159 NewECP "SD(10,MDF)" end
V> 0.7496 4.954 14.3 16.534 NewECP "SD(10,MDF)" end
V> 0.7496 7.431 12.87 16.159 NewECP "SD(10,MDF)" end
V> 0.7496 2.477 7.15 11.489 NewECP "SD(10,MDF)" end
V> 0.7496 0 8.58 11.863 NewECP "SD(10,MDF)" end
V> 0.7496 0 11.44 11.489 NewECP "SD(10,MDF)" end
V> 0.7496 4.954 8.58 11.863 NewECP "SD(10,MDF)" end
V> 0.7496 4.954 11.44 11.489 NewECP "SD(10,MDF)" end
V> 0.7496 2.477 12.87 11.863 NewECP "SD(10,MDF)" end
V> 0.7496 7.431 12.87 11.863 NewECP "SD(10,MDF)" end
V> 0.7496 2.477 7.15 14.198 NewECP "SD(10,MDF)" end
V> 0.7496 0 11.44 14.198 NewECP "SD(10,MDF)" end
V> 0.7496 7.431 10.01 13.824 NewECP "SD(10,MDF)" end
```

```
V> 0.7496 4.954 14.3 13.824 NewECP "SD(10,MDF)" end
*
```

Bibliography

[1] Christianson, D. *Prog. Biophys. Molec. Biol.* **1997**, *67*, 217–252.

[2] Pecoraro, V. L.; Baldwin, M. J.; Gelasco, A. *Chem. Rev.* **1994**, *94*, 807–826.

[3] Holm, R. H.; Kennepohl, P.; Solomon, E. I. *Chem. Rev.* **1996**, *96*, 2239–2314.

[4] Lancaster, K. M. *Mol. Electron. Struct. Transit. Met. Complexes I*; Springer Berlin Heidelberg, 2011; pp 119–153.

[5] Jackson, T. a.; Brunold, T. C. *Acc. Chem. Res.* **2004**, *37*, 461–470.

[6] Sugio, S.; Hiraoka, B. Y.; Yamakura, F. *Eur. J. Biochem.* **2000**, *267*, 3487–3495.

[7] Tabares, L. C.; Bittel, C.; Carrillo, N.; Bortolotti, A.; Cortez, N. *J. Bacteriol.* **2003**, *185*, 3223–3227.

[8] Roos, K.; Siegbahn, P. E. M. *J. Biol. Inorg. Chem.* **2012**, *17*, 363–373.

[9] Wennman, A.; Oliw, E. H.; Karkehabadi, S.; Chen, Y. *J. Biol. Chem.* **2016**, *291*, jbc.M115.707380.

[10] Hamberg, M.; Su, C.; Oliw, E. *J. Biol. Chem.* **1998**, *273*, 13080–13088.

[11] Reece, S. Y.; Nocera, D. G. *Annu. Rev. Biochem.* **2009**, *78*, 673–699.

[12] Coggins, M. K. Small Molecule Activation Studies Involving Thiolate-Ligated Manganese (II) Complexes and Biologically-Relevant Oxidants. Ph.D. thesis, University of Washington, 2012.

[13] Whittaker, J. W. **2012**, *525*, 111–120.

[14] Wu, A. J.; Penner-Hahn, J. E.; Pecoraro, V. L. *Chem. Rev.* **2004**, *104*, 903–938.

[15] Stubbe, J.; Nocera, D. G.; Yee, C. S.; Chang, M. C. Y. *Chem. Rev.* **2003**, *103*, 2167–2201.

[16] Yokoyama, K.; Smith, A. a.; Corzilius, B.; Griffin, R. G.; Stubbe, J. *J. Am. Chem. Soc.* **2011**, *133*, 18420–32.

[17] Minnihan, E. C.; Seyedsayamdost, M. R.; Uhlin, U.; Stubbe, J. *J. Am. Chem. Soc.* **2011**, *133*, 9430–40.

[18] Migliore, A.; Polizzi, N. F.; Therien, M. J.; Beratan, D. N. *Chem. Rev.* **2014**, *114*, 3381–3465.

[19] Boal, A. K.; Cotruvo, J. a.; Stubbe, J.; Rosenzweig, A. C. *Science* **2010**, *329*, 1526–1530.

[20] Cotruvo, J. a.; Stich, T. a.; Britt, R. D.; Stubbe, J. *J. Am. Chem. Soc.* **2013**, *135*, 4027–4039.

[21] Cox, N.; Ogata, H.; Stolle, P.; Reijerse, E.; Auling, G.; Lubitz, W. *J. Am. Chem. Soc.* **2010**, *132*, 11197–213.

[22] Roos, K.; Siegbahn, P. E. M. *Inorg. Chem.* **2013**, *52*, 4173–4184.

[23] Boal, A. K.; Cotruvo, J. A.; Stubbe, J.; Rosenzweig, A. C. *Biochemistry* **2012**, *51*, 3861–3871.

[24] Cotruvo Jr, J.; Stubbe, J. *Biochemistry* **2010**, *49*, 1297–1309.

[25] Högbom, M. *Metallomics* **2011**, *3*, 110–120.

[26] Leto, D. F.; Jackson, T. A. *J. Biol. Inorg. Chem.* **2014**, *19*, 1–15.

[27] Kovacs, J. a. *Acc. Chem. Res.* **2015**, *48*, 2744–2753.

[28] Coggins, M. K.; Sun, X.; Kwak, Y.; Solomon, E. I.; Rybak-Akimova, E.; Kovacs, J. A. *J. Am. Chem. Soc.* **2013**, *135*, 5631–5640.

[29] Rees, J. A.; Martin-Diaconescu, V.; Kovacs, J. A.; DeBeer, S. *Inorg. Chem.* **2015**, *54*, 6410–6422.

[30] McEvoy, J. P.; Brudvig, G. W. *Chem. Rev.* **2006**, *106*, 4455–83.

[31] Pérez-Navarro, M.; Neese, F.; Lubitz, W.; Pantazis, D. A.; Cox, N. *Curr. Opin. Chem. Biol.* **2016**, *31*, 113–119.

[32] Krewald, V.; Retegan, M.; Cox, N.; Messinger, J.; Lubitz, W.; DeBeer, S.; Neese, F.; Pantazis, D. A. *Chem. Sci.* **2015**, *6*, 1676–1695.

[33] Cox, N.; Retegan, M.; Neese, F.; Pantazis, D. a.; Boussac, A.; Lubitz, W. *Science* **2014**, *345*, 804–808.

[34] Pushkar, Y.; Long, X.; Glatzel, P.; Brudvig, G. W.; Dismukes, G. C.; Collins, T. J.; Yachandra, V. K.; Yano, J.; Bergmann, U. *Angew. Chemie Int. Ed.* **2010**, *49*, 800–803.

[35] Kern, J. *et al. Science* **2013**, *340*, 491–495.

[36] Sauer, K.; Yano, J.; Yachandra, V. K. *Photosynth. Res.* **2005**, *85*, 73–86.

[37] Kuzek, D.; Pace, R. J. Probing the Mn oxidation states in the OEC. Insights from spectroscopic, computational and kinetic data. 2001; `http://www.ncbi.nlm.nih.gov/pubmed/11115629`.

[38] Beckwith, M. a.; Ames, W.; Vila, F. D.; Krewald, V.; Pantazis, D. a.; Mantel, C.; Pécaut, J.; Gennari, M.; Duboc, C.; Collomb, M.-N.; Yano, J.; Rehr, J. J.; Neese, F.; DeBeer, S. *J. Am. Chem. Soc.* **2015**, 150929154742000.

[39] Retegan, M.; Cox, N.; Pantazis, D. A.; Neese, F. *Inorg. Chem.* **2014**, *53*, 11785–11793.

[40] Retegan, M.; Krewald, V.; Mamedov, F.; Neese, F.; Lubitz, W.; Cox, N.; Pantazis, D. *Chem. Sci.* **2015**, *7*, 72–84.

[41] Coggins, M. K.; Martin-Diaconescu, V.; DeBeer, S.; Kovacs, J. A. *J. Am. Chem. Soc.* **2013**, *135*, 4260–4272.

[42] Coggins, M. K.; Kovacs, J. A. *J. Am. Chem. Soc.* **2011**, *133*, 12470–3.

[43] So, H.; Park, Y. J.; Cho, K.-B.; Lee, Y.-M.; Seo, M. S.; Cho, J.; Sarangi, R.; Nam, W. *J. Am. Chem. Soc.* **2014**, 8–11.

[44] Colmer, H. E.; Howcroft, A. W.; Jackson, T. a. *Inorg. Chem.* **2016**, acs.inorgchem.5b02398.

[45] Leto, D. F.; Jackson, T. A. *Inorg. Chem.* **2014**, *53*, 6179–6194.

[46] Shook, R. L.; Gunderson, W. a.; Greaves, J.; Ziller, J. W.; Hendrich, M. P.; Borovik, a. S. *J. Am. Chem. Soc.* **2008**, *130*, 8888–9.

[47] Geiger, R. a.; Leto, D. F.; Chattopadhyay, S.; Dorlet, P.; Anxolabéhère-Mallart, E.; Jackson, T. a. *Inorg. Chem.* **2011**, *50*, 10190–203.

[48] Annaraj, J.; Cho, J.; Lee, Y.-M.; Kim, S. Y.; Latifi, R.; de Visser, S. P.; Nam, W. *Angew. Chemie Int. Ed.* **2009**, *48*, 4150–4153.

[49] Yoon, H.; Morimoto, Y.; Lee, Y.-M.; Nam, W.; Fukuzumi, S. *Chem. Commun. (Camb).* **2012**, *48*, 11187–9.

[50] Chen, J.; Lee, Y.-M.; Davis, K. M.; Wu, X.; Seo, M. S.; Cho, K.-B.; Yoon, H.; Park, Y. J.; Fukuzumi, S.; Pushkar, Y. N.; Nam, W. *J. Am. Chem. Soc.* **2013**,

[51] Cho, J.; Sarangi, R.; Nam, W. *Acc. Chem. Res.* **2012**, *45*, 1321–1330.

[52] Yoon, H.; Lee, Y.-m.; Wu, X.; Cho, K.-b.; Sarangi, R.; Nam, W.; Fukuzumi, S. *J. Am. Chem. Soc.* **2013**, *135*, 9186–9194.

[53] Lassalle-Kaiser, B. *et al. Inorg. Chem.* **2013**, *52*, 12915–12922.

[54] Krewald, V.; Lassalle-Kaiser, B.; Boron, T. T.; Pollock, C. J.; Kern, J.; Beckwith, M. A.; Yachandra, V. K.; Pecoraro, V. L.; Yano, J.; Neese, F.; DeBeer, S. *Inorg. Chem.* **2013**, *52*, 12904–12914.

[55] Tsui, E. Y.; Tran, R.; Yano, J.; Agapie, T. *Nat. Chem.* **2013**, *5*, 293–299.

[56] Zhang, Y.; Mukamel, S.; Khalil, M.; Govind, N. *J. Chem. Theory Comput.* **2015**, acs.jctc.5b00763.

[57] Eady, R. *Coord. Chem. Rev.* **2003**, *237*, 23–30.

[58] Seefeldt, L. C.; Hoffman, B. M.; Dean, D. R. *Annu. Rev. Biochem.* **2009**, *78*, 701–722.

[59] Kim, J.; Rees, D. C. *Science* **1992**, *257*, 1677–82.

[60] Kim, J.; Rees, D. C. *Nature* **1992**, *360*, 553–60.

[61] Ribbe, M. W.; Hu, Y.; Hodgson, K. O.; Hedman, B. *Chem. Rev.* **2014**, *114*, 4063–4080.

[62] Rees, D. C.; Howard, J. B. *Curr. Opin. Chem. Biol.* **2000**, *4*, 559–566.

[63] Chan, M. K.; Kim, J.; Rees, D. C. *Science* **1993**, *260*, 792–4.

[64] Einsle, O.; Tezcan, F. A.; Andrade, S. L. A.; Rees, D. C. *Science* **2002**, *297*, 1696–1700.

[65] MacKay, B. A.; Fryzuk, M. D. *Chem. Rev.* **2004**, *104*, 385–401.

[66] Harris, T. V.; Szilagyi, R. K. *Inorg. Chem.* **2011**, *50*, 4811–4824.

[67] Lee, S. C.; Holm, R. H. *Chem. Rev.* **2004**, *104*, 1135–1158.

[68] Lancaster, K. M.; Roemelt, M.; Ettenhuber, P.; Hu, Y.; Ribbe, M. W.; Neese, F.; Bergmann, U.; DeBeer, S. *Science* **2011**, *334*, 974–977.

[69] Spatzal, T.; Aksoyoglu, M.; Zhang, L.; Andrade, S. L. A.; Schleicher, E.; Weber, S.; Rees, D. C.; Einsle, O. *Science* **2011**, *334*, 940–940.

[70] Lancaster, K. M.; Hu, Y.; Bergmann, U.; Ribbe, M. W.; DeBeer, S. *J. Am. Chem. Soc.* **2013**, *135*, 610–612.

[71] Wiig, J. A.; Hu, Y.; Lee, C. C.; Ribbe, M. W. *Science* **2012**, *337*, 1672–1676.

[72] Noodleman, L.; Lovell, T.; Liu, T.; Himo, F.; Torres, R. a. *Curr. Opin. Chem. Biol.* **2002**, *6*, 259–273.

[73] Bjornsson, R.; Lima, F. A.; Spatzal, T.; Weyhermüller, T.; Glatzel, P.; Bill, E.; Einsle, O.; Neese, F.; DeBeer, S. *Chem. Sci.* **2014**, *5*, 3096–3103.

[74] Bortels, H. *Zentralbl Bakt II Abt* **1933**, *87*, 476–477.

[75] Lee, C. C.; Hu, Y.; Ribbe, M. W. *Proc. Natl. Acad. Sci.* **2009**, *106*, 9209–9214.

[76] Arber, J.; Dobson, B.; Eady, R. R.; Stevens, P.; Hasnain, S.; Garner, C. D.; Smith, B. *Nature* **1987**, *325*, 372–374.

[77] George, G.; Coyle, C.; Hales, B. J.; Cramer, S. P. *J. Am. Chem. Soc.* **1988**, *110*, 4057–4059.

[78] Simpson, F. B.; Burris, R. H. *Sci. (New York, NY)* **1984**, *224*, 1095–1097.

[79] Stacey, G. S.; Burris, R. H.; Evans, H. J. *Biological Nitrogen Fixation*; Chapman & Hall: New York, NY, 1992.

[80] Hoffman, B. M.; Lukoyanov, D.; Yang, Z. Y.; Dean, D. R.; Seefeldt, L. C. *Chem. Rev.* **2014**, *114*, 4041–4062.

[81] George, S. J.; Barney, B. M.; Mitra, D.; Igarashi, R. Y.; Guo, Y.; Dean, D. R.; Cramer, S. P.; Seefeldt, L. C. *J. Inorg. Biochem.* **2012**, *112*, 85–92.

[82] Hwang, J.; Chen, C.; Burris, R. H. *Biochim. Biophys. Acta* **1973**, *292*, 256–270.

[83] Davis, L. C.; Henzl, M. T.; Burris, R. H.; Orme-Johnson, W. H. *Biochemistry* **1979**, *18*, 4860–4869.

[84] Scott, A. D.; Pelmenschikov, V.; Guo, Y.; Yan, L.; Wang, H.; George, S. J.; Dapper, C. H.; Newton, W. E.; Yoda, Y.; Tanaka, Y.; Cramer, S. P. *J. Am. Chem. Soc.* **2014**, *136*, 15942–15954.

[85] Spatzal, T.; Perez, K. A.; Einsle, O.; Howard, J. B.; Rees, D. C. *Science* **2014**, *345*, 1620–1623.

[86] Lee, C. C.; Hu, Y.; Ribbe, M. W. *Science* **2010**, *329*, 642.

[87] Lee, C. C.; Fay, A. W.; Weng, T.-C.; Krest, C. M.; Hedman, B.; Hodgson, K. O.; Hu, Y.; Ribbe, M. W. *Proc. Natl. Acad. Sci.* **2015**, *112*, 13845–13849.

[88] Lawrence Berkeley National Lab, *X-ray Data Booklet*; 2009.

[89] Kowalska, J. K.; Lima, F. A.; Pollock, C. J.; Rees, J. A.; DeBeer, S. *Isr. J. Chem.* **2016**, *14853*, 1–14.

[90] DeBeer George, S.; Petrenko, T.; Neese, F. *J. Phys. Chem. A* **2008**, *112*, 12936–12943.

[91] Rehr, J. J.; Albers, R. C. *Rev. Mod. Phys.* **2000**, *72*, 621–654.

[92] Pollock, C. J.; Delgado-Jaime, M. U.; Atanasov, M.; Neese, F.; DeBeer, S. *J. Am. Chem. Soc.* **2014**, *136*, 9453–9463.

[93] Levine, I. N. *Molecular Spectroscopy.*

[94] McHale, J. L. *Molecular Spectroscopy*, 1st ed.; Prentice-Hall, Inc., 1999.

[95] Rees, J. A.; Wandzilak, A.; Maganas, D.; Wurster, N. I. C.; Hugenbruch, S.; Kowalska, J. K.; Pollock, C. J.; Lima, F. A.; Finkelstein, K. D.; DeBeer, S. *J. Biol. Inorg. Chem.* **2016**,

[96] Levine, I. N. *Quantum Chemistry.*

[97] Kowalska, J.; DeBeer, S. *Biochim. Biophys. Acta - Mol. Cell Res.* **2015**, *1853*, 1406–1415.

[98] Kowalska, J. K.; Hahn, A. W.; Albers, A.; Schiewer, C. E.; Bjornsson, R.; Lima, F. A.; Meyer, F.; DeBeer, S. *Inorg. Chem.* **2016**, *55*, 4485–4497.

[99] Glaser, T.; Hedman, B.; Hodgson, K. O.; Solomon, E. I. *Acc. Chem. Res.* **2000**, *33*, 859–868.

[100] Kovacs, J. A.; Brines, L. M. *Acc. Chem. Res.* **2007**, *40*, 501–509.

[101] Solomon, E. I.; Szilagyi, R. K.; DeBeer George, S.; Basumallick, L. *Chem. Rev.* **2004**, *104*, 419.

[102] de Groot, F. *Chem. Rev.* **2001**, *101*, 1779–1808.

[103] Glatzel, P.; Bergmann, U. *Coord. Chem. Rev.* **2005**, *249*, 65–95.

[104] Hugenbruch, S.; Shafaat, H. S.; Krämer, T.; Delgado-Jaime, M. U.; Weber, K.; Neese, F.; Lubitz, W.; DeBeer, S. *Phys. Chem. Chem. Phys.* **2016**, *18*, 10688–10699.

[105] Pollock, C. J.; DeBeer, S. *J. Am. Chem. Soc.* **2011**, *133*, 5594–5601.

[106] Pollock, C. J.; DeBeer, S. *Acc. Chem. Res.* **2015**, *48*, 2967–2975.

[107] Pollock, C. J.; Grubel, K.; Holland, P. L.; DeBeer, S. *J. Am. Chem. Soc.* **2013**, *135*, 11803–11808.

[108] Kupper, C.; Rees, J. A.; Dechert, S.; DeBeer, S.; Meyer, F. *J. Am. Chem. Soc.* **2016**, *138*, 7888–7898.

[109] Rees, J. A.; Bjornsson, R.; Schlesier, J.; Sippel, D.; Einsle, O.; DeBeer, S. *Angew. Chemie Int. Ed.* **2015**, *54*, 13249–13252.

[110] Hämäläinen, K.; Siddons, D. P.; Hastings, J. B.; Berman, L. E. *Phys. Rev. Lett.* **1991**, *67*, 2850–2853.

[111] Lima, F. A.; Bjornsson, R.; Weyhermüller, T.; Chandrasekaran, P.; Glatzel, P.; Neese, F.; DeBeer, S. *Phys. Chem. Chem. Phys.* **2013**, *15*, 20911–20920.

[112] Wang, X.; Randall, C. R.; Peng, G.; Cramer, S. P. *Chem. Phys. Lett.* **1995**, *243*, 469–473.

[113] Leidel, N.; Chernev, P.; Havelius, K. G. V.; Ezzaher, S.; Ott, S.; Haumann, M. *Inorg. Chem.* **2012**, *51*, 4546–4559.

[114] Coggins, M. K.; Toledo, S.; Shaffer, E.; Kaminsky, W.; Shearer, J.; Kovacs, J. A. *Inorg. Chem.* **2012**, *51*, 6633–44.

[115] Roemelt, M.; Beckwith, M. A.; Duboc, C.; Collomb, M.-N.; Neese, F.; DeBeer, S. *Inorg. Chem.* **2012**, *51*, 680–687.

[116] Lee, N.; Petrenko, T.; Bergmann, U.; Neese, F.; DeBeer, S. *J. Am. Chem. Soc.* **2010**, *132*, 9715–9727.

[117] Neese, F. *Wiley Interdiscip. Rev. Comput. Mol. Sci.* **2012**, *2*, 73–78.

[118] Lenthe, E. V.; Avoird, A. V. D.; Wormer, P. E. S. *J. Chem. Phys.* **1998**, *109*, 392.

[119] Grimme, S.; Ehrlich, S.; Goerigk, L. *J. Comput. Chem.* **2011**, *32*, 1456.

[120] Grimme, S.; Antony, J.; Ehrlich, S.; Krieg, H. *J. Chem. Phys.* **2010**, *132*, 154104.

[121] Pantazis, D. A.; Chen, X. Y.; Landis, C. R.; Neese, F. *J. Chem. Theory Comput.* **2008**, *4*, 908–919.

[122] Weigend, A. *Phys. Chem. Chem. Phys.* **2006**, *8*, 1057.

[123] Klamt, A.; Schüürmann, G. *J. Chem. Soc., Perkin Trans. 2* **1993**, *5*, 799–805.

[124] Becke, A. *Phys. Rev. A* **1988**, *38*, 3098–3100.

[125] Perdew, J. *Phys. Rev. B* **1986**, *33*, 8822–8824.

[126] Hess, B. A.; Marian, C. M.; Wahlgren, U.; Gropen, O. *Chem. Phys. Lett.* **1996**, *251 (5-6)*, 365.

[127] Beckwith, M. A.; Roemelt, M.; Collomb, M.-N.; DuBoc, C.; Weng, T.-C.; Bergmann, U.; Glatzel, P.; Neese, F.; DeBeer, S. *Inorg. Chem.* **2011**, *50*, 8397–8409.

[128] Hirata, S.; Head-Gordon, M. *Chem. Phys. Lett.* **1999**, *314*, 291–299.

[129] Neese, F.; Olbrich, G. *Chem. Phys. Lett.* **2002**, *362*, 170–178.

[130] Dunlap, B. I.; Connolly, J. W. D.; Sabin, J. R. *J. Chem. Phys.* **1979**, *71*, 3396–3402.

[131] Feyereisen, M.; Fitzgerald, G.; Komornicki, A. *Chem. Phys. Lett.* **1993**, *208*, 359–363.

[132] Neese, F. *Coord. Chem. Rev.* **2009**, *253*, 526–563.

[133] Delgado-Jaime, M. U.; DeBeer, S. *J. Comput. Chem.* **2012**, *33*, 2180–2185.

[134] Pettersen, E. F.; Goddard, T. D.; Huang, C. C.; Couch, G. S.; Greenblatt, D. M.; Meng, E. C.; Ferrin, T. E. *J. Comput. Chem.* **2004**, *13*, 1605.

[135] Bauer, M. *Phys. Chem. Chem. Phys.* **2014**, *16*, 13827–37.

[136] Hayashi, H.; Udagawa, Y.; Caliebe, W. a.; Kao, C.-C. *Chem. Phys. Lett.* **2003**, *371*, 125–130.

[137] Delgado-Jaime, M. U.; DeBeer, S.; Bauer, M. *Chem. - A Eur. J.* **2013**, *19*, 15888–15897.

[138] Pollock, C. J.; Tan, L. L.; Zhang, W.; Lancaster, K. M.; Lee, S. C.; DeBeer, S. *Inorg. Chem.* **2014**, *53*, 2591–2597.

[139] Bergmann, U.; Horne, C. R.; Collins, T. J.; Workman, J. M.; Cramer, S. P. *Chem. Phys. Lett.* **1999**, *302*, 119–124.

[140] Yamanaka, S.; Kawakami, T.; Nagao, H.; Yamaguchi, K. *Chem. Phys. Lett.* **1994**, *231*, 25–33.

[141] MacNaughton, J. B.; Näslund, L.-A.; Anniyev, T.; Ogasawara, H.; Nilsson, A. *Phys. Chem. Chem. Phys.* **2010**, *12*, 5712–5716.

[142] Seo, M. S.; Kim, J. Y. J.; Annaraj, J.; Kim, Y.; Lee, Y.-M.; Kim, S.-J.; Kim, J. Y. J.; Nam, W. *Angew. Chemie Int. Ed.* **2007**, *46*, 377–380.

[143] Pollock, C. J.; Lancaster, K. M.; Finkelstein, K. D.; DeBeer, S. *Inorg. Chem.* **2014**, *53*, 10378–10385.

[144] Burgess, B. K. *Chem. Rev.* **1990**, *90*, 1377–1406.

[145] Robson, R. L.; Eady, R. R.; Richardson, T. H.; Miller, R. W.; Hawkins, M.; Postgate, J. R. *Nature* **1986**, *322*, 388.

[146] Hales, B. J.; Case, E. E.; Morningstar, J. E.; Dzeda, M. F.; Mauterer, L. A. *Biochemistry* **1986**, *25*, 7251–7255.

[147] Hu, Y.; Lee, C. C.; Ribbe, M. W. *Science* **2011**, *333*, 753–755.

[148] Yang, Z. Y.; Dean, D. R.; Seefeldt, L. C. *J. Biol. Chem.* **2011**, *286*, 19417–19421.

[149] Sarma, R.; Barney, B. M.; Keable, S.; Dean, D. R.; Seefeldt, L. C.; Peters, J. W. *J. Inorg. Biochem.* **2010**, *104*, 385–389.

[150] Chen, J.; Christiansen, J.; Tittsworth, R. C.; Hales, B. J.; George, S. J.; Coucouvanis, D.; Cramer, S. P. *J. Am. Chem. Soc.* **1993**, *115*, 5509–5515.

[151] Fay, A. W.; Blank, M. A.; Lee, C. C.; Hu, Y.; Hodgson, K. O.; Hedman, B.; Ribbe, M. W. *J. Am. Chem. Soc.* **2010**, *132*, 12612–12618.

[152] Blank, M. A.; Lee, C. C.; Hu, Y.; Hodgson, K. O.; Hedman, B.; Ribbe, M. W. *Inorg. Chem.* **2011**, *50*, 7123–7128.

[153] Hu, Y.; Corbett, M. C.; Fay, A. W.; Webber, J. A.; Hedman, B.; Hodgson, K. O.; Ribbe, M. W. *Proc. Natl. Acad. Sci.* **2005**, *102*, 13825–13830.

[154] Hu, Y.; Lee, C. C.; Ribbe, M. W. *Dalt. Trans.* **2012**, *41*, 1118–1127.

[155] Rebelein, J. G.; Hu, Y.; Ribbe, M. W. *Angew. Chemie Int. Ed.* **2014**, *53*, 11543–11546.

[156] Newton, J.; Wilson, P. *Antonie Van Leeuwenhoek* **1953**, *19*, 71.

[157] Dilworth, M. *Biochim. Biophys. Acta* **1966**, *127*, 285–294.

[158] Hess, B. A. *Phys. Rev. A At., Mol., Opt. Phys.* **1985**, *32*, 756.

[159] Jansen, G.; Hess, B. A. *Phys. Rev. A At., Mol., Opt. Phys.* **1989**, *39*, 6016.

[160] Hess, B. A. *Phys. Rev. A At., Mol., Opt. Phys.* **1986**, *33*, 3742.

[161] Weigend, F.; Ahlrichs, R. *Phys. Chem. Chem. Phys.* **2005**, *7*, 3297–3305.

[162] Eady, R. R.; Antonyuk, S. V.; Hasnain, S. S. *Curr. Opin. Chem. Biol.* **2016**, *31*, 103–112.

[163] Einsle, O. *J. Biol. Inorg. Chem.* **2014**, *19*, 737–745.

[164] Corbett, M. C.; Hu, Y.; Naderi, F.; Ribbe, M. W.; Hedman, B.; Hodgson, K. O. *J. Biol. Chem.* **2004**, *279*, 28276–28282.

[165] Ribbe, M. W.; Hu, Y.; Guo, M.; Schmid, B.; Burgess, B. K. *J. Biol. Chem.* **2002**, *277*, 23469–23476.

[166] Spatzal, T.; Einsle, O.; Andrade, S. L. A. *Angew. Chemie Int. Ed.* **2013**, *52*, 10116–10119.

[167] Spatzal, T.; Schlesier, J.; Burger, E.-M.; Sippel, D.; Zhang, L.; Andrade, S. L.; Rees, D. C.; Einsle, O. *Nat. Commun.* **2016**, *7*, 10902.

[168] Lukoyanov, D.; Yang, Z.-Y.; Khadka, N.; Dean, D. R.; Seefeldt, L. C.; Hoffman, B. M. *J. Am. Chem. Soc.* **2015**, *137*, 3610–3615.

[169] Lovell, T.; Torres, R. a.; Han, W.-G.; Liu, T.; Case, D. a.; Noodleman, L. *Inorg. Chem.* **2002**, *41*, 5744–5753.

[170] Spatzal, T.; Perez, K. A.; Howard, J. B.; Rees, D. C. *eLife* **2015**, *4*, 1–11.

[171] Lee, S. C.; Lo, W.; Holm, R. H. *Chem. Rev.* **2014**, *16*, 3579–3600.

[172] Coucouvanis, D.; Al-Ahmad, S.; Salifoglou, A.; Dunham, W. R.; Sands, R. H. *Angew. Chemie Int. Ed. English* **1988**, *27*, 1353–1355.

[173] Malinak, S.; Demadis, K. D.; Coucouvanis, D. *J. Am. Chem. Soc.* **1995**, *117*, 3126–3133.

[174] Bjornsson, R.; Neese, F.; Schrock, R. R.; Einsle, O.; DeBeer, S. *J. Biol. Inorg. Chem.* **2015**, *20*, 447–460.

[175] Hedman, B.; Frank, P.; Gheller, S. F.; Roe, a. L.; Newton, W. E.; Hodgson, K. O. *J. Am. Chem. Soc.* **1988**, *110*, 3798–3805.

[176] Conradson, S. D.; Burgess, B. K.; Newton, W. E.; McDonald, J. W.; Rubinson, J. F.; Gheller, S. F.; Mortenson, L. E.; Adams, M. W. W.; Mascharak, P. K. *J. Am. Chem. Soc.* **1985**, *107*, 7935–7940.

[177] Fomitchev, D. V.; McLauchlan, C. C.; Holm, R. H. *Inorg. Chem.* **2002**, *41*, 958–966.

[178] Kovacs, J. A.; Holm, R. H. *J. Am. Chem. Soc.* **1986**, *108*, 340–341.

[179] Carney, M. J.; Kovacs, J. A.; Zhang, Y. P.; Papaefthymiou, G. C.; Spartalian, K.; Frankel, R. B.; Holm, R. H. *Inorg. Chem.* **1987**, *26*, 719–724.

[180] Sumegi, B.; Sherry, A. D.; Malloy, C. R. *Biochemistry* **1990**, *29*, 9106–9110.

[181] Hu, Y.; Ribbe, M. W. *J. Biol. Inorg. Chem.* **2014**, *20*, 435–445.

[182] Bjornsson, R.; Delgado-Jaime, M. U.; Lima, F. a.; Sippel, D.; Schlesier, J.; Weyhermüller, T.; Einsle, O.; Neese, F.; DeBeer, S. *Zeitschrift für Anorg. und Allg. Chemie* **2015**, *641*, 65–71.

[183] Cramer, S. P.; Hodgson, K. O.; Gillum, W. O.; Mortenson, L. E. *J. Am. Chem. Soc.* **1978**, *100*, 3398–3407.

[184] Cramer, S. P.; Gillum, W. O.; Hodgson, K. O.; Mortenson, L. E.; Stiefel, E. I.; Chisnell, J. R.; Brill, W. J.; Shah, V. K. *J. Am. Chem. Soc.* **1978**, *100*, 3814–3819.

[185] Arber, J. M.; Dobson, B. R.; Eady, R. R.; Hasnain, S. S.; Garner, C. D.; Matsushita, T.; Nomura, M.; Smith, B. E. *Biochem. J.* **1989**, *258*, 733–737.

[186] Fay, A. W.; Blank, M. A.; Lee, C. C.; Hu, Y.; Hodgson, K. O.; Hedman, B.; Ribbe, M. W. *Angew. Chemie Int. Ed.* **2011**, *50*, 7787–7790.

[187] Strange, R. W.; Eady, R. R.; Lawson, D.; Hasnain, S. S. *J. Synchrotron Radiat.* **2003**, *10*, 71–75.

[188] Singh, J.; Alayon, E. M. C.; Tromp, M.; Safonova, O. V.; Glatzel, P.; Nachtegaal, M.; Frahm, R.; Van Bokhoven, J. A. *Angew. Chemie - Int. Ed.* **2008**, *47*, 9260–9264.

[189] Kroll, T.; Hadt, R. G.; Wilson, S. A.; Lundberg, M.; Yan, J. J.; Weng, T.-c.; Sokaras, D.; Alonso-Mori, R.; Casa, D.; Upton, M. H.; Hedman, B.; Hodgson, K. O.; Solomon, E. I. *J. Am. Chem. Soc.* **2014**, *136*, 18087–18099.

[190] Wang, X.; de Groot, F.; Cramer, S. *Phys. Rev. B* **1997**, *56*, 4553–4564.

[191] Wang, X.; Grush, M. M.; Froeschner, a. G.; Cramer, S. P. *J. Synchrotron Radiat.* **1997**, *4*, 236–242.

[192] Lambertz, C.; Chernev, P.; Klingan, K.; Leidel, N.; Sigfridsson, K. G. V.; Happe, T.; Haumann, M. *Chem. Sci.* **2014**, *5*, 1187–1203.

[193] Pirngruber, G. D.; Grunwaldt, J.-D.; van Bokhoven, J. A.; Kalytta, A.; Reller, A.; Safonova, O. V.; Glatzel, P. *J. Phys. Chem. B* **2006**, *110*, 18104–18107.

[194] Smolentsev, G.; Soldatov, A. V.; Messinger, J.; Merz, K.; Weyhermüller, T.; Bergmann, U.; Pushkar, Y.; Yano, J.; Yachandra, V. K.; Glatzel, P. *J. Am. Chem. Soc.* **2009**, *131*, 13161–13167.

[195] Solé, V.; Papillon, E.; Cotte, M.; Walter, P.; Susini, J. *Spectrochim. Acta, Part B* **2007**, *62*, 63–68.

[196] Stoll, S.; Schweiger, A. *J. Magn. Reson.* **2006**, *178*, 42–55.

[197] Douglas, N.; Kroll, N. *Ann. Phys. (N. Y).* **1974**, 82–89.

[198] Poater, A.; Ragone, F.; Correa, A.; Cavallo, L. *Dalton Trans.* **2011**, *40*, 11066–11079.

[199] Shannon, R. D. *Acta Crystallogr.* **1976**, *A32*, 751–767.

[200] Yao, S.; Meier, F.; Lindenmaier, N.; Rudolph, R.; Blom, B.; Adelhardt, M.; Sutter, J.; Mebs, S.; Haumann, M.; Meyer, K.; Kaupp, M.; Driess, M. *Angew. Chemie Int. Ed.* **2015**, *54*, 12506–12510.

[201] Musgrave, K. B.; Isaac, H.; Li, L.; Burgess, B. K.; Watt, G.; Hedman, B.; Hodgson, K. O. *J. Biol. Inorg. Chem.* **1998**, *3*, 344–352.

[202] Musgrave, K. B.; Angove, H. C.; Burgess, B. K.; Hedman, B.; Hodgson, K. O. *J. Am. Chem. Soc.* **1998**, *120*, 5325–5326.

[203] Shulman, G. R.; Yafet, Y.; Eisenberger, P.; Blumberg, W. E. *Proc. Natl. Acad. Sci.* **1976**, *73*, 1384–1388.

[204] Westre, T. E.; Kennepohl, P.; DeWitt, J. G.; Hedman, B.; Hodgson, K. O.; Solomon, E. I. *J. Am. Chem. Soc.* **1997**, *119*, 6297–6314.

[205] Wang, X.; Grush, M. M.; Froeschner, a. G.; Cramer, S. P. *J. Synchrotron Radiat.* **1997**, *4*, 236–242.

[206] de Groot, F. M. F.; Pizzini, S.; Fontaine, A.; Hämäläinen, K.; Kao, C. C.; Hastings, J. B. *Phys. Rev. B* **1995**, *51*, 1045–1052.

[207] Corbett, M. C.; Hu, Y.; Fay, A. W.; Ribbe, M. W.; Hedman, B.; Hodgson, K. O. *Proc. Natl. Acad. Sci.* **2006**, *103*, 1238–1243.

[208] Seefeldt, L. C.; Hoffman, B. M.; Dean, D. R. *Curr. Opin. Chem. Biol.* **2012**, *16*, 19–25.

[209] Mamedov, E.; Cortés Corberán, V. *Appl. Catal. A Gen.* **1995**, *127*, 1–40.

[210] Blasco, T.; Lopez-Nieto, J. *Appl. Catal. A Gen.* **1997**, *157*, 117–142.

[211] Rehder, D. *Inorg. Chem. Commun.* **2003**, *6*, 604–617.

[212] Rehder, D. *Coord. Chem. Rev.* **1999**, *182*, 297–322.

[213] Crans, D. C.; Smee, J. J.; Gaidamauskas, E.; Yang, L. *Chem. Rev.* **2004**, *104*, 849–902.

[214] Rehder, D. *Metallomics* **2015**, *7*, 730–742.

[215] Butler, A. *Coord. Chem. Rev.* **1999**, *187*, 17–35.

[216] Thompson, K. H.; Orvig, C. *Coord. Chem. Rev.* **2001**, *219-221*, 1033–1053.

[217] Gupta, R.; Hou, G.; Renirie, R.; Wever, R.; Polenova, T. *J. Am. Chem. Soc.* **2015**, *137*, 5618–5628.

[218] Krzystek, J.; Ozarowski, A.; Telser, J.; Crans, D. C. *Coord. Chem. Rev.* **2015**, *301-302*, 123–133.

[219] Fukui, K.; Ueki, T.; Ohya, H.; Michibata, H. *J. Am. Chem. Soc.* **2003**, *125*, 6352–6353.

[220] Maganas, D.; Roemelt, M.; Weyhermüller, T.; Blume, R.; Hävecker, M.; Knop-Gericke, A.; DeBeer, S.; Schlögl, R.; Neese, F. *Phys. Chem. Chem. Phys.* **2014**, *16*, 264–276.

[221] DeBeer George, S.; Brant, P.; Solomon, E. I. *J. Am. Chem. Soc.* **2005**, *127*, 667–674.

[222] Atkins, A. J.; Bauer, M.; Jacob, C. R. *Phys. Chem. Chem. Phys.* **2013**, *15*, 8095–8105.

[223] MacMillan, S. N.; Walroth, R. C.; Perry, D. M.; Morsing, T. J.; Lancaster, K. M. *Inorg. Chem.* **2015**, *54*, 205–214.

[224] March, A. M.; Assefa, T. A.; Bressler, C.; Doumy, G.; Galler, A.; Gawelda, W.; Kanter, E. P.; Németh, Z.; Pápai, M.; Southworth, S. H.; Young, L.; Vankó, G. *J. Phys. Chem. C* **2015**, *119*, 14571–14578.

[225] Lancaster, K. M.; Finkelstein, K. D.; DeDeer, S. *Inorg. Chem.* **2011**, *50*, 6767–6774.

[226] Boubnov, A.; Carvalho, H. W. P.; Doronkin, D. E.; Gu, T.; Gallo, E.; Atkins, A. J.; Jacob, C. R.; Grunwaldt, J.-D. *J. Am. Chem. Soc.* **2014**, *136*, 13006–13015.

[227] Chandrasekaran, P.; Chiang, K. P.; Nordlund, D.; Bergmann, U.; Holland, P. L.; DeBeer, S. *Inorg. Chem.* **2013**, *52*, 6286–6298.

[228] Delgado-Jaime, M. U.; Mewis, C. P.; Kennepohl, P. *J. Synchrotron Radiat.* **2010**, *17*, 132–137.

[229] Jones, J. B.; Urch, D. S. *J. Chem. Soc. Dalt. Trans.* **1975**, 1885.

[230] Schafer, A.; Horn, H.; Ahlrichs, R. *J. Chem. Phys.* **1992**, *97*, 2571–2578.

[231] Lee, C.; Yang, W.; Parr, R. G. *Phys. Rev. B* **1988**, *37*, 785–789.

[232] Maganas, D.; DeBeer, S.; Neese, F. *Inorg. Chem.* **2014**, *53*, 6374–6385.

[233] Roe, A. L.; Schneider, D. J.; Mayer, R. J.; Pyrz, J. W.; Widom, J.; Que, L. *J. Am. Chem. Soc.* **1984**, *106*, 1676–1681.

[234] Chanda, A.; Shan, X.; Chakrabarti, M.; Ellis, W. C.; Popescu, D. L.; Tiago de Oliveira, F.; Wang, D.; Que, L.; Collins, T. J.; Münck, E.; Bominaar, E. L. *Inorg. Chem.* **2008**, *47*, 3669–3678.

[235] Feng, X.; Bott, S. G.; Lippard, S. J. *J. Am. Chem. Soc.* **1989**, *111*, 8046–8047.

[236] de Groot, F. M. *Inorg. Chim. Acta* **2008**, *361*, 850–856.

[237] Kroll, T.; Solomon, E. I.; De Groot, F. M. F. *J. Phys. Chem. B* **2015**, *119*, 13852–13858.

[238] Romelt, M.; Ye, S.; Neese, F. *Inorg. Chem.* **2009**, *48*, 784–785.

VITA

Julian Avery Rees was born in Pittsfield, MA and raised from an early age in Seattle, WA. In 2009 he received a Bachelor of Arts in chemistry from Goucher College in Baltimore, MD, working for Professor Scott P. Sibley on the synthesis and inhibitory effects of group 10 metalloquinoline complexes on amyloid-β fibril formation. He also spent the summer of 2008 as an undergraduate research intern in the protein biochemistry group at the Seattle campus of Amgen, Inc., where he developed a protocol for high-throughput screening of potential antibody-drug conjugates for oncological biotherapeutics. In 2011 Julian moved back to Seattle for graduate studies in chemistry, and joined the research group of Professor Julie A. Kovacs. He spent the 2014-2015 academic year living in Mülheim an der Ruhr, Germany, where he was a DAAD graduate scholar under the direction of Professor Dr. Serena DeBeer at the Max Planck Institute for Chemical Energy Conversion. In his free time, Julian enjoys taking advantage of the Pacific Northwest's opportunities to ski, sail, and hike, and also works on more edible forms of chemistry, including brewing beer and curing and smoking meat.

Kowalska, J.K.; Lima, F.A.; Pollcok, C.J.; Rees, J.A.; DeBeer, S. "A Practical Guide to High-resolution X-ray Spectroscopic Measurements and their Applications in Bioinorganic Chemistry". *Isr. J. Chem.* **2016**, Early view. DOI: 10.1002/ijch.201600037

Rees, J.A.; Wandzilak, A.; Maganas, D.; Wurster, N.; Hugenbruch, S.; Kowalska, J.K.; Pollock, C.J.; Lima, F.A.; Finkelstein, K.D.; DeBeer, S. "Experimental and Theoretical Correlations Between Vanadium K-edge X-ray Absorption and Kβ Emission Spectra." *J. Biol. Inorg. Chem.* **2016**, Epub online, DOI: 10.1007/s00775-016-1358-7

Kupper, C.; Rees, J.A.; Dechert, S.; DeBeer, S.; Meyer, F. "Complete Series of $\{FeNO\}^8$, $\{FeNO\}^7$ and $\{FeNO\}^6$ Complexes Stabilized by a Tetracarbene Macrocycle." *J. Am. Chem. Soc.* **2016**, *138*, 7888-7898

Rees, J. A.; Bjornsson, R.; Schlesier, J.; Sippel, D.; Einsle, O.; DeBeer, S. "The Fe-V Cofactor of Vanadium Nitrogenase Contains an Interstitial Carbon Atom." *Angew. Chem. Int. Ed.* **2015**, *54*, 13249-13252

Rees, J. A.; Martin-Diaconescu, V.; Kovacs, J. A.; DeBeer, S. "X-ray Absorption and Emission Study of Dioxygen Activation by a Small-Molecule Manganese Complex." *Inorg. Chem.* **2015**, *54*, 6410-6422